Contributors to This Volume

W. Parker Alford
M. Kamimura
K. Nagamine
Joseph Speth
Brian M. Spicer
A. W. Thomas

ADVANCES IN NUCLEAR PHYSICS

Edited by
J.W. Negele
and Erich Vogt

VOLUME 24

ADVANCES IN NUCLEAR PHYSICS

VOLUME 24

CONTRIBUTORS TO THIS VOLUME

W. Parker Alford

University of Western Ontario
London, Ontario, Canada, and
TRIUMF
Vancouver, British Columbia, Canada

M. Kamimura

Department of Physics
Kyushu University
Hakozaki, Fukuoka, Japan

K. Nagamine

High Energy Accelerator Research Organization (KEK)
Tsukuba-shi, Ibaraki-ken, Japan, and
The Institute of Physical and Chemical Research (RIKEN)
Wako, Saitama, Japan

Joseph Speth

Institut für Kernphysik
Forschungzentrum Jülich
Jülich, Germany, and
Institut für Theoretische Kernphysik
Universität Bonn
Bonn, Germany

Brian M. Spicer

School of Physics
University of Melbourne
Parkville, Victoria, Australia

A. W. Thomas

Department of Physics and Mathematical Physics and
Institute for Theoretical Physics
The University of Adelaide
Adelaide, South Australia, Australia

ADVANCES IN NUCLEAR PHYSICS

Edited by

J. W. Negele

Center for Theoretical Physics
Massachusetts institute of Technology
Cambridge, Massachusetts

Erich Vogt

Department of Physics
University of British Columbia
Vancouver, British Columbia, Canada

VOLUME 24

KLUWER ACADEMIC PRESS • NEW YORK, BOSTON, DORDRECHT, LONDON, MOSCOW

eBook ISBN: 0-306-47073-X
Print ISBN: 0-306-45757-1

New York, Boston, Dordrecht, London, Moscow

Created in the United States of America

ARTICLES PUBLISHED IN EARLIER VOLUMES

Volume 1

The Reorientation Effect • *J. de Boer and J. Eichler*
The Nuclear SU_3 Model • *M. Harvey*
The Hartree-Fock Theory of Deformed Light Nuclei • *G. Ripka*
The Statistical Theory of Nuclear Reactions • *E. Vogt*
Three-Particle Scattering—A Review of Recent Work on the Nonrelativistic Theory •
I. Duck

Volume 2

The Giant Dipole Resonance • *B. M. Spicer*
Polarization Phenomena in Nuclear Reactions • *C. Glashausser and J. Thirion*
The Pairing-Plus-Quadrupole Model • *D. R. Bes and R. A. Sorensen*
The Nuclear Potential • *P. Signell*
Muonic Atoms • *S. Devons and I. Duerdoth*

Volume 3

The Nuclear Three-Body Problem • *A. N. Mitra*
The Interactions of Pions with Nuclei • *D. S. Koltun*
Complex Spectroscopy • *J. B. French, E. C. Halbert, J. B. McGrory, and S. S. M. Wong*
Single Nucleon Transfer in Deformed Nuclei • *B. Elbeck and P. O. Tjøm*
Isocalar Transition Rates in Nuclei from the (α, α') Reaction *A. M. Bernstein*

Volume 4

The Investigation of Hole States in Nuclei by Means of Knockout and Other Reactions •
Daphne F. Jackson
High-Energy Scattering from Nuclei • *Wieslaw Czyz*
Nucleosynthesis by Charged-Particle Reactions • *C. A. Barnes*
Nucleosynthesis and Neutron-Capture Cross Sections • *B. J. Allen, J. H. Gibbons, and R. L. Macklin*
Nuclear Structure Studies in the $Z = 50$ Region • *Elizabeth Urey Baranger*
An *s-d* Shell-Model Study for $A = 18-22$ • *E. C. Halbert, J. B. McGrory, B. H. Wildenthal. and S. P. Pandy*

Volume 5

Variational Techniques in the Nuclear Three-Body Problem • *L. M. Delves*
Nuclear Matter Calculations • *Donald W. L. Sprung*
Clustering in Light Nuclei • *Akito Arima, Hisashi Horiuchi, Kuniharu Kubodera, and Noburu Takigawa*

Volume 6

Nuclear Fission · *A. Michaudon*
The Microscopic Theory of Nuclear Effective Interactions and Operators • *Bruce R. Barrett and Michael W. Kirson*
Two-Neutron Transfer Reactions and the Pairing Model • *Ricardo Broglia, Ole Hansen, and Claus Riedel*

Volume 7

Nucleon-Nucleus Collisions and Intermediate Structure • *Aram Mekjian*
Coulomb Mixing Effects in Nuclei: A Survey Based on Sum Rules • *A. M. Lane and A. Z. Mekjian*
The Beta Strength Function • *P. G. Hansen*
Gamma-Ray Strength Functions • *G. A. Bartholemew, E. D. Earle. A. J. Ferguson. J. W. Knowles, and M. A. Lone*

Volume 8

Strong Interactions in Λ-Hypernuclei • *A. Gal*
Off-Shell Behavior of the Nucleon-Nucleon Interaction • *M. K. Strivastava and D. W. L. Sprung*
Theoretical and Experimental Determination of Nuclear Charge Distributions • *J. L. Friar and J. W. Negele*

Volume 9

One- and Two-Nucleon Transfer Reactions with Heavy Ions • *Sidney Kahana and A. J. Baltz*
Computational Methods for Shell-Model Calculations • *R. R. Whitehead, A. Watt, B. J. Cole, and I. Morrison*
Radiative Pion Capture in Nuclei • *Helmut W. Baer, Kenneth M. Crowe. and Peter Truöl*

Volume 10

Phenomena in Fast Rotating Heavy Nuclei • *R. M. Lieder and H. Ryde*
Valence and Doorway Mechanisms in Resonance Neutron Capture • *B. J. Allen and A. R. de L. Musgrove*
Lifetime Measurements of Excited Nuclear Levels by Doppler-Shift Methods • *T. K. Alexander and J. S. Forster*

Volume 11

Clustering Phenomena and High-Energy Reactions • *V. G. Neudatchin, Yu. F. Smirnov, and N. F. Golovanova*
Pion Production in Proton-Nucleus Collisions • *B. Holstad*
Fourteen Years of Self-consistent Field Calculations: What Has Been Learned • *J. P. Svenne*
Hartree-Fock-Bogoliubov Theory with Applications to Nuclei • *Alan L. Goodman*
Hamiltonian Field Theory for Systems of Nucleons and Mesons • *Mark Bolsterli*

Volume 12

Hypernetted-Chain Theory of Matter at Zero Temperature • *J. G. Zabolitzky*
Nuclear Transition Density Determinations from Inelastic Electron Scattering • *Jochen Heisenberg*
High-Energy Proton Scattering • *Stephen J. Wallace*

Volume 13

Chiral Symmetry and the Bag Model: A New Starting Point for Nuclear Physics • *A. W. Thomas*
The Interacting Boson Model • *A. Arima and F. Iachella*
High-Energy Nuclear Collisions • *S. Nagamiya and M. Gyullasy*

Volume 14

Single-Particle Properties of Nuclei Through *(e, e′p)* Reactions • *Salvatore Frullani and Jean Mougey*

Volume 15

Analytic Insights into Intermediate-Energy Hadron-Nucleus Scattering • *R. D. Amado*
Recent Developments in Quasi-Free Nucleon Scattering • *P. Kitching, W. J. McDonald, Th. A. J. Maris, and C. A. Z. Vasconcellos*
Energetic Particle Emission in Nuclear Reactions • *David H. Boal*

Volume 16

The Relativistic Nuclear Many-Body Problem • *Brian D. Serot and John Dirk Walecka*

Volume 17

P-Matrix Methods in Hadronic Scattering • *B. L. G. Bakker and P. J. Mulders*
Dibaryon Resonances • *M. P. Locher. M. E. Saino. and A. Švarc*
Skyrmions in Nuclear Physics • *Ulf-G. Meissner and Ismail Zahed*
Microscopic Description of Nucleus-Nucleus Collisions • *Karlheinz Langanke and Harald Friedrich*

Volume 18

Nuclear Magnetic Properties and Gamow-Teller Transitions • *A. Arima, K. Shimizu, W. Bentz, and H. Hyuga*
Advances in Intermediate-Energy Physics with Polarized Deuterons • *J. Arvieux and J. M. Cameron*
$\bar{p}p$ Interaction and the Quest for Baryonium • *C. Amsler*
Radiative Muon Capture and the Weak Pseudoscalar Coupling in Nuclei • *M. Gmitro and P. Truöl*
Introduction to the Weak and Hypoweak Interactions • *T. Goldman*

Volume 19

Experimental Methods for Studying Nuclear Density Distributions • *C. J. Batty, H. J. Gils, and H. Rebel*
The Meson Theory of Nuclear Forces and Nuclear Structure • *R. Machleidt*

Volume 20

Single-Particle Motion in Nuclei • *C. Mahaux and R. Sartor*
Relativistic Hamiltonian Dynamics in Nuclear and Particle Physics • *B. D. Keister and W. N. Polyzou*

Volume 21

Multiquark Systems in Hadronic Physics • *B. L. G. Bakker and I. M. Narodetskii*
The Third Generation of Nuclear Physics with the Microscopic Cluster Model • *Karlheinz Langanke*
The Fermion Dynamical Symmetry Model • *Cheng-Li Wu, Da Hsuan Feng, and Mike Guidry*

Volume 22

Nucleon Models • *Dan Olof Riska*
Aspects of Electromagnetic Nuclear Physics and Electroweak Interactions • *T. W. Donnelly*
Color Transparency and Cross-section Fluctuations in Hadronic Collisions • *Gordon Baym*
Many-Body Methods at Finite Temperature • *D. Vautherin*
Nucleosynthesis in the Big Bang and in the Stars • *K. Langanke and C. A. Barnes*

Volume 23

Light Front Quantization • *Matthias Burkardt*
Nucleon Knockout by Intermediate Energy Electrons • *James J. Kelly*

ARTICLES PLANNED FOR FUTURE VOLUMES

Large N Techniques and Their Application to Baryons • *Aneesh Manohar*
The Spin Structure of the Nucleon • *Bradley Fillipone*
Rotational Phenomena in Atomic Nuclei • *David Ward and Paul Fallon*

PREFACE

The three articles of the present volume pertain to very different subjects, all of considerable current interest. The first reviews the fascinating history of the search for nucleon substructure in the nucleus using the strength of Gamow–Teller excitations. The second deals with deep inelastic lepton scattering as a probe of the non-perturbative structure of the nucleon. The third describes the present state of affairs for muon catalyzed fusion, an application of nuclear physics which many new experiments have helped to elucidate. This volume certainly illustrates the broad range of physics within our field.

The article on Nucleon Charge-Exchange Reactions at Intermediate Energy, by Parker Alford and Brian Spicer, reviews recent data which has clarified one of the greatest puzzles of nuclear physics during the past two decades, namely, the "missing strength" in Gamow–Teller (GT) transitions. The nucleon-nucleon interaction contains a GT component which has a low-lying giant resonance. The integrated GT strength is subject to a GT sum rule. Early experiments with *(n,p)* charge exchange reactions found only about half of the strength, required by the sum rule, in the vicinity of the giant resonance. At the time, new theoretical ideas suggested that the GT strength was especially sensitive to renormalization from effects pertaining to nucleon substructure, particularly the delta excitation of the nucleon in the nucleus. Many conferences, in the early 1980's heralded the charge-exchange experiments as the "smoking gun" for QCD effects in the nucleus at the low energies for which the shell model had so successfully described everything for several generations. Others, more cautious, maintained that the "missing strength" explanation could lie in the domain of the nuclear shell model without specific reference to new QCD effects. The present authors were pioneers in new techniques which provided much new data for both *(p, n)* and *(n, p)* charge exchange, first at TRIUMF and then elsewhere, which solved the mystery. The present review summarizes the techniques and the wealth of new data for many areas of physics with the recent advent of a full range of nucleon-nucleus charge exchange experiments. The review also shows how this data has demolished the "smoking gun."

Josef Speth and Tony Thomas have chosen to write a timely review of the role of the pion cloud of the nucleon in deep inelastic lepton scattering. It is a subject in which they have been world leaders for more than a decade and which is of crucial importance in clarifying the spin and flavor structure of the nucleon, a matter which now engages the interest of many nuclear and particle physicists. They give a thorough description of the theoretical ideas and of the various experiments which can be used to test them.

The subject of muon catalyzed fusion, reviewed in the third article by Kanetada Nagamine and Masayasu Kamimura, should be part of the general culture of every nuclear physicist, just like nucleosynthesis to which it is slightly related. It is fifty years ago since the muon was identified as a “heavy electron” a somewhat mischievous interloper in science whose role in nature was not immediately clear. Almost immediately it was suggested that the muon, in its short lifetime (several microseconds), might catalyze the fusion of the hydrogen isotopes by “hiding” the charge of one of the isotopes, thus enabling the close proximity required for fusion. It did not take long for the catalyzed fusions to be observed or for the understanding that the production of useful energy by this means required that each muon should catalyze a thousand or more fusions. The early results came within an order of magnitude of this goal but also found that being so tantalizingly close wasn’t good enough: nature played a cruel trick in aborting the chain of catalyzed reactions, after about a hundred cycles, by capture of the muon by the alpha particle emerging from the fusion. But such “checkmates” in physics aren’t always absolute. Further the muon is always a vehicle for exciting physics. Molecular resonance processes (very similar to nuclear resonance processes) were found to enhance the fusions and even the number of cycles. Very recent experiments at the Rutherford–Appleton Laboratory by Nagamine, and theoretical work by Kamimura have given new insights into all of the physics of muon catalyzed fusion. The present review focuses on this new work and its physics, giving also the necessary historical background. Although the ultimate goal of useful energy production still remains elusive, muon catalyzed fusion is providing other applications and its new physics should give pleasure to all.

J. W. NEGELE
E. W. VOGT

CONTENTS

Chapter 1

NUCLEON CHARGE-EXCHANGE REACTIONS AT INTERMEDIATE ENERGY

W. P. Alford and B. M. Spicer

Chapter 2

MESONIC CONTRIBUTIONS TO THE SPIN AND FLAVOR STRUCTURE OF THE NUCLEON

J . Speth and A . W . Thomas

Chapter 3

MUON CATALYZED FUSION: INTERPLAY BETWEEN NUCLEAR AND ATOMIC PHYSICS

K . Nagamine and M . Kamimura

ADVANCES IN NUCLEAR PHYSICS

VOLUME 24

Chapter 1

NUCLEON CHARGE-EXCHANGE REACTIONS AT INTERMEDIATE ENERGY

W. P. Alford

University of Western Ontario
London, Ontario, Canada
and
TRIUMF
Vancouver, British Columbia, Canada

and

B. M. Spicer

School of Physics
University of Melbourne
Parkville, Victoria, Australia

Advances in Nuclear Physics, Vol. 24, edited by J. W. Negele and E. W. Vogt. Plenum Press, New York, ©1998.

1. INTRODUCTION

For many decades, the Gamow–Teller (GT) or spin-flip, isospin-flip interaction has been central to many important areas of nuclear physics research. First identified as a component of the weak interaction in allowed beta-decay, it plays a critical role in the initial step of the hydrogen fusion reaction leading to nucleosynthesis, and in the electron capture reactions leading to stellar collapse and supernova formation. It also gives rise to an important mode of nuclear excitation, the Gamow–Teller giant resonance (GTGR). Over the past decade, a great deal of interest has focussed on the GTGR both as an example of a nuclear giant resonance, and as a possible indicator of new directions in nuclear physics encompassing effects beyond the usual shell model of nuclear structure, and involving the substructure of the nucleons themselves.

It has also long been recognized that the strong nucleon-nucleon interaction includes a GT component. This was demonstrated in low energy (p, n) reactions over forty years ago, and the connection between allowed beta-decay rates and (p, n) reaction cross sections was clearly recognised at that time. Interest in this field was high, but until about fifteen years ago there was a very limited data base for comparison with the large body of theoretical speculation. This situation changed dramatically with the demonstration at Michigan State University, and soon after more convincingly at the Indiana University Cyclotron Facility (IUCF), that the (p, n) reaction at intermediate energies provided a quantitative tool for the study of GT-transitions corresponding to β^--decay, usually referred to as GT^- transitions.

Comparable studies of (n,p) reactions corresponding to β^+ decay soon became feasible with the development of new experimental facilities first at TRIUMF and then at LAMPF and Uppsala. Thus it became possible to carry out systematic studies of both GT^- and GT^+ giant resonances and to investigate fully the implications of the very powerful GT sum rule.

This review describes the field of intermediate energy charge-exchange reactions at a time when a large body of experimental data has been accumulated and is available for comparison with theoretical models. It has also been a time of excitement in the field of nuclear physics, with the GTGR providing an important testing ground for new ideas about the importance of sub-nucleon degrees of freedom in nuclear structure. The presentation here reflects an experimentalist's viewpoint; an excellent review of the field from a theoretical viewpoint has recently been given by Osterfeld [1]. The two reviews may be regarded as complementary.

As an introduction, a historical review of the development of ideas pertaining to the GTGR is given, appropriate to its central role in the development of the whole field. We then describe the emergence of new techniques for the study of charge-exchange reactions, particularly the technical advances which have yielded the recent volume of new data. The present status of charge-exchange studies is reviewed and assessed to provide a perspective which goes beyond the principal focus of the GTGR. In the (p, n) reaction the GTGR arising from the $\Delta L = 0$, or monopole, response dominates the spectrum at small momentum transfers, with higher multipoles observable at high excitation and larger scattering angles. By contrast, in (n,p) reactions in the heavier nuclei, the Gamow–Teller transitions are substantially Pauli-blocked and the spin dipole resonance dominates, with contributions from higher multipoles also identifiable.

To provide some insight into the problems and uncertainties in studying these multipoles, a description of the multipole decomposition procedure used in the data analysis is presented. This is followed by a discussion of the information available regarding the spin-dipole and higher multipole strength excited in charge-exchange reactions.

In conclusion, the nuclear spin-isospin response at large momentum transfer in the quasifree region of excitation is discussed. The study of this region may provide new insights into the problem of the nucleon-nucleon interaction in nuclear matter. A summary then reviews important open questions and possibilities for further advances in this field.

2. EARLY RESULTS IN THE STUDY OF SPIN AND ISOSPIN EXCITATIONS

The results to be described involve both the weak beta decay interaction and the strong nuclear interaction. A brief discussion of some concepts from these two fields essential for our purposes is therefore included here.

2.1. Beta Decay

The process of allowed beta decay is known to take place by two different modes, the Fermi (F) or Gamow–Teller (GT) modes. In the Fermi mode the transition operator is $O_F = \tau^{\pm}$, the isospin raising or lowering operator corresponding to beta decay by positron or electron emission. These transitions occur between isobaric analogue states, the quantum numbers of which differ from one another only in the third component of isospin, $T_z = (N - Z)/2$. Thus the selection rule for Fermi transitions is $\Delta J = 0$, $\Delta\pi$ = no. The comparative half-life for such a transition is given by [2, 3]

$$ft_{\frac{1}{2}} = \frac{6135}{B_F} \quad \text{seconds}$$

where the transition strength is defined by [4]

$$B_F = \frac{1}{(2J_i + 1)} \left| \left\langle \Psi_f \left\| \sum_{j=1}^{A} \tau_j^{\pm} \right\| \Psi_i \right\rangle \right|^2 \tag{2.1}$$

Since initial and final wave functions are essentially identical in these transitions, the comparative half-life is short and the transitions are said to be superallowed.

The second decay mode, the GT mode, involves the nuclear transition operator $O_{GT} = \vec{\sigma}\tau^{\pm}$ where $\vec{\sigma}$ is the usual Pauli spin operator. In this case selection rules are $\Delta J = 0, \pm 1$ (no $0^+ \to 0^+$), $\Delta\pi =$ no, and the transition strength is defined as

$$B_{GT} = \frac{1}{(2J_i + 1)} \left| \left\langle \Psi_f \left\| \sum_{j=1}^{A} \vec{\sigma}_j \tau_j^{\pm} \right\| \Psi_i \right\rangle \right|^2 \tag{2.2}$$

The comparative half life is then

$$ft_{\frac{1}{2}} = \frac{6135}{(g_A/g_V)^2 B_{GT}}$$

where g_V, g_A are the vector and axial vector weak coupling constants. We finally note that for transitions between isobaric analogue states in odd-A nuclei, both modes may contribute so that

$$ft_{\frac{1}{2}} = \frac{6135}{B_F + (g_A/g_V)^2 B_{GT}}$$

A long-standing puzzle in beta decay studies was posed by the observation that decay rates for GT transitions were generally one to two orders of magnitude slower than predicted with single-particle model wave functions. A great deal of progress in understanding this problem has come from nuclear reaction studies, and some essential ideas in the theory of nuclear reactions are now outlined.

2.2. Direct Nuclear Reactions

The nucleon-nucleon interaction may be described in a variety of ways, but for present purposes its spin and isospin structures are emphasized. It is known to include central, spin-exchange, spin–orbit and tensor components both without and with an isospin-exchange character. Thus the interaction may be written as

$$V_{NN} = V_{ij}(r_{ij}) = V_0 + V_\sigma(\vec{\sigma}_i \cdot \vec{\sigma}_j) + V_{so}\left(\vec{S} \cdot \vec{L}\right) + V_T S_T$$
$$+\vec{\tau}_i \cdot \vec{\tau}_j \left(V_\tau + V_{\sigma\tau}(\vec{\sigma}_i \cdot \vec{\sigma}_j) + V_{so}^\tau\left(\vec{S} \cdot \vec{L}\right) + V_T^\tau S_T\right) \qquad (2.3)$$

Here $\vec{S} = \vec{s}_i + \vec{s}_j, \vec{L} = (\vec{r}_i - \vec{r}_j) \times (\vec{p}_i - \vec{p}_j)$ and S_T is the two-body tensor operator. In general, each of the V's is a function of internucleon separation. In a nuclear reaction involving a transition between two states, the differential cross section is given in the non-relativistic theory by [5]

$$\frac{d\sigma}{d\Omega} - \left(\frac{\mu}{2\pi\hbar^2}\right)^2 \frac{k_f}{k_i} \frac{1}{(2J_i + 1)} \sum_{m_i, m_f} |T_{fi}|^2 \qquad (2.4)$$

T_{fi} is the transition amplitude for the reaction, and the sum is taken over magnetic substates. The transition amplitude is given by

$$T_{fi} = \left\langle \vec{k}_f, \phi_f \left| \sum_{j=1}^{A} V_{\text{eff}}(r_{pj}) \right| \vec{k}_i, \phi_i \right\rangle$$

where $\vec{k}_i$ $\vec{k}_f$, are the momenta of the incoming and outgoing particles, ϕ_i , ϕ_f are wave functions of initial and final nuclear states, and $V_{\text{eff}}(\vec{r}_{pj})$ is some effective interaction between the incoming projectile and target nucleons. The main focus of interest here will be on nucleon charge-exchange ((*p,n*), (*n,p*)) reactions at intermediate energies. At energies above about 100 MeV, the impulse approximation [6, 7] is believed to be applicable, and V_{eff} is the free nucleon-nucleon interaction. With the restriction to charge-exchange reactions, only the isospin dependent terms will be involved. As an aside it should be noted that in an actual calculation, the wave functions must be antisymmetrized between projectile and target nucleons. This leads to knock-on exchange terms in T_{fi} which make important contributions to the calculated cross section.

In order to describe the essential features of the calculated reaction cross section, it is convenient to consider an effective interaction which depends only on the distance between the interacting particles, $v_{\text{eff}} = v\ (r_{ij})$. This is not a limitation on the validity of the results, but simplifies the notation in the discussion below.

The transition amplitude which *is* written above in ordinary space can be Fourier transformed and written in terms of the momentum transfer in the reaction $\vec{q} = \vec{k}_f - \vec{k}_i$. In $\vec{q}$ space the transition amplitude then can be written

$$T_{fi}\ \left(\vec{k}_f, \vec{k}_i\right) = \int D\left(\vec{k}_f, \vec{k}_i, \vec{q}\right)\ V(\vec{q})\ \rho_{if}\ (\vec{q})\ d\vec{q}$$

In this expression

$$D\left(\vec{k}_f,\vec{k}_i,\vec{q}\right) \equiv \frac{1}{(2\pi)^3} \int \chi^{-*}\left(\vec{k}_f,\vec{r}_p\right) \exp - (i\vec{q}\cdot\vec{r}_p)\ \chi^{+}\left(\vec{k}_i,\vec{r}_p\right) d\vec{r}_p$$

is the projectile distortion function. In a distorted wave theory D is evaluated numerically as part of a standard computer code such as DW81 [8]. In the absence of distorting potentials the theory reduces to a plane wave Born approximation and $D = 1$. The function

$$\rho_{if}(\vec{q}) = \left\langle \phi_f \left| \sum_{j=1}^{A} \exp\ (i\vec{q}\cdot\vec{r}_j) \right| \phi_i \right\rangle$$

is the nuclear transition density and carries the information about the nuclear states involved. Since it is usual to consider transitions between states of definite spin and parity, it is convenient to represent ρ in terms of a multipole expansion. For a given transition $\phi_i \rightarrow \phi_f$ only a limited number of terms can contribute, and usually only the lowest allowed multipole need be considered. The specific form of these multipoles will be discussed in the context of their application in later sections.

2.3. Early Investigations of Charge-Exchange (Isovector) Interactions

A possible connection between nuclear beta decay rates and (p,n) reactions was noted at least as early as 1957 [9], but the first paper to really investigate the potential of charge-exchange reactions for studies of the effective interaction in nuclei was that of Bloom, Glendenning and Mozkowski [10] entitled "The proto–neutron interaction and the (p,n) reaction in mirror nuclei." In it they assumed that the effective interaction could be expressed as an isoscalar and an isovector part $v = v_a + v_b\,\tau^-$. In a (p, n) reaction between isobaric analogue states such as $^{13}C(p,n)^{13}N$, the transition amplitude would be dominated by Vb because of the complete overlap of initial and final wave functions. The other part of the interaction va could contribute through knock-on exchange, but this would lead to poor overlap of the wave functions and the contribution would be small. Thus the (p, n) reaction would single out the isovector part of the effective interaction. A subsequent study [11] of the $^{13}C(p,n)\,^{13}N_{gs}$ and $^{15}N(p,n)^{15}O_{gs}$ reaction was carried out at energies between 6.5 and 13.6 MeV. The interpretation of the results was complicated by the low beam energy used, and no estimate of the magnitudes of the interaction strengths could be obtained. It was concluded however that both the spin singlet ($V_\tau \equiv V_F$) and spin-triplet

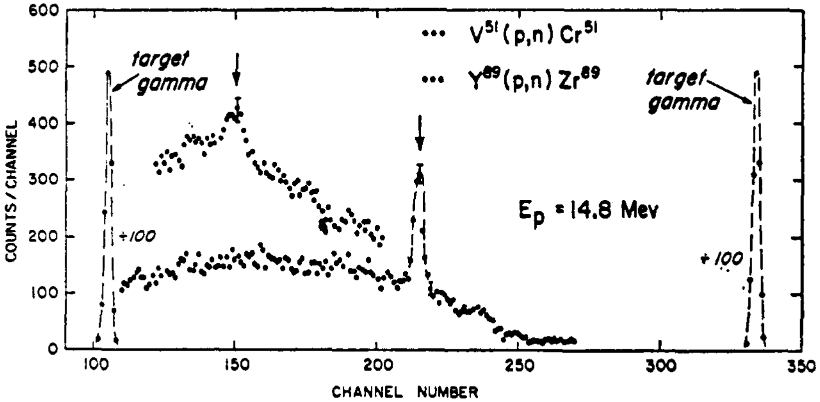

Fig. 2.1. Time of flight spectra from proton bombardment of ^{51}V and ^{89}Y at 14.8 MeV, showing the strong excitation of the isobaric analog of the ^{51}V ground state. Reprinted from [12] with permission.

($V_{\sigma T} \equiv V_{GT}$) parts of the isovector interaction were contributing to the reaction, and that the relative strength of the two contributions was $V_{GT}/V_F \sim 0.4$.

Shortly before this study appeared, measurements of *(p, n)* cross sections on heavier nuclei [12] at 14.8 MeV, showed a very strong transition to what appeared to be a single final state as shown in Fig. 2.1, This state was identified as the isobaric analogue of the target ground state, and led to the recognition of the fact that isospin was a useful quantum number even in nuclei in which Coulomb effects are large [13].

In the first of several papers which became the basis for much of the later development of ideas relating to charge-exchange reactions, the strong excitation of the isobaric analogue state (IAS) was recognized by Ikeda *et al.* [14] as a manifestation of a giant resonance, in this case excited by the isospin operator $T^- = \sum_{j=1}^{A} \tau_j^-$ which is responsible both for Fermi transitions in beta decay, and for a part of the transition amplitude in (*p*,*n*) reactions. This insight then led Ikeda *et al.* [15] to suggest that a giant resonance should also exist, associated with the isovector spin-flip operator, $\sum_{j=1}^{A} \vec{\sigma}_j \tau_j^-$, which mediates the GT component of beta decay. The observed weakness of allowed GT beta transitions was ascribed to the fact that most of the strength of the giant resonance was located at excitation energies which were inaccessible to beta decay, They further suggested that this GT giant resonance should also be excited in the (*p,n*) reaction and that the ratio of cross sections for the excitation of the GT and F giant resonances should be proportional to the ratio of the squares of the appropriate interaction strengths, $V_{\sigma\tau}$ and V_τ, in the isovector effective interaction.

During the following decade a number of studies investigated the properties of the isovector effective interaction utilizing the correspondence between beta-decay matrix elements and those for the (*p, n*) reaction cross section [16, 17, 18, 19, 20, 21]. It was recognized that the momentum transfer in beta decay was small, so that the transition amplitude for the (*p,n*) reaction should also be evaluated for $q \simeq 0$, i.e., near scattering angle $\theta = 0$. In the limit $q = 0$ it is expected that the spin–orbit and tensor components of the effective interaction can be neglected. For states connected by allowed beta decay, the angular momentum transfer is at most one unit, with no parity change, so that the lowest term in the multipole expansion of the nuclear transition density will be the monopole with $\Delta L = 0$. Thus for the (*p,n*) reaction cross section near $\theta = 0^{\circ}$, the connection with beta decay can be expressed as [22]

$$\frac{d\sigma}{d\Omega}(q \sim 0] = \left(\frac{\mu}{\pi\hbar^2}\right)^2 \frac{k_f}{k_i} \left[N_\tau |v_\tau(0)|^2 B_F + N_{\sigma\tau} |v_{\sigma\tau}(0)|^2 B_{GT}\right] \qquad (2.6)$$

Here N_τ and $N_{\sigma\tau}$ are distortion factors, $v_\tau(0)$ and $v_{\sigma\tau}(0)$ are integrals of the effective interaction at $q = 0$ over the nuclear volume, while B_F and B_{GT} are the appropriate beta transition strengths, evaluated from observed $ft_{\frac{1}{2}}$ values.

The relation above seems to have first been written explicitly in [21], but the ideas behind it were assumed, if not explicitly stated, in all the prior studies of interest here. In these, the most clear-cut conclusions were obtained from studies of the (*p,n*) reaction on the $J^\pi = 0^+$, $T = 1$ targets ^{14}C [17] and ^{18}O [16]. In both cases the reaction populated final states with $J^\pi = 0^+$ via the V_τ component of the interaction and states with $J^\pi = 1_+$ via $V_{\sigma\tau}$, and reaction calculations using very simple shell model wave functions yielded estimates of the interaction strengths. Initial analyses of the data assumed only monopole ($\Delta L = 0$) contributions to the reaction and only Fermi and GT contributions to the effective interaction. However, in the ^{14}C(*p,n*) reaction, the transition to the ground state of ^{14}N was found to be much stronger than predicted from the strength of the corresponding beta decay and this indicated the importance of the tensor part of the effective interaction. Also, for the ^{18}O target, transitions were observed leading to known states with $J^\pi = 2^+$, indicating contributions from multipole components of the interaction with $\Delta L = 2$.

Most of the above studies were carried out at energies below about 15 MeV, where the assumed direct reaction mechanism was complicated by compound nucleus effects although some measurements of the ^{6,7}Li(*p,n*) reaction [19] extended to energies of about 50 MeV. These showed that the strength of the Fermi interaction decreased by a factor of about 2 over the energy range from 10 to 50 MeV, while the GT interaction strength was nearly constant over the same range. Thus by about 1975, some important characteristics of both the

Fermi and GT parts of the effective interaction had been extensively studied for projectile energies below about 50 MeV [23], and the stage had been set for the much more definitive results which would be obtained using intermediate energy facilities which were just about to come into operation.

2.4. Giant Resonances and Sum Rules

A giant resonance can be described as a state which can be represented by (a) a collective model wave function, involving many nucleons, or alternatively, (b) a wave function which represents a superposition of single particle excitations. In either case, the excitation occurs via an appropriate transition operator. Probably the best known example of such an excitation is the electric dipole giant resonance which had been extensively studied since its discovery in 1948 [24]. In general, the giant resonance state is an eigenstate of an appropriate model nuclear Hamiltonian, not the true Hamiltonian. The residual interaction, which is the difference between true and model Hamiltonian then spreads the giant resonance over many states in the final nucleus. The transition probability to a single final state will depend on the properties of that state, as well as the target ground state, and any calculation of transition probability requires some model wave function for both states. In contrast to this situation, the total transition probability to all components of the giant resonance will depend only on the properties of the target ground state, and the specific transition operator involved, without reference to the details of the final states. Sum rules are relations involving the total transition probability, or alternatively the total strength excited by a transition operator. Specific examples will be discussed shortly.

Since the early work of Anderson and Wong [25], and its interpretation by Ikeda *et al.* [14], the large *(p,n)* cross section for excitation of the isobaric analogue of the target ground state had been recognized as the signature of a giant resonance, in this case arising from the isospin-lowering operator $T^- = \sum_{j=1}^{A} \tau_j^-$. This excitation, which we will refer to as the Fermi giant resonance, has a very special property. Since isospin is a conserved quantum number, at least in light nuclei, the Fermi giant resonance is in fact an eigenstate of the nuclear Hamiltonian, so that the full transition strength appears in a single state, the isobaric analog state. In this case the sum rule for the total strength is just $\sum_f B_{Fj} = S_F = N - Z$ where the summation is a formality since the full strength SF is carried in a single transition. This result was first derived by Ikeda [26], although it was at that time expressed in somewhat different form, in terms of the (*p, n*) reaction cross section.

In contrast to this, in predicting the GT giant resonance, Ikeda *et al.* [15], noted its spreading over many final states. The sum rule for this GR was also given by [26], at least for heavy nuclei in which valence protons and neutrons occupied different major shells. In this case, only β^- transitions are allowed and the sum rule is written

$$\sum_f B^-_{GT_f} = S^-_{GT} = 3\,(N-Z) \tag{2.7}$$

The more general form of the sum rule, applicable when both β– and β+ transitions are allowed is

$$\sum_f B^-_{GT_f} - \sum_{f'} B^+_{GT_{f'}} = S^-_{GT} - S^+_{GT} = 3(N-Z) \tag{2.8}$$

where the superscripts ± refer to β^+ and β^- decay respectively. This result assumes only that the nucleus is comprised of neutrons and protons and consequently is usually described as being model-independent. A detailed derivation of the sum rule is given in [27].

In the decade following the discovery of the Fermi giant resonance many investigations of it were reported, but the GT giant resonance was not observed. However, in a study of the (*p,n*) reaction on targets of ^{48}Ca, ^{90}Zr, ^{120}Sn and ^{208}Pb at 25, 35 and 45 MeV at Michigan State University, Doering *et al.* [28], observed a broad bump in the 0° reaction cross section for excitation energies a few MeV above the known isobaric analogue resonance as shown in Fig. 2.2a. The bump was not seen at 25 MeV, but was prominent at 45 MeV. For ^{90}Zr the excitation energy of the centroid of the bump was close to that expected for a particle–hole state with configuration $(\pi g_{7/2})\ (\nu g_{9/2})^{-1}$, while the angular distribution of the cross section for the bump was similar to that for transitions to known 1^+ states at lower excitation arising from the $(\pi g_{9/2})\ (\nu g_{9/2})^{-1}$ configuration. Finally, the magnitude of the cross section was comparable to that predicted by DWIA calculations for a transition to the $(\pi g_{7/2})\ (\pi g_{9/2})^{-1}$ configuration. Thus it was concluded that the observed transition did indeed correspond to the GT giant resonance which had been predicted more than a decade earlier.

The identification of the GT giant resonance showed that it was more strongly excited relative to the rest of the (*p,n*) spectrum as the beam energy was increased from 35 MeV to 45 MeV, and it was suggested [30, 31, 32] that spin-flip transitions would dominate the (*p*, *n*) spectrum at beam energies greater than 65 MeV. This suggestion was also supported by early results at 120 MeV [33], and the full confirmation of this prediction was soon provided by extensive studies of the (*p*, *n*) reaction at the Indiana University Cyclotron Facility (IUCF). The IUCF time-of flight neutron spectrometer came into operation about 1978

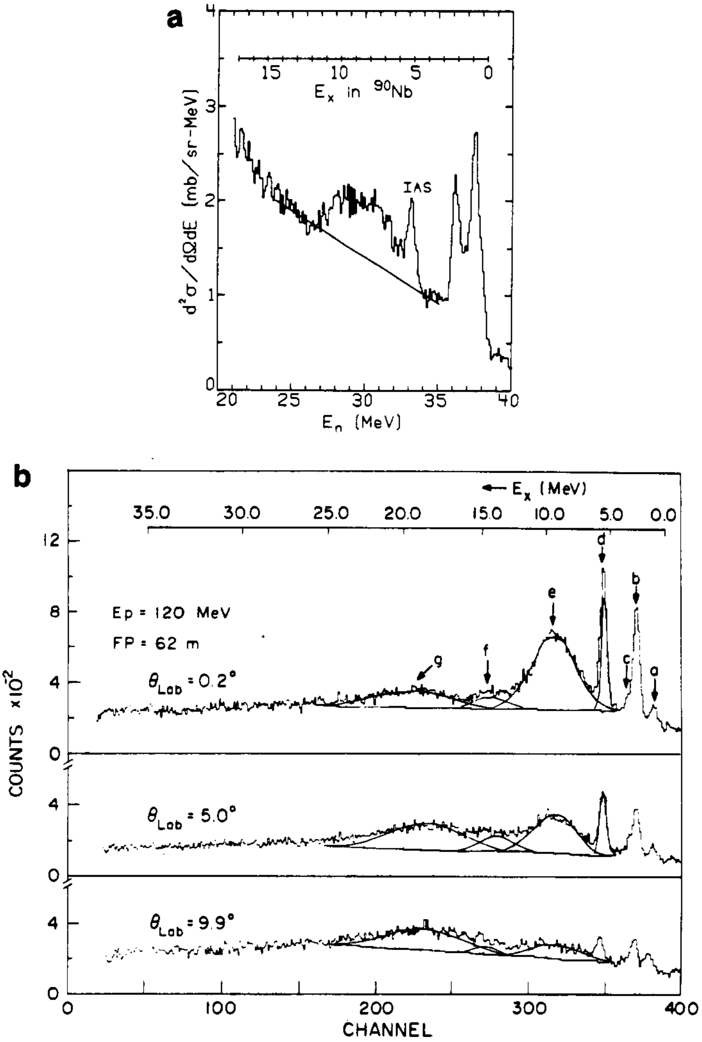

Fig. 2.2. (a) Differential cross section for the ^{90}Zr (*p*,*n*) reaction versus neutron energy, at 45 MeV and 0°. The broad structure (6 MeV < E_x < 12 MeV) is the Gamow–Teller giant resonance. Reprinted from [28] with permission. (b) Time of flight spectra for the ^{90}Zr (*p*,*n*) reaction, at 120 MeV and 0, 5, and 10° laboratory angles. The peak marked ‘e’ is the Gamow–Teller giant resonance, and ‘d’ is the isobaric analog state. Peaks ‘b,’ ‘c,’ ‘f’ show $\Delta L = 0$ angular distribution; peak ‘g,’ $\Delta L = 1$. Reprinted from [29] with permission.

and provided the capability to measure neutron spectra from (*p, n*) reactions with an energy resolution ≤ 1 MeV for incident proton energies 60 MeV $\leq E_p \leq$ 200 MeV. The system is described in more detail in the next section.

In initial (*p,n*) studies at IUCF [34], the most striking observation was the strong excitation of known $\Delta S = 1$ transitions in forward angle spectra, and it was observed that the spectra were very similar to what would be expected for a reaction driven by a one-pion exchange potential [35, 36]. The cross section for excitation of $\Delta S = 0$ transitions was found to decrease steadily relative to $DS = 1$ transitions as incident energy increased up to 200 MeV. At that energy, the zero-degree spectrum at low excitation energies resulted almost entirely from a single component, $V_{\sigma\tau}$, of the effective interaction. Provided that energy resolution was good enough to observe transitions to discrete final states, the reaction provided the opportunity to study the properties of(almost) isolated components ofthe effective interaction.

On light targets (A ≤ 20) the (*p,n*) reaction excited mainly discrete shell-model states. For most heavier targets, a broad peak was observed at an excitation energy a few MeV above the isobaric analogue state. The cross section for this peak showed an angular distribution characteristic of a transition with $\Delta L = 0$, and was identified as the GTGR. In particular, a detailed study of the ^{90}Zr(*p,n*) reaction at 120 MeV at IUCF [29] showed that the bump identified as the GTGR in the MSU experiments at 45 MeV was the dominant feature ofthe zero degree spectrum. The resulting 0° spectrum at 120 MeV is shown in Fig. 2.2b. In addition, at an angle of about 4°, a second broad peak was observed, at an energy several MeV above the GTGR. This peak showed an angular distribution characteristic of $\Delta L = 1$ and was identified as a dipole giantresonance.

A second important result ofthe initial IUCF measurements was the confirmation of the expected proportionality between zero degree cross section and beta-decay transition strength as noted in Eq. (2.6). At a beam energy of 120 MeV, (*p,n*) cross sections were measured at 0° for transitions of known beta decay strength on targets of ^{7}Li, ^{12,13}C, ^{25,26}Mg 27Al, ^{28}Si and ^{90}Zr. Distortion factors were estimated as $N = [(d\sigma/d\Omega)_{DW} / (d\sigma/d\Omega)_{PW}]_{\theta=0^\circ}$ where *DW* and *PW* indicate reaction cross sections calculated in a distorted wave, and plane wave impulse approximation. The results [22] showed the predicted proportionality, with a value $|v_{\sigma\tau}(0)|^2 \simeq 168$ MeV-fm^3. This may be compared with the value of 122 MeV-fm^3 expected for a pure one-pion exchange potential. The observed proportionality indicated that the reaction model was valid at energies above about 100 MeV and that measured (*p,n*) cross sections could be used to estimate beta decay strengths for transitions that were not energetically accessible to normal beta decay.

Given the relationship between beta decay strength and (*p, n*) cross section at small momentum transfer, the IUCF results provided a measurement of the total GT strength arising from the target ground state. However, when this was compared with the lower limit of $3\,(N-Z)$ required by the GT sum rule, it was found that only about half the predicted strength could be identified in the spectrum below about 30 MeV excitation energy. The search for the missing strength became the focus of a great deal of research over the next decade as discussed in Section 5.2.

Except for the demonstration of missing GT strength, the IUCF results had been foreshadowed by many studies over the previous two decades. However, the new results provided a much clearer demonstration of the connection between beta decay and the (*p, n*) charge-exchange reaction. They generated widespread interest in the study of GT transitions, and stimulated a great deal of further work in the field, both experimental and theoretical, over the following decade.

3. EXPERIMENTAL FACILITIES

The quantitative study of isovector spin-flip excitations at intermediate energies was made possible by the development of new experimental facilities. The IUCF neutron time-of-flight spectrometer was the first of these and it opened up this field by demonstrating the strong excitation of spin-flip transitions at energies above ~ 100 MeV. This stimulated the construction of other facilities for both (*p*,*n*) and (*n*,*p*) studies. In this section, a brief description of the most important new facilities is given.

3.1. (*p*,*n*) Reactions

3.1.1. *Neutron Time-of-Flight Spectroscopy*

The commonest method for measuring neutron energy involves the measurement of neutron velocity, by measuring flight time over a known distance from source to detector. The start time is determined by using a pulsed proton beam to produce the neutrons. The arrival time is signalled by the occurrence of a nuclear reaction in the detector (usually the ^{1}H(*n*,*p*) or ^{12}C(*n*,*x*) reaction) which produces a charged reaction product.

The fractional uncertainty in the measured energy E is proportional to $\Delta\tau/L$ where $\Delta\tau$ is the uncertainty in measurement of flight time and L the length of the flight path. The timing uncertainty is determined by characteristics of the beam pulsing system and the detector and is typically less than a nanosecond.

TABLE 3.1
Flight Path Required for ΔE = 0.5 MeV ($\Delta\tau$= 0.5 ns)

E(MeV)	100	200	300	500
L(m)	30	91	178	440

For a given neutron energy and value of $\Delta\tau$ the flight path required to achieve a specified energy resolution is then readily calculated. For a typical value of $\Delta\tau = 0.5$ ns the flight path required for an energy resolution $\Delta E = 0.5$ MeV is shown as a function of neutron energy in Table 3.1. Such long flight paths imply the need for large detectors in order to obtain reasonable solid angle.

The detectors also need to be as thick as possible, consistent with the required time resolution, in order to maximize the detection efficiency. To measure angular distributions of reaction cross sections the direction of the beam on the target is rotated, rather than moving the bulky, massive detectors. Most of the measurements of (p,n) cross sections at energies above 100 MeV have been carried out with such facilities using either the IUCF or the LAMPF time-of-flight spectrometers.

With the IUCF system [37] proton beams are available in the energy range 60–200 MeV. The direction of the beam on target is rotated by a beam swinger consisting of three magnets as shown in Fig. 3.1. The first, located on the beam line bends the incident beam to one side, where the second magnet bends it back to intersect the original beam line at the target position but at a finite angle of incidence. Bend angles up to 27° are available. Behind the target, a third magnet bends the beam into a shielded beam dump, thus allowing (p,n) cross section measurements at an angle of 0°.

The detectors [39, 40] consist of bars of plastic scintillator, approximately 10 cm × 10 cm × 1 m in size, viewed by photomultipliers at each end of the long dimension. With the bars oriented with the long axis normal to the beam direction, mean timing is used to determine time of flight. To improve timing resolution, and hence energy resolution, the long axis may be oriented parallel to the flight path, and flight time inferred from the time difference between the two photomultipliers. The overall timing resolution of the system is 0.5 nsec. A second system using liquid scintillators has been constructed, with comparable properties [41].

Two flight paths are available. One at 0o to the incident beam may be varied between 45 m and 90 m in length. The second, at an angle of 24° is 45 m long. Thus angular distributions may be measured out to about 50°. The overall energy resolution ranges from about 300 keV near 100 MeV incident energy to about 1 MeV near 200 MeV.

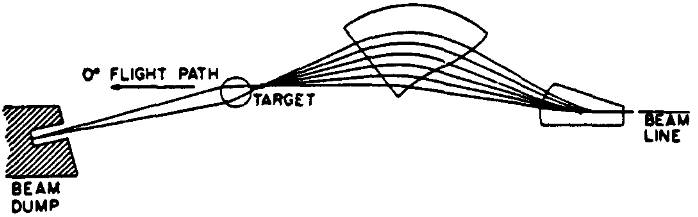

Fig. 3.1. Beam swinger system (schematic) as used at IUCF. The first magnet deflects the beam to one side, and the second bends it in the opposite direction to strike the target at a variable angle. The third magnet then deflects the beam into a shielded dump in order to permit cross section measurements at 0^o. Reprinted from [38] with permission.

This system can also be used with a second detector plane behind the first in order to measure polarization of the emitted neutrons [42]. Thus with an incident polarized beam, the system can measure the spin transfer coefficient *Dnn* in the $(\vec{p}, \vec{n})$ reaction.

The LAMPF system [43] was similar to that at IUCF, but permitted measurements at energies up to 800 MeV with a flight path up to 600 m. More details are given in [44]. Although this system provided some interesting results [45, 46] it has now been decommissioned and the detectors are being used at IUCF.

3.1.2. Proton Recoil Spectroscopy

Neutron energy may be determined from a measurement of the energy of the recoil protons produced in the ^{1}H(n,p) reaction at 0°, and a system using this approach was commissioned at TRIUMF in 1985, utilizing the existing medium resolution spectrometer (MRS) to detect the recoil protons.

A diagram of the TRIUMF system is shown in Fig. 3.2. The incident proton beam initiates the (p, n) reaction in a target mounted over the pivot of the MRS. After passing through the target the proton beam is deflected by about 20° into a shielded beam dump, so that cross section measurements can be made at 0° reaction angle. In the original system, the recoil protons are produced in a plastic scintillator 2 cm $\times$6 cm in area and 2 cm thick which is mounted on the MRS carriage about 90 cm from the primary target. The protons are then detected and their energy measured with the MRS. The measured energy is corrected for energy loss in the scintillator (up to 10 MeV) using a signal from the scintillator, With this system, energy resolution ranges from about 0.8 MeV at 200 MeV to 1 MeV at 450 MeV.

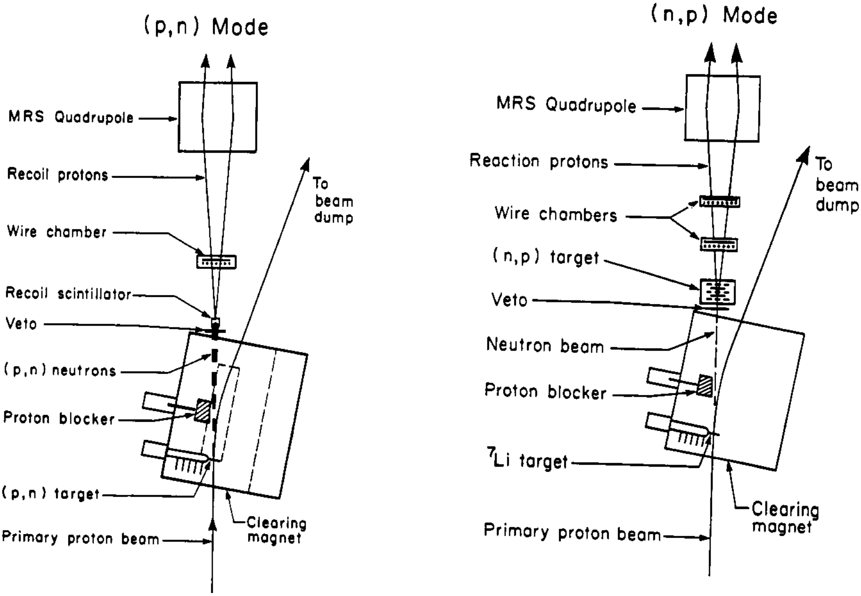

Fig. 3.2. (a) The TRIUMF CHARGEX arrangement, set up for the study of (*p*, *n*) reactions. The (*p, n*) target is located over the axis of the MRS. (b) The CHARGEX arrangement, set up for the study of *(n,p)* reactions. In this case, the (*n,p*) reaction target is placed over the axis of the MRS, and the ^{7}Li neutrom–production target is 90 cm upstream from it.

The TRIUMF system adapted easily for the study of (*n,p*) reactions also, as described in the following section, and represented a major advance in the study of nucleon charge-exchange reactions. A more detailed description of the system has been given by Helmer [47].

3.2. *(n,p)* Reactions

Spectrometers for (*n,p*) studies require two basic components, the incident neutron beam, followed by the proton detector. The first system to provide useful results for the *(n,p)* reaction at intermediate energies was that of Measday and Palmieri [48, 49]. The source of neutrons was the *d*(*p,n*) reaction at 160 MeV and the proton detector was a plastic scintillator telescope plus a sodium iodide detector. In spite of the rather poor energy resolution (~ 6 MeV) the authors were able to identify the excitation of giant resonances in nuclei. In most current intermediate energy spectrometers the neutron beam is produced in the ^{7}Li(p,n)^{7}Be reaction at 0°. This reaction has the advantage of a large reaction cross section, about 35 mb/sr (lab) at 0°, but the disadvantage that the neutron spectrum includes two peaks of comparable intensity resulting from transitions to the ground state of ^{7}Be, and to an excited state at 0.43 MeV. This could result in a significant contribution to the energy resolution of the spectrometer, though it is not the dominant one in any existing system. The spectrum also exhibits a weak continuum extending to high excitation energies, which adds some complication to data analysis. The proton detection systems generally employ a combination of magnetic deflection, plus ray-tracing with suitable drift chambers to identify protons from the target and measure their energy. More detail on existing systems is as follows:

3.2.1. University of California at Davis

This facility, operating at 60 MeV, is at the lower end of the energy range of interest. It deserves note however as the first system in this energy range to produce useful measurements of (n,p) cross sections [50].

The incident neutron beam is collimated to 1.8 cm ×3.6 cm and provides a flux of 10^{6} n/sec on target. The target is mounted in a magnetic field and the trajectories of reaction protons are determined by two multi-wire chambers which permit measurements to be made over the angular range 0°–48°. Overall energy resolution is about 1 MeV.

3.2.2. TRIUMF

The TRIUMF spectrometer is essentially the same as is used for (p,n) measurements [47] except that the ^{7}Li neutron production target is mounted about 90 cm upstream from the MRS pivot, and the recoil scintillator is replaced by the (n,p) target mounted over the pivot. An important feature of this system (Fig, 3.2b) is a segmented target box which allows a large target thickness while maintaining good energy resolution [51]. In this target box, up to six separate targets are mounted between wire chambers which identify the origin of each reaction proton, and permit correction to be made for energy loss in subsequent layers of the target stack. Neutron flux is 10^{6} n/sec on targets of area 2 cm ×5 cm. The overall energy resolution of the system, 0.8 MeV at 200 MeV incident energy, made it possible for the first time to obtain (n,p) data over a wide range of intermediate energies, comparable in quality to the (p,n) data from neutron time-of-flight spectrometer systems.

The continuum in the neutron source spectrum gives rise to a background which must be subtracted using a deconvolution procedure [52]. This presents no difficulties at low excitation energy, but limits the maximum useable range to an excitation energy of about 50 MeV. This is not a serious constraint on the usefulness of the system for a wide range of charge-exchange studies.

3.2.3. Los Alamos

The WNR facility produces an intense neutron source with a continuous energy distribution by bombarding a thick tungsten target with 800 MeV protons. In the (*n,p*) system, neutrons from this source are collimated and their energy determined by time of flight over a 90 m flight path. The (*n,p*) target is mounted at the end of this flight path, and reaction protons detected in a system shown in Fig. 3.3. The system permits measurements to be carried out over a range of incident energies (70–240 MeV) in a single measurement, and has been useful in studying the excitation of isovector giant resonances as a function of incident energy [53, 54]. Its most serious drawback is that the neutron flux per unit energy range is low. The system is described in [53].

3.2.4. Uppsala

This system, which permits (*n,p*) studies in the energy range 100–200MeV, is basically similar to that at Los Alamos. Neutron flux is 10^6/sec on a 7 cm diameter target. Overall energy resolution is 2 MeV at 100 MeV incident energy. The system is described in more detail in [55].

3.3. Other Reactions

Because of the experimental problems in (*p,n*) and (*n,p*) measurements, there has been considerable interest in the use of other reactions with more massive projectiles which permit the study of charge-exchange transitions with charged particles in both entrance and exit channels. Although these other reactions are not the principal focus of this review, it is useful to discuss their characteristics, and note the facilities available for their use.

3.3. 1. (^{3}He,t)

This reaction was used in early searches for the GTGR [56, 57, 58]. The beam energies were rather low however, (< 100 MeV) and the GTGR was not very strongly excited. In addition it was shown [58] that two-step contributions to the reaction were important at low energy, and that transition amplitudes with $\Delta L = 2$ were significant.

Following the IUCF results, the (^{3}He, t) reaction was investigated at higher energies using beams of 600 MeV, 1.2 GeV and 2 GeV from Saturne [59]

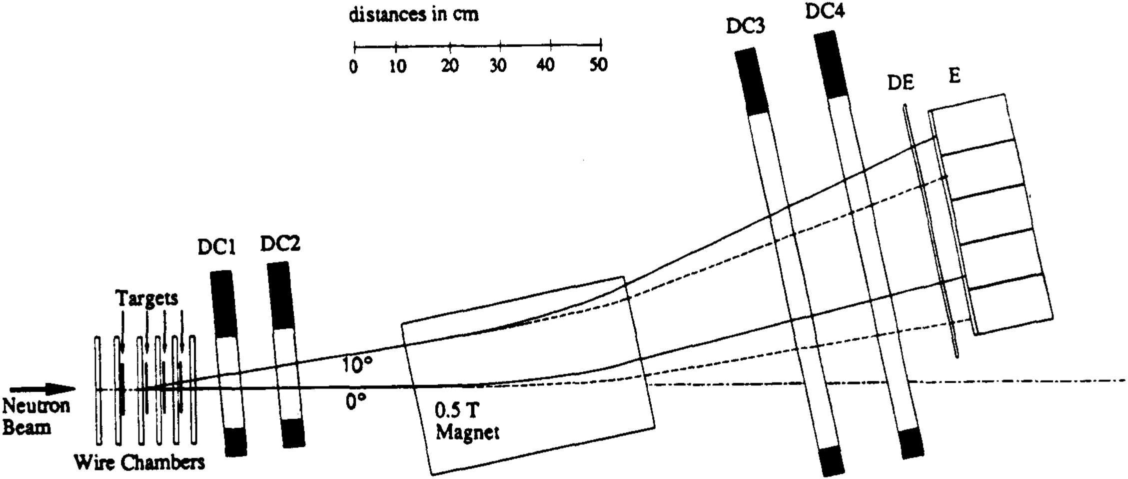

Fig. 3.3. Target and detector system used at the LAMPF (*n,p*) spectrometer. The targets are mounted between wire chambers as with the TRIUMF target system [51]. DC1-DC4 are drift chambers to permit ray tracing for the reaction protons. DE is a thin timing scintillator and *E* is a calorimeter of CsI crystals. Similar systems are used in the Davis and Uppsala (*n,p*) spectrometers. Reprinted from [54] with permission.

and targets of ^{13}C, ^{54}Fe and ^{89}Y. The reaction tritons were detected in a large magnetic spectrograph, SPES4 [60] with a momentum resolution $\Delta p/p = 5 \times 10^{-4}$. At 600 MeV it was found that the triton spectra at 0o were similar to neutron spectra from the (*p, n*) reaction at 200 MeV, and that the $\vec{\sigma}\tau$ part of the effective interaction was dominant. Results with the ^{13}C target at 600 MeV also provided an estimate of the ratio of spin-flip to non-spin-flip effective interactions which was consistent with that obtained from (p,n) measurements at 200 MeV. More detailed studies were reported for ^{12,13}C(^{3}He, *t*) at energies between 600 MeV and 2.3 GeV, which concluded that this is a single step direct reaction which is well described by DWIA calculations [61]. Thus it appeared that the (^{3}He, *t*) and (*p, n*) reactions would provide comparable probes of spin-isospin excitations for the same value of E_{in}/A.

Most recently, a new facility has been commissioned at RCNP [62] which permits studies at an energy of 450 MeV with a high resolution magnetic spectrometer for detection of the reaction tritons. Initial results have been reported for a number of targets ranging from ^{9}Be to ^{154}Sm, which again demonstrate the strong excitation of GT transitions [63]. In addition, the good energy resolution in these measurements (210 keV) has revealed fine structure in the GTGR of medium mass nuclei such as ^{58}Ni, which permits interesting comparisons with the M1 strength distributions observed in high resolution (*e,e′*) measurements [64].

The (^{3}He, t) reaction is more complex than (*p,n*) in that the structure of the ^{3}He and triton must be considered. This does not present a serious problem in principle, but does add some uncertainty for the detailed analysis of the reaction. Another difference between the reactions arises because the heavier particles are more strongly absorbed than the proton and neutron, so that (^{3}He, *t*) can be considered a surface reaction. As a result, the (^{3}He, *t*) reaction provides stronger excitation of transitions with $L > 0$, and may be useful in studies of $2\hbar\omega$ excitations such as the spin isovector monopole resonance [65, 66].

3.3.2. (d,^{2} He)

This reaction excites the same isospin-raising transitions as the (*n,p*) reaction and has long been recognized as a possible probe of such excitations. Actually, "^{2}He" or the diproton has no bound states, but the two-proton system has a well known $^1S_0$ cross section maximum near zero energy, often referred to as a "virtual" state. In the studies of interest here, "^{2}He" is defined by detecting the two protons emitted with small angular separation from the decay of this state.

Early studies at the relatively low energies of 55 MeV [67] and 99 MeV [68] used counter telescopes to detect coincident protons emitted at an angle of a few degrees to one another. Because of the background of single protons from breakup of the incident deuteron, measurements could only be made at angles greater than 15°. It was found however that angular distributions were not characteristic of the L transfer for known transitions, and it was concluded that the reaction was not a useful probe of GT strength at such low energies.

Renewed interest in the reaction was stimulated by the prediction [69, 70] that with a tensor-polarized deuteron beam, measurements of tensor analyzing power (TAP) would yield the same information as obtained in much more difficult spin-transfer measurements in the $(\vec{p}, \vec{n})$ reaction. The reaction was then studied [71] at energies of 650 MeV and 2 GeV using facilities at Saturne. Using the magnetic spectrograph SPES4, it was possible to select the 1S0 final state with less than 1% contribution from ^3P states. Cross section measurements on the $N = Z$ targets ^{12}C and ^{40}Ca showed spectra similar to those from the (p,n) reaction and led to the conclusion that the reaction was well described as a simple one-step reaction. Measurements of TAP in the $p\left(\vec{d},{}^2\mathrm{He}\right)n$ reaction were also carried out and the results showed good agreement with impulse approximation calculations out to momentum transfer $q = 2\ \mathrm{fm}^{-1}$.

Similar results have recently been reported at the lower energy of 260 MeV using the RIKEN accelerator and a magnetic spectrograph with detector system similar to that of SPES4 [72]. In a study of the $^{12}\mathrm{C}(\vec{d},{}^2\mathrm{He})$ reaction [73] an overall energy resolution of 460 keV was achieved. Measurements of TAP were also carried out and showed good agreement with calculations for transitions to the 1^+ ground state, and the broad 2^- and 4^- states near 4.5 MeV excitation. Measurements of the $(d,\ {}^2\mathrm{He})$ reaction at 125 MeV have also been reported from a new facility at Texas A&M [74]. Results suggest that the reaction is useful for GT measurements even at this relatively low energy.

Given the possibility of determining both transition strength and total spin transfer in charged particle angular distribution measurements it is likely that $(\vec{d},\ {}^2\mathrm{He})$ studies will be of great interest and importance in the future.

3.3.3. Heavy Ion Reactions

Over the past two decades a variety of heavy ions ranging from ^{6}Li to ^{20}Ne have been used to investigate charge-exchange spin-flip transitions. Most interest has focussed on the (^{6}Li, ^{6}He) reaction as an analogue of the (p,n) reaction and (^{12}C, ^{12}N) as an analogue of the (n,p) reaction. In both cases, the transition to the ground state of the ejectile requires a spin change $\Delta S = 1$, so that only spin-flip transitions in the target are excited. In addition, both ^{6}He and ^{12}N have only a single bound state, the ground state, which greatly simplifies the interpretation of results.

In an early study of the (^{6}Li, ^{6}He) reaction at an energy of 34 MeV [75], it was concluded that the observed transitions involved sizeable two-step contributions. In spite of this, a correlation was noted between $\Delta L = 0$ cross sections and known GT beta decay strengths, leading to the conclusion that the reaction should be useful for measurements of GT strength. Several subsequent studies have investigated the reaction mechanism at higher energies [76, 77, 79, 80] leading to the conclusion that, for strong transitions at least, a simple one-step direct reaction model is appropriate at incident energies greater than about 25A MeV. In [79] and in another study at 156 MeV involving known GT transitions [81] it was shown that zero degree cross sections were proportional to GT strength, so that the reaction can be used as an alternative to (p,n) for measurements of GT strength. The reaction has also been studied at an energy of 100A MeV [82] where results very similar to those for intermediate energy (p, n) measurements were demonstrated for target nuclei ranging from ^{12}C to ^{208}Pb.

Since ^{6}Li has spin $J = 1$, the ($^6\vec{\mathrm{Li}}$, ^{6}He) reaction permits measurements of tensor analyzing power as in the ($\vec{d}$, ^{2}He) reaction. One such measurement has been reported at 32 MeV [83] but the energy is too low to ensure a simple one-step reaction.

Comparable studies have been reported for the (^{12}C, ^{12}N) reaction. At an incident energy of 35A MeV [84], it was concluded that the cross section was dominated by two- step contributions, but that the direct one-step reaction should predominate at energies above 50A MeV. In a theoretical study at energies between 30A and 100A MeV it was shown that the energy at which the one-step reaction became dominant was state dependent, but that two-step contributions were relatively unimportant for all states at the highest energy [85]. The calibration of the reaction as a probe of GT strength has been investigated at an energy of 70A MeV [86] with the conclusion that the reaction should be a useful alternative to (n,p) but that higher energies were required. This has been confirmed in measurements of the ^{12}C(^{12}C, ^{12}N)^{12}B reaction at 135A MeV [87].

It is clear that heavy-ion charge-exchange reactions can provide quantitative measurements of GT strength without the experimental problems associated with the neutrons in nucleon-induced reactions. There are however other problems which up to now have limited the usefulness of heavy-ion reactions. Some of these are the following.

(i) The momentum transfer Δq increases very rapidly with angle for heavy-ion reactions with the result that angular distributions of most interest are compressed into an angular range of a few degrees near 0°, and angular distributions for different ΔL transfers are difficult to discriminate. The necessary angular resolution may be obtained by accurate ray-tracing in the detector, as shown in [87] where the overall resolution was less than 0. 1°, but few systems currently have such capabilities.

(ii) The high energy required in order to ensure a simple one-step reaction makes it difficult to obtain energy resolution much better than is currently available in (*p,n*) and (*n,p*) reactions. For instance the most recent results show energy resolution of 850 keV for (^{6}Li, ^{6}He) at 600 MeV, and 700 keV for (^{12}C, ^{12}N) at 1600 MeV, to be compared with about 300 keV for (*p,n*) at 100 MeV and 800 keV for (*n,p*) at 200 MeV.

(iii) The internal structure of the beam and ejectile introduce complications in the analysis of results, though these do not lead to serious difficulties. It is also found that the internal structure may contribute reaction amplitudes which are not related to GT strength, but these have been shown to be small in existing data [86].

(iv) Heavy-ion reactions tend to be localized near the nuclear surface because of strong absorption of both projectile and ejectile. This tends to favor transitions with DL > 0, and it is observed that resonances with $\Delta L = 1{,}2$ are more prominent in heavy- ion than in nucleon-induced reactions. It is also expected that resonances associated with $2\hbar\omega$ excitations, such as the spin isovector monopole should be more prominent, though this has not yet been demonstrated.
At first sight it would seem that in a surface reaction the $\Delta L = 0$ cross section would not necessarily be proportional to GT strength. This is because GT transition densities all peak at $q = 0$, but for momentum transfers greater than $1\,\mathrm{fm}^{-1}$ the densities show a strong variation from state to state which should result in state-dependent variations in the ratio of cross section to GT strength, along with an admixture of cross section with $\Delta L = 2$. However, quantitative calculations using a strong absorption model [88] have shown that the $\Delta L = 0$ part of the cross section is almost completely insensitive to momentum transfers greater than 0.8 fm^{-1}, thus accounting for the observed proportionality.

It is clear that heavy-ion charge-exchange reactions can provide information about spin-isospin excitations comparable to that obtained from nucleon-induced reactions. It remains to be seen, however, whether their experimental limitations can be sufficiently reduced to permit significant extensions of existing results.

4. MEASUREMENT OF GT STRENGTH

4.1. Direct Determination

The early results from IUCF provided a convincing demonstration of the proportionality between $d\sigma/d\Omega\,|_{pn}$, ($\theta = 0_o$) and the beta decay strength B ($\beta-$) for transitions between the same states. It was shown that the ratio $[d\sigma/d\Omega\ (\theta = 0^o)] / D$, where D is the nuclear distortion factor (Eq. (2.5)), was proportional to B (β^-) with a proportionality constant reflecting the strength of the appropriate interaction. The effects of nuclear distortions were not negligible, but the observed proportionality was taken as an indication that for energies above about 100 MeV, they could be reliably calculated using the DWIA. In most subsequent work, an alternative but equivalent statement of the proportionality was used, and the experimental cross section written [89]

$$\frac{d\sigma}{d\Omega}\ (\alpha, q = 0) = \hat{\sigma}(E_p, A) B\ (\alpha)$$

Here a labels a particular transition while the unit cross section $\hat{\sigma}$ is the measured ratio $d\sigma/d\Omega$ (q = 0) /B for an appropriate transition of known beta decay strength. It was assumed that $\hat{\sigma}(A)$ is a constant for all transitions originating from a given target, and that its A dependence could be calculated for neighboring targets. The dependence on E_p can also be calculated, or determined by measurements at different incident energies. With either approach the important conclusion was that measurements of the *(p,n)* cross section may be used to determine beta decay strength between states that are not energetically accessible in beta decay.

From the outset it was recognized that the observed proportionality was affected by a number of factors which could limit the reliability of strengths estimated from cross section measurements. The nature and magnitude of such effects are now discussed.

4.1.1. Correction for Finite Momentum Transfer in Measured Cross Sections

This correction is relatively straightforward. For transitions with ΔL = 0, the q dependence of the cross section near q = 0 goes as $\exp(-qR)^2$ where R is some characteristic length comparable with the nuclear radius. This dependence is clearly shown in measured cross sections, which may be used to estimate R. For a reaction Q-value equal to zero, data taken at angles greater than zero can be trivially extrapolated to $\theta = 0$ corresponding to $q = 0$. For reactions with non-zero Q value, the required correction is given by the ratio

σ_{DWIA} ($Q = q = 0$) / σ_{DWIA} (Q, θ). Although the magnitude of the DWIA cross section may be sensitive to optical model parameters, the ratio is much less so and the resulting correction should introduce small uncertainty in final results.

4.1.2. State Dependence of $\hat{\sigma}$

The observed proportionality between GT strength and (*p, n*) cross section arises as a result of the fact that the spin and isospin structure of the central part of the nuclear effective interaction V_{eff} is the same as for the beta interactions. However, the radial dependence of the interactions is different, and this can lead to differences between nuclear and beta transition matrix elements which depend on the particular states involved. In addition, the non-central parts of V_{eff} will contribute to the reaction cross section, with increasing importance as the momentum transfer q increases. Such effects have been considered by Taddeucci et al. [89], with results shown in Fig. 4.1. For GT transitions involving simple particle–hole transition amplitudes, the calculated value of $\hat{\sigma}$ for a given mass number may vary by as much as 10% for different amplitudes. In Fig. 4.1, the dashed line represents a DWIA calculation of the mean A dependence of $\hat{\sigma}$, and the individual transitions show a standard deviation of about 7% about the mean. This result suggests that for transitions to different final states the value of $\hat{\sigma}$ would be subject to an uncertainty of at least this magnitude, or, conversely that values of B_{GT} extracted from measured cross sections would have the same uncertainty.

Figure 4.1 also shows calculated values of $\hat{\sigma}_F = \sigma(q = 0) / B_F$ for Fermi transitions between isobaric analog states. In this case, calculations predict large differences between transitions of the types $j>$, $(j>)^{-1}$ and $j<$, $(j<)^{-1}$ where $j> = l + \frac{1}{2}$, $j< = l - \frac{1}{2}$. These will be discussed in more detail in Section 4.1.4.

4.1.3. Dependence on A, E_p

If the idea of a unit cross section is to be generally useful for determination of GT strength, then its dependence on target mass must be known. This has been determined empirically for nuclei in which a transition of known β strength is excited directly in the corresponding charge-exchange reaction. For other nuclei it must be assumed that $\hat{\sigma}(A)$ can be reliably calculated with a model for the reaction.

The question of a suitable model has been investigated in considerable detail in [89]. There it was shown that experimental results at 120, 160 and 200 MeV could be fitted by an expression of the form $\hat{\sigma}(A) = C \exp(-XA^{\frac{1}{3}})$. This form

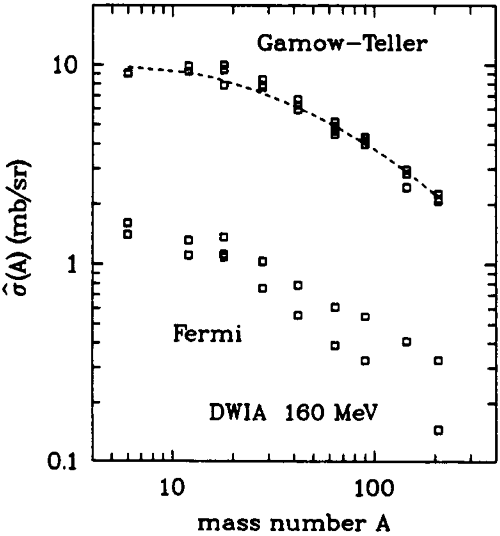

Fig. 4.1. Results of DWIA calculations of $\hat{\sigma}$. For a given A, boxes show the results of using different particle transition amplitudes. Note the large variations for Fermi transitions. Reprinted from Nucl. Phys. A, v 469 T. N. Taddeucci *et al.*, The *(p,n)* reaction as a probe of beta decay strength (1987) 125–172 [89], with kind permission of Elsevier Science-NL Sara Burgerhartstraat 25, 1055KV Amsterdam, The Netherlands.

for the A dependence was that predicted by the eikonal approximation, while the energy-dependent parameters C and X were estimated by least-squares fits to data. The resulting fit at 160 MeV is shown as the dashed curve in Fig. 4.2. For even-A targets the curve provides a reasonable fit to the data, with deviations usually within the quoted experimental uncertainties. For targets with $A \leq 60$, these uncertainties are typically about 10%, which are not much greater than the variation in the predicted state-dependence of $\hat{\sigma}$. For heavier targets, suitable beta transitions carry little strength, resulting in rather large uncertainties in the small measured (p,n) cross sections.

For many odd-A targets, the measured values of $\hat{\sigma}$ are significantly greater than the curve in Fig. 4.2, with particularly large deviations, ranging up to 50%, for masses A = 13, 15 and 39 [90]. The cause of these deviations is not understood at the present time, but it may be significant that the largest ones all involve mixed GT + F transitions between isobaric analog states. In a number of non-analog transitions such as ^{37}Cl [91, 921], ^{51}V [93] or 71Ge [94], the measured value of $\hat{\sigma}$ is consistent with values for nearby even-A nuclei. Even in the case of the ^{13}C$(p,n)^{13}$N reaction, the GT transition to the $\frac{3}{2}^-, T = \frac{3}{2}$ state

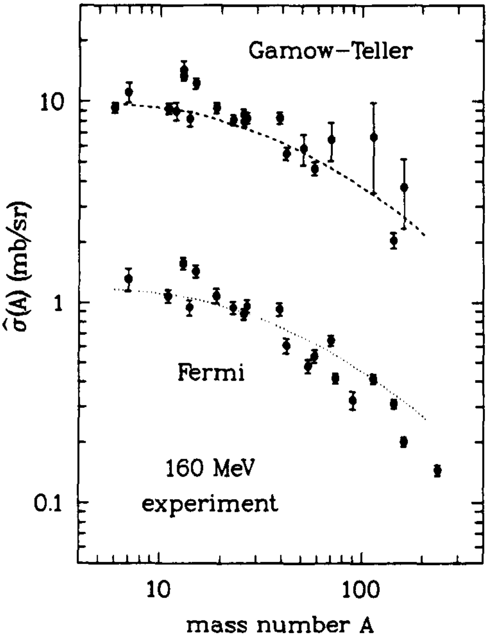

Fig. 4.2. Experimental results for measurements of $\hat{\sigma}$GT and $\hat{\sigma}_F$at 160 MeV. The dashed curve shows the A-dependence predicted by the eikonal approximation. The dotted curve is the dashed curve reduced by the ratio $(55/160)^2$. Reprinted from Nucl. Phys. A, v 469 T. N. Taddeucci *et al.*. The *(p.n)* reaction as a probe of beta decay strength (1987) 125–172 [89], with kind permission of Elsevier Science-NL Sara Burgerhartstraat 25. 1055KV Amsterdam, The Netherlands.

at 15.06 MeV yields a value of $\hat{\sigma}$ = 9.8 ± 0.9 mb/sr [95] which is in satisfactory agreement with results for ^{12}C$(p,n)^{12}$N.

4.1.4. Weak Transitions

In early studies of the proportionality between $d\sigma/d\Omega$ $(q = 0)$ and B_{GT} it was noted that contributions to the cross section from non-central parts of the effective interaction would become important if the GT strength was small [34]. In this context, "small" was generally taken as relative to the strength of pure single particle–hole transitions, which is of the order of magnitude of unity. An estimate of the expected effect is shown in Fig. 4.3 from [96]. In this figure, $\hat{\sigma}$ is calculated for transitions in which the GT matrix element is decreased relative to that for the pure single-particle value for two cases, $A = 12$ involving $p_{\frac{3}{2}}$ and $p_{\frac{1}{2}}$ states and $A = 29$ involving $d_{\frac{5}{2}}$ and $d_{\frac{3}{2}}$ states. The results show that for $j_>$, $(j_>)^{-1}$ and $j_>$, $(j_<)^{-1}$ transitions $\hat{\sigma}$ varies by less than a few percent for $A = 12$, and less than 10% for $A = 29$, for GT strength greater than about 1% of the single particle value. In contrast to this behavior, $j_<$, $(j_<)^{-1}$ transitions are strongly affected, with $\hat{\sigma}$ increasing by a factor of two for transitions with a few percent of the single-particle strength.

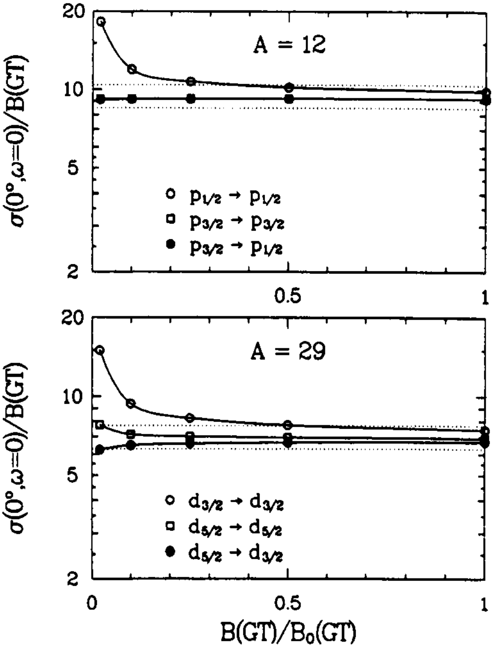

Fig. 4.3. Values of $\hat{\sigma}_{GT}$ calculated for A = 12 and 29. Starting with the pure particl–hole transitions shown ($B/B_0 = 1$). the GT-amplitude was decreased, holding other amplitudes fixed. The dotted lines indicate 10% variation from the average values at B/B_0 = 1. Reprinted from [96] with permission.

This problem has also been studied by Austin *et al.* [97], who calculated $\hat{\sigma}$ for states populated in the ^{37}Cl(p, n) reaction. Wave functions were calculated for the full ($2s1d$) shell, and reaction cross sections were calculated with DWIA including knock-on exchange. The calculations showed that if only $\Delta L = 0$ transition amplitudes were considered, then $\hat{\sigma}$ shows variations of no more than about 10%, even for the weakest transitions. If $\Delta L = 2$ amplitudes are included, however, then calculated values of $\hat{\sigma}$ frequently showed increases of about 20%, and in one case by a factor of two, for transitions with $B_{GT} < 0.4$. It is usually assumed that $\Delta L = 2$ contributions can be identified by the characteristic shape of their angular distributions and that a multipole analysis can be carried out to determine the $\Delta L = 0$ part of the cross section. Austin *et al.*, showed, however, that the interference of different transition amplitudes may result in an angular distribution that cannot be represented as a simple sum of $\Delta L = 0$ and $\Delta L = 2$ cross sections. The conclusion was that for transitions with a strength BGT less than a few tenths of a unit, the strength estimated from (p, n) measurements was subject to large uncertainty, as much as a factor of two for very weak transitions.

4.2. Comparison with Fermi Transitions

In heavy nuclei, GT transitions to nuclear ground states are weak, and the direct determination of $\hat{\sigma}_{\mathrm{GT}}$ is no longer feasible. One solution to this difficulty has been to calibrate $\hat{\sigma}_{\mathrm{GT}}$ relative to $\hat{\sigma}_{\mathrm{F}}$, the unit cross section for the Fermi transition.

It is known that the Fermi transition excites a single state (or a compact group of states) in the final nucleus, the isobaric analogue of the target ground state, with the known beta decay strength $B_{\mathrm{F}} = N - Z$. Using the model implied by Eq. (2.6) the ratio of cross sections for GT and F transitions can be written

$$\frac{d\sigma(q=0)_{\mathrm{GT}}}{d\sigma(q=0)_{\mathrm{F}}} = \frac{N_{\mathrm{GT}}\,|v_{\mathrm{GT}}(0)|^2 B_{\mathrm{GT}}}{N_{\mathrm{F}}\,|v_{\mathrm{F}}(0)|^2 B_{\mathrm{F}}} \tag{4.1}$$

Thus a comparison of GT and F transitions in any suitable nucleus (^{14}C is most convenient) provides an experimental determination of the quantity

$$\frac{\hat{\sigma}_{\mathrm{GT}}}{\hat{\sigma}_{\mathrm{F}}} = \frac{N_{\mathrm{GT}}}{N_{\mathrm{F}}}\left|\frac{v_{\mathrm{GT}}(0)}{v_{\mathrm{F}}(0)}\right|^2$$

The distortion factors can be calculated using DWIA. It is found that either factor alone is subject to uncertainties of up to about 50% depending on the choice of optical model parameters, but the ratio is largely unaffected by this uncertainty. Thus the ratio of interaction strengths may be determined directly from the (p, n) cross section data. Measurements of this ratio as a function of beam energy [46, 98, 99, 100] have been reported over the energy range 50 MeV $\leq E_{\mathrm{p}} <$ 800 MeV, with results shown in Fig. 4.4. These results were obtained using the $^{14}\mathrm{C}(p, n)$ reaction in which strong transitions of known strength can be clearly resolved. If it is assumed that this ratio is truly characteristic of the free N–N interaction, then the GT unit cross section for other nuclei can be determined from Eq. (4.1).

Although this approach has often been used to calibrate $\hat{\sigma}_{\mathrm{GT}}$, there is evidence that it may be subject to large uncertainties at least for odd-A nuclei. In the energy range 50 MeV $< E_{\mathrm{p}} <$ 200 MeV, data for a number of even-A nuclei show that the energy dependence of the ratio of unit cross sections is $\hat{\sigma}_{\mathrm{GT}}/\hat{\sigma}_{\mathrm{F}} = R_2(E_{\mathrm{p}}) = (E_{\mathrm{P}}/E_0)^2$ with $E_0 = 55.1 \pm 1.4$ MeV [98]. For many odd-A nuclei, however, a value $E_0 \simeq 45$ MeV is required [101], and for the $^{35}\mathrm{Cl}\,(p,n)$ reaction a value $E_0 \simeq 35$ MeV has been reported. In this case it has been shown that the value of $\hat{\sigma}_{\mathrm{F}}$ is smaller and $\hat{\sigma}_{\mathrm{GT}}$ is larger than for the neighboring nucleus ^{34}S. Thus what are expressed as differences in the

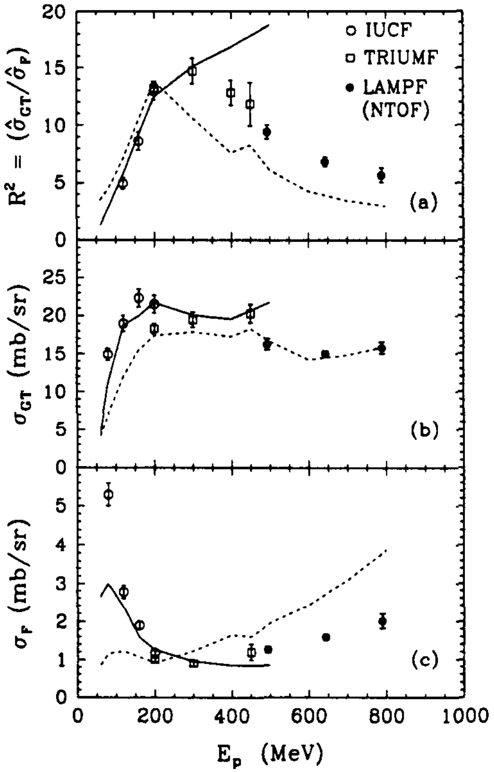

Fig.4.4. (a) The ratio of cross sections of the ^{14}C (p,n) ^{14}N reaction populating the 2.31 and 3.95 >MeV states of ^{14}N. The 2.31 MeV state is populated via the Fermi component ofthe NN-interaction. and the 3.95 MeV state by the Gamow–Teller component. Parts (b) and (c) show the GT and F cross sections separately. The solid line is the result ofa calculation using a *G*-matrix interaction based on the Bonn potential. The dashed line is obtained using a *t*-matrix based on free ,*N*-*N* amplitudes. Reprinted from [46] with permission.

energy dependence of the ratio may well reflect an unexpected A dependence of $\hat\sigma_F$ and/or $\hat\sigma_{GT}$

Taddeucci [89] has noted that values of $\hat\sigma_F$ calculated by DWIA showed a strong dependence on the assumed transition amplitude as shown in Fig. 4.1. In addition, the data of Fig. 4.2, from the same reference shows that values of $\hat\sigma_F$ measured at 160 MeV for $A \geq 40$ tend to lie close to one of two curves. The curve shown in Fig. 4.2 corresponds to a value $R(E_p) = E_p/55$ MeV. A similar curve fitted to the lower data points would imply $E_0 \simeq 40$ MeV. Thus at 160 MeV, the experimental ratio $\hat\sigma_{GT}/\hat\sigma_F$ for heavy nuclei shows variations of almost a factor of two for different targets. The conclusion from this result must be that estimates of GT strength in heavy nuclei based on a comparison with the Fermi transition are considerably less certain than is often implied in discussions of experimental results.

5. GAMOW–TELLER GIANT RESONANCE

For the Gamow–Teller giant resonance (GTGR), spread among many compound nuclear states by the residual interaction, the interesting physical properties are the position of the centroid, the spreading width, and the total integrated strength which can be compared to the Gamow–Teller sum rule. As discussed in Section 5.1, the location and spreading width have not been the subject of serious controversy. In contrast however, the integrated strength, discussed in Section 5.2, gave rise to the "missing strength" or "quenching" problem which has been the subject of lively debate for more than a decade, but which is now largely resolved.

5.1. Strength Distribution

The IUCF results of Bainum *et al.* [29], for the reaction ^{90}Zr(p, n)^{90}Nb at 120 MeV exhibit the typical features of the GTGR, as shown in Fig. 2.2b About 80% of the observed strength is found in the peak centered near an excitation energy of 8.7 MeV, with a width of about 4 MeV. Most of the remaining strength is found in the peak at 2.3 MeV. The low-lying state arises from a $j_>^{-1}\, j_>$ (here $g_{9/2}^{-1}\, g_{9/2}$) transition while the peak at higher energy is associated with the $j_>^{-1}\, j_<$ $\left(g_{9/2}^{-1}\, g_{7/2}\right)$ transition. The residual particle–hole interaction shifts transition strength from the lower to the higher state, while mixing with other more complicated states results in the observed broad peak. A systematic study [34] showed similar results for a number of target nuclei in the mass range $90 \le A \le 208$. For lighter nuclei, particularly $A \le 40$, the collective enhancement of the resonance strength is less pronounced, and the strength distribution can be described in terms of a simple shell model.

The excitation energy of the GTGR and the main features of the strength distribution can be readily accounted for by a Tamm–Dancoff Approximation (TDA) or Random Phase Approximation (RPA) model of $1p-1h$ excitations with a residual p–h interaction. The important inputs for such a calculation are an estimate of single particle energies, particularly the spin–orbit splitting, and of the strength of the residual interaction. In an early treatment, Bertsch [102] assumed a simple residual interaction of the form $V(1,2) = V_{\sigma\tau}\delta(\vec{r}_1 - \vec{r}_2)$. Using observed excitation energies for the resonance he concluded that the magnitude of $V_{\sigma\tau}$ was generally consistent with other estimates, and that the observed strength distribution was accounted for. A similar approach by Gaarde et al. [34], concluded that the data could be fitted well with a value of $V_{\sigma\tau} = 245$ MeV. fm^3. In other, mostly later, treatments [103]; [104]; [105]; [106]; the particle–hole interaction was assumed to arise from one-pion plus one-rho exchange, plus a pair correlation function to account for effects of other exchanges. In all these studies it was concluded that the model gave a satisfactory account of the data using reasonable values of model parameters.

Several calculations have also been reported in which a straightforward shell model is used to model the GTGR. The first of these was by Gaarde *et al.* [58], to fit the location and spreading of the "bump" observed in the ^{48}Ca(^{3}He, t)^{48}Sc reaction at 66 MeV. Following the publication of the results of Bainum *et al.*, for the ^{90}Zr(*p,n*)^{90}Nb reaction at 120 MeV, Mathews *et al.* [107], showed that the observed distribution of GT strength was well accounted for by a shell model calculation with a model space of the (2*p*1*g*) shells. Another calculation by Muto *et al.* [108], assumed a closed core of ^{88}Sr with single particle excitations into the (3*s*, 2*d*, 1*g*) shells. Using single particle energies and two-body matrix elements from fits to level schemes in that mass region, a satisfactory fit to the GT strength distribution was obtained.

A better understanding of the width of the GTGR requires an extension of the basic 1*p*–1*h* model to include mixing with more complex many particle–many hole excitations. In an early calculation, Bertsch and Hamamoto [109] used a schematic model to investigate the effect of mixing with 2*p*–2*h* excitations. They concluded that the GT strength distribution would be fragmented and spread over several tens of MeV in excitation energy mainly by the tensor component of the *p*–*h* interaction. The shell model wave functions used in the calculations of Mathews *et al.,* and Muto *et al.,* contained components corresponding to 2*p*–2*h* excitations, and in both cases the authors showed that mixing of these with the 1*p*–1*h* excitations led to a spreading of the strength distributions that was in reasonable agreement with the data.

A number of RPA type calculations have also been reported in which the effects of 2*p*–2*h* excitations are included. An early paper by Schwesinger and Wambach [110] considered the general problem, which was then followed by an application of their ideas to spin-isospin excitations by Cha *et al.* [106]. In the latter paper it was argued that it was not necessary to consider excitations more complex that 2*p*–2*h*. In such a model space it was then shown that a correlated one-boson exchange effective interaction was able to reproduce measured GT strength distributions for ^{90}Zr and ^{208}Pb. In general, this spreading of GT strength results in a decrease in strength at low excitations, as will be discussed in the following section.

In summary, both the excitation energy and the shape of the strength distribution of the GTGR can be readily accounted for on the basis of the model originally suggested by Ikeda *et al.* [15], using a reasonable model space and reasonable residual interactions.

5.2. Transition Strength — The Missing Strength Problem

The transition strength of the GTGR is of great interest since the total strength is predicted by the model-independent GT sum-rule, $S^{-} - S^{+} = 3\,(N - Z)$, while it may be determined experimentally using charge-exchange reactions. Only about 60% of the predicted strength can be clearly identified experimentally however, and the reasons for this discrepancy were not fully understood for about a decade.

In the initial proposal of the existence of the GTGR, it was assumed that particle–hole interactions had shifted strength from the low-lying states observed in beta decay to the region of the giant resonance, which was energetically inaccessible to beta decay. The total sum-rule strength was conserved however, and would be observable with suitable experimental techniques. As early as 1963 it had been suggested [15] that the (*p, n*) reaction should provide the experimental capability. The first real test of this possibility was provided by the observation at MSU of the GTGR in the ^{90}Zr(*p, n*) reaction at 45 MeV [28]. Although the resonance peak was superposed on a large background, the cross section of the peak itself was estimated, and compared with DWIA predictions. It was concluded that the measured cross section was consistent with the GT sum-rule.

With the higher energy available at IUCF, the GTGR was much more clearly defined relative to background, and cross sections could be estimated with greater precision. In a study of the ^{26}Mg(*p, n*) reaction [111], the measured cross section was compared with shell model predictions using the full (2*s* 1*d*) shell model space and it was concluded that only about 60% of the predicted strength was observed. For a target of ^{42}Ca, it is expected that (*n,p*) transitions would be blocked giving $S^{+} = 0$, and $S^{-} = 3\,(N - Z) = 6$ units. The shape of the strength distribution observed in the ^{42}Ca(*p,n*) reaction [112] agreed well with shell model predictions although the total strength observed up to an excitation energy of 30 MeV was only 3.2 units. In further studies of ^{48}Ca(*p,n*) and ^{90}Zr(*p,n*) it was also concluded that only 40 to 50% of the predicted strength could be identified.

For targets with $A \geq 40$, the GTGR is superposed on a continuum and in the above studies it was initially assumed that the continuum represented a background to be subtracted from the GTGR peaks. Calculations by Osterfeld [113] showed however that in the (*p,n*) spectra at 0°, transitions with $\Delta L > 0$ made very little contribution to the cross section in the vicinity of the GTGR, indicating that the assumed background in fact was part of the GTGR. This led to a significant increase in the estimate of observed GT strength, but measurements on many targets up to $A = 238$ showed conclusively that 30 to 40% of the predicted GT strength could not be identified at excitation energies below

30 MeV [114]. This result defined the "missing strength" problem. With this, over the next decade, the GTGR provided a strong focus for the general elucidation of quenching effects in nuclear physics.

During the previous decade there had been much speculation about the possible observation of subnucleonic effects in nuclear structure [115, 116]. With the demonstration of the missing strength it was immediately pointed out that this could be a signature of such an effect. In particular, it was noted that the quantum numbers involved in GT transitions, $\Delta S = \Delta T = 1$, were the same as those required for the excitation of a nucleus to the Δ resonance. Thus the *p–h* excitation involved in the GTGR could mix with Δ–hole excitations resulting in a shift of GT strength to the region of the Δ resonance at an excitation energy of about 300 MeV. In spite of the high energy of the Δ excitations it was argued that this effect was important because all the nucleons in the nucleus could participate in the Δ–hole excitation, while most particle–hole excitations corresponding to the GTGR were blocked by the Pauli principle. Quantitative calculations [117, 118] of this effect were carried out using estimates of the coupling between Δ–hole and particle–hole excitations based on coupling constants for the $(\pi\text{–}\Delta)$ and $(\pi\text{–}N)$ interactions. The results of these calculations showed that the missing strength could in fact be accounted for by this model. It appeared to be a major experimental discovery, heralding important new directions in nuclear physics.

This result was criticized on several grounds. Speth [119] noted that the coupling between Δ–hole and particle–hole states was poorly known. The conventional estimate from meson theory noted above was not reliable because exchange effects were much different for the two types of interactions. It was also known that isoscalar spin-flip transitions show a quenching [120] similar to GT transitions even though the isoscalar excitations would not be mixed with Δ–hole excitations. A different mechanism for quenching was pointed out by Bertsch and Hamamoto [109] as noted earlier. Calculations of GT excitations using a realistic particle–hole interaction showed that the tensor component of the force produced strong fragmentation of the excitation with the resulting strength spread over several tens of MeV excitation, where it would be difficult to identify experimentally. This problem of identifying distributed strength is discussed later in Sec. 6.

The polarization of opinion on the cause of the quenching is illustrated in discussions at an international conference on spin excitations in nuclei (devoted mainly to the problem of GT quenching) in 1982. The exchange epitomized the intensity of the debate on the subject which persisted at many workshops and conferences for several years. At that time, Rho [121] argued that the Δ–hole mixing must be the most important mechanism involved. Arima [122] on the other hand argued strongly that quenching could be accounted for by conventional nuclear structure effects such as core polarization and configuration mixing. As early as 1954, Arima and Horie [123] had demonstrated the importance of $2p$–$2h$ excitations in fragmenting and spreading the strength of simple excitations, and this idea had been extended in many subsequent papers. Following the demonstration of the quenching of the GTGR, a large number of theoretical studies were carried out in an effort to provide quantitative estimates of the relative importance of Δ–hole excitations and conventional configuration mixing effects in this quenching. A few of these are described below, and references to other work are given in those discussed here.

Towner and Khanna [I24] carried out a careful investigation of GT and M1 matrix elements in (closed-shell ± one nucleon) nuclei at $A = 16$ and $A = 40$. For such nuclei, first order corrections to the matrix elements vanish, and second order corrections arise mainly from non-central components of the effective interactions. The calculation included second-order core polarization, meson-exchange currents and isobar currents. The effective interaction was taken as a one-boson exchange potential, and the second order corrections were carried out explicitly to excitations of $12\hbar\omega$ and then extrapolated to infinity. The final results showed reasonable agreement with experiment, especially in the light of the fact that extensive cancellations occurred among the eight terms contributing to M1 matrix elements and among the nine terms for GT. The authors concluded that while isobar excitations contribute to quenching they are not the dominant effect. They also presented a careful discussion of the uncertainties in their results arising from the model used in the calculations.

In a subsequent calculation Cha *et al.* [106], concluded that $2p$–$2h$ excitations alone could not account for the observed quenching below 40 MeV excitation. A similar calculation by Drożdż *et al.* [125], concluded that the inclusion of Δ excitations would reduce the calculated strength below experiment. They noted however that direct coupling of the ground state to $2p$–$2h$ excitations would be expected to increase the calculated strength and that satisfactory agreement with experiment should be obtained without a contribution from Δ excitations.

In most studies, the GT strength extracted from experimental spectra was compared with theoretical calculations. However, Osterfeld *et al.* [126], took a different approach in modelling the complete spectrum which was then compared with experiment for ^{90}Zr(p, n)^{90}Nb. Structure calculations were carried out for all isovector spin excitations up to $\Delta J^{\pi} = 5^{+}$, and the resulting wave functions were then used in DWIA to calculate (p, n) cross sections. These cross sections were normalized by comparison with calculations of the cross section for the ^{42}Ca(p,n)^{42}Sc reaction. The authors concluded that the experimental spectra could be accounted for without invoking quenching from Δ-excitations.

They noted that this conclusion could be modified if the measured cross sections included substantial contributions from core excitations in the target, and suggested that a measurement of the ^{90}Zr(*n,p*) cross section would provide a definitive test of the importance of Δ-excitations. A very similar calculation by Klein *et al.* [193], concluded that mixing between $1p$–$1h$ and $2p$– $2h$ excitations provides the most plausible explanation for the quenching.

In another approach to the missing strength problem, orbital occupancies for single-particle states in nuclei ranging from 3He to ^{208}Pb have been measured at NIKHEF using the (*e, e'p*) reaction. A review of the experimental work has been given by de Witt Huberts [127] and the theoretical interpretation of such results has been discussed in detail by Mahaux and Sartor [128].

Since this reaction proceeds via the electromagnetic interaction rather than the strong nuclear interaction there is relatively little uncertainty in the calculated cross section. Comparison with measured cross sections provides a determination of orbital occupancies with an estimated uncertainty of about 10%. The conclusion from such measurements is that only about 50 to 60% of the single particle strength predicted by shell model calculations can be identified.

Such results have helped to motivate a number of theoretical studies [129, 130, 131] which have shown that, in general, quasiparticle excitations mix strongly with more complex excitations, with the result that the single particle strength, or response function, is spread over an excitation energy region extending beyond 100 MeV. This spreading of the single-particle strength leads to a quenching of particle–hole excitations of all angular momenta and in all reactions. The specific treatment of GT and spin-dipole excitations has been discussed in detail for targets of ^{48}Ca and ^{90}Zr [132, 133]. For instance, because of excitations in the target ground state, it was calculated that the total GT strength in ^{48}Ca (*p,n*) is 30 units, 6 units greater than the sum rule limit 3 (N– Z). Only 14.5 units, or 60% of the limit, lie below 20 MeV excitation however, with the remainder spread more or less uniformly up to 80 MeV. The GT strength in ^{48}Ca (*n,p*) is then 6 units which is spread over a similar energy range with a density of about 0.1 unit/MeV.

The general conclusion is that this spreading of single-particle strength provides an understanding of much, if not all, of the phenomenon of quenching in nuclear physics. While Δ-excitations cannot be completely excluded, it appears that any contribution of this sort accounts for only a small fraction of the total quenching.

What then is the possibility ofexperimental verification ofthe fragmentation ofGT strength described above? In a word, it is slight at best. At high excitation the momentum transfer, even at zero degrees, becomes large enough that the tensor component of the effective interaction becomes dominant relative to the $\vec{\sigma}\tau$ component. As a result, in the (*p,n*) reaction the cross sections for transitions with $\Delta L > 0$ become large and tend to dominate the spectrum. Since experimental angular distributions are no longer forward peaked for high excitations the identification of the $\Delta L = 0$ component of the cross section becomes subject to large experimental uncertainties, as discussed in Sec. 6. At the same time, $\Delta L = 0$ contributions arising from the isovector monopole GR, a $2\hbar\omega$ excitation, are expected to appear. Thus, even if $\Delta L = 0$ strength is identified it cannot be unambiguously related to the GTGR. This problem has been considered in some detail by Raywood *et al.* [52].

The final conclusion must be that it is very unlikely that much of the missing GT strength can be identified experimentally. However, a wide range of theoretical studies has now concluded that most, if not all, the observed quenching can be understood within the framework of conventional nuclear structure calculations using large vector spaces and realistic effective interactions. The role of Δ excitations appears to be at most a small contribution to the total effect.

5.3. β+ Strength and the *(n,p)* Reaction

The foregoing sections have focussed on the (*p,n*) reaction and the measurement of β^- strength. However, the GT sum-rule involves both β^- and β^+ strength and may be written

$$S^- = 3(N - Z) + S^+ \tag{5.1}$$

In nuclei with a large neutron excess, allowed β^+ transitions are strongly suppressed by Pauli blocking, so that a knowledge of S^+ may not be needed in comparing measured values of S^- with the limit $3\,(N - Z)$. Indeed the demonstration of the missing GT strength in (*p, n*) reactions did not require a measurement of S^+. In general, however, a knowledge of S^+ is needed for a quantitative comparison with the sum-rule. In addition, a knowledge of the GT strength distribution for β^+ transitions is important in a number of other areas.

Given the symmetry between (*p,n*) and (*n,p*) reactions it is expected that the relation between (*n,p*) cross sections and corresponding β^+ strength will be the same as that between (*p, n*) cross sections and β^- strength. As the initial test of this expectation, measurements of $\hat{\sigma}_{\mathrm{np}} = [d\sigma/d\Omega\ (q = 0)]_{np} / B^+$ were carried out for strong GT transitions for targets of ^{6}Li, ^{12}C and ^{13}C [134]. The resulting comparison with measured values of $\hat{\sigma}_{pn}$ for these targets is shown in Table 5.1. All transitions are to the ground state of the final nucleus except for 13C (p,n)13N in which case the final state is the $\frac{3}{2}^-, T = \frac{3}{2}$ (15.06 MeV) isobaric analogue of the ^{13}B ground state. For each target it is seen that $\hat{\sigma}_{\mathrm{np}} = \hat{\sigma}_{\mathrm{pn}}$ within the quoted uncertainties. In a later, more detailed study [135]

TABLE 5.1
Comparison of Measured Values of Reduced Cross Sections for *(p, n)* and *(n,p)* Reactions at 200 MeV

Target	σ_{pn}	$\hat{\sigma}_{np}$
^{6}Li	9.1 ±0.5^{a})	9.90± 0.36^{b})
^{12}C	9.2 ±0.9^{a})	9.42±0.31^{b})
^{13}C	9.8 ±0.8^{c})	10.96±0.56^{b})
a) ref. [89]	b) ref. [134]	c) ref. [95]

a comparison of (*p,n*), (*p,p′*) and (*n,p*) reactions on ^{6}Li and ^{12}C was able to conclude that isospin was conserved between the different reactions, within the experimental uncertainty of 3%. The only other relevant measurement, in the ^{64}Ni (*n,p*) reaction [54, 136], is in reasonable agreement with results of (*p,n*) measurements in the mass region near A = 60, but the existence of a 1^{+} state at an excitation energy of about 300 keV in the final nucleus ^{64}Co introduces a rather large uncertainty in this conclusion.

Given the correspondence between (*n,p*) and (*p,n*) cross sections where useful comparisons are possible, it is generally assumed that GT^{+} strength distributions can be deduced from (*n,p*) measurements using the ratios σ_{pn}/B^{-} for which extensive data are available. Of course, the problems expected for weak transitions with this approach would be the same for (*n,p*) as for (*p,n*) studies.

5.4. Experimental Results of GT Studies

In the foregoing, the emphasis has been on the problem of measuring GT strength distribution, and on understanding the significance of the missing strength. A number of other interesting problems in nuclear physics involve GT transitions however, and some of these will be reviewed briefly.

5.4.1. Effective Interactions

Much of the initial interest in (*p, n*) studies was motivated by the possibility of determining the properties of the Fermi and GT parts of the effective interaction $V_F = V_\tau$ and $V_{GT} = V_{\sigma\tau}$, as discussed earlier. The IUCF results showed that at intermediate energies, interaction strengths could be extracted from the forward angle (*p, n*) cross sections with much less uncertainty than at low energies. They also provided a striking demonstration of the strong energy dependence of the ratio of the strengths between 60 and 200 MeV [98] which motivated a number of theoretical investigations.

Love [137] and Petrovich [138] showed that the measured ratio was reproduced quite well with a *G*-matrix interaction, and soon afterwards Love and Franey [139] showed that a *t*-matrix interaction derived from measured nucleon-nucleon phase shifts also gave a good fit to the data. The observed energy dependence was shown by Brown *et al.* [140], to arise naturally in a one-boson exchange model with π and ρ mesons. The actual magnitude of their calculated ratio was in fair agreement with the results of Love and of Petrovich, and with the data up to 200 MeV,

Measurements of the ratio were later extended to 450 MeV at TRIUMF [99] and to 800 MeV at LAMPF [46, 141]. The solid line is the result of a calculation using a *G*-matrix interaction based on the Bonn potential. The dashed line is obtained using a *t*-matrix based on free *N–N* amplitudes. At energies above 200 MeV, the calculated ratio did not fit the data as well as at lower energies, and it was shown that the disagreement arose mainly because of difficulties in calculating V_F, the Fermi part of the interaction. This part arises from a second order exchange [140] and is much more sensitive to finite density effects and other details of the calculation than is the GT part which arises mainly from one-boson exchange. The calculated magnitude of V_{GT} appears to be in satisfactory agreement with experiment [142].

It should be noted that the measured values of V_F and V_{GT} have all assumed that at small momentum transfer only the central parts of the effective interaction need be considered. Love *et al.* [143] have shown however that the ratio of cross sections for the strong transitions in ^{14}C$(p,n)^{14}$N are sensitive to the non-central parts of the interaction, and also to the optical model spin–orbit interaction. Since this sensitivity arises mainly in the calculation of V_F, it is likely that the theoretical comparisons with V_{GT} directly are more significant than with the ratio V_{GT}/V_F.

5.4.2. Nuclear Structure — Model Comparisons

GT transitions and strength distributions from (*p, n*) and (*n,p*) studies now provide a large body of experimental data for a well-defined simple nuclear excitation. As such they have been of considerable interest for shell model comparisons. In principle, the (*n,p*) results should be of particular interest, since the blocking of β^+ transitions for nuclei with $N > Z$ makes the model predictions very sensitive to the choice of shell-model effective interactions [144].

Many reported measurements of GT strength distributions have included model comparisons. For 1*p* and (2*s*1*d*) shell nuclei, calculations can be carried out in the full $0\hbar\omega$ model space, and the resulting distributions usually show reasonable agreement with the data, although the measured strength is typically only about 60% of the model prediction. Typical results which illustrate such a comparison may be noted for ^{10}B [145], ^{16,18}O [45], ^{26}Mg [146] and ^{32}S [78].

For (2*p* 1*f*) shell nuclei, with the energy resolution available, discrete final states are rarely observable. Furthermore, calculations can only be carried out in a truncated model, but it is found that the main features of the measured distributions are reproduced fairly well. In this mass region, some typical results for (p,n) studies are those reported for ^{40}Ca [147], ^{42}Ca [112], ^{51}V [148] and ^{54}Fe [27, 149]. For the (*n,p*) reaction the quality of the model comparison is exemplified by results for ^{40}Ca [53], ^{45}Sc [150], ^{55}Mn, ^{56}Fe and ^{58}Ni [151] and again ^{54}Fe [152]. For all these comparisons except ^{42}Ca and ^{45}Sc, the calculations must be renormalized by a factor of about 0.3 as a result of the truncation of the model space.

5.4.3. *Electron Capture in Supernova Formation*

An interesting application of the (*n,p*) reaction has been in the measurement of GT transition rates required in calculations of presupernova stellar collapse [153]. In the late stages of the evolution of a massive star, most of the core has been converted to elements in the Fe–Ni region. At this point no further energy can be generated by nuclear reactions in the core, and much of the support for outer layers of the star is provided by the pressure of the degenerate electron gas in the core. In the absence of an energy source, the core contracts and its temperature rises. Eventually the thermal energy of the electrons is large enough that electron capture becomes important:

$$^{Z}A + e^{-} \rightarrow {}^{Z-1}A + \nu$$

Once this process starts, the loss of core electrons, plus the additional loss of energy via neutrino emission leads to collapse of the star and possible supernova formation. In order to model the onset of collapse a knowledge of transition rates for electron capture on nuclei in the core are required.

In early model calculations [154] the necessary strength distributions were estimated using a very simple nuclear model, since little experimental information was available. However, with the development of facilities for intermediate energy (*n,p*) measurements beginning at TRIUMF in 1986, it has become possible to measure some of these strength distributions and so test the validity of the earlier models. In the (2p1f) shell, measurements of GT^{+} strength have been reported for ^{45}Sc [150], ^{48}Ti [155], ^{51}V, 59Co [156], ^{54}Fe [27], ^{55}Mn, ^{56}Fe, ^{58}Ni [151], ^{60,62,64}Ni [136], and ^{70,72}Ge [157]. Calculations of electron capture rates using some of these new results have been carried out and compared with results of earlier calculations [158, 159]. For some nuclei there is little difference, but for ^{59}Co for example the new result leads to a reduction in the calculated rate by a factor of at least 4.5.

It should be noted that the astrophysics calculations involve unstable as well as stable nuclei. Also, at the temperatures reached in the collapsing core, nuclei will undergo thermal excitation so that strength distributions for excited states are also required. Thus, the available data should be viewed as calibrations for model calculations of GT^{+} strengths. Conventional truncated shell model calculations have been carried out, and comparisons with data are discussed in the experimental papers noted. The overall agreement between theory and data is generally reasonable, but it would be desirable to have a better understanding of the deviations and the extent to which they could point to shortcomings in the model. Some work in this direction has been reported [160, 161] using a shell model Monte Carlo approach which permits calculations to be carried out in a full ($2p1f$) model space. The results show good agreement with measured GT^{+} strength distributions with the same quenching as is found for such comparisons in ($2s1d$) shell nuclei.

5.4.4. Calibration of Neutrino Detectors

The measurement of the neutrino flux from the sun involves the absorption of neutrinos in a GT transition:

$$v+{}^{Z}A + {}^{Z+1}A+e^{-}$$

and the calibration of detector efficiency requires a knowledge of the GT strength distribution for the target nucleus. In the initial experiment in this field the detector was ^{37}Cl, with the GT strength for the ground state transition known from the electron-capture decay rate of ^{37}Ar. The strength of excited state transitions was inferred from the β^{+} decay of ^{37}Ca [242] with the assumption of isospin symmetry between the $^{37}\mathrm{Ca} \rightarrow {}^{37}\mathrm{K}$ and the $^{37}\mathrm{Cl} \rightarrow {}^{37}\mathrm{Ar}$ transitions. The detector is sensitive mainly to the high-energy neutrinos resulting from the beta decay of ^{8}B in a minor branch of the solar energy production cycle.

Following the demonstration of the deficit of ^{8}B neutrinos [162] there has been widespread interest in the problem of detecting solar neutrinos, especially the lower energy neutrinos arising from the basic *p–p* cycle. Detectors have been proposed based on ^{71}Ga [163], ^{81}Br [164], ^{98}M0 [165], ^{115}In [166] and ^{127}I [167]. The (*p, n*) reaction has been used to measure the distribution of GT strength for most of these.

The most interesting case is ^{71}Ga, since this is used in the GALLEX detector and in the SAGE detector [168, 169]. In this case the (p,n) results [94] yield a strength of 0.085 ± 0.015 units for the ground state transition, compared with 0.091 units determined from the decay of ^{71}Ge. In addition, an excited state at 0.5 Me V cames a strength of 0.010±0.005 units and the total strength up to the particle emission threshold (7.4 MeV) is 4.3 ± 0.7 units. In the ^{98}Mo(*p,n*)^{98}Tc reaction, B_{GT} = 0.44 units is measured for an unresolved group of states near the ground state [170]. However, since the low-lying 1^+ states have not been identified in ^{98}Tc, it is not possible to use this measurement to estimate the sensitivity of the proposed detector for low energy neutrinos. For ^{115}In, a state of spin $7/2^+$ at 0.614 MeV in ^{115}Sn has B_{GT} = 0.17, with very little additional strength to any level below about 4 MeV. For the ^{127}I (*p,n*) reaction [101] full details of the strength distribution are not given, but it is claimed the measured strength is substantially less than earlier estimates [167] which means that the sensitivity of the proposed ^{127}I detector would not be much different than that for ^{37}C1.

It is of some interest to note that the ^{37}Cl (*p, n*) reaction was also studied [91] and significant discrepancies with the ^{37}Ca decay results were found. Although the discrepancies had only a small effect on the calculated efficiency of the ^{37}Cl solar neutrino detector, they led to the suggestion that the (*p,n*) reaction did not provide a reliable determination of GT strength [171]. As a result of this problem, further measurements of both the (*p,n*) reaction [92] and the ^{37}Ca β^+ decay [172] were carried out, and the source of most of the discrepancy identified as the unexpected gamma decay of a proton unbound level in ^{37}K. The remaining disagreement is probably the result of uncertainties in the (*p, n*) results for weak transitions as discussed earlier.

Clearly the (*p, n*) measurements have been helpful in assessing the feasibility of new proposals, such as for the ^{127}I detector. In every case, however, the low-lying states of interest carry only a small amount of GT strength so that its determination via the (*p,n*) reaction is subject to the uncertainties discussed in Section 4.1.4. It appears likely the final accurate calibration of detector response must involve the use of strengths determined from beta decay, or directly by neutrino absorption using a radioactive source to provide a known flux of neutrinos, as has been done for the ^{71}Ga detector [169, 173].

6. MULTIPOLE ANALYSIS: GT STRENGTH AT HIGHER EXCITATION ENERGY

The measured spectra in (*p, n*) reactions show transitions to discrete states or broad resonances at low excitation energy exhibiting forward peaked angular distributions which are fitted satisfactorily by DWIA calculations for $\Delta L = 0$. The forward peaking is the characteristic signature of transitions with $\Delta L = 0$, and these transitions are clearly identified as part of the GT strength. At higher excitation energies, typically above 10 to 15 MeV, angular distributions no longer show forward peaking, and generally are not characteristic of a single L-transfer. GT strength is expected in this region due to the spreading discussed in Section 5.2, but is not unambiguously identifiable, as at lower excitation. The problem of determining GT strength in this situation is often approached through a multipole decomposition analysis (MDA). The essential ideas behind such an analysis have been discussed by Moinester [174], and typical applications are illustrated in a number of data analyses, both for *(p, n)* [45, 53, 148] and *(n,p)* reactions [52, 156, 175].

The method has serious limitations, but provides a useful general procedure for identifying the major components of measured spectra. In spite of its limitations it has been extensively used in the analysis of charge-exchange data, and will be discussed in some detail below.

In the MDA, measured spectra at several angles are used to construct angular distributions of the differential cross section as a function of the excitation energy in the final nucleus. For each energy bin, it is assumed that the measured angular distribution can be fitted by a sum of cross sections arising from different suin transfers:

$$\left.\frac{d\sigma(\theta)}{d\Omega}\right|_{\text{exp}} = \sum_{J} a_{J^\pi} \cdot \left.\frac{d\sigma(\theta)}{d\Omega}\right|_{J^\pi} \tag{6.1}$$

In this expression, the cross section for each value of J^π is the result of a DWIA calculation, while the coefficients $a_{J\pi}$ are determined by a least squares fit to the data with the constraint that each coefficient must be non-negative. Sincc the number of angles at which measurements are made is limited — usually no more than six in typical intermediate energy charge-exchange experiments — the number of terms in the sum must be small in order to carry out a meaningful least squares fit.

Characteristically, the experimental data is limited to the forward direction, usually to angles less than ~ 20°, with the consequence that small values of the orbital angular momentum transfer will be the most important. For a (p, n) reaction on a nucleus with $A = 60$ at 200 MeV, the condition $\Delta L_{\text{max}}, = \Delta kR$ gives an estimate of $\Delta L_{\text{max}} \simeq 4$. For a target nucleus with $A = 238$ at 300 MeV, the same condition gives $\Delta L_{\text{max}} \simeq 8$. Since spin-flip transitions are known to be strong at these energies, for $A = 60$ transitions would be expected for $\Delta J^\pi = 0^+, 1^+$ ($\Delta L = 0$); $0^-, 1^-, 2^-$ ($\Delta L = 1$); $1^+, 2^+, 3^+$ ($\Delta L = 2$); $2^-, 3^-, 4^-$ ($\Delta L = 3$); and $3^+, 4^-, 5^+$ ($\Delta L = 4$), a total of fourteen ΔJ values in all.

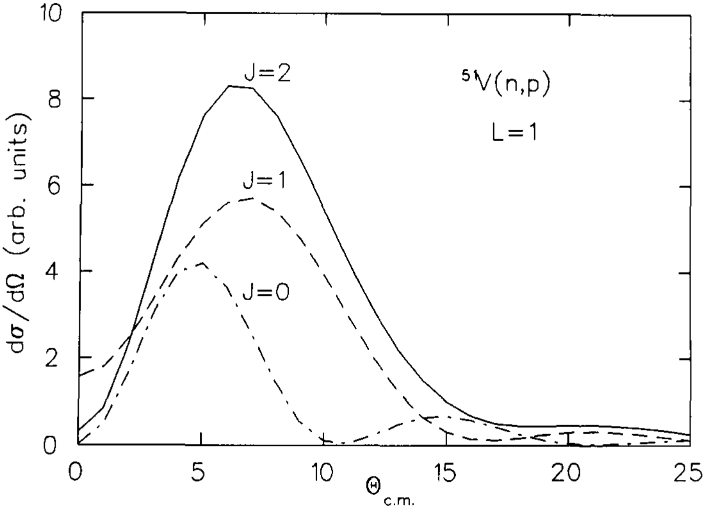

Fig. 6.1. Calculated differential cross sections for ΔL = 1 transitions with DJp = 0^-,1^- and 2–. For the 0– case the particle–hole transition was assumed to be $(f_{7/2})^{-1}$($g_{7/2}$), and for the 1^- and 2^- $(f_{7/2})^{-1}$ ($g_{9/2}$).

However, it is known that nuclear reaction angular distributions are characterized mainly by the orbital angular momentum transfer, ΔL, and are only weakly dependent on the total angular momentum transfer, ΔJ. This justifies the restriction of the number of terms in the least squares fit to the number of DL values involved. This point is illustrated in Fig. 6.1, where calculated angular distributions for ΔL = 1, ΔJ^π = 0^-, 1^-, 2^- for 1*p*–1*h* transitions expected to be important at low excitation energies in the ^{51}V (*n,p*) reaction, i.e., $\left(\pi f_{\frac{7}{2}}\right)^{-1}\left(\nu g_{\frac{7}{2}}\right)$ for 0–, and $\left(\pi f_{\frac{7}{2}}\right)^{-1}\left(\nu g_{\frac{9}{2}}\right)$ for 1^- and 2^-. The main peak of the angular distribution occurs at about the same angle for 1^- and 2^- transitions, and at a slightly smaller angle for the 0– transition. The magnitude of the peak cross section is about the same for ΔJ^π = 1^- and 2^-, and somewhat less for the 0^- case. From this it is concluded that all contributions with ΔL = 1 can be adequately represented by a DWIA angular distribution for ΔJ^π = 1^-. In passing, it may be noted that the difference in angles at the peak of the 0^- and 1^- angular distributions decreases as the mass number of the target increases.

Comparable results are found for transitions with ΔL = 2, 3, 4 and it is usually assumed that the representative shape for each of these is given by a DWIA angular distribution for $\Delta J = \Delta L$ or $\Delta L + 1$.

It should be noted here that except for $\Delta L = 1$, spin-flip transitions with $\Delta J = \Delta L - 1$ can also be excited with orbital angular momentum $\Delta L' = \Delta L - 2$. Thus in general, unnatural parity transitions will occur with a coherent mixture of two orbital angular momentum transfers, and the shapes of the DWIA angular distributions might be expected to show the effect of interference between the two contributions; however it is found that the angular distribution for a given ΔJ is usually similar to that for the smaller of the two allowed values of ΔL. It is also found that the DWIA shapes for unnatural parity transitions show somewhat more variability in their dependence on the assumed transition amplitude than do natural parity transitions with $\Delta J = \Delta L$. This presumably reflects the effects of the interference in ΔL.

Other inputs required for the DWIA calculations are the optical model potentials, the nucleon-nucleon interaction responsible for creating the *p–h* excitation, and the one body density matrix elements (OBDME) involved in the transition.

For the purposes of the MDA, the results of DWIA calculations are insensitive to the choice of effective interaction and optical model potentials. The magnitude of the cross section depends on these inputs, but the characteristic shape of the angular distributions, i.e., the location and width of the primary peak, is not significantly sensitive to reasonable variations in either optical potentials or effective interaction. The effects of such changes are illustrated in [45]. On the other hand, details of the distributions are affected; in particular the magnitude of the cross section at 0° for transitions with $\Delta L > 0$ is sensitive to distortions in the scattering channels, i.e., the optical potentials. This point is particularly important in estimating GT strength at high excitation energy, as is discussed later.

In the calculations described below the Franey–Love *N–N* interaction [176] was used. Optical potentials were calculated by folding this interaction with nuclear charge distributions from electron scattering. All the DWIA results of this section were calculated using the code DW81 [8].

The OBDME may be obtained as the result of a model calculation, particularly for lighter nuclei. Another approach is to use a transition amplitude generated by the application of an appropriate excitation operator to the assumed target ground state. The simplest procedure, which is often used, is to assume a simple $1p$–$1h$ transition involving the single particle states expected to be most important in the region of excitation of interest. Although this may appear a rather drastic approximation, it turns out to be a reasonable one. DWIA calculations show that the main features of the angular distribution shapes for given ΔJ^{π} are not very sensitive to the choice of the OBDME. This is illustrated in Fig. 6.2 which shows results for $\Delta J^{\pi} = 1^{-}$ for a variety of single *p–h* transition amplitudes. To the extent that the ΔJ dependence of transitions

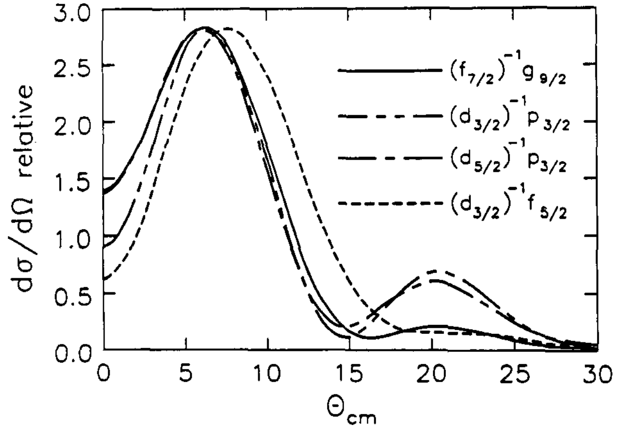

Fig. 6.2. Calculated angular distributions for $\Delta J^{\pi} = 1^{-}$ transitions in the 51V (*n*,*p*) reaction. The different particle–hole transitions are indicated. The result for the $(d_{3/2})^{-1}$ $(f_{5/2})$ transition shows a marked deviation from the average.

of given ΔL can be ignored, it would appear reasonable to use such a simple approximation in the calculations. This approach is adequate for small values of ΔL, but becomes increasingly questionable as ΔL increases. For one thing, the angular separation of the peaks for successive values of ΔL decreases as ΔL increases, as is seen in Fig. 6.3. For another thing, it is found that the DWIA shapes for a given $\Delta J = \Delta L$ show increasing sensitivity to the assumed transition amplitude as ΔL increases. As a result of these two tendencies, there is an increasing systematic uncertainty in cross section estimates as ΔL increases, and the MDA procedure becomes of questionable value for values of $\Delta L \geq 3$.

As a consequence of the above discussions, the series which is least-squares fitted to the experimental differential cross sections is given by

$$\left[\frac{d\sigma(\theta)}{d\Omega}\right]_{\text{exp}} = \sum_{L} a_L \left[\frac{d\sigma(\theta)}{d\Omega}\right]_{L,\text{calc.}} \tag{6.2}$$

As discussed earlier, the calculated cross section for a given L is the DWIA result for $\Delta J = L$, except $L = 0$ for $\Delta J^{\pi} = 1^{+}$. Some typical results are shown in Fig. 6.4 for a MDA of data for the ^{51}V(*n*,*p*)^{51}Ti reaction at 200 MeV. In this case it was assumed that the data could be represented as a sum of four terms with $\Delta L = 0, 1, 2, 3$, $\Delta J = 1^{+}, 1^{-}, 2^{+}, 3^{-}$. The assumed transition amplitudes were $\left(\pi f_{\frac{7}{2}}\right)^{-1}\left(\nu f_{\frac{5}{2}}\right)$ for $1^{+}, 2^{+}$ and $\left(\pi f_{\frac{7}{2}}\right)^{-1}\left(\nu g_{\frac{9}{2}}\right)$ for $1^{-}, 3^{-}$, and the shapes are shown in Fig. 6.3. The MDA provides a good fit to the measured spectra at the five smallest angles and a reliable estimate of the distribution of GT strength

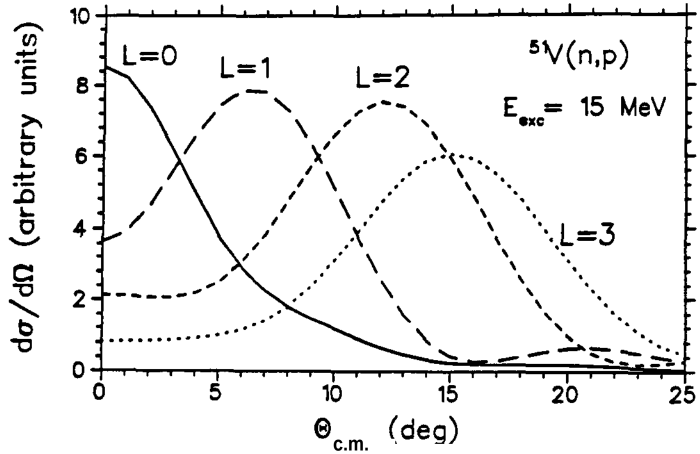

Fig. 6.3. Calculated angular distributions for transitions with ΔL = 0, 1, 2, 3 in the 51V (*n,p*) reaction using *p–n* configurations noted in the text. Note that the angular difference between the peak angles ofthe distributions decreases as ΔL increases. Reprinted from [156] with permission.

up to an excitation of 8 MeV, with the total strength $\Sigma_{E<8\ \mathrm{MeV}} B_{GT} = 1.2 \pm 0.1$ units. The analysis indicates a comparable amount of GT strength at higher excitation, but with much larger uncertainty, perhaps as much as a factor of two. At 20.7°, the calculated cross section is less than the data; this indicates the need for a further term, $\Delta L = 4$, in the analysis. It is also of interest that the $\Delta L = 2$ contribution is small.

Another representation of these results of the MDA is shown in Fig. 6.5, where the cross section is plotted for each value of ΔL at the angle closest to the peak of the DWIA distribution for that value. The error bars in this figure represent the uncertainties in the least-squares fit arising from statistical uncertainties in the data. An indication of uncertainties arising from the assumption of a particular *p–h* transition in the DWIA calculation is shown in Fig. 6.6. Here, the cross sections for $\Delta L = 0$ and $\Delta L = 1$ are shown for different choices of the *p–h* transition in the $\Delta L = 1$ contribution. The error bars again reflect statistical uncertainties in the data, while the different curves show the effect of changing the DWIA shapes. At low excitation energy, where the measured angular distributions show a clear forward peaking, the estimate of $\Delta L = 0$ cross section is not sensitive to the choice of DWIA shapes. However, at high excitation, the $\Delta L = 0$ cross section depends sensitively on the ratio $\sigma(0°)$ /s(peak) for the $L = 1$ DWIA shape. The large $\Delta L = 0$ cross section is obtained using the $L = 1$ shape for the transition amplitude $\left(\pi d_{\frac{3}{2}}\right)^{-1}\left(\nu f_{\frac{5}{2}}\right)$,

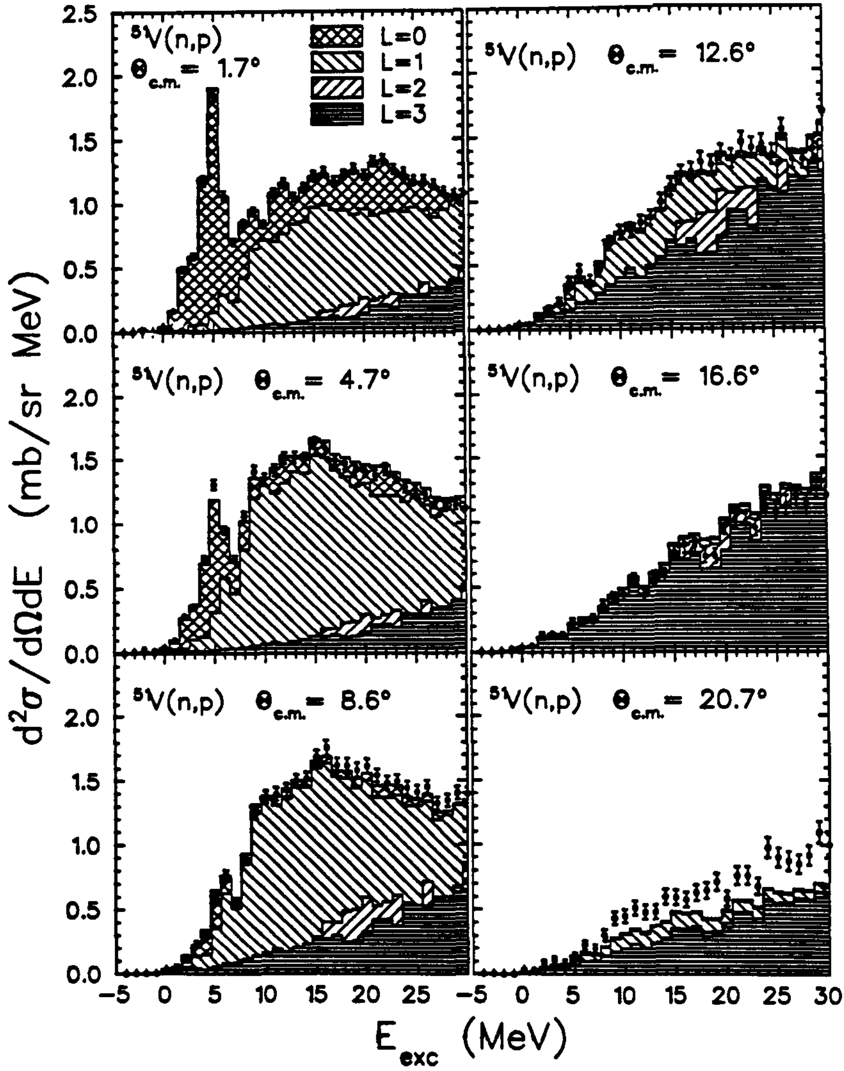

Fig. 6.4. Results of a multipole decomposition analysis of the data from the ^{51}V (*n,p*) reaction showing the contribution of each multipole to the measured cross section as a function of scattering angle and excitation energy. Points with error bars represent the measured cross section. Reprinted from [156] with permission.

which is seen in Fig. 6.2 to have a small value for the ratio. At the same time, it is seen that the estimate of $\Delta L = 1$ cross section is not much affected by choice of DWIA shapes. The conclusion that may be drawn from this is that the cross section for a given component is determined with an uncertainty arising from statistics, in the region of excitation in which that component is dominant, In regions in which a given component makes only a small contribution to the cross section, then the results of the MDA become sensitive to the details of the DWIA shapes and the magnitude of that component may be much more uncertain than the statistical estimate of the MDA would indicate. Thus the component with $\Delta L = 0$ is well determined up to an excitation energy of about 8 MeV, but is very uncertain at higher energies. Similarly, the $\Delta L = 1$ contribution is well determined up to an excitation energy of about 15 MeV. At higher excitation, the $\Delta L = 3$ contribution becomes large, and the magnitude of the $\Delta L = 1$ component from the MDA becomes sensitive to details of the DWIA shapes for both $\Delta L = 1$ and $\Delta L = 3$. Note that the shape for $\Delta L = 3$ was not varied in the results shown in Fig. 6.6.

An example of the result obtained in using the MDA for a heavy nucleus, where there is no large GT-peak, is shown in Fig. 6.7 for the 120Sn(n,p)120In reaction [177], measured at 300 MeV. In this case the cross section is plotted for each value of ΔL ($0 \leq \Delta L \leq 3$) at the angle of measurement which is closest to the peak of the DWIA distribution for that value of ΔL. In this reaction, the DLmax = 6; however, only the values of $\Delta L \leq 3$ are of interest. To minimize the number of terms in the series in DL, a single composite curve was used, for DL = 4,5,6; $\Delta J = 4^+, 5^-, 6^+$. The error bars in the figure represent the uncertainties in the least squares fit arising from statistical uncertainties in the data.

In concluding this section it should be emphasized that the MDA does not provide a routine that can be applied casually to any data set. In practice it requires some care to establish that the *p–h* amplitudes used in the DWIA are reasonable, and that the resulting shapes are indeed characteristic of the ΔL transfers used in the analysis. Properly applied, the procedure provides a useful measurement of the dominant low-multipole components of the data. Small contributions may be identified and semi-quantitative estimates of their strength may be obtained, but the uncertainty in such estimates is very difficult to quantify.

7. SPIN DIPOLE AND HIGHER MULTIPOLE TRANSITIONS

The previous section has discussed the relation between allowed GT beta decay transitions, mediated by the transition operator $\vec{\sigma}\tau_{\pm}$, and the cross sec-

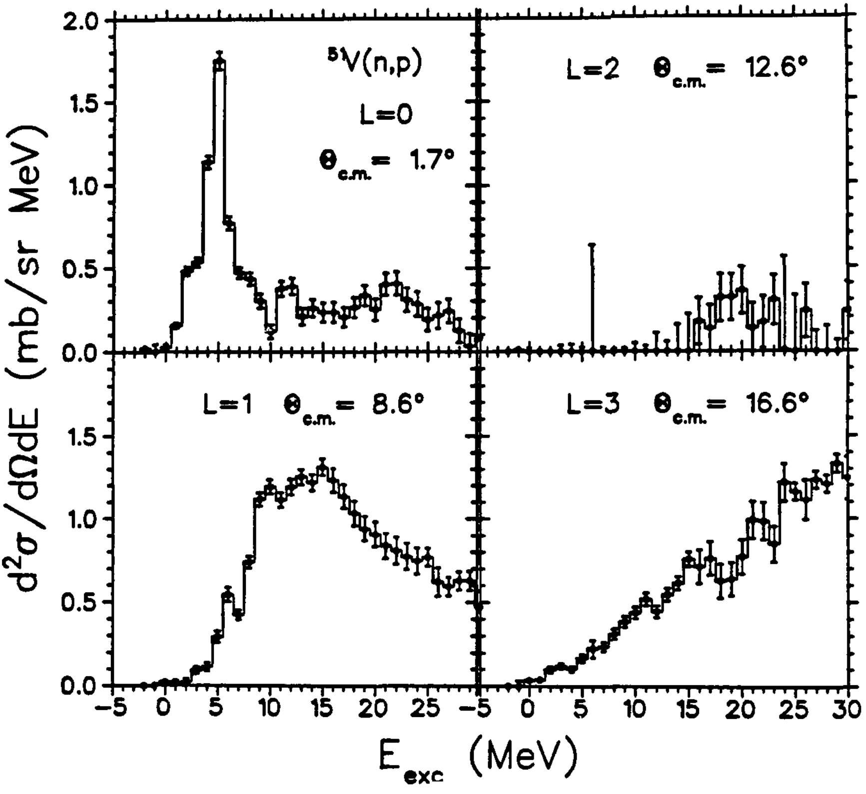

Fig. 6.5. An alternative representation of the results of the MDA for the data shown in Fig. 6.4. In this case, each multipole contribution is shown as a function of excitation energy at the angle of maximum cross section for that multipole. Reprinted from [156] with permission.

tion for charge-exchange reactions with $\Delta L = 0$. More generally, a multipole expansion of the matrix element of the effective interaction includes higher order terms with transition operators of the form $O^J_{GT} \sim r^L \ (Y_L \otimes \vec{\sigma})_J \vec{\tau}$ with $J = L, L \pm 1$. The resulting transitions are referred to as forbidden GT transitions. In contrast to allowed GT β transitions, these proceed with non-zero momentum transfer with the consequence that the non-central (tensor and spin–orbit) parts of the nuclear effective interaction may also make substantial contributions to reaction cross sections.

It should be noted that the proportionality between beta decay matrix elements and reaction cross sections which is so useful in the analysis of $\Delta L = 0$ GT strength, has not been established for transitions with $\Delta L \geq 1$. It has not

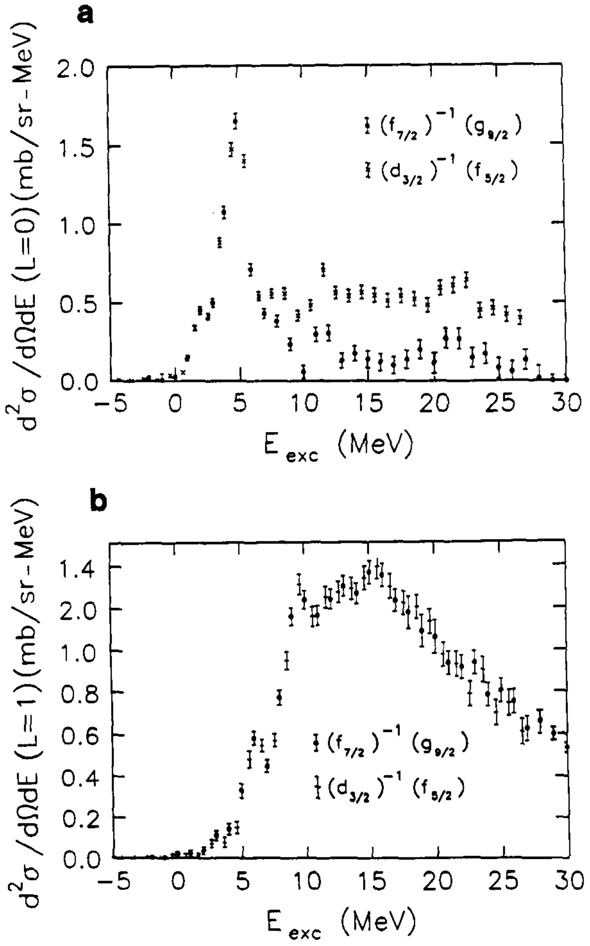

Fig. 6.6. (a) The effect on extracted L = 0 cross section of different choices of particle–hole configuration for the ΔL = 1 shape in the MDA. At high excitation there may be large differences in the inferred cross section. Data was for the ^{51}V (n,p) reaction at 200 MeV. **(b)** The effect on extracted L = 1 cross section ofusing the two configurations as in Fig. 6.6a for the ΔL = 1 shape in the MDA. The different shapes have very little effect on the inferred cross section. Data was for the ^{51}V (n,p) reaction at 200 MeV.

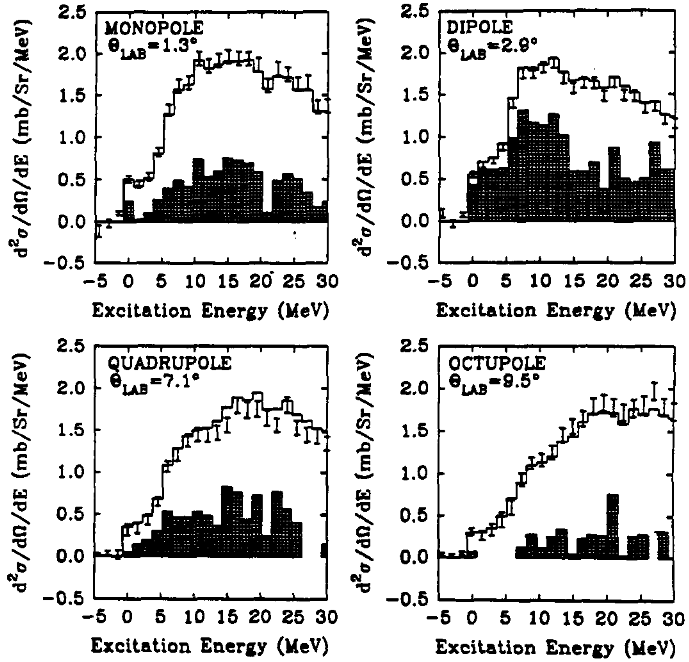

Fig. 6.7. Result of the MD analysis of the data for the ^{120}Sn (*n,p*) reaction, taken at 300 MeV. The error bars represent uncertainties in the least-squares fit to the cross section data arising from counting statistics. The shaded areas show the estimate of the cross section arising from the particular multipole noted on each panel. Note the absence of any prominent GT peak.

been feasible to search for such a relation experimentally since very few transitions of known β decay strength are observable with the energy resolution available in cross section measurements. Beyond the experimental problems, calculations indicate that there may be large variations in the ratio, especially for transitions with $\Delta J = \Delta L$.

The investigation of higher order multipole transitions has not been driven by the compelling issues which made the study of the $\Delta L = 0$, GT transition so important. Nevertheless, for the sake of completeness we present a brief survey of our present knowledge of the higher multipole transitions.

7.1. Spin Dipole Transitions

The first identification of a dipole transition excited in the (*p, n*) reaction was in the IUCF results of Bainum *et al.* [29] in the same paper in which they showed the strong excitation of the GTGR in ^{90}Zr (p,n) ^{90}Nb at 120 MeV. They noted a broad peak at an excitation energy about 9 MeV above the GTGR (the peak labelled “g” in Fig. 2.2b) with an angular distribution characteristic of $\Delta L = 1$ transfer. This excitation is about 4 MeV lower than the location of the 1^- $T = 5$ analog of the known El GR in ^{90}Zr, and it was suggested that this state is the $T = 4$ anti-analog of the El GR.

The systematics of this excitation were investigated by Sterrenberg et al. [178] using the *(p, n)* reaction at 45 MeV. Though the excitation of spin-flip transitions is less prominent at this energy than at 120 MeV, they were able to identify the GTGR and the $\Delta L = 1$ resonance in sixteen targets ranging from ^{90}Zr to ^{208}Pb. Both resonances shifted towards the IAS with increasing A, leading the authors to conclude that the shift resulted from the change in isospin splitting between T and $T-1$ states. Soon after this, Horen *et al.* [179] measured the cross section for excitation of the DL = 1 resonance as a function of incident energy in the ^{208}Pb *(p, n)* reaction. The energy dependence was the same as for the GTGR leading to the conclusion that this was a spin excitation, the spin-dipole giant resonance (SDGR).

The properties of the SDGR were investigated further by Gaarde et al. [34], using data from the *(p, n)* reaction on targets of mass $40 \leq A \leq 208$ at 200 MeV. In each spectrum, a peak was observed at an excitation energy several MeV above the GTGR, with an angular distribution characteristic of $\Delta L = 1$ transfer. The excitation energy of the peak was fairly well defined, but the cross section was uncertain because of the large background beneath the peak.

For the spin-flip transitions with $\Delta L = 1$, the SDGR would contain three components representing total angular momentum transfers DJ = 0, 1 ,2 arising from the transition operator $O_{SD} \sim [r\,(Y_1 \otimes \vec{\sigma})\,\vec{\tau}^-]_{\Delta J\pi = 0,1,2-}$. They showed that for each ΔJ value a sum rule analogous to the GT sum rule could be derived for 0^+ targets.

$$S_-^{(J)} - S_+^{(J)} = (2J+1)\,\frac{(N-Z)}{4\pi}\,\langle r^2 \rangle_{\text{neutron excess}} \tag{7.1}$$

It was claimed that the *(p,n)* cross section at the peak of the $\Delta L = 1$ angular distribution ($\theta \simeq 5^\circ$) was approximately proportional to the square of the spin-dipole matrix element, independent of ΔJ transfer; and they also showed that a schematic RPA model was able to account for the general features of the Δ-dependence of the total cross section and excitation energy of the SDGR.

The structure of the SDGR was investigated in more detail by Osterfeld *et al.* [180], in an RPA calculation of isovector excitations arising in the ^{208}Pb *(p,n)* ^{208}Bi reaction assuming F, GT, El and spin-dipole excitations. They showed that the strength of the transitions to states with $J^\pi 0^+$, 1^+, 0^-, and

1^- ($\Delta S = 0$) were all concentrated in a single state. The 1^- ($\Delta S = 1$) strength was fragmented, though the state at highest excitation carried much of the total strength. The 2^- states showed little collectivity, with strength spread fairly uniformly from about 18 to 26 MeV excitation. The lack of collectivity for the 2^- states was explained by the fact that the nuclear transition density for these states was peaked at a momentum transfer of $\Delta q \simeq 1$ fm^{-1}. At this momentum transfer, the $\boldsymbol{\vec{\sigma}\tau}$ particle–hole interaction is much weaker than at $\Delta q \simeq 0$, with the result that the collectivity of such states is reduced. A number of subsequent RPA calculations have been carried out to study the structure of the isovector spin response for $\Delta L = 1$ excitations [181, 182]. The different treatments involve somewhat different model assumptions and approximations, but all reach conclusions similar to those of [180].

The effect of $2p$–$2h$ excitations in the target ground state has been calculated by Sagawa and Brown [183]. For ^{12}C they conclude that such excitations have the effect of quenching low-lying strength by about 25%. The effect of $2p$–$2h$ excitations in the final state has been considered by Drozdz *et al.* [184] with the conclusion that mixing between $1p$–$1h$ and $2p$–$2h$ results in a large asymmetric spreading of the strength of the resonances, with about 30% of the total strength shifted to excitation energies greater than 35 MeV. Thus, the mechanisms responsible for the missing GT strength are calculated to have much the same effect on the spin-dipole resonance.

7.7.1. Experimental Results

A number of studies dealing specifically with dipole transitions and the SDGR have been reported but the interpretation of the results is hampered by the difficulty of identifying contributions from the different J components. DWIA calculations show that angular distributions for (p, n) or (n,p) transitions with $\Delta J^\pi = 1^-$ or 2^- are quite similar, and would not distinguish between these. The angular distributions for $\Delta J^\pi = 0^-$ show a characteristic shape, but the cross section per unit transition strength is predicted to be at least a factor of 3 less than for other components, so that 0^- transitions would tend to be hidden by the other $\Delta L = 1$ transitions.

In principle, a measurement of suitable spin observables would permit the identification of the ΔJ of the transition [185]. The simplest observable to measure in the $(\vec{p}, n)$ reaction is the analyzing power A_y, but it is found that this observable is more sensitive to nuclear structure than to the value of ΔJ [186]. The spin-transfer coefficient Δ_{nn}, which is measured in the $(\vec{p},\vec{n})$ reaction is predicted to depend on ΔJ in such a way that a measurement of D_{nn}, along with ΔL (from the angular distribution) generally provides a unique determination of ΔJ. This prediction has been confirmed for F and GT transitions on many nuclei [185] and has been applied in studies of the SDGR [187].

A careful study of spin-dipole strength in the ^{12}C $(p,n)^{12}$N reaction has been carried out by Gaarde *et al.* [188]. They reported prominent peaks in the spectrum at excitation energies of 4.2 and 7 MeV in ^{12}N, which showed angular distributions peaked near 8°, characteristic of $\Delta L = 1$ for ^{12}C. In addition, the continuum between 7 and 19 MeV excitation showed an angular distribution for $\Delta L = 1$. The peak at 4.2 MeV was identified as arising mainly from a 2^{-} state which was predicted in model calculations. This assignment is supported by the identification of the analogue state at 19.4 MeV excitation in ^{12}C in the ^{12}C(e,e') reaction [189]. The peak at 7 MeV was identified as arising from transitions to several 1^{-} states which were predicted in the same calculation which was based on an extension of the Cohen–Kurath model [190] to $1\hbar\omega$ excitations [191]. DWIA calculations were carried out using the model wave functions, and the results provided a good fit to the measured cross section for $\Delta L = 1$ transitions. It was noted, however, that the calculated ratio σ / B $(\Delta L = 1)$ showed a strong dependence on ΔJ. This means that the model results may be compared with the data, but that the $\Delta L = 1$ strength cannot be extracted from the data in a model-independent way, as for $\Delta L = 0$ strength.

It is interesting to note that a later study of the ^{12}C $(\vec{p},\vec{n})$ reaction [53] showed that the measured value of D_{nn} was consistent with the assignment of $J^{\pi} = 2-$ for the 4.2 MeV state, but not with the assignment of 1^{-} for the 7 MeV state. This result has been confirmed in a study of the analogue states excited in the ^{12}C $(\vec{d},{}^{2}\text{He})$ reaction [73] in which case a measurement of the tensor analyzing power provides the J discrimination.

Another case in which a serious effort has been made to identify the components of the SDGR is in the case of the ^{16}O $(\vec{p},\vec{n})$ and ^{40}Ca $(\vec{p},\vec{n})$ reactions [187]. For both cases, the measurement of D_{nn} provides an indication of the J-dependence of the cross section which is consistent with results of a TDA-DWIA calculation. Of particular interest is the identification of the elusive $J^{\pi} = 0^{-}$ strength which is predicted to lie at the high-excitation edge of the SDGR.

A measurement of spin-dipole strength has also been reported in connection with a study of the ^{90}Zr (n,p) reaction [52]. Several model calculations [182, 192, 193] provide reasonable overall agreement with the data although all the calculations show more pronounced structure than does the experimental data. Wambach *et al.* [182] found that the inclusion of $2p$–$2h$ excitations did not spread the $1p$–$1h$ strength as much as had been found in earlier structure calculations, such as [109]. Yabe [192] showed that by empirically increasing the spreading width from 2 to 8 MeV the prominent structure was suppressed and good agreement with the data was obtained.

In the ^{208}Pb *(n,p)* reaction, both the GT and SD giant resonances are Pauli-blocked to first order, but measurements at TRIUMF [194] show a peak in the proton spectrum at 5.5 MeV excitation which was interpreted as a ΔL = 1 peak, However, later MD analysis [177, 195] showed that this peak contained both ΔL = *0* and ΔL = 1 components in roughly equal proportion. RPA calculations [181] predict a SDGR with a centroid at an excitation energy near **7** MeV, about 1.5 MeV higher than is observed. Also, Krmpotic, Ebert and Wild [196] have, in a calculation of the charge-exchange collective modes in the lead region, predicted that in ^{208}T1, the major portion of 0^- and 1^- strength is near 7 MeV excitation, while the 2^- strength is spread over the region from about 8 to 20 MeV.

Finally, it may be noted that several measurements of SD strength distributions in (2p1f) shell nuclei have been reported both in (*p,n*) [148, 149, 197] and (*n,p*) [27, 150, 151, 156] reactions, but no serious effort in modelling these results has been reported.

In summary we note that extensive data have been reported on the excitation of spin-dipole transitions in charge-exchange reactions. The general features of the results, including the quenching of predicted strength, can be understood within the same theoretical framework as for GT transitions. More detailed and careful comparisons between experiment and theory should be stimulated by future ($\vec{p}$,$\vec{n}$) and ($\vec{d}$,^{2}He) measurements which may provide strength distributions for each of the predicted J^π components of the SDGR.

7.2. *L* = 2 Strength

Relatively little work has been reported on the study of isovector excitations with angular momentum change ΔL = 2. Auerbach and Klein [181] have carried out RPA calculations for both (*p,n*) and (*n,p*) reactions on ^{60}Ni, ^{90}Zr and ^{208}Pb. Calculations were reported for transition strengths and excitation energies for all three components of the excitations with $J^\pi = 1^+, 2^+$ and 3^+. The calculated strength is 85 to 105% of the non-energy weighted sum rule limit for all targets and both reactions. Average excitation energies in the (n,p) reaction range from 22.5 MeV for ^{60}Ni to 15.6 MeV for ^{208}Pb. For the (p,n) reaction energies are nearly constant at about 33 MeV.

The only clear experimental result is for the ^{10}B (*p,n*)^{10}C$_{\text{g.s.}}$ reaction at 186 MeV [145]. In this case the ground state group is well resolved and provides a unique example of a transition with ΔL = 2, ΔJ^π = 3+. The measured angular distribution is fitted well in both shape and magnitude by DWIA calculations which assume 1*p*–1*h* excitations within the (1*s*, 1*p*, 2*s*1*d*) shell model space.

The most promising approach to broader experimental studies of these excitations is through the multipole decomposition analysis of the continuum in (*n,p*) measurements, since the ΔL = 2 excitations are predicted to occur at substantially lower excitation in the (*n,p*) than in the (*p,n*) reaction. In this connection it is useful to recall that in such an analysis, multipole contributions up to some maximum value of $\Delta L_{\max}$ are assumed, and futher contributions are neglected. In fact, the component of largest ΔL used in the analysis really measures contributions with $\Delta L \geq \Delta L_{\max}$, and may not provide useful data on the single component $\Delta L = \Delta L_{\max}$. Thus, in the analysis of (*n,p*) data from targets of medium mass nuclei, $\Delta L_{\max} = 3$. In this case, estimates of the contributions with $\Delta L = 0, 1, 2$ should be meaningful, while the component with $\Delta L = 3$ is probably not. In the heavier nuclei, interest is limited to ΔL-values up to 3, and the final $\Delta L_{\max}$ was in most cases a composite angular distribution for $\Delta L = 4,5,6$.

A striking result from the multipole decomposition analyses of (*n,p*) reactions studied at TRIUMF is the lack of $\Delta L = 2$ strength in most spectra [155, 150, 156, 151]. In fact, the only cases where a substantial $\Delta L = 2$ contribution is found are for targets of ^{55}Mn, ^{120}Sn, ^{181}Ta and ^{208}Pb. Figure 7.1 shows the results of MDAs of data from targets of ^{55}Mn and ^{56}Fe [151], nuclei adjacent in the periodic table, but showing very different distributions of strength for $\Delta L = 2$ and 3. Also, Fig. 7.2 shows the results of MDAs of data for ^{181}Ta and ^{238}U, targets which both show rotational band structure at low excitations, indicating a quadrupole deformation. Again, there is a marked difference in the distributions of $L = 2$ and 3 strength in these two cases.

Another situation in which ΔL = 2 strength is unexpectedly small is found in charge-exchange pion scattering [198]. Conventional model calculations predict that the monopole, dipole and quadrupole giant resonances should be strongly excited. The monopole and dipole resonances were observed but no compact electric quadrupole strength was identified. A possible mechanism to explain this missing strength has been proposed by Leonardi *et al.* [199]. In a schematic model in which the nuclear Hamiltonian includes an isovector quadrupole term they show that the effect of such a term suggests the need to generalize both the Hamiltonian and the quadrupole transition operator to include non-local terms. With a suitable choice for the magnitudes of the non-local contributions they found that the total quadrupole transition strength was strongly damped for $\Delta T = -1$ [(*p,n*) transitions], and was almost zero for $\Delta T = +1$ [(*n,p*) transitions]. It must be noted however that the theory was developed for non-spin flip transitions, and it is not clear how applicable it might be for the isovector spin flip transitions involved in (*n,p*) and (*p,n*) reactions.

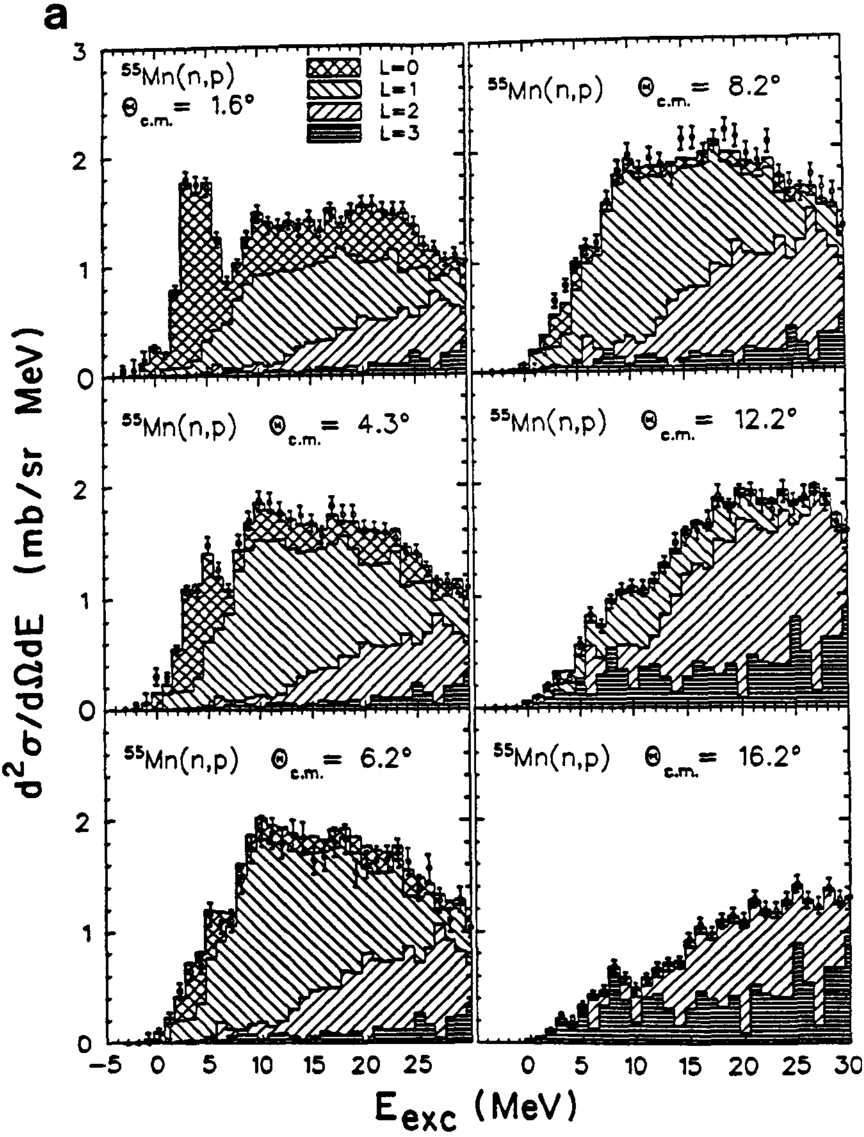

Fig. 7.1. Results of the MD analyses for (a) the ^{55}Mn (*n,p*) reaction, and (b) the ^{56}Fe (*n,p*) reaction both at 200 MeV. Note the great difference in the $\Delta L = 2$ contribution in the two cases. Reprinted from [151] with permission.

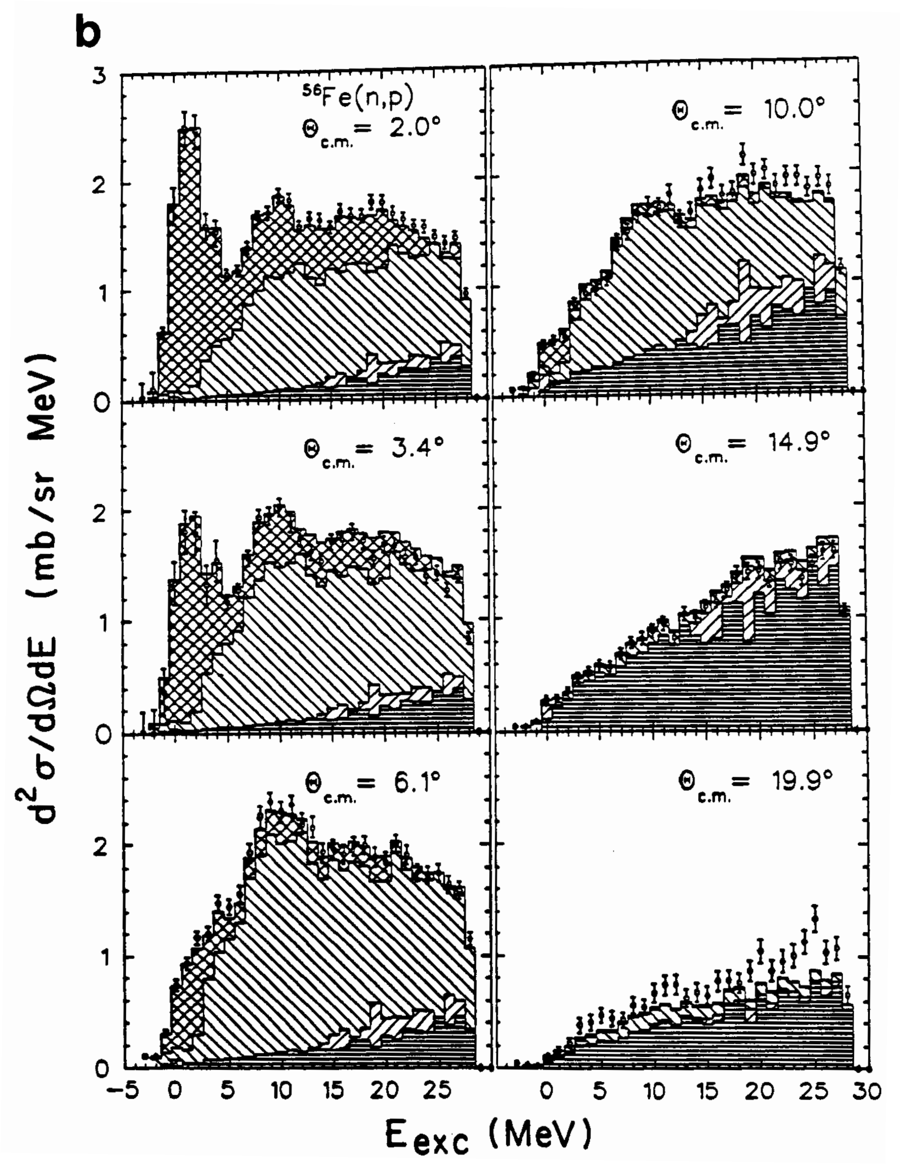

Fig. 7.1. *(continued).*

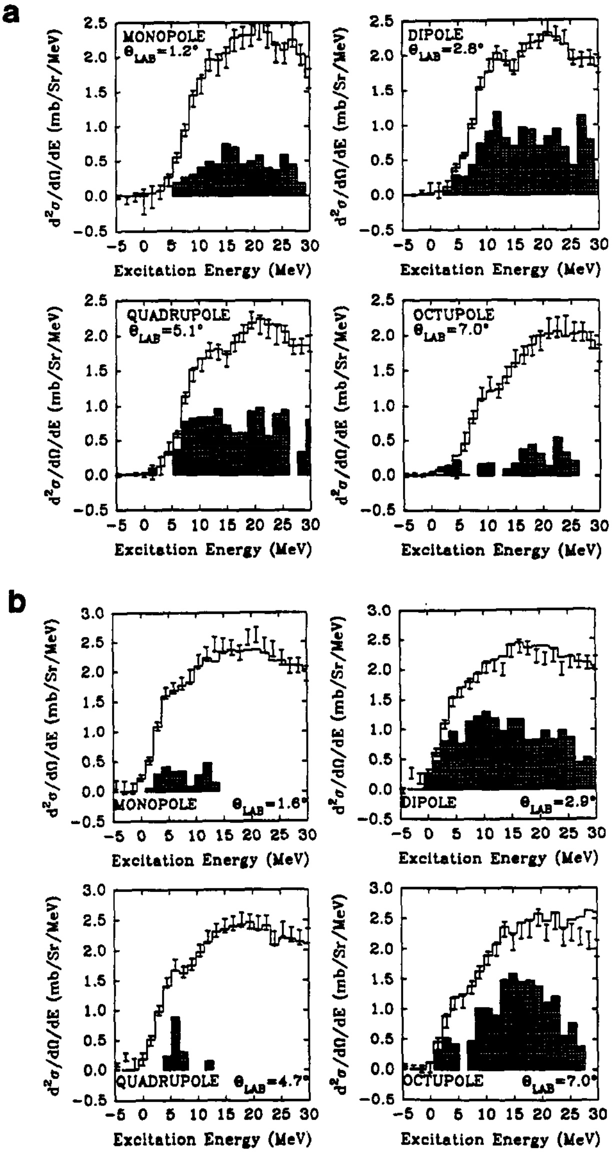

Fig. 7.2. Results of the MD analyses for (a) the ^{181}Ta (*n,p*) reaction at 300 MeV (upper four panels), and (b) the ^{238}U (*n,p*) reaction at 320 MeV (lower four panels). The error bars and shaded areas have the same significance as in Fig. 6.7. Note the large difference in the $\Delta L = 2$ and $\Delta L = 3$ contributions, even though both targets have well-defined rotational band structures at low excitation.

It should be noted that large components with $\Delta L = 2$ have been reported from analyses of spectra of (p,n) reactions from $(2p1f)$ nuclei [148, 149]. However, these analyses assumed $\Delta L_{\max}$, $= 2$, so that any contribution with $\Delta L > 2$ would be included with $\Delta L = 2$.

At the moment it must be concluded that the absence of significant strength with $\Delta L = 2$ in most of the (n,p) results is not well understood.

7.3. An Attempt at Systematics for the *L* = 1 and *L* = 3 Transitions

As the mass of the target nucleus increases, the centroid energy of the giant resonances decreases as $A^{-1/3}$ [200], and therefore a large number of ΔL-values will be compressed into an excitation energy region whose range is constant. This means that, in targets of heavy nuclei, the $\Delta L = 3$ giant resonance will most certainly be present. Indeed, as has been noted earlier, ΔL-values up to 7 or 8 are possible, theoretically at least, in the case of ^{238}U. Because the single particle levels one oscillator quantum above the Fermi surface, in closed shell nuclei at least, cluster around the neutron binding energy, the transitions will occur at relatively low excitations, say below about 30 MeV excitation. If consideration is limited to $1p$–$1h$ transitions of energy $1\hbar\omega$, then it is reasonable to expect that these will occur at the lower excitation energies. Indeed, it is known that, even when a residual interaction is used in a nuclear structure calculation involving the use of single particle energies, the calculated levels always lie within the excitation region below about 25 MeV (see, for example, [201]).

The only ΔL-values of interest in the heavy nuclei ($A > 80$, say), those which can be described in terms of $1p$–$1h$ transitions of $1\hbar\omega$ unperturbed energy, are the $\Delta L = 1$ and $\Delta L = 3$ transitions. The strength of these giant resonances can be calculated using sum rules given by Macfarlane [202] for T-raising and T-lowering components of isovector excitations. For (n,p) reactions the sum rule is written:

$$S^{+} = \frac{1}{2L+1} \sum_{\rho,\rho'} \left| \langle \rho' \| r^{L} \left[Y_L(\hat{r}) \otimes \vec{\sigma} \right]_J \| \rho \rangle \right|^2 n_{\rho}^{\pi} (1 - n_{\rho'}^{\nu}) \qquad (7.2)$$

where L is the multipole order, J the spin of the final state and ρ, ρ′ represent the single particle (nlj) components of the wavefunctions of initial and final states. The quantities n_{ρ}^{π} and $n_{\rho'}^{\pi}$ are the occupation probabilities of the proton and neutron single particle states respectively.

Given the restriction to $\Delta L = 1$ and $\Delta L = 3$ resonances arising from $1p$–$1h$ transitions it is feasible to evaluate the sum rule and this has been done for

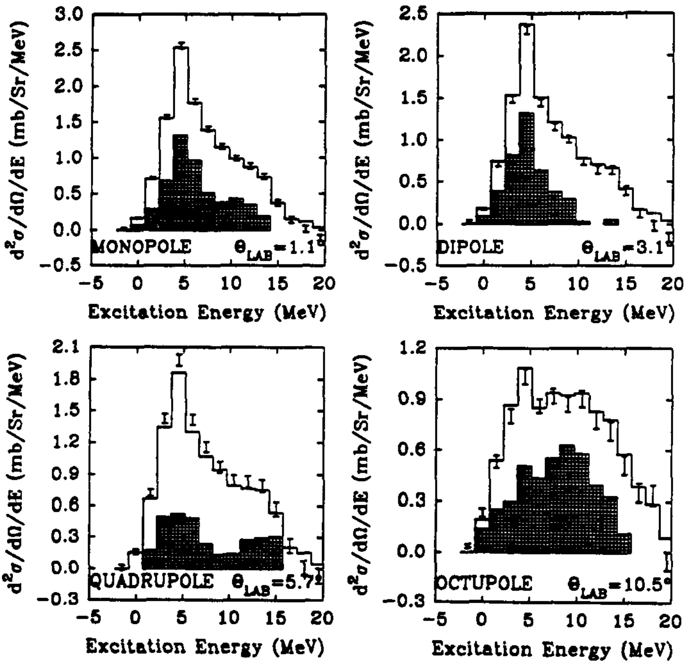

Fig. 73. Results ofthe multipole decomposition analysis of data from the ^{208}Pb (*n,p*) reaction at 200 MeV after subtraction of the quasifree scattering contribution. The shaded areas have the same significance as in Fig. 6.7.

targets of ^{90}Zr, ^{120}Sn, ^{181}Ta, ^{208}Pb and ^{238}U, using occupation probabilities from[203].

To make a comparison with experimental results, these should include only the $1p$–$1h$, $1\hbar\omega$ excitations assumed in the calculation. A simple plausible appproximation to this requirement may be obtainedby subtracting a quasifree contribution which must consist of transitions of excitation energy at least $1\hbar\omega$, from the raw data. Such a subtraction has been made by Long [177] for results of (n,p) measurements on targets of ^{90}Zr, ^{120}Sn, ^{181}Ta, ^{208}Pb and ^{238}U, and the spectra then analyzed with a MDA. The result ofsuch an analysis for the ^{208}Pb (n,p) reaction is shown in Fig. 7.3.

A comparison ofthe measured cross sections, for $\Delta L = 1$ and $\Delta L = 3$ with strengths from the sum rule calculation is shown in Fig. 7.4. In this comparison it was assumed that the cross section was proportional to the strength and that the Δ-dependence of the proportionality could be neglected. The factor of

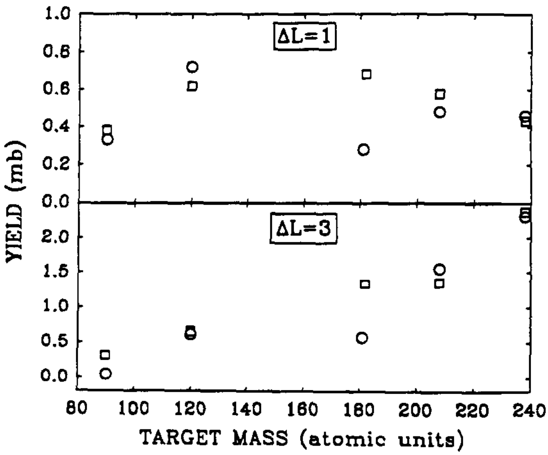

Fig. 7.4. Comparison of the results ofthe limited sum rule calculation (squares) with measured cross sections for transitions with ΔL = 1 and 3 (circles). A quasifree contribution was subtracted from the data before multipole decomposition analysis (see text).

proportionality was determined for each value of ΔL separately by normalizing calculations to the data.

Agreement between theory and experiment is reasonable, considering the approximations made, except for the case of ^{181}Ta. The deficiency in experimental strength for both $\Delta L = 1$ and $\Delta L = 3$ in the case of ^{181}Ta may well be due to the spreading of $1p$–$1h$ strength in both cases by the deformation as well as by $2p$–$2h$ configurations. For both $\Delta L = 1$ and $\Delta L = 3$ transitions the trends shown make physical sense. In the case of the $\Delta L = 1$ transitions, the yield rises to flat maximum at about $A = 150$, and then falls. The decrease is due to the commencement of Pauli blocking of these transitions. By contrast, the $\Delta L = 3$ yield rises continually through this part of the periodic table. This must be due, at least in part, to the $A^{-1/3}$ dependence of the $\Delta L = 3$ resonance energy bringing more and more of the cross section for this multipole into the excitation region considered.

7.4. Stretched States

There is very little information available regarding isovector resonances with large angular momentum transfer ($\Delta L \geq 3$). As noted in the discussion of Section 6 the measurement of the cross section in the continuum for a given multipole order becomes increasingly uncertain as ΔL increases, and charge-exchange studies to date have provided little useful information about such resonances.

There is however another class of transitions of high multipole order, the stretched-state transitions, for which interesting results have been obtained. Stretched states are $1p$–$1h$ excitations with total angular momentum $J = J_{\max} = j_p + j_h$ with $j_p = l_p + \frac{1}{2}$, $j_h = l_h + \frac{1}{2}$ where l_p, 1h are the largest orbital angular momentum within a given oscillator shell. Thus a stretched state is described as a unique $1p$–$1h$ configuration with the maximum angular momentum possible within the model space.

Such states have been extensively studied in (p,p') (e,e'), and (π, π') reactions. Examples of early measurements are given in references [204, 205, 240]. In the case of the ^{28}Si(p,p') reaction, polarized protons over the energy range 80 to 180 MeV have been used [241]. The energy and momentum-transfer dependences of the differential cross section and analyzing power were shown to be capable of testing the various forms of the interaction used. It was shown that although the $1p$–$1h$ configuration was unique, this was not an eigenstate of the nuclear Hamiltonian, so that the strength of the excitation was spread over other states by residual interactions. The cross section for excitation of a particular state however was proportional to the strength of the stretched configuration in the wave function of that state [206]. Thus the (e, e') reaction, involving the well understood electromagnetic interaction, may be used to determine the 1p–1h transition density; this may then be used in the analysis of (p,p') results to study the effective N–N interaction.

It had been pointed out by Moffa and Walker [207] that the study of such states with charge-exchange reactions would provide a valuable addition to the information available from the (e,e') and (p,p') reactions. For instance in the (p,p') reaction both isoscalar and isovector transitions are excited, with only isovector excitations in charge-exchange reactions. In the absence of the isoscalar background, transitions of interest should be more clearly resolved in charge-exchange measurements. Also, comparison of analog states excited in the two reactions permits the identification of the isospin of the inelastic excitations, and in the case of the (p,n) reaction the determination of the isospin, $T_f = T_0$ or $(T_0 - 1)$, of the states in the final nucleus.

The comparison of inelastic scattering with charge-exchange results implies the excitation of a particle into the next higher oscillator shell, or a $1\hbar\omega p$–h excitation. However, $0\hbar\omega$ excitations are also possible (GT transitions for instance), but $0\hbar\omega$ stretched-states are necessarily n–p or p–n excitations, which can only be reached with a charge-exchange reaction.

The experimental study of stretched state excitation via charge-exchange reactions has been carried out largely by the Kent State group of Anderson, Watson *et al.*. In an early measurement [208] they identified major components of the strength inreactions ^{16}O (*p,n*) ^{16}F(4–), ^{28}Si(*p,n*) ^{28}P(6–)and ^{48}Ca(*p,n*) ^{48}Sc (7^+). The first two of these are $1\hbar\omega$ excitations which had been studied in (*e, e'*) and (*p,p'*) reactions. The ^{48}Sc (7^+) state is an example of a $0\hbar\omega$ excitation which is only accessible via the (*p, n*) reaction. For the 16O and ^{28}Si targets, the measured differential cross sections showed angular distributions with the same shape as in corresponding (*p,p'*) measurements. The magnitudes of the (*p, n*) cross sections were a factor of 2 larger than for (*p,p'*) as expected from the ratio of squares of the appropriate Clebsch–Gordan coefficients. However, DWIA fits to the angular distribution using a pure 1*p*–1*h* transition density required renormalization by factors of 0.3 1 and 0.23 respectively, indicating the strong fragmentation of the strength, as found in the (*p,p'*) and (*e, e'*) results.

A number of subsequent measurements have been reported for both the (*p,n*) [209, 210, 211, 212] and (*n,p*) [213] reactions.

The results for $0\hbar\omega$ excitations have provided new data on this class of stretched states. Measurements for the $1\hbar\omega$ excitations however provide only a limited extension of the inelastic scattering results. At present, the most interesting aspect of the study of stretched configurations is the fragmentation of the strength [206]. Charge-exchange measurements have not contributed to such studies though, because of the relatively poor energy resolution available, about 300 keV for (*p,n*) measurements and 1 MeV for (*n,p*).

8. QUASIELASTIC SCATTERING

Conceptually, quasifree, or quasielastic, scattering is scattering of an incident nucleon from a nucleon within a nucleus at an incident energy high enough for the struck nucleon to be considered unbound. This reaction has proved useful in the direct investigation of the single particle structure of nuclei, via the (*p,2p*) reaction, and also in the study of the effect of the nuclear medium on the nucleon-nucleon interaction at large momentum transfers.

8.1. Spectral Shapes

Quasifree scattering was first studied in the (*p,p'*) reaction, with early measurements of the energy spectrum by Chrien *et al.* [214, 2 15] showing a broad peak centered near the energy corresponding to that for free NN-scattering. Such spectra have been fitted reasonably well with calculations based on the semi-infinite slab model [216]. A number of further measurements have been reported, including spin observables as well as cross sections. Moss *et al.* [217] measured the angular distribution of the continuum in the (*p,p'*) reactions on ^{116}Sn (800 MeV), and the spin transfer coefficient Dnn' for ^{208}Pb (400 MeV) and of ^{90}Zr (500 MeV) and concluded that the data were satisfactorily described by a model which treated properly the surface nature of the interaction and the effects of Pauli blocking. Chen *et al.* [218] measured analyzing power and spectral data for the inelastic proton scattering from ^{208}Pb at 290 MeV, for excitation energies up to 160 MeV. They concluded that the semi-infinite slab model of Esbensen and Bertsch [219] gave a good description of the shape of the continuum. They noted that the analyzing power, measured at the quasielastic peak, was less than the free nucleon value at this momentum transfer, and that this was a possible indicator of relativistic effects.

A summary of such measurements was provided by Smith [220] in which he investigated the effects of several approximations in theoretical treatments. It was concluded that two-step contributions to the cross section were small, although they became increasingly important at higher excitations. Particle–hole interactions are important and calculations of the nuclear response must include them. The damping of the $1p$–$1h$ response through $2p$–$2h$ mixing must be taken into account, particularly for the isovector spin-flip part of the interaction. It was also important to use the "optimal" reference frame for specification of the NN-scattering amplitudes, and to include the effects of distortions in impulse approximation calculations. The final result was to provide a simple but comprehensive model for the description of scattering to the continuum.

In another study, Häusser *et al.* [22 1] measured a complete set of polarization variables in the inelastic proton scattering from ^{54}Fe at 290 MeV. They also demonstrated the dominance of the isoscalar component in the (p,p') reaction by taking data from the purely isovector ^{54}Fe (n,p) reaction [27], and, using the Clebsch–Gordan coefficients relating the scattering cross section to the charge exchange cross section, showed that the isovector scattering cross section is but a small part of the total.

In contrast to this situation, charge exchange reactions involve only the isovector part of the *N–N* interaction and should permit simpler comparisons between theory and experiment. Energy spectra analogous to those measured for the (p,p') reaction have been measured for the (p,n) reaction by Taddeucci *et al.* [222] and Prout *et al.* [223]. The (p, n) quasifree peak has a shape similar to that in the (p,p') reaction, but the peak is found to be shifted to an excitation energy about 25 MeV higher than that of the proton peak at the same momentum transfer. A similar shift had been observed in inelastic electron scattering, which also involves an isovector probe. The magnitude of the shift is shown in Fig. 8.1 which is taken from [223]. This result has been accounted for, at least qualitatively, by Wambach [224] using a sum rule approach based on the theory of Fermi liquids. Later, Pandharipande *et al.* [225] arrived at the same result in calculations for ^{2}H, ^{4}He and 16O using realistic models of nuclear forces.

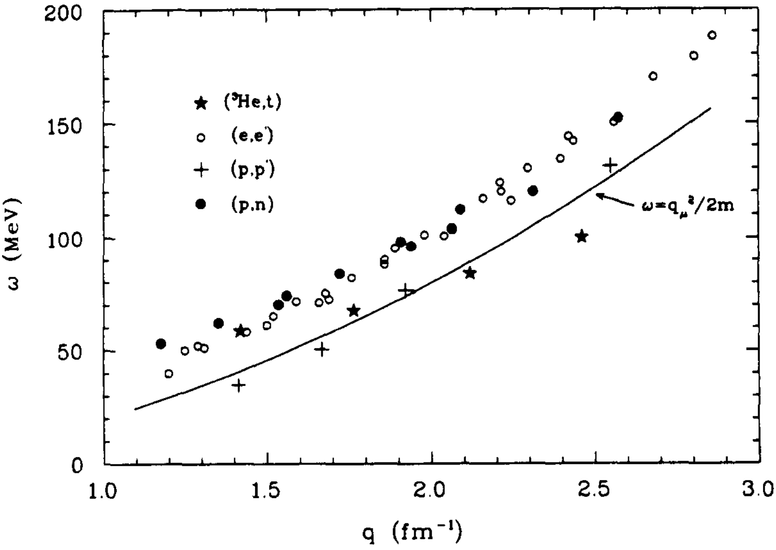

Fig. 8.1. The quasielastic peak position, as seen in (*e,e'*), (*p,p'*), (p,n) and (^{3}He, *t*) reactions. These are compared with free NN kinematics (solid line). Reprinted from [223] with permission.

Similar measurements for the (^{3}He, *t*) reaction show a peak shift as for the (*p, n*) reaction at low momentum transfer but this peak shift decreases in excitation at higher momentum transfers until it moves below the line describing the (*p,p'*) reaction, as is shown in Fig. 8.1. This particular feature is not understood, though it has been suggested that it may be the result of greater absorption or distortions in the (^{3}He, *t*) reaction. Support for this suggestion comes from measurements of the quasifree spectrum in the (*p, n*) reaction at 186 MeV where the shift of the quasifree peak mirrors the (^{3}He, *t*) data for large momentum transfer. In this case, the neutrons have energies of less than 100 MeV and will be subject to large distortions [226].

In summary, the shape of the quasifree peak in both (*p,p'*) and (*p, n*) experiments is fitted satisfactorily using the semi-infinite slab model, The shift in the centroid of the peak for isovector probes appears to arise from collective effects in the nuclear medium but current models do not provide a quantitative understanding of the shift.

8.2. Nuclear Response Functions

The effect of *p–h* interactions on the quasielastic response has been considered by Alberico *et al.* [227]. In an initial paper they studied the collective response of symmetric, infinite nuclear matter to a spin-isospin sensitive probe within an RPA framework. The elementary particle–hole interaction carries the quantum numbers $S = T = 1$, but M_s, the projection of S on the direction of the momentum transfer must also be specified. The longitudinal channel with coupling $(\vec{\sigma}\cdot\vec{q})$ corresponds to $M_s = 0$, and arises from pion exchange. The transverse channel coupling $(\vec{\sigma}\times\vec{q})$ corresponds to $M_s = \pm 1$, and arises from ρ-exchange. The two separate channels are not coupled, and so can be investigated separately. They calculated that the collective effect produces measurably different effects in the two responses. In the longitudinal channel, they found that the response was enhanced due to the attractive particle–hole interaction, with a shift of its maximum effect to smaller momentum transfer (a softening). The transverse response on the other hand, was found to be quenched and hardened; both shifts were with respect to the response of a free Fermi gas. The result of these collective effects was that the value of the ratio of longitudinal to transverse responses, R_L/R_T, was predicted to be significantly greater than unity for large momentum transfers as in the quasifree region.

This prediction has led to a number of interesting experiments. In the first of these, Carey *et al.* [228] measured the diagonal spin transfer coefficients for the quasifree scattering of 500 MeV protons on ^{2}H and ^{208}Pb at a momentum transfer of $1.72f^{-1}$, corresponding to the peak of the quasifree cross section at 18°. Their measurements yielded a value of the ratio of the responses which was close to unity, in serious disagreement with predictions. They showed that the inclusion of surface effects in the scattering resulted in a substantial reduction in the predicted ratio, though it was not enough to produce agreement with the data. It was also noted that the interpretation of this result was complicated by the fact that both isovector and isoscalar interactions were involved in inelastic proton scattering.

In one of the studies attempting to understand this result, Ichimura *et al.* [229] calculated R_L and R_T for the conditions of this experiment. Three factors were found to be most important in decreasing the ratio. The effect of finite nuclear size was found to be large, especially in the longitudinal response. The effects of distortion decreased the softening of the longitudinal response, and the hardening of the transverse response due to nuclear correlation, but the enhancement and quenching remained in the respective responses. The inclusion of the isoscalar component in the analysis also decreased the ratio. These effects combined to reduce the calculated ratio to approximately 1.4 at an energy loss of 30 MeV, decreasing to unity at an energy loss of 120 MeV.

The calculations of Pandharipande *et al.* [225], which were referred to earlier, also predict an enhancement of the spin-longitudinal response over the spin-transverse response of about 25% in nuclei such ^{16}O at $q = 1.77$ fm^{-1}. Perhaps more interesting is their prediction that in ^{2}H and ^{4}He, the longitudinal response is significantly enhanced over the transverse response, even without any $\pi N\Delta$ coupling effects. They also comment that their calculated energy-weighted sums are larger than those predicted by the RPA by some 50% for momentum transfers below 2 fm^{-1} .

Subsequent experiments have measured the isovector responses without isoscalar contributions by utilizing the (*p, n*) reaction. McClelland *et al.* [230] measured a complete set of spin transfer coefficients for the $(\vec{p}, \vec{n})$ reaction on ^{2}H, ^{12}C and Ca targets at 494 MeV and $q = 1.72\mathrm{f}^{-1}$ The ratio R_L/R_T was again found to be close to unity, and this result was confirmed by more detailed measurements on these same targets by Chen *et al.* [231]. In the most recent experiment Taddeucci *et al.* [232] investigated the momentum dependence of the two responses with $(\vec{p}, \vec{n})$ measurements at 494 MeV on targets of ^{2}H, ^{12}C and Ca at angles of 12.5° ($q = 1.2f^{-1}$), 18° ($q = 1.72f^{-1}$) and 28_o ($2.5f^{-1}$). They concluded that the longitudinal response was consistent with RPA calculations [229] except at 12.5° where it was significantly larger. The transverse response was significantly enhanced over the RPA predictions, and over that measured in the (*e, e'*) reaction. Thus the earlier results which failed to show an enhancement in the ratio were shown to arise as a consequence of an enhancement in the transverse response. The cause of this enhancement is still not understood. There was a suggestion that it could be explained if distortion effects were different in the two channels, but a transverse distortion twice as large as the longitudinal distortion would be required to fit the data.

Brown *et al.* [233, 2341 have noted that a ratio of unity, implying equal responses in both transverse and longitudinal channels would result if the isovector tensor interaction was negligible in the measurements. The vanishing of the tensor force at $q = 1.72f^{-1}$ would require a ρ meson reduced mass of 0.84 times the free mass, but is not clear that this would account for the observed momentum dependence of the ratio.

In a different approach to the problem, Horowitz and Piekarewicz [235] calculated the ratio of the spin-longitudinal to spin-transverse responses in quasielastic (*p, n*) scattering using a relativistic random phase approximation to the Walecka model of nuclear structure. Inherent in this model is a dynamical reduction of the nuclear mass in the nuclear medium, that is, the need for a reduced nucleon mass, which in turn is responsible for a shift in the position and width of the quasifree peak. This modification to the peak shape is sufficient to account for the quenching and hardening of the transverse response relative to a free Fermi gas. A further effect caused by the reduced nucleon mass is a suppression of the πNN-coupling in the medium, which reduces the enhancement of the longitudinal response, thus predicting the ratio of spin-longitudinal to spin-transverse responses to be close to unity, as seen experimentally.

Further predictions were provided by Hillhouse and De Kock [236] on the basis of relativistic plane wave calculations of complete sets of polarization variables for targets from ^{12}C to ^{208}Pb, and for incident energies from 135 to 500 MeV, at fixed momentum transfer of 1.97 fm^{-1}. They noted that only the analyzing power shows an unambiguous relativistic signature at the highest energy, a fact pointed out earlier by Horowitz and Murdock [237]. They also pointed out that the polarization transfer observable, $D_{nn'}$, was extremely sensitive to whether the pion–nucleon vertex was taken as pseudoscalar or pseudovector, particularly for incident energies under 200 MeV, and that this sensitivity should not be masked by the effect of spin–orbit distortions nor any "effective mass" effect.

The first experiments to look for such effects were those of Hicks et al. [238, 239] which measured analyzing powers as well as cross sections in the ^{12}C, ^{54}Fe ($\vec{p}$,n) reactions at 290 and 420 MeV. They noted that the shape of the quasifree spectrum was target dependent, indicating the need for caution in any use of a "universal" model for quasifree scattering. It was also found that analyzing powers were decreased with respect to the free *N*–*N* scattering values for ^{12}C at both incident energies, and for ^{54}Fe at 290 MeV, as predicted by [237].

Another experiment which has specifically investigated relativistic effects on spin observables is that of Wang *et al.* [226]. In addition to measurements of the (p, n) quasifree cross section noted earlier, they also measured the spin observables A_y, P and D_{nn} for ^{10}B ($\vec{p}$, $\vec{n}$) at 15° and 20°. For the first two observables there is very little difference between free-nucleon-values and the relativistic predictions. For D_{nn} however, the data are in reasonable agreement with the relativistic prediction with the assumption of pseudovector pion–nucleon coupling, and in clear disagreement with that for pseudoscalar coupling.

The relativistic plane wave impulse approximation has been successful in fitting some of the experimental results of isovector quasifree scattering. It is found, however, that it is not clearly superior to more conventional approaches, and in some cases the non-relativistic theories show better agreement with data [239].

The study of quasifree scattering in the (p, n) reaction has provided important new insights about the isovector effective interaction at large momentum transfer. Though many of the results appear to be understood, there are still interesting problems to be addressed, such as the shift of peak in the quasifree spectrum, and the observed enhancement of the transverse nuclear response.

9. SUMMARY

Our review of charge-exchange reactions has attempted to describe the development of an important subfield of nuclear physics following the introduction of new facilities which provided important new data. This occurred at a time when nuclear physics itself was in ferment with new ideas, originating in the standard model of quarks, leptons and unified forces. For almost a decade the investigation of charge-exchange reactions unfolded with considerable drama, with hints of the importance of nucleon substructure in low-energy nuclear physics. As we have shown, the end of the drama yielded not that Holy Grail, but rather a great deal of very good and very rich nuclear physics.

Recognition of the parallel between allowed beta decay and nuclear charge-exchange reactions is now about forty years old. The correspondence was demonstrated in 1962 for Fermi transitions in the discovery of the strong excitation of the isobaric analogues of target ground states in the (*p, n*) reaction. These transitions were mediated by the isospin-flip, non spin-flip component of the nucleon-nucleon interaction, and provided a striking example of a nuclear giant resonance. Soon after this the existence of a second giant resonance was predicted, arising from the spin- and isospin-flip, or Gamow–Teller part of the nucleon-nucleon interaction, and very powerful model-independent sum rules were given for the total strengths of these resonances. Over the next decade many (*p*, *n*) measurements were carried out to investigate the properties of the Fermi and Gamow Teller parts of the effective interaction, but the interpretation of the results was hampered by the low beam energies available for such studies, and the GT giant resonance was not seen.

Major breakthroughs in this field came with the development of new accelerator facilities in the 1970's, first at Michigan State University and then at Indiana University. At IUCF it was clearly shown that at energies above about 100 MeV the (*p,n*) cross section at 0° provided a quantitative measurement of the strength of the GT β^- transition between the two states involved. This result was to provide the impetus for major advances in the understanding of nuclear structure and effective interactions over the next decade.

The most exciting development was the demonstration that only about half the total strength required by the GT sum rule could be identified in (*p,n*) measurements at energies near the peak of the GT resonances. This result, following on a decade of speculation about the role of nucleon substructure in nuclear physics was immediately interpreted as evidence for mixing of the high energy Δ-resonance with the low-lying nuclear states involved in GT transitions. This “missing strength'' problem led to a strong polarization of opinion regarding the importance of Δ excitations in nuclear structure and stimulated a great deal of further work.

Although the lack of observable GT strength is consistent with the existence of Δ excitations, this turned out to be not the only possible explanation. Unfortunately there is no unambiguous signature of Δ excitations in the relevant data of charge-exchange reactions, and the resolution of the missing strength problem has emerged mainly in the results of a variety of model calculations. By now it is generally agreed that the missing strength can be accounted for in terms of excitations of the target ground state, plus spreading of the $1p$–$1h$ excitations over more complex nuclear configurations. The missing strength appears to be spread fairly uniformly over many tens of MeV in the final nucleus where it is unlikely to be detectable with current experimental capabilities. If Δ excitations are relevant, they make only a minor contribution to the structure of low lying excitations or to the total missing strength. Beyond the question of Δ excitation in nuclear structure, the study of GT transitions and the GTGR have led to important advances in our understanding of the isovector effective interactions. By the choice of suitable transitions ($J^\pi = 0^+ \rightarrow J^\pi = 1^+$ for GT and $J^\pi = 0^+ \rightarrow J^\pi = 0^+$ for F transitions) nuclear states serve as filters to permit the study of (almost) pure single components of the nucleon-nucleon effective interaction. Measurements of the ^{14}C (p, n) reaction leading to the 2.13 MeV, 0^+ state and the 3.95 MeV, 1^+ states of ^{14}N have provided a determination of the energy dependence of the F and GT components of the interaction from 60 to 800 MeV. Model calculations have been able to account for the GT component, but above 200 MeV the predictions for the F component are in rather poor agreement with the data.

Another determination of the GT effective interaction is provided by the location of the GTGR. This is sensitive to the particlehole interaction involved in the $1p$–$1h$ excitations which make up the giant resonance. Calculations have shown that this interaction, (i.e., the location of the GTGR) is satisfactorily accounted for in terms of a correlated one-boson (π+ ρ) exchange.

In quite another direction there have been interesting applications of results of GT studies to astrophysical problems. One of these is the use of the (p,n) reaction to measure β^- strengths needed for the calibration of solar neutrino detectors. The transitions of interest are all rather weak however, which implies large uncertainties (perhaps as much as a factor of two in some cases) in the measured strengths. In spite of such large uncertainties the measurements have provided information which is useful in establishing the suitability of various materials such as ^{127}I which have been proposed for new detectors.

Early on, in studies of the missing strength problem, it had been suggested that measurements of (n,p) cross reactions, corresponding to β^+ decay or electron capture, could provide an unequivocal signature for Δ excitations. This led to the development of several new spectrometers for intermediate energy (n,p) measurements, which were able to produce data of similar quality to the (*p, n*) results. As it turned out the *(n,p)* results did not resolve the missing strength problem. They have however provided extensive data on GT strengths for electron capture on nuclei in the iron–nickel region. These results are needed for the calculation of pre-supernova collapse of massive stars initiated by the onset of electron capture reactions at high temperatures. Little data has been previously available on these electron capture cross sections, and in some cases the (*n,p*) results have led to substantial changes in estimates of the relative importance of different nuclear species in initiating stellar collapse.

The above discussion has emphasized the importance of GT transitions with angular momentum transfer $\Delta L = 0$, corresponding to allowed β^- or β^+ decay. Nuclear transitions of higher multipolarity have also been investigated though, with $\Delta L \geq 1$. The spin dipole giant resonance with $\Delta L = 1$, $\Delta J^\pi = 0^-, 1^-, 2^-$ is a prominent feature of (*p, n*) or (*n,p*) spectra at angles and excitation energies corresponding to momentum transfer $\Delta q \simeq 0.5 - 1.0 fm^{-1}$. Model calculations are able to give a reasonable account of observed strength distributions, but more detailed model comparisons are limited by our inability to clearly identify the three different components of the resonance.

The same measurements that show the spin dipole giant resonance as an ubiquitous feature of nuclear excitations have yielded another rather surprising result. This is the almost complete absence of $\Delta L = 2$,or quadrupole strength in many (*n,p*) reaction cross sections. A model to explain this result has been proposed, based on non-local contributions to the quadrupole part of the model Hamiltonian and the quadrupole transition operator, but this remains an interesting problem for further investigation.

The other important problem that has been investigated in the last few years is that of quasifree charge-exchange scattering. Early predictions of the ratio of the spin longitudinal to spin transverse response in this reaction had been made but were found to be in serious disagreement with experimental results. The disagreement has been shown to arise in part because of inadequate treatment of distortion effects. There is however some suggestion that the nucleon-nucleon effective interaction is modified in the nuclear medium in a way that is not fully understood at present.

Finally, we note that the last few years have seen the development of new facilities for the study of charge-exchange reactions using more massive projectiles to initiate reactions of greater complexity than *(p, n)* and *(n,p)*. These include (d, ^{2}He), (^{3}He, t), (^{6}Li, ^{6}He) (^{12}C, ^{12}B) and (^{12}C, ^{12}N). In addition to providing cross section data the (d, ^{2}He) and (^{6}Li, ^{6}He) reactions can be studied using tensor polarized incident beams and this may lead to major advances in the identification of the different components of the giant resonances with $\Delta L > 0$.

At this point we can say that our understanding of the GT giant resonance as an important mode of nuclear excitation is reasonably complete. Our understanding of the response function for large momentum transfers is much less so, and we may expect further studies to answer outstanding questions in this domain. While we can look forward to much interesting new work in charge-exchange studies it is difficult just now to imagine developments that will have the same impact on the field of nuclear physics as did the discovery about 1980 of the dramatic appearance of the GT giant resonance as the dominant feature of intermediate energy (*p, n*) reactions.

ACKNOWLEDGMENTS

The authors would like to thank Erich Vogt for the invitation to prepare this review and for his encouragement and advice in its completion. We have benefitted from discussions with many colleagues, and particularly wish to thank S. M. Austin, C. D. Goodman and M. Moinester for helpful comments on the final manuscript. Financial support for this work was provided by TRIUMF, and by the National Science and Engineering Research Council of Canada (WPA) and by the Ian Potter Foundation and the Department of Industry Science and Technology (Australia) (BMS). We also wish to thank Raso Samarasekera for her care and cheeful patience in typing the many revisions and corrections required for the final manuscript.

REFERENCES

1. F. Osterfeld, Rev. Mod. Phys. **64** (1992) 491.
2. D. H. Wilkinson, Nucl. Phys. **A511** (1990) 301.
3. I. S. Towner, Nucl. Phys. **AS46** (1992) 478.
4. A. Bohr and B. Mottelson, Nuclear Structure [Benjamin, New York (1969)] Vol. 1, 345, 349,411.
5. G. R. Satchler, Nucl. Phys. **55** (1965) 1.
6. A. K. Kerman, H. McManus, and R. M. Thaler, Ann. of Phys. **8** (1959) 551.
7. M. L. Goldberger and K. M. Watson, “Collision Theory” [Wiley, New York (I 964)] 683-690.
8. J. R. Comfort, computer code DW8 1, Arizona State University (1984); extended version of DWBA70, R. Schaeffer and J. Raynal (unpublished).
9. W. M. Visscher and R. A. Ferrell, Phys. Rev. **107** (1957) 781.
10. S. Bloom, N. Glendenning, and S. Mozkowski, Phys. Rev. Lett. **3** (1959) 98.
11. C. Wong, J. D. Anderson, S. D. Bloom, J. W. McClure, and B. D. Walker, Phys. Rev. **123** (1961) 598.
12. J. D. Anderson, C. Wong, and I. W. McClure, Phys. Rev. **126** (1962) 2170.
13. A. M. Lane and J. M. Soper, Phys. Lett. **1** (1962) 28.
14. K. Ikeda, S. Fujii, and J. I. Fujita, Phys. Lett. **2** (1962) 169.

15. K. Ikeda, S. Fujii, and J. I. Fujita, Phys. Lett. **3** (1963) 271.
16. S. D. Bloom, J. D. Anderson, W. F. Hornyak, and C. Wong, Phys. Rev. Lett, **15** (1 965) 264.
17. C. Wong, J. D. Anderson, J. McClure, B. Pohl, V. A. Madsen, and F. Schmittroth, Phys. Rev. **160** (1 967) 769.
18. P. J. Locard, S. M. Austin, and W. Benenson, Phys. Rev. Lett. **19** (1967) 1141.
19. A. S. Clough et ai., Nucl. Phys. **A137** (1969) 222.
20. J. D. Anderson, S. D. Bloom, C. Wong, W. F. Hornyak, and V. A. Madsen, Phys. Rev. **177** (1969) 1416.
21, J. D. Anderson, C. Wong, and V. Madsen, Phys. Rev. Lett. **24** (1970) 1074.
22. C. D. Goodman, C. A. Goulding, M. B. Greenfield, J. Rapaport, D. E. Bainum, C. C. Foster, W. G. Love, and F. Petrovich, Phys. Rev. Lett. **44** (1980) 1755.
23. S. M. Austin, "The Two-Body Force in Nuclei," ed. S. M. Austin and G. M. Crawley [Plenum, New York (1972)J].
24. G. C. Baldwin and G. S. Klaiber, Phys. Rev. **73** (1948) 11 56.
25. J. D. Anderson and C. Wong, Phys. Rev. Lett. **7** (1961) 250.
26. K. Ikeda, Prog. Theor. Phys. **31** (1964) 434.
27. M. C. Vetterli, O. Häusser, R. Abegg, W. P. Alford, A. Celler, D. Frekers, R. Helmer, R. Henderson, K. H. Hicks, K. P. Jackson, R. G. Jeppesen, C. A. Miller, K. Raywood, and S. Yen, Phys. Rev. **C40** (1989) 559.
28. R. R. Doering, Aaron Galonsky, D. M. Patterson, and G. F. Bertsch, Phys. Rev. Lett. **35** (1975) 1691.
29. D. E. Bainum, J. Rapaport, C. D. Goodman, D. J. Horen, C. C. Foster, M. B. Greenfield, and C. A. Goulding, Phys. Rev. Lett. **44** (1980) 1751.
30. Sam M. Austin, L. E. Young, R. R. Doering, R. De Vito, R. K. Bhowmik, and S. D. Schery, Phys. Rev. Lett. **44** (1980) 972.
31. S. M. Austin, in "The (*p, n*) Reaction and the Nucleor–Nucleon Force," ed. C. D. Goodman, S. M. Austin, S. D. Bloom, J. Rapaport, and G. R. Satchler [Plenum, New York (1980)] 203.
32. W. A. Sterrenburg, S. M. Austin, V. E. P. Berg, and R. de Vito, Phys. Lett. **91B** (1980) 337.
33. C. D. Goodman, in "The (*p,n*) Reaction and the Nucleon–Nucleon Force," ed. C. D. Goodman, S. M. Austin, s. D. Bloom, J. Rapaport, and G. R. Satchler [Plenum, New York (1 980)] 149.
34. C. Gaarde, J. Rapaport, T. N. Taddeucci, C. D. Goodman, C. C. Foster, D. E. Bainum, C. A. Goulding, M. B. Greenfield, D. J. Horen, and E. Sugarbaker, Nucl. Phys. **A369** (1981) 258.
35. G. L. Moake, L. J. Gutay, R. P. Scharenberg, P. T. Debevec, and P. A. Quin, Phys. Rev. **C21** (1980) 2211.
36. F. Petrovich, W. G. Love, andR. J. McCarthy, Phys. Rev. **21** (1980) 1718.
37. C. D. Goodman *et al.,* IEEE Trans. Nucl. Sci. **NS-26** (1979) 2248.
38. C. D. Goodman, Can. Jour. Phys. 65 (1987) 549.
39. C. D. Goodman, J. Rapaport, and D. E. Bainurn, IEEE Trans. Nucl. Sci. **NS-25** (1978) 577.
40. C. D. Goodman, J. Rapaport, and D. E. Bainum, Nucl. Instrum. Methods 151 (1978) 125.
41. R. Madey *et al.,* Nucl. Instrum. Meth. **214** (1983) 401.
42. T. N. Taddeucci, C. D. Goodman, R. C. Byrd, T. A. Carey, D. J. Horen, J. Rapaport, and E. Sugarbaker, Nucl. Instrum. Meth. **A241** (1995) 448.
43. J. B. McClelland, Can. Jour. Phys. **65** (1987) 633.
44. J. B. McClelland, D. A. Clark, J-L. Davis, R. C. Haight, R. W. Johnson, N. S. P. King, G. L. Morgan, L. J. Rybarcyk, J. Ullmann, P. Lisowski, W. R. Smythe, D. A. Lind, C. D. Zafiratos, and J. Rapaport, Nucl. Instrum. Methods Phys. Res. Sect. **A276** (1989) 35.

45. D. J. Mercer, J. Rapaport, C. A. Whitten, Jr., D. Adams, R. Byrd, X. Y. Chen, A. Fazely, T. Gaussiran, E. Gülmez, C. Goodman, D. W. Huang, G. Igo, A. Ling, D. Marchlenski, D. Prout, L. Rybarcyk, E. Sugarbaker, and T. N. Taddeucci, Phys. Rev. **C49** (1994) 3104.
46. E. Sugarbaker *et al.,* Phys. Rev. Lett. **65** (1990) 55 1.
47. R. Helmer, Can. Jour. Phys. **65** (1987) 588.
48. D. F. Measday, Phys. Lett. **21** (1966) 66.
49. D. F. Measday and J. N. Palmieri, Phys. Rev. **161** (1967) 1071.
50. F. P. Brady, Can. Jour. Phys. **65** (1987) 578.
51. R. S. Henderson, W. P. Alford, D. Frekers, 0. Häusser, R. L. Helmer, K. H. Hicks, K. P. Jackson, C. A. Miller, M. C. Vetterli, and s. Yen, Nucl. Instrum. Methods **A257** (1987) 97.
52. K. J. Raywood, B. M. Spicer, S. Yen, S. A. Long, M. A. Moinester, R. Abegg, W. P. Alford, A. Celler, T. E. Drake, D. Frekers, P. E. Green, O. Häusser, R. L. Helmer, R. S. Henderson, K. H. Hicks, K. P. Jackson, R. G. Jeppesen, J. D. King, N. S. P. King, C. A. Miller, V. C. Officer, R. Schubank, G. G. Shute, Phys. Rev. **C41** (1990) 2836.
53. B. K. Park, J. Rapaport, J. L. Ullmann, A. G. Ling, D. S. Sorenson, F. P. Brady, J. L. Romero, C. R. Howell, W. Tornow, and C. T. Rönnqvist, Phys. Rev. **C45** (1992) 1791.
54. A. Ling, X. Aslanoglu, F. P. Brady, W. R. Finlay, R. C. Haight, G. R. Howell, N. S. P. King, P. W. Lisowski, B. K. Park, J. Rapaport, J. L. Romero, D. S. Sorenson, W. Tornow, and J. L. Ullmann, Phys. Rev. **C44** (1991) 2794.
55. H. Conde, Nucl. Inst. and Meth. in Phys. Res. **A292** (1990) 121.
56. A. Galonsky, J. P. Didelez, A. Djaloeis, and W. Oelerd, Phys. Lett. **748** (1978) 176.
57. D. Ovazza, A. Willis, M. Morlet, N. Marty, P. Martin, P. de Saintignon, and M. Buenerd, Phys. Rev. **C18** (1978) 2438.
58. C. Gaarde, J. S. Larsen, M. N. Harakeh, S. Y. Vander Werf, M. Igarishi, and A. Müller-Arnke, Nucl. Phys. **A334** (1980) 248.
59. C. Ellegaard *et al.*, Phys. Rev. Lett. **50** (1 983) 1745.
60. E. Grorud, J. L. Laclare, A. Ropert, A. Tkatchenko, J. Banaigs, and M. Boivin, Nucl. Instrum. Methods **188** (1981) 549.
61. I. Bergqvist, A. Brockstedt, L. Carlén, L. P. Ekström, B. Jakobsson, C. Ellegaard, C. Gaarde, J. S. Larsen, C. Goodman, M. Bedjidian, D. Contardo, J. Y. Grossiord, A. Guichard, R. Haroutunian, J. R. Pizzi, D. Bachelier, J. J. Boyard, T. Hennino, J. C. Jourdain, M. Roy-Stephan, M. Boivin, and P. Radvanyi, Nucl. Phys. **A469** (1987) 648.
62. 1. Miura *et al.,* RCNP Annual Report (1991) 149.
63. H. Akimure, I. Daito, Y. Fujita, M. Fujiwara, M. B. Greenfield, M. N. Harakeh, T. Inomata, J. Jänecke, K. Katori, S. Nakayama, H. Sakai, Y. Sakemi, M. Tanaka, and M. Yosoi, Nucl. Phys. **A569** (1 994) 245c.
64. W. Mettner *et al.*, Nucl. Phys. **A473** (1987) 160.
65. A. Schulte, T. Udagawa, F. Osterfeld, and D. Cha, Phys. Lett. **183B** (1987) 243.
66. N. Auerbach, F. Osterfeld, and T. Udagawa, Phys. Lett. **219B** (1989) 184.
67. D. P. Stahel, R. Jahn, G. J. Wozniak, and J. Cerny, Phys. Rev. **C20** (1979) 1680.
68. K. B. Beard, J. Kasagi, E. Kashy, B. H. Wildenthal, D. L. Freisel, H. Nann, and R. E. Warner, Phys. Rev. **C26** (1982) 720.
69. C. Wilkin and D. V. Bugg, Phys. Lett. **154B** (1985) 243.
70. D. V. Bugg and C. Wilkin, Nucl. Phys. **A467** (1987) 575.
71. C. Ellegaard, Can. Journ, of Phys. **65** (1987) 600.
72. H. Ohnuma *et al.,* Phys. Rev. **C47** (1993) 648.
73. H. Okamura *et al.,* Phys. Lett. **3456** (1 995) I.
74. H. M. Xu, G. K. Ajupova, A. C. Betker, C. A. Gagliardi, B. Kokenge, Y.-W. Lui, and A. P. Zaruba, Phys. Rev. **C52** (1 995) R1 161.
75. W. R. Wharton and P. T. Debevec, Phys. Rev. **C11** (1975) 1963.

76. D. V. Aleksandrov, Yu. A. Glukhov, A. S. Demyanova, A. A. Ogloblin, S. B. Sakuta, V. V. Sokharevsky, S. V. Tolokonnikov, S. A. Fayans, F. A. Gareev, S. N. Ershov, I. N. Borzov, and J. Bang, Nucl. Phys. **A436** (1985) 338.
77. N. Anantaraman, J. S. Winfield, Sam M. Austin, A. Gabnsky and J. van der Plicht, Phys. Rev. Lett. **57** (1986) 2375.
78. B.D. Anderson,T.Chittrakam, A. R.Baldwin, C. Lebo, R.Madey, P. C.Tandy, J. W. Watson, C. C. Foster, B. A. Brown, and B. H. Wildenthal, Phys. Rev. **C36** (1987) 2195.
79. J. S. Winfield, N. Anantaraman, Sam M. Austin, Ziping Chen, A. Galonsky, J. van der Plicht, H.-L. Wu, C. C. Chang, and G. Ciangaru, Phys. Rev. **C35** (1987) 1734.
80. H. Wirth, E. Aschenauer, W. Eyrich, A. Lehmann, M. Moosburger, H. Schlösser, H. J. Gils, H. Rebel, and S. Zagromski, Phys. Rev. **C41** (1990) 2698.
81. M. Moosburger, E. Aschenauer, H. Deunert, W. Eyrich, A. Lehmann, R. Rudeloff, H. Schlösser, H. Wirth, H. J. Gils, H. Rebel, and S. Zagromski, Phys. Rev. **C41** (1990) 2925.
82. H. Laurent, S. Gales, D. Beaumel, G. M. Crawley, J. E. Finck, S. Fortier, J. M. Maison, C. P. Massolo, D. J. Mercer, J. S. Winfield, and G. H. Yoo, Nucl. Phys. **AS69** (1994) 297c.
83. L. Reber, K. W. Kemper, P. L. Kerr; A. J. Mendez, E. G. Myers, B. G. Schmidt, and N. M. Clarke, Phys. Rev. **C47** (1993) 2190.
84. J. S. Winfield, N. Anantaraman, Sam M. Austin, L. H. Hanvood, J. van der Plicht, H.-L. Wu, and A. F. Zeller, Phys. Rev. **C33** (1986) 1333.
85. H. Lenske, H. H. Wolter, and H. G. Bohlen, Phys. Rev. Lett. **62** (1989) 1457.
86. N. Anantaraman, J. S. Winfield, Sam M. Austin, J. A. Cam, C. Djalali, A. Gillibert, W. Mittig, J. A. Nolen, Jr., and Zhan Wen Long, Phys. Rev. **C44** (1991) 398.
87. T. Ichihara, M. Ishihara, H. Ohnuma, T. Niizeki, Y. Tajima, T. Yamamoto, Y. Fuchi, S. Kubono, M. H. Tanaka, H. Okamura, S. Ishida, S. Miyamoto, and H. Toyakawa, Phys. Lett. **323B** (1 994) 278.
88. F. Osterfeld, N. Anantaraman, S. M. Austin, J. A. Carr, and J. S. Winfield, Phys. Rev. **C45** (1992) 2854.
89. T. N. Taddeucci, C. A. Goulding, T. A. Carey, R. C. Byrd, C. D. Goodman, C. Gaarde, J. Larsen, D. Horen, J. Rapaport, and E. Sugarbaker, Nucl. Phys. **A469** (1987) 125.
90. J. W. Watson, W. Pairsuwan, B. D. Anderson, A. R. Baldwin, B. S. Flanders, R. Madey, R. J. McCarthy, B. A. Brown, B. H. Wildenthal, and C. C. Foster Phys. Rev. Lett. **55** (1985) 1369.
91. J. Rapaport, T. Taddeucci, P. Welch, C. Gaarde, J. Larsen, C. Goodman, C. C. Foster, C. A. Goulding, D. Horen, E. Sugarbaker, and T. Masterson, Phys. Rev. Lett. **47** (1981) 1518.
92. D. P. Wells, Bull. Am. Phys. Soc. **37** (1992) 1296.
93. C. Gaarde, J. S. Larsen, and J. Rapaport, in “Spin Excitations in Nuclei,” ed. F. Petrovich, G. E. Brown, G. T. Garvey, C. D. Goodman, R. A. Lindgren, and W. G. Love [Plenum, N. Y. (1984)] 65.
94. D. Krofchek, E. Sugarbaker, J. Rapaport, D. Wang, J. N. Bahcall, R. C. Byrd, C. C. Foster, C. D. Goodman, I. J. van Heerden, C. Gaarde, J. S. Larsen, D. J. Horen, and T. N. Taddeucci, Phys. Rev. Lett. **55** (1985) 105 1.
95. J. L. Mildenberger *et al.,* Phys. Rev. **C43** (1991) 1777.
96. T. N. Taddeucci, in “Spin Observables of Nuclear Probes,” ed. Charles J. Horowitz, Charles D. Goodman, and George E. Walker [Plenum, N. Y. (1988)] 425.
97. S. M. Austin, N. Anantaraman, and W. G. Love, Phys. Rev. Lett. **73** (1994) 30.
98. T. N. Taddeucci, J. Rapaport, D. E. Bainum, C. D. Goodman, C. C. Foster, C. Gaarde, J. Larsen, C. A. Goulding, D. J. Horen, T. Masterson, and E. Sugarbaker, Phys. Rev. **C25** (1981) 1094.

99. W. P. Alford, R. L. Helmer, R. Abegg, A. Celler, 0. Häuser, K. Hicks, K. P. Jackson, C. A. Miller, S. Yen, R. E. Azuma, D. Frekers, R. S. Henderson, H. Baer, and C. D. Zafiratos, Phys. Lett. **179B** (1986) 20.
100. J. Rapaport *et al.,* Phys. Rev. **C39** (1989) 1929.
101. Y. Wang *et al.,* IUCF Scientific and Technical Report (May 1990–April 1991) ed. by E. J. Stephenson and R. D. Bent, 37.
102. G. Bertsch, Nucl. Phys. **A354** (1981) 157c.
103. S. Krewald and F. Osterfeld, Phys. Rev. Lett. **46** (198 I) 103.
104. G. E. Brown and M. Rho, Nucl. Phys. **A372,** (1981) 397.
105. T. Izumoto, Nucl. Phys. **A395** (1983) 189.
106. D. Cha, B. Schwesinger, J. Wambach, and J. Speth, Nucl. Phys. **A430** (1984) 321.
107. G. J. Mathews, S. D. Bloom, and R. F. Hausman, Jr., Phys. Rev. **C28** (1983) 1367.
108. K. Muto, H. Yamazaki, T. Oda, and H. Horie, Phys. Lett. **165B** (1985) 25.
109. G. F. Bertsch and I. Hamamoto, Phys. Rev. **C26** (1982) 1323.
110. B. Schwesinger and J. Wambach, Nucl. Phys. **A426** (1984) 253.
111. S. D. Bloom, C. D. Goodman, S. M. Grimes, and R. F. Hausman, Jr., Phys. Lett. **107B** (1981) 336.
112. C. D. Goodman, C. C. Foster, D. E. Bainum, S. D. Bloom, C. Gaarde, J. Larsen, C. A. Goulding, D. J. Horen, T. Masterson, J. Grimes, J. Rapaport, T. N. Taddeucci, and E. Sugarbaker, Phys. Lett. **107B** (1981) 406.
113. F. Osterfeld, Phys. Rev. **C26** (1982) 762.
114. C. Gaarde, Nucl. Phys. **A396** (1983) 127c.
115. M. Ericson, A. Figureau, and C. Thévenet, Phys. Lett. **45B** (1973) 19.
116. M. Rho, Nucl. Phys. **A231** (1974) 493.
117. E. Oset and M. Rho, Phys, Rev. Lett. **42** (1 979) 47.
118. A. Bohr and B. Mottelson, Phys. Lett. **100B** (1980) 10.
I19. J. Speth, Nucl. Phys. **A396** (1983) 153c.
120. N. Anantaraman, B. A. Brown, G. M. Crawley, A. Galonsky, C. Djalali, N. Marty, M. Morlet, A. Willis, and J-C. Jourdain, Phys. Rev. Lett. **52** (1984) 1409.
121. M. Rho, in "Spin Excitations in Nuclei," ed. F. Petrovich, G. E. Brown, G. T. Garvey, C. D. Goodman, R. A. Lindgren, W. G. Love [Plenum, N. Y. (1984)] 249.
122. A. Arima, in "Spin Excitations in Nuclei," ed. F. Petrovich, G. E. Brown, G. T. Garvey, C. D. Goodman, R. A. Lindgren, and W. G. Love [Plenum, N. Y. (1984)] 249.
123. A. Arima and H. Horie, Prog. Theor. Phys. **11** (1954) 509; 12 (1954) 623.
124. I. S. Towner and F. Khanna, Nucl. Phys. **A399** (1983) 334.
125. S. Drozdz, V. Klemt, J. Speth, and J. Wambach, Phys. Lett. **166B** (1986) 18.
126. F. Osterfeld, D. Cha, and J. Speth, Phys. Rev. **C31** (1985) 372.
127. P. K. A. de Witt Huberts, Jour. Phys. **G16** (1990) 507.
128. C. Mahaux and R. Sartor, Advances in Nuclear Physics (Plenum, New York–London) V. **20** (1991) 1.
129. B. E. Vonderfecht, W. H. Dickhoff, A. Polls, and A. Ramos, Phys. Rev. **C44** (1991) R1265.
130. D. van Neck, M. Waroquier, V. vander Sluys, and J. Ryckenbusch, Phys. Lett. **274B** (1992) 143.
13 I. D. van Neck, A. E. L. Dieperink, and E. Moya de Guerra, Phys. Rev. **C51** (1995) 1800.
132. G. A. Rijsdijk, W. J. M. Geurts, M. G. E. Brand, K. Allaart, and W. H. DickhofF, Phys. Rev. **C48** (1993) 1752.
133. W. J. Geurts, K. Allaart, and W. H. Dickhoff, Phys. Rev. **C50** (1994) 514.
134. K. P. Jackson *et al.,* Phys. Lett. **201B** (1988) 25.
135. J. Mildenberger *et al.,* Phys. Rev. **C42** (1990) 732.
136. A. Williams *et al.,* Phys. Rev. **C51** (1995) 1144.

137. W. G. Love, in “The (*p,n*) reaction and the nucleon-nucleon force,” ed. by C. D. Goodman *et al.* [Plenum, New York (1980)] 30.
138. F. Petrovich, in “The (*p,n*) reaction and the nucleon-nucleon force,” ed. by C. D. Goodman *et al.* [Plenum, New York (1980)] 135.
139. W. G. Love and M. A. Franey, Phys. Rev. **C24** (1981) 1073.
140. G. E. Brown, J. Speth, and J. Wambach, Phys. Rev. Lett. **46** (1981) 1057.
141. N. S. P. King, P. W. Lisowski, G. L. Morgan, P. N. Craig, R. G. Jeppesen, D. A. Lind, J. R. Shepard, J. L. Ullmann, C. D. Zafiratos, C. D. Goodman, and C. A. Goulding, Phys. Lett. **175B** (1 986) 279.
142. W. P. Alford, R. Helmer, R. Abegg, A. Celler, D. Frekers, O. Häusser, R. Henderson, K. Hicks, K. P. Jackson, R. Jeppesen, C. A. Miller, and M. Vetterli, Phys. Rev. **C39** (1989) 1189.
143. W. G. Love, Amir Klein, M. A. Franey, and K. Nakayama, Can. Jour. Phys. **65** (1987) 536.
144. B. H. Wildenthal, in “Progress in Particle and Nuclear Physics,” ed. by D. Wilkinson [Pergamon Press, Oxford, (1984)] **11**,5.
145. L. Wang, X. Yang, J. Rapaport, C. D. Goodman, C. C. Foster, Y. Wang, R. A. Lindgren, E. Sugarbaker, D. Marchlenski, S. de Lucia, B. Luther, L. Rybarcyk, T. N. Taddeucci, and B. K. Park, Phys. Rev. **C47** (1993) 2123.
146. R. Madey, B. S. Flanders, B. D. Anderson, A. R. Baldwin, C. Lebo, J. W. Watson, Sam M. Austin, A. Galonsky, B. H. Wildenthal, and C. C. Foster, Phys. Rev. **C35** (1987) 2011.
147. T. Chittrakarn, B. D. Anderson, A. R. Baldwin, C. Lebo, R. Madey, and J. W. Watson, Phys. Rev. **C34** (1986) 80.
148. J. Rapaport, R. Alarcon, B. A. Brown, C. Gaarde, J. Larsen, C. D. Goodman, C. C. Foster, D. Horen, T. Masterson, E. Sugarbaker, and T. N. Taddeucci, Nucl. Phys. **A427** (1984) 332.
149. J. Rapaport, T. Taddeucci, T. P. Welch, C. Gaarde, J. Larsen, D. J. Horen, E. Sugarbaker, P. Koncz, C. C. Foster, C. D. Goodman, C. A. Goulding, and T. Masterson, Nucl. Phys. **A410** (1983) 371.
150. W. P. Alford, A. Celler, B. A. Brown, R. Abegg, K. Ferguson, R. Helmer, K. P. Jackson, S. Long, K. Raywood, and S. Yen, Nucl. Phys. **A531** (1991) 97.
151. S. El-Kateb, K. P. Jackson, W. P. Alford, R. Abegg, R. E. Azuma, B. A. Brown, A. Celler, D. Frekers, 0. Häusser, R. Helmer, R. S. Henderson, K. H. Hicks, R. Jeppesen, J. D. King, K. Raywood, G. E. Shute, B. M. Spicer, A. Trudel, M. Vetterli, and S. Yen, Phys. Rev. **C49** (1994) 3128.
152. M. Vetterli, O. Häusser, W. P. Alford, D. Frekers, R. Helmer, R. Henderson, K. Hicks, K. P. Jackson, R. G. Jeppesen, C. A. Miller. M. A. Moinester, K. Raywood, and S. Yen, Phys. Rev. Lett. **59** (1987) 439.
153. H. A. Bethe, G. E. Brown, J. Applegate, and J. Lattimer, Nucl. Phys. **A234** (1979) 487.
154. G. M. Fuller, W. A. Fowler, and J. Newman, Astrophys. J. (1985) 293; Astrophys. J. Suppl. (1982) 48, 279; Astrophys. J. (1982) 252, 715.
155. W. P, Alford, R. L. Helmer, R. Abegg, A. Celler, D. Frekers, P. Green, 0. Häusser, R. Henderson, K. Hicks, K. P. Jackson, R. Jeppesen, C. A. Miller, A. Trudel, M. Vetterli, and S. Yen, Nucl. Phys. **A514** (1990) 49.
156. W. P. Alford, B. A. Brown, S. Burzynski, A. Celler, D. Frekers, R. Helmer, R. Henderson, K. P. Jackson, K. Lee, A. Rahav, A. Trudel, and M. C. Vetterli, Phys. Rev. **C48** (1993) 28 18.
157. M. Vetterli, K. P. Jackson, A. Celler, J. Engel, D. Frekers, 0. Häusser, R. Helmer, R. Henderson, K. H. Hicks, R. G. Jeppesen, B. Larson, B. Pointon, A. Trudel, and S. Yen, Phys. Rev. **C45** (1992) 997.
158. M. B. Aufderheide, S. D. Bloom, D. A. Rester, and G. J. Mathews, Phys. Rev. **C48** (1993) 1667.

159. M. B. Aufderheide, S. D. Bloom, G. J. Mathews, and D. A. Resler, Phys. Rev. **C53** (1996 3139.
160. D. J. Dean, P. B. Radha, K. Langanke, Y. Alhassid, S. E. Koonin, and W. E. Ormand, Phys Rev. Lett. **72** (1994) 4066.
161, K. Langanke, D. J. Dean, P. B. Radha, Y. Alhassid, and S. E. Koonin, Phys. Rev. **C52** (1995 718.
162. J. K. Rowley, B. T. Cleveland, and R. Davis, Jr., in "Solar Neutrinos and Neutrino Astronomy," ed. by M. L. Cherry, W. A. Fowler, and K. Lande, AIP Conference proceedings No 126 [Amer. Inst. Phys., New York, (1985)] 1.
163. J. N. Bahcall, B. T. Cleveland, R. Davis, Jr., I. Dostrovsky, J. C. Evans, W. Frati, G. Fried lander, K. Lande, J. K. Rowley, R. W. Stoenner, and J. Weneser, Phys. Rev. Lett. **40** (1978) 1351.
164. J. N. Bahcall, Phys. Rev. **C24** (1981) 2216.
165. G. A. Cowan and W. C. Haxton, Science **216** (1982) 51.
166. R. S. Raghavan, Phys. Rev. Lett. **37** (1976) 259.
167. W. C. Haxton, Phys. Rev. Lett. **60** (1988) 768.
168. P. Anselmann *et al.* (Gallex Collaboration), Phys. Lett. **285B** (1992) 376.
169. J. N. Abdurashitov *et al.* (SAGE collaboration), Phys. Rev. Lett. **77** (1 996) 4708.
170. J. Rapaport, P. Welch, J. Bahcall, E. Sugarbaker, T. N. Taddeucci, C. D. Goodman, C. F. Foster, D. Horen, C. Gaarde, J. Larsen, and T. Masterson, Phys. Rev. Lett. **54** (1985) 2325.
171. E. G. Adelberger, A. Garcia, P. V. Magnus, and D. P. Wells, Phys. Rev. Lett. **67** (1991) 3658.
172. W. Trinder, E. G. Adelberger, Z. Janas, H. Keller, K. Krumbholz, V. Kunze, P. Magnus, F. Meissuer, A. Piechaczek, M. Pfützner, E. Roeck, K. Rykacqewski, W. P. Schmidt-Ott, and M. Weber, Phys. Lett. **349B** (1995) 267.
173. P. Anselmann *et al.*, (Gallex Collaboration), Phys. Lett. **342B** (1995) 440.
174. M. A. Moinester, Can. Jour. Phys. **65** (1987) 660.
175. A. Celler *et al.*, Phys. Rev. **C47** (1993) 1563.
176. M. A. Franey and W. G. Love, Phys. Rev. **C31** (1985) 488.
177. S. A. Long, Ph. D Thesis (unpublished), University of Melbourne (1995).
178. W. A. Sterrenburg, Sam M. Austin, R. P. De Vito, and Aaron Galonsky, Phys. Rev. Lett. **45** (1980) 1839.
179. D. J. Horen, C. D. Goodman, C. C. Foster, C. A. Goulding, M. B. Greenfield, J. Rapaport, D. E. Bainum, E. Sugarbaker, T. G. Masterson, F. Petrovich, and W. G. Love, Phys. Lett. **95B** (1980) 27.
180. F. Osterfeld, S. Krewald, H. Dermawan, and J. Speth, Phys. Lett. **105B** (1981) 257.
181. N. Auerbach and A. Klein, Phys. Rev. **C30** (1984) 1032.
182. J. Wambach, S. Drozdz, A. Schultz, and J. Speth, Phys. Rev. **C37** (1988) 1322.
183. H. Sagawa and B. A. Brown, Phys. Lett. **143B** (1984) 283.
184. S. Drozdz, F. Osterfeld, J. Speth, and J. Wambach, Phys. Lett. **189B** (1987) 271.
185. T. N. Taddeucci, Can. Jour. Phys. **65** (1987) 557.
186. J. W. Watson, B. D. Anderson, and R. Madey, Can. Jour. Phys. **65** (1987) 566.
187. J. W. Watson, B. D. Anderson, A. R. Baldwin, C. C. Foster, D. Lamm, R. Madey, Marco R. Plumley, and P. J. Pella, Nucl. Phys. **A577** (1994) 79c.
188. C. Gaarde, J. S. Larsen, H. Sagawa, N. Ohtsuka, J. Rapaport, T. N. Taddeucci, C. D. Goodman, C. C. Foster, C. A. Goulding, D. Horen, T. Masterson, and E. Sugarbaker, Nucl. Phys. **A422** (1984) 189.
189. T. E. Drake, E. L. Tomusiak, and H. S. Caplan, Nucl. Phys. **A118** (1968) 138.
190. S. Cohen and D. Kurath, Nucl. Phys. **73** (1965) 1.
191, A. G. M. Van Hees and P. W. M. Glaudemans, Nucl. Phys. **A396** (1983) 105c.
192. M. Yabe, Phys. Rev. **C36** (I 987) 858.
193. A. Klein, G. W. Love, and N. Auerbach, Phys. Rev. **C31** (1985) 710.

194. M. Moinester *et al.,* Phys. Lett. **230B** (1989) 41.
195. K. J. Raywood, S. A. Long, and B. M. Spicer, Nucl. Phys. **A625** (1997) 675.
196. F. Krmpotic, K. Ebert, and W. Wild, Nucl. Phys. **A342** (1980) 497.
197. D. Wang, J. Rapaport, D. J. Horen, B. A. Brown, C. Gaarde, C. D. Goodman, E. S. Sugarbaker, and T. N. Taddeucci, Nucl. Phys. **A480** (1988) 285.
198. A. Erell, J. Alster, J. Lichenstadt, M. A. Moinester, J. D. Bowman, M. D. Cooper, F, Iron, H. S. Matis, E. Piatetzsky, and V. Sennhauser, Phys. Rev. **C34** (1986) 1822.
199. R. Leonardi. E. Lipparini, and S. Stringari, Phys. Rev. **C35** (1987) 1489.
200. A. Bohr and B. R. Mottelson, Nuclear Structure [Benjamin, New York (1975)] Vol. 2, 670-676.
201. V. Gillet and N. Vinh-Mau, Nucl. Phys. **54** (1964) 32 1.
202. M. H. Macfarlane, Can. J. Phys. **65** (1987) 626.
203. K. Bleuler, M. Beiner, and R. de Tourreil, I1 Nuovo Cimento **52B** (1967) 45; I1 Nuovo Cimento **52B** (1967) 149.
204. G. S. Adams, A. D. Bacher, G. T. Emery, W. P. Jones, R. R. Kouzes, D. W. Miller, A. Picklesimer, and G. E. Walker, Phys. Rev. Lett. **38** (1977) 1387.
205. S. Yen, R. Sobie, H. Zarck, B. O. Pich, T. E. Drake, C. F. Williamson, S. Kowalski, and C. P. Sargent, Phys. Lett. **93B** (1980) 250.
206. J. A. Carr, S. D. Bloom, F. Petrovich, and R. J. Philpott, Phys. Rev. **C45** (1992) 1 145.
207. P. J. Moffa and G. E. Walker, Nucl. Phys. **A222** (1974) 140.
208. B. D. Anderson, A. Fazely, C. Lebo, J. W. Watson, and R. Madey, in “Spin Excitations in Nuclei,” ed. F. Petrovich, G. E. Brown, G. T. Garvey, C. D. Goodman, R. A. Lindgren, and W. G. Love [Plenum, N. Y. 1984)] 391.
209. N. Tamimi, B. D. Anderson, A. R. Baldwin, T. Chittrakarm, M. Elasaar, R. Madey, D. M. Manley, M. Mostajaboddavati, J. W. Watson, W-M. Zhang, J. A. Carr, andC. C. Foster, Phys. Rev. **C45** (1992) 1005.
210. B. D. Anderson, A. R. Baldwin, L. A. C. Garcia, R. Madey, D. M. Manley, R. Pourang, E. Steinfelds, J. M. Watson, J. D. Brown, E. R. Jacobsen, R. Sherr, B. A. Brown, and C. C. Foster, Phys. Rev. **C46** (1 993) 504.
211, B. D. Anderson, C. Lebo, A. R. Baldwin, T. Chittrakarm, R. Madey, and J. W. Watson, Phys. Rev. Lett. **52,** (1 984) 1872.
212. R. Pourang *et al.*, Phys. Rev. **C44** (1991) 689.
213. R. Pourang *et al.*, Phys. Rev. **C47** (1993) 2751.
214. R. E. Chrien, T. J. Krieger, R. J. Sutter, M. May, H. Palevsky, R. L. Steams, T. Kozlowski, andT. Bauer, Phys. Rev. **C21** (1980) 1014.
215. N. S. Wall and P. G. Roos, Phys. Rev. **150** (1966) 81 1.
216. H. Esbensen and G. F. Bertsch, Phys. Rev. **C34** (1986) 1419.
217. J. M. Moss, T. A. Carey, J. B. McClelland, N. J. Di Giacomo, S. J. Seestrom-Morris, G. F. Bertsch, O. Scholten, G. S. Adams, M. Gazzaly, N. M. Hintz, and S. Nanda, Phys. Rev. Lett. **48** (1982) 789.
218. X. Y. Chen, L. W. Swenson, F. Farzanpay, D. K. McDaniels, Z. Tang, Z. Xu, D. M. Drake, I. Bergqvist, A. Brockstedt, F. E. Bertrand, D. J. Horen, J. Lísantti, K. Hicks, M. Vetterli, and M. J. Iqbal, Phys. Lett. **205B** (1988) 436.
219. H. Esbensen and G. F. Bertsch, Annals of Physics **157** (1984) 255.
220. R. D. Smith, in “Spin Observables of Nuclear Probes,” eds. C. J. Horowitz, C. D. Goodman, and G. E. Walker [Plenum, New York (1988)] 15.
221. O. Häuser, M. C. Vetterli, R. W. Fergerson, C. Glashausser, R. G. Jeppesen, R. D. Smith, R. Abegg, F. T. Baker, A. Celler, R. L. Helmer, R. Henderson, K. Hicks, M. J. Iqbal, K. P. Jackson, K. W. Jones, J. Lissantti, J. Mildenberger, C. A. Miller, R. S. Sawafta, and S. Yen, Phys. Rev. **C43** (1991) 230.

222. T. N. Taddeucci, R. C. Byrd, T. A. Carey, D. E. Ciskowski, C. D. Goodman, E. Gülmez, W. Huang, D. Marchlenski, J. B. McClelland, D. Prout, J. Rapaport, L. Rybarcyk, W. C. Sailor, and E. Sugarbaker, Nucl. Phys. **A527** (1991) 393c.
223. D. L. Prout, C. Zafiratos, T. N. Taddeucci, J. Ullmann, R. C. Byrd, T. A. Carey, P. Lisowski, J. B. McClelland, L. J. Rybarcyk, W. Sailor, W. Amian, M. Braunstein, D. Lind, D. J. Mercer, D. Cooper, S. DeLucia, B. Luther, D. G. Marchlenski, E. Sugarbaker, J. Rapaport, B. K. Park, E. Gülmez, C. A. Whitten, Jr., C. D. Goodman, W. Huang, D. Ciskowski, and W. P. Alford, Phys. Rev. **C52** (1995) 228.
224. J. Wambach, Phys. Rev. **C46** (1992) 807.
225. V. R. Pandharipande, J. Carlson, S. C. Pieper, R. B. Wiringa, R. Schiavilla, Phys. Rev. **C49** (1994) 789.
226. L. Wang, X. Yang, J. Rapaport, C. D. Goodman, C. C. Foster, Y. Wang, J. Piekarewicz, E. Sugarbaker, D. Marchlenski, S. DeLucia, B. Luther, L. Rybarcyk, T. N. Taddeucci, and B. K. Park, Phys. Rev. **C50** (1994) 2438.
227. W. M. Alberico, M. Ericson, and A. Molinari, Nucl. Phys. **A379** (1982) 429.
228. T. A. Carey, K. W. Jones, J. B. McClelland, J. M. Moss, L. B. Rees. N. Tanaka, and A. D. Bacher, Phys. Rev. Lett. **53** (1984) 144.
229. M. Ichimura, K. Kawahigashi, T. S. Jørgensen, and C. Gaarde, Phys. Rev. **C39** (1989) 1446.
230. J. B. McClelland, T. N. Taddeucci, X. Y. Chen, W. P. Alford, R. C. Byrd, T. A. Carey, S. De Lucia, C. D. Goodman, E. Gülmez, W. Huang, B. Luther, D. G. Marchlenski, D. J. Mercer, D. L. Prout, J. Rapaport, L. J. Rybarcyk, W. Sailor, E. Sugarbaker, Y. Wang, and C. Whitten, Jr., Phys. Rev. Lett. **69** (1993) 582.
231. X. Y. Chen, T. N. Taddeucci, J. B. McClelland, T. A. Carey, R. C. Byrd, L. J. Rybarcyk, W. C. Sailor, D. J. Mercer, D. L. Prout, S. De Lucia, B. Luther, D. G. Marchlenski, E. Sugarbaker, J. Rapaport, E. Gülmez, C. A. Whitten, Jr., C. D. Goodman, W. Huang, Y. Wang, and W. P. Alford, Phys. Rev. **C47** (1993) 2159.
232. T. N. Taddeucci, B. A. Luther, L. J. Rybarcyk, R. C. Byrd, J. B. McClelland, D. L. Prout, S. De Lucia, D. A. Cooper, D. G. Marchlenski, E. Sugarbaker, B. K. Park, Thomas Sams, C. D. Goodman, J. Rapaport, M. Ichimura, and K. Kawahigashi, Phys. Rev. Lett. **73** (1994) 3516.
233. G. E. Brown and J. Wambach, Nucl. Phys. **A568** (1994) 895.
234. G. E. Brown, M. Buballa, Z. B. Li, and J. Wambach, Nuclear Physics **A593** (1995) 295.
235. C. J. Horowitz and J. Piekarewicz, Phys. Lett. **301B** (1993) 321.
236. G. C. Hillhouse and P. R. De Kock, Phys. Rev. **C49** (1994) 391.
237. C. J. Horowitz and D. P. Murdock, Phys. Rev. **C37** (1988) 2032.
238. K. H. Hicks, M. C. Vetterli, A. Celler, R. L. Helmer, R. S. Henderson, K. P. Jackson, R. G. Jeppesen, A. Trudel, and S. Yen, Phys. Rev. **C40** (1989) R2445.
239. K. H. Hicks, W. P. Alford, A. Celler, R. S. Henderson, K. P. Jackson, C. A. Miller, M. C. Vetterli, S. Yen, F. Brieva, C. J. Horowitz, and J. Piekarewicz, Phys. Rev. **C47** (1993) 260.
240. C. Olmer, B. Zeidman, D. F. Geesaman, T-S. H. Lee, R. E. Segel, L. W. Swenson, R. L. Boudrie, G. S. Blanpied, H. A. Thiessen, C. L. Moms, and R. E. Anderson, Phys. Rev. Lett. **43** (1979) 612.
241. C. Olmer, A. D. Bacher, G. T. Emery, W. P. Jones, D. W. Miller, H. Nann, P. Schwandt, S. Yen, T. E. Drake, and R. J. Sobie, Phys. Rev. **C29** (1984) 361.
242. R. G. Sextro, R. A. Gouch, and J. Cerny, Nucl. Phys. **A234** (1974) 130.

Chapter 2

MESONIC CONTRIBUTIONS TO THE SPIN AND FLAVOR STRUCTURE OF THE NUCLEON

J. Speth
Institut für Kernphysik
Forschungszentrum Jülich
52425 Jülich, Germany
and
Institut für Theoretische Kernphysik
Universität Bonn
Bonn, Germany

and

A. W. Thomas
Department of Physics and Mathematical Physics and
Institute for Theoretical Physics
The University of Adelaide
Adelaide, South Australia 5005, Australia

Advances in Nuclear Physics, Vol. 24, edited by J. W. Negele and E. W. Vogt. Plenum Press, New York,©1998.

1. INTRODUCTION

Since its initial investigation at SLAC in the late 60's, deep-inelastic lepton scattering has provided a wonderful tool to explore perturbative QCD and to test many features of the Standard Model. The crucial theoretical tools needed to understand deep-inelastic scattering, namely the operator product expansion and the renormalization group (which are now used throughout particle physics), were developed in parallel with the data taking. Using these techniques one can often eliminate the need to understand the detailed structure of a target in order to make a rigorous test of QCD. Famous examples include the Adler, Gross, Llewellyn Smith and Bjorken sum-rules.

With perturbative QCD now well tested and established there are three important frontiers in deep-inelastic scattering. Two of these, namely the behavior at very small values of Bjorken x (defined in Section 2 below) which is currently being explored at HERA and the higher-twist corrections (again see Section 2), have traditionally been the domain of high energy physicists. The third frontier, which lies at the boundary of nuclear and particle physics, is our major concern. This is the wealth of information that deep-inelastic scattering data contains on the non-perturbative structure of hadrons [1].

The idea of using deep-inelastic scattering to probe non-perturbative structure first reached prominence in connection with the discovery of the nuclear EMC effect [2]. The fact that the structure function of a nucleus was not simply A times the structure function of a free nucleon, even in the valence region, suggested that the quark structure of the nucleon itself may be changed inside nuclear matter. Then quark degrees of freedom would play a vital role in understanding nuclear structure. This is one issue which still needs further study and we refer the interested reader to some recent reviews [3,4].

We shall focus on the non-perturbative structure of the free nucleon and particularly its meson cloud. Although the role of the pion cloud of the nucleon in deep-inelastic scattering began with Drell, Yan and Levy in 1970 [5] and Sullivan [6] in 1972, modem interest in it also sprang from the nuclear EMC effect. Realizing that virtual pion exchange plays a crucial role in nuclear binding, Llewellyn Smith [7] and Ericson and Thomas [8] explored the consequences for nuclear structure functions of an enhancement of the number of virtual pions per nucleon in a nucleus — see also Berger *et al.* [9]. This led naturally to a renewed interest in the role of the pion cloud in the free nucleon. In particular, it was shown by one of us [10] that one could put an upper limit on the hardness of the pion–nucleon form factor from the excess of non-strange over strange sea quarks seen in deep-inelastic scattering. It was also realized that the pion cloud necessarily led to an excess of $\bar{d}$ over $\bar{u}$ quarks in the proton.

Since 1983, and particularly since the New Muon Collaboration's confirmation of the excess of $\bar{d}$ over $\bar{u}$ in the proton [11], there has been a great deal of theoretical and experimental activity. Much has already been learnt about nucleon structure and an exciting program of experiments needs to be carried out in the next few years to teach us more. Our purpose is to review these developments for the community of physicists fascinated by the strong interaction, whether nuclear or particle physicists by background.

We begin with a brief review of the notation and ideas of deep-inelastic scattering and the general features of the data. Then we turn to the role of the long-range, pion cloud of the nucleon required by chiral symmetry as well as by the Heisenberg Uncertainty Principle! Having reviewed the traditional covariant approach we explain the importance of working in the infinite momentum frame. We explain why a pion cloud leads to important predictions such as an excess of anti-down over anti-up quarks, and look at the quantitative predictions.

Having explained the theoretical ideas we turn to the various experiments which can be used to test or constrain them. This includes using exclusivepp reactions to constrain meson–nucleon form factors, measurements of the Gottfiied sum-rule, Drell–Yan experiments and polarized deep-inelastic scattering. We also discuss semi-inclusive deep-inelastic experiments.

2. ELEMENTARY IDEAS OF DEEP-INELASTIC SCATTERING

There are a number of fine reviews of the ideas of inclusive lepton scattering at high energy and momentum transfer — the deep-inelastic regime [12, 13, 14, 15, 16, 17, 18, 19]. Our intention here is simply to explain the usual notation and summarize the essential ideas without any attempt at a formal derivation, which would take far too long.

We consider the inclusive scattering of a high energy lepton with initial (final) energy E (E') and scattering angle θ from a hadronic target of mass M and initial four-momentum p. The space like four-momentum transferred to the target is denoted q. For an unpolarized target the laboratory differential cross-section for electromagnetic scattering is calculated by contracting the lepton tensor $L_{\mu\nu}$ with the hadronic tensor $W^{\mu\nu}$;

$$W^{\mu\nu} = \tilde{g}^{\mu\nu} W_1 + \frac{\tilde{p}^{\mu}\tilde{p}^{\nu}}{M^2} W_2 \tag{2.1}$$

with

$$\tilde{g}^{\mu\nu} = -g^{\mu\nu} + \frac{q^\mu q^\nu}{q^2} \tag{2.2}$$

$$\tilde{p}^\mu = p^\mu - \frac{p \cdot q}{q^2} q^\mu \tag{2.3}$$

and the two arbitrary functions W_1 and W_2 contain all the information we can learn about the target from such experiments.

After contracting the tensors and integrating over phase space we find:

$$\frac{d^2\sigma}{dE'd\Omega} = \frac{4\alpha^2 (E')^2}{q^4} \left[\cos^2 \frac{\theta}{2} \frac{F_2}{\nu} + 2 \sin^2 \frac{\theta}{2} \frac{F_1}{M}\right] \tag{2.4}$$

All of the information concerning the structure of the target is now contained in the structure functions F_1 ($= MW_1$) and F_2 ($= \nu W_2$), with $\nu = E - E'$ (the photon energy in the laboratory frame) which can depend on at most two variables. One usually chooses those to be the Lorentz invariant quantities Q_2 ($= -q^2 > 0$) and Bjorken x ($= -q^2 / 2p.q = Q^2/2$ Mv). The deep-inelastic regime corresponds to the case where Q^2 and v are both very large ($Q^2 > 2$ GeV^2, $\nu > 1$ GeV) but x lies in the range (0,1). In the case of neutrino scattering from an unpolarized target we find a third structure function, F3, associated with parity violation:

$$\frac{d^2\sigma^{\nu(\bar{\nu})}}{dE'd\Omega} = \frac{G_F^2 (E')^2}{2\pi^2} \left(\frac{M_W^2}{M_W^2 + Q^2}\right)^2 \times \left[\cos^2 \frac{\theta}{2} \frac{F_2^{\nu(\bar{\nu})}}{\nu} + 2 \sin^2 \frac{\theta}{2} \frac{F_1^{\nu(\bar{\nu})}}{M} \pm \frac{E+E'}{M\nu} \sin^2 \frac{\theta}{2} F_3^{\nu(\bar{\nu})}\right] \tag{2.5}$$

There has recently been tremendous interest in polarized deep-inelastic scattering. In the case where a polarized electron (or muon) scatters from a polarized, spin-1/2 target, there are two more structure functions which can be measured, g_1 and g_2. Denoting beam and target helicity with arrows top and bottom respectively we find:

$$\frac{d^2\sigma}{dE'd\Omega} \left(\substack{\rightarrow \\ \rightarrow} - \substack{\rightarrow \\ \leftarrow}\right) = \frac{4\alpha^2 E'}{M\nu Q^2 E} \left[\left(E + E' \cos\theta\right) g_1 - 2Mxg_2\right] \tag{2.6}$$

Clearly the second term on the right of Eq. (2.6) will be negligible (in the deep-inelastic region) if g_1 and g_2 are of the same order. To determine g_2 one needs to work with a longitudinally polarized beam and a transversely polarized target. However, even then the cross-section is of order $(1/Q)$ times that given in Eq. (2.6):

$$\frac{d^2\sigma}{dE'd\Omega}\left(\vec{\uparrow}-\vec{\downarrow}\right)=\frac{4\alpha^2(E')^2}{M\nu Q^2E}\left[g_1+\frac{2Eg_2}{E+E'}\right]\sin\theta \tag{2.7}$$

(Here, an arrow up indicates that the target is polarized in the direction at right angles to the incident beam, in the scattering plane but pointing opposite to the side where the final lepton exits.)

In the late 1960s, tremendous excitement was generated by the discovery at SLAC that the structure functions were almost independent of Q^2 over a very wide range. That is, they were functions of the single variable — Bjorken x. It is very easy to see that this is what one would expect if the nucleon contained a collection of elementary constituents (initially called partons by Feynman but later identified with quarks) with low mass, which do not interact strongly during the deep-inelastic collision. For simplicity it is usual to consider this problem in a so-called infinite momentum frame, e.g., one where the nucleon has momentum $P \gg M$ in the $z-$ direction so that its 4-momentum is $p=(P,0,0,P)$. Under the assumptions of the parton model, only a parton with fraction x of the momentum of the nucleon can absorb the exchanged photon (or W-boson). Deep-inelastic structure functions are then determined by the number density of partons in the nucleon with momentum fraction x.

It is usual to define distributions $q^{\uparrow\downarrow}(x)$ which give the number density of quarks in the target with helicity parallel or anti-parallel to that of the target. For example, $u(x)xdx$ gives the fraction of momentum of u quarks in the proton with momentum between xP and $(x+dx)P$ in the infinite momentum frame (and with either helicity). By charge symmetry, u also gives the distribution of d quarks in the neutron, but we note in passing that there are reasons to doubt the accuracy of this for the valence d-quarks in the proton at the 5% level [20, 21].

The structure functions mentioned earlier are directly related to these distribution functions. For an electromagnetic probe one finds:

$$F_1(x)=\frac{1}{4}\sum_q e_q^2\left(q^\uparrow(x)+q^\downarrow(x)\right) \tag{2.8}$$

$$F_2(x)=2x\mathrm{F}_1(x) \tag{2.9}$$

$$g_1(x)=\frac{1}{2}\sum_q e_q^2\left(q^\uparrow(x)-q^\downarrow(x)\right) \tag{2.10}$$

with e_q the charge, in units of e, of the quark of flavor q. Eq. (2.9) is the Callan–Gross relation and relies on the partons having spin 1/2 and no transverse momentum (in the infinite momentum frame). In general we have

$$F_2 = 2xF_1 \frac{1+R}{1+2Mx/\nu} \tag{2.11}$$

where R is the ratio of cross-sections for absorbing a longitudinal photon to that for a transverse absorbing photon. Experimentally R is small [22] (≤ 0.1) for all x, for $Q^2 \leq 5$ GeV^2.

For neutrino scattering from an isoscalar target one finds

$$F_2^{(\bar{\nu})} = x\ (u + \bar{u} + d + \bar{d} + s + \bar{s})$$

which measures the total quark content of the proton. Even more important, by combining ν and $\bar{\nu}$ data one can measure the combination

$$F_3^{(\nu,\bar{\nu})} = (u - \bar{u} + d - \bar{d}) \tag{2.13}$$

which isolates the excess of quarks over antiquarks, i.e., the valence quark distribution of the nucleon. Clearly we would expect the sum rule (due to Gross and Llewellyn Smith)

$$\int_0^1 dx F_3^{(\nu,\bar{\nu})}(x) = 3 \tag{2.14}$$

to be obeyed. It will also be useful to define the nth moment of a structure function like xF_3, F_2 or xF_1, as, e.g.,

$$M_{3n} = \int_0^1 dx x^{n-2} [xF_3(x)] \tag{2.15}$$

2.1. Scaling Violations

It is clear from the analysis ofthe experimental data that even in the Bjorken region the structure functions have a weak Q^2-dependence, and therefore so do the distribution functions which we write as $q(x, Q^2)$. If one sticks to any one data set in order to (partially) avoid systematic errors, this variation of the structure functions (scaling violation) is essentially logarithmic. In order to understand it one must go beyond the naive parton model to QCD.

Suppose we assume that the wavefunction of the target has no high-momentum components (i.e., $p_T^2 \ll$ Q2). Then any Q^2-dependence can only come from the lepton–quark scattering process. Scaling results if the quark is treated as point-like and the trivial Q^2-dependence of the Mott cross-section is factored out. On the other hand, in an interaction field theory, the lepton–quark scattering amplitude will involve radiative corrections, some of which add coherently (e.g., wave function and vertex renormalization) while others are incoherent (e.g., bremsstrahlung). It is well known that such radiative processes lead to corrections which vary logarithmically with the appropriate cut-off scale — in this case Q^2 This is formally described using the operator product expansion and the renormalization group.

On the basis of the operator product expansion and the renormalization group one can show that the moments of the structure functions can be written as the product of a coefficient function C_n (which is independent of the target) and the matrix element of a local operator. In fact one finds that the Q^2 variation of the moments of the structure functions resides entirely in the coefficient functions which can be calculated by perturbative QCD.

To leading order one finds:

$$M\,(Q^2)=M_n\,(Q_0^2)\left(\frac{\alpha(Q^2)}{\alpha(Q_0^2)}\right)^{d_0^n} \qquad (2.16)$$

and hence for fixed Q_0^2 it is easily shown that

$$\ln M_n\,(Q^2)=\frac{d_0^n}{d_0^m}\ln M_m\,(Q^2)+\text{constant} \qquad (2.17)$$

so that a log–log plot of any two moments should be a straight line whose slope is predicted by QCD. (The power d_0^n is known as the anomalous dimension.)

All of the above discussion of Q^2 evolution applies only to the non-singlet structure functions like F3 which cannot involve gluons. The Q^2 evolution of singlet structure functions such as F_2 is more complicated because the quarks and gluon operators mix under QCD renormalization. While the corresponding analysis is not much more difficult (it involves a 2 × 2 matrix), it would divert us too much to explain it here. Instead we refer to the previously mentioned texts, e.g., there is a summary in Table 2 of the review by Altarelli [18].

Given an analytic continuation of a set of moments, $M_n(Q^2)$, there is a standard method for reconstructing the corresponding function — this is the inverse Mellin transform (IMT):

$$xF_3\,(x,Q^2)=\frac{1}{2\pi i}\int_{c-i\infty}^{c+i\infty} dn\,x^{1-n}M_{3n}\,(Q^2) \qquad (2.18)$$

where C is chosen so that the integral exists. If, as we explained above, the moments of the structure function can be written as a product of a coefficient function, Cn (Q2, μ2) with the target matrix element, $\langle N | O_n(\mu^2) | N \rangle$;

$$M_{2n}(Q^2) = C_n(Q^2,\mu^2)\, \langle N | O_n(\mu^2) | N \rangle \tag{2.19}$$

the inverse Mellin transform, xF3, is just a convolution of the IMT of C_n (denoted by C_3) and $\langle N | O_n | N \rangle$ (denoted F_3), viz:

$$xF_3(x,Q_2) = \int_x^1 \frac{dy}{y} C_3(x/y, Q^2, \mu^2)\,(yF_3(y,\mu^2)) \tag{2.20}$$

This is an extremely important result. In particular, C3 is totally independent of the structure of the target — a property known as factorization. Clearly if we can evaluate the structure function of the target at any renormalization scale μ_2, Eq. (2.20) allows us to calculate it at all higher values of W^2 Higher order QCD corrections do not alter this result in principle, they just make C_3 harder to compute. For this reason μ^2 cannot be too low.

2.2. Features of Nucleon Data

Current experiments at HERA are pushing back the kinematic boundaries within which the structure functions are known. For example, one can now reach values of x as low as $2-3 \times 10^{-5}$ at $Q2 \sim 2$ GeV^2, whereas fixed target experiments can only get to x of order 8 x 10–4 at very low Q2 (0.3 GeV2). Furthermore, the perturbative evolution of the structure functions can be followed to Q^2 as high as 10^3–10^5 GeV^2 at large x. For a summary of the present status of the HERA experiments we refer to the proceedings of the recent HERA Workshop on proton, photon and Pomeron structure [23] especially the review by Badelek *et al.* [24].

Since our main concern is not with the small x behavior, it is sufficient to view the data on a linear scale. Figure 2.1 summarizes an enormous amount of experimental work carried out over the last 20 years with muon and neutrino beams and illustrates some very important features.

First, we note that the anti-quark distribution, which is one half of the sea of virtual-pairs that one sees when looking deep into any hadron, is concentrated in the region below $x = 0.3$. In fact, $x\bar{q}(x)$ is typically parameterized as $(1-x)^\gamma$ (with γ= 7–9). Note that the sea quarks, q_s are usually defined to have the same shape as $\bar{q}$. On the other hand, there are suggestions that $s(x)$ may not have the same shape as $\bar{s}(x)$ [25, 26, 27] and this will be important to test. Later we shall explicitly review the evidence from NMC [11] and NA51 [28] that $\bar{d} > \bar{u}$ which leads to a violation of the Gottfried sum-rule. Finally, we note that

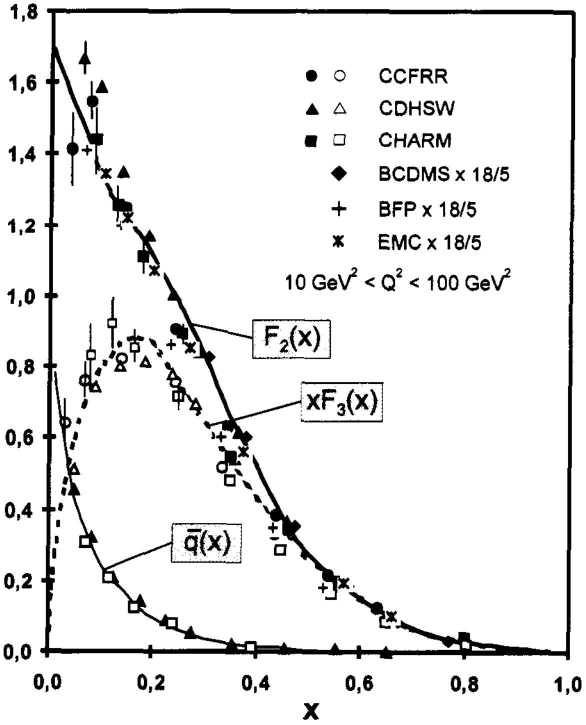

Fig. 2.1. Summary of structure function data taken with neutrinos and muons by various groups.

neutrino induced deep-inelastic scattering to di-muon final states can be used to check the relative strange versus non-strange sea. It seems that strangeness is suppressed for $Q^2 \sim$ 5–10 GeV^2, with [29]

$$\frac{2\bar{s}}{\bar{u}+\bar{d}} = 0.45 \pm 0.05$$

As the second feature of Fig. 2.1 we note that the valence quarks (recall Eq. (2.13)) dominate for x beyond 0.3. This is confirmed by the closeness of $xF3$ and $F_2^{\nu N}$ for $x \geq 0.3$, after allowing for the electromagnetic charges of the quarks $\left(\frac{5}{18} = 12\left(\frac{4}{9} + \frac{1}{9}\right)\right)$. In the early days of deep-inelastic scattering this provided vital confirmation that the partons of Feynman were, in fact, quarks.

The same counting rules (Drell–Yaw–West) which led one to expect the sea quark distributions to behave like $(1 - x)^7$ as $x \rightarrow 1$ suggest that the valence distributions should behave as, $qv\,(x) = x^{\alpha}\,(1 - x)^{\beta}$ with $\alpha = -0.5$ (from Regge theory) and β = 3. Of course, QCD evolution implies that α and β will also depend slowly on Q^2 and for recent parameterizations we refer to Badalek *et al.,* [24] and Martin, Stirling and Roberts [30]. The one feature worth noting about the fits discussed there is that they all assume $d_V/u_V \sim (1-x)$ and hence vanishes as $x \rightarrow 1$. Recent re-analysis of the binding and Fermi motion corrections in the deuteron suggest that this may not be correct [3 1] and that, in agreement with perturbative QCD [32], d/u may decrease like $(1-x)$ for x below 0.7 but tend to a constant as $x \rightarrow 1$. This needs further testing but one should keep this uncertainty in mind in situations where the actual d/u ratio is important.

3. SULLIVAN PROCESSES

The virtual meson-cloud of the nucleon plays an important role in the understanding of the nucleo–ucleon interaction [33] and the pion-cloud in particular has always been considered as crucial in understanding the nucleon's long-range structure. For example, it was recognized even in the 1950's that the process $n \rightarrow p\pi^-$ naturally explains the negative tail of the neutron's charge distribution. Furthermore, from PCAC, and the successes of chiral quark models [34, 35, 36, 37] we know that the nucleon has a pion cloud.

In 1972, Sullivan [6] showed that in deep-inelastic lepton scattering from a nucleon, the process in which the virtual photon strikes a pion from the meson cloud, and smashes the pion into debris, scales in the Bjorken limit. The reason for this is that, in contrast to processes such as exclusive pion-production, which are suppressed by form factors of the order $1/Q^2$, here the inelastic structure function of the pion itself is probed. The pion contribution to the structure function of the nucleon was investigated later [10] in connection with $SU(3)$-symmetry breaking in the quark sea content of the proton. Here it was also pointed out that the pion cloud could be responsible for generating an asymmetry between the $\bar{u}$ and $\bar{d}$ quark content, through the preferred proton dissociation into a neutron and π^+. Furthermore, DIS data on the momentum fraction carried by antiquarks were used to obtain an upper limit on this non-perturbative pionic component and therefore on the number of virtual pions in the nucleon [39, 50].

These early analyses came to the conclusion that the pionic component is small, which indicates that the pion–nucleon form factor has to be rather 'soft.' This finding was in strong contradiction with the 'hard' form factors which were used in meson-exchange potentials [33] at that time. As we will see in the following there is not much left from this controversy. Hwang *et al.* [40] pointed out that at moderate Q^2 the total quark sea, including strange quarks, could be connected with the meson cloud. Zoller [41] showed that the meson–baryon form factors which enter in the analysis of deep-inelastic processes are probed under similar kinematical conditions in semi-inclusive high energy proton–proton reactions. Holtmann *et al.* [27] extended the corresponding analysis to include not only pseudoscalar but also vector mesons. The form factors deduced from such combined analyses turned out to be a little harder than those in the initial investigations of the sea of the nucleons associated with pions only. On the other side it has been shown [42, 43, 44] that more sophisticated meson-exchange potentials can also reproduce the experimental nucleow–nucleon phase shifts with pion–nucleon form factors which are somewhat softer than those which were traditionally used in OBE potentials and are, in fact, close to those derived from DIS.

The concept of the pionic cloud may be extended by taking into account first of all the full pseudoscalar nonet and also the vector meson nonet. These mesons are not only crucial in meson-exchange potentials but it has been known for a long time that they give important contributions to low energy nucleon properties, such as the electromagnetic nucleon form factors or magnetic moments.

The one caution we should add, to which we return in Sec. 6, is that it is not established to what extent one can add incoherently the contributions from mesons of increasing mass. In principle there is the possibility of interference between terms where one reaches the same final state, X, from both $\gamma^* MB \rightarrow X$ and $\gamma^* M'b' \rightarrow X$. Indeed, as we shall see in Sec. 3.6 and 4.7, for spin-dependent structure functions we require some interference between the final states reached from $\gamma^* \pi N^\uparrow$ and $\gamma^* \pi \Delta^\uparrow$. We regard the resolution of this question as being essentially empirical, while noting that apart from the r-meson the heavier mesons play only a minor role.

3.1. The Convolution Model

The convolution model relies on the assumption that the nucleon wave function can be written as the following sum of Fock states

$$|N\rangle = \sqrt{Z}\,|N\rangle_{\text{bare}} + \sum_{MB} \int dy\, d^2\vec{k}_\perp\, \phi_{BM}\left(y, k_\perp^2\right) \left| B\left(y, \vec{k}_\perp\right); M\left(1-y, -\vec{k}_\perp\right)\right\rangle \tag{3.1}$$

where $\phi_{BM}\left(y, k_\perp^2\right)$ is the probability amplitude to find a physical nucleon in a state consisting of a virtual meson M and a virtual baryon B with longitudinal momentum fractions y and $1-y$ and transverse momenta $\vec{k}_\perp$ and $-\vec{k}_\perp$, respectively. Z is the standard wave function renormalization factor and can

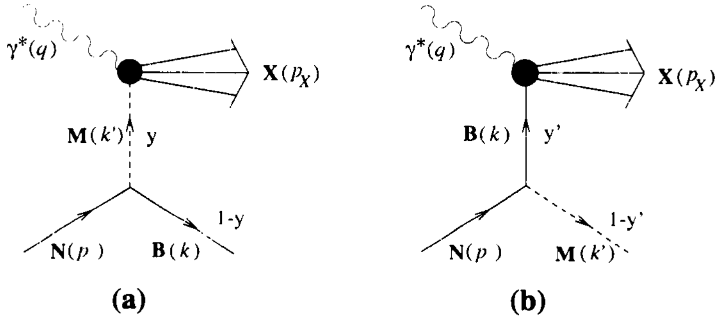

Fig. 3.1. DIS from the virtual (a) meson, and (b) baryon components of a physical nucleon.

be interpreted as the probability of finding a bare nucleon in the physical nucleon. In the following, we are concerned with first order corrections to the bare nucleon only. Preliminary calculations [41] suggest that higher order corrections are rather small provided that the form-factors used are not too hard. The infinite momentum frame (IMF) is particularly useful in the study of DIS phenomena. In the infinite momentum frame (i.e., $|\vec{p}| \rightarrow \infty$with $\vec{p}$ the nucleon momentum c.f. Sec. 2) the constituents of the nucleon can be assumed to be free during the DIS reaction time [45].

The basic hypothesis of the convolution approach is that there are no interactions among the particles in a multi-particle Fock state during the interaction with the hard photon in deep-inelastic scattering. This enables one to relate the contribution of a certain Fock state, BM, to the nucleon structure function *F2,* to the structure functions of either the struck meson *M* or the struck baryon B (see Fig. 3.1 a, b) using

$$\delta_M F_2^N(x) = \int_x^1 dy f_{MB/N}(y) F_2^M\left(\frac{x}{y}\right) \tag{3.2}$$

$$\delta_B F_2^N(x) = \int_x^1 dy f_{BM/N}(y) F_2^B\left(\frac{x}{y}\right) \tag{3.3}$$

or written in terms of quark distributions:

$$\delta q_N(x) = \int_x^1 f_{MB/N}(y) q_M\left(\frac{x}{y}\right)\frac{dy}{y} + \int_x^1 f_{BM/N}(y) q_B\left(\frac{x}{y}\right)\frac{dy}{y} \tag{3.4}$$

The main ingredients in these formulas are the splitting functions*fMB/N* (y) and $f_{BM/N}$ (y) which are related to the probability amplitudes ϕ_{BM} in the IMF via

$$f_{BM/N}(y) = \int_0^\infty dk_\perp^2 \, |\phi_{BM}(y, k_\perp^2)|^2 \tag{3.5}$$

$$f_{MB/N}(y) = \int_0^\infty dk_\perp^2 \, |\phi_{BM}(1-y, k_\perp^2)|^2 \tag{3.6}$$

Because the description of the nucleon as a sum of *MB* Fock states is independent of the DIS process, the relation

$$f_{MB/N}(y) = f_{BM/N}(1-y) \tag{3.7}$$

must hold. It simply expresses the fact that if a meson with longitudinal momentum fraction y is struck by the photon, the remaining part of the nucleon is a baryon with the remaining longitudinal momentum fraction, $1-y$. Moreover, this relation automatically ensures global charge conservation

$$\langle n \rangle_{MB} = \langle n \rangle_{BM} \tag{3.8}$$

with $\langle n \rangle_{MB} = \int_0^1 f_{MB/N}(y)\, dy$ and $\langle n \rangle_{BM} = \int_0^1 f_{BM/N}(y)\, dy$, and momentum conservation

$$\langle y \rangle_{MB} + \langle y \rangle_{BM} = \langle n \rangle_{MB} \tag{3.9}$$

where $\langle y \rangle_{MB} = \int_0^1 dy y f_{MB}(y)$ and $\langle y \rangle_{BM} = \int_0^1 dy y f_{BM}(y)$ are the average momentum fractions carried by meson M and the virtual baryon B, respectively. $\langle n \rangle$ and $\langle y \rangle$ are called the first and second moments of the splitting functions.

It should be noted that, because of the probabilistic interpretation of $|\phi_{MB}(y, k_\perp^2)|^2$, the wave function renormalization constant Z can be expressed as

$$Z = \left(1 + \sum_{MB} \langle n \rangle_{MB}\right)^{-1} \tag{3.10}$$

The quark distribution functions $qN(x)$ of a nucleon within the Fock state expansion are given as:

$$qN(x) = q_N^{\mathrm{bare}}(x) + \delta qN(x) \tag{3.11}$$

where $q_N^{\mathrm{bare}}(x)$ is the quark distribution of the "bare" nucleon (see Sec. 4.2).

In the following, we shall explicitly evaluate the splitting functions f_{MB} and f_{BM}, and examine the conditions under which Eq. (3.7) is fulfilled. The calculation can be performed in two different ways: (a) within the covariant perturbation theory developed by Feynman, Schwinger and Dyson, and (b) in time ordered perturbation theory (TOPT) in the infinite momentum frame, as developed by Weinberg and Drell, Levy and Yan [5,46]. In the first case relativistic covariance is explicitly fulfilled, but particles are not always on their mass shell. This is a severe drawback in DIS because one is forced to make assumptions about (or to model) [47] the off-mass shell behavior of the hadron structure functions and, in addition, the basic relation in Eq. (3.7) is not fulfilled without further assumptions. In TOPT manifest relativistic covariance is lost. However, Weinberg [46] and later Drell, Levy and Yan [5] have shown that by applying TOPT in the infinite-momentum frame (IMF) one can ensure Lorentz invariance with substantial calculational simplifications which make this method especially suited for DIS —as first pointed out by Bjorken [48].

In his pioneering work Sullivan [6] used covariant perturbation theory and so did everyone else until the early nineties, when new interest started in these processes, in connection with the violation of the Gottfiied sum-rule. Sullivan only considered the process shown in Fig. 3.1a, where the photon hits the pion. In order to conserve momentum and charge, one must also include the contribution shown in Fig. 3.1b where the photon hits the recoiling baryon after the meson is emitted. Previous treatments of this process in the covariant framework were made by several authors [38, 39, 40, 49, 50, 51, 52]. The results, however, were only in qualitative agreement with each other. The main reason was that different procedures were used to fulfill the conservation laws. Moreover, the whole approach was questioned because of the unknown off-mass-shell behavior of the hadron [47]. For all these reasons, in the more recent work [27, 41, 53] the formalism of TOPT was used in the infinite momentum frame, where these drawbacks do not exist. A review of the covariant formulation and its various problems can be found in Ref. [54]. In the following, we will concentrate on the calculation of various splitting functions within TOPT in the IMF.

3.2. Calculation of the Probability Amplitudes ϕ_{BM} in TOPT

The main virtues of this formulation are that off-mass-shell ambiguities in the structure functions of virtual particles can be avoided, and that the meson and baryon splitting functions satisfy Eq. (3.7) exactly.

In TOPT the analogue of Fig. 3.1a involves two diagrams, as shown in Fig. 3.2, where the meson moves forward and backward in time, respectively. The advantage of the infinite momentum frame (IMF), where the target nucleon is moving fast in the z direction (with longitudinal momentum $|\vec{p}| = p_z \rightarrow \infty$), is that only diagrams involving forward moving mesons have to be considered.

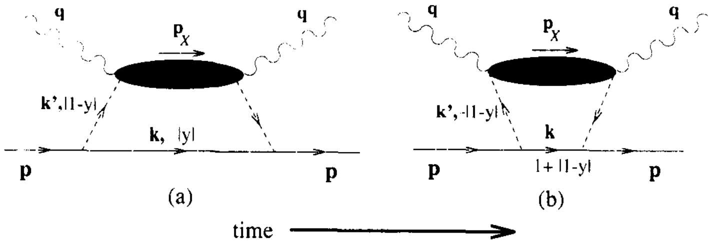

Fig. 3.2. Time-ordered diagrams moving (a) forwards, and (b) backwards in time. Time is increasing from left to right.

Diagrams with backward moving particles give no contributions in the limit $p_z \to \infty$

The essential ingredients in the convolution model are the probability amplitudes $\phi_{BM}(y, k_\perp^2)$. In TOPT in the IMF one is able to write down explicitly the intermediate Fock states

$$\phi_{BM}\left(\vec{p},\vec{k},\vec{k}' = \vec{p}-\vec{k}\right) = N_N \frac{N_B}{(2\pi)^{\frac{3}{2}}} \frac{N_M}{(2\pi)^{\frac{3}{2}}} \frac{V\left(\vec{p},\vec{k},\vec{p}-\vec{k}\right)}{E_N - E_M - E_B} \tag{3.12}$$

This formula gives the probability amplitude of finding a nucleon with momentum $\vec{p}$ in a Fock state where the baryon B has momentum $\vec{k}$ and the meson M momentum $\vec{k}' = \vec{p} - \vec{k}$. The factors $(2p)^{\frac{3}{2}}$ come in because we are working in momentum representation. The factors N_N (N_B) are the usual fermion wave function normalization factors, $N_N = \sqrt{m_N/E_N}$, $N_B = \sqrt{m_B/E_B}$; N_M is a bosonic normalization factor, $N_M = 1/\sqrt{2E_M}$. The important feature of TOPT is, in contrast to the covariant perturbation theory, that the intermediate particles are on their mass-shell, i.e., their energies are given by

$$E_N = \sqrt{m_N^2 + \vec{p}^2}, E_B = \sqrt{m_B^2 + \vec{k}^2}, E_M = \sqrt{m_M^2 + \vec{k}'^2} \tag{3.13}$$

Therefore, one can calculate the vertex function V in Eq. (3.12) because one can use on-mass shell wave functions. V depends on a particular model, i.e., on the form of the Lagrangian used. In general V can be written as

$$V\left(\vec{p},\vec{k},\vec{k}'\right) = \bar{u}_N(\vec{p})_\alpha \, v^{\alpha\beta\gamma} \chi_\beta\left(\vec{k}'\right) \Psi_\gamma\left(\vec{k}\right) \tag{3.14}$$

where summing and averaging over all possible spin-states is implicity assumed. α, β and γ are bi-spinor and/or vector indices dependent on the representation used for particles of a given type. X and Ψ are the wave functions (field operators) of the intermediate meson and baryon, respectively.

It has been shown [5] for the πN case, that in the infinite momentum limit contributions of Fock states with anti-particles vanish and only contributions with (forward moving) particles survive if appropriate form factors are introduced. This statement is also true for the other Fock states with which we deal. In the IMF the momenta of the particles involved can be parametrized in terms of y and $\vec{k}_\perp$:

$$\vec{k} = y\vec{p} + \vec{k}_\perp, \quad \vec{k}_\perp \cdot \vec{p} = 0, \quad \vec{k}' = (1-y)\vec{p} - \vec{k}_\perp \tag{3.15}$$

Thus, in the limit $p = |\vec{p}| \to \infty$

$$E_N = p + \frac{m_N^2}{2p}, \; E_B = |y|p + \frac{m_B^2 + k_\perp^2}{2|y|p}, \; E_M = |1-y|p + \frac{m_M^2 + k_\perp^2}{2|1-y|p} \tag{3.16}$$

and the energy denominator becomes:

$$E_N - E_B - E_M = \begin{cases} 2yp + O\left(\frac{1}{p}\right) & \text{for } y < 0 \\ 2(1-y)p + O(\frac{1}{p}) & \text{for } y > 1 \\ \frac{1}{2p}(m_N^2 - M_{BM}^2(y, k_\perp^2)) + O(\frac{1}{p^2}) & \text{for } y \in [0,1] \end{cases} \tag{3.17}$$

where $M_{BM}^2\left(y, k_\perp^2\right)$ is the invariant mass squared of the intermediate BM Fock state

$$M_{BM}^2\left(y, k_\perp^2\right) = \frac{m_B^2 + k_\perp^2}{y} + \frac{m_M^2 + k_\perp^2}{1-y} \tag{3.18}$$

Only states with $y \in [0,1]$ survive in the IMF-limit. In this limit the probability amplitudes can be expressed as

$$\phi_{BM}\left(y, k_\perp^2\right) = \frac{\sqrt{m_N m_B}\, V_{\mathrm{IMF}}\left(y, k_\perp^2\right)}{2\pi\sqrt{y(1-y)}\left(m_N^2 - M_{BM}^2\left(y, k_\perp^2\right)\right)} \tag{3.19}$$

with V_{IMF} being the vertex-function in the IMF-limit. In the formula above an extra factor $(\pi p)^{-1/2}$ has been taken out. It would cancel when going to probability densities by an appropriate factor of the Jacobian of the transformation Eq. (3.15).

Formula (3.19) can be used to calculate $\phi_{BM}\left(y, k_\perp^2\right)$ for all cases of interest — see Refs. [27, 41, 54, 55]. Using TOPT this way has one disadvantage in comparison with the typical calculation involving traces: one has to calculate VIMF for every spin configuration and calculate the spin average afterwards. On the other hand this turns out to be most useful for polarized DIS, as we will see in Sec. 4.5.

3.3. Meson–Baryon Form Factors

The symmetry given by Eq. (3.7) is automatically fulfilled for vertices involving point-like particles. Because of the extended structure of the hadrons involved one has to introduce phenomenological vertex form factors, which parametrize the unknown microscopic effects. It is interesting to mention that Drell *et al.* [5] also had to introduce cut-offs in the transverse-momentum $k_\perp^2$, when they derived the parton model for deep-inelastic electron scattering within the same formalism. For these reasons, the vertex function, $V(y,k_\perp^2)$, should be replaced by $V'(y,k_\perp^2) = G(y,k_\perp^2)\,V(y,k_\perp^2)$. Equation (3.7) now imposes a severe restriction on these form factors:

$$G_{BM}(y,k_\perp^2) = G_{MB}(1-y,k_\perp^2) \tag{3.20}$$

The form factors often used in meson exchange models and convolution models are functions of t only, the four-momentum squared of the meson, and do not satisfy Eq. (3.20). In terms of the IMF variables y and $k_\perp^2$, t is given by (for comparison we also write down u, the four-momentum squared of the intermediate baryon)

$$t = \frac{k_\perp^2}{y} - (1-y)\left(\frac{m_B^2}{y} - m_N^2\right) \tag{3.21}$$

$$u = \frac{k_\perp^2}{1-y} - y\left(\frac{m_M^2}{1-y} - m_N^2\right) \tag{3.22}$$

Thus, form factors depending on t only, like the dipole form factor

$$G(t) = \left(\frac{\Lambda^2 - m_M^2}{\Lambda^2 - t}\right)^2 \tag{3.23}$$

are ill-defined for the convolution models. They do not conserve basic quantities like charge and momentum. One simple method to obtain form factors with the right symmetry is to multiply a t-dependent form factor by a u-dependent one with the same functional form, with m'M replaced by mB

$$G_{\mathrm{sym}}(t,u) = G(t,m_{\mathrm{M}})\,G(u,m_{\mathrm{B}}) \tag{3.24}$$

The importance of using such symmetric form factors was noticed only recently [41, 55]. Another possible approach, namely to fix the cut-off parameters to assure number sum rules (global charge conservation) (see [56, 57]), is somewhat arbitrary, and does not guarantee momentum conservation, and gives rise to very different functional behavior of $f_{N\pi}(y)$ and $f_{\pi N}(1-y)$.

In recent publications dipole parametrizations [54]

$$G_{NBM}(y,k_\perp^2) = \left(\frac{\Lambda^2 + m_N^2}{\Lambda^2 + M_{BM}^2(y,k_\perp^2)}\right)^2 \tag{3.25a}$$

and exponential forms [27,41,55] have been used

$$G_{NBM}(y,k_\perp^2) = \exp\left(\frac{m_N^2 - M_{BM}^2(y,k_\perp^2)}{2\Lambda^2}\right) \tag{3.25b}$$

with the invariant mass, M_{BM}^2, defined in Eq. (3.18). Using Eqs. (3.21) and (3.22) one can show, that the exponential form given in Eq. (3.25b) is equivalent to the symmetrized form

$$G_{NBM}(t,u) = \exp\left(\frac{t - m_M^2}{2\Lambda^2}\right)\exp\left(\frac{u - m_B^2}{2\Lambda^2}\right) \tag{3.2c}$$

3.4. Spin-Averaged Splitting Functions

Equations (3.5) and (3.19) allow one to write the spin-averaged splitting functions as:

$$f_{BM/N}(y,k_\perp^2) = \frac{1}{4\pi^2}\frac{m_N m_B}{y(1-y)}\frac{|V_{\mathrm{IMF}}|^2}{[m_N^2 - M_{BM}^2(y,k_\perp^2)]^2} \tag{3.26}$$

where the vertex functions define the model. The vertex functions for the Lagrangians listed in Appendix A are given in Appendix B. For the $N\pi$ and $\Delta\pi$ Fock states we find:

$$f_{N\pi/N}(y) = \frac{g^2}{16\pi^2}\frac{1}{y^2(1-y)}\int_0^\infty dk_\perp^2\,|G_{N\pi}(y,k_\perp^2)|^2\,\frac{m_N^2(1-y)^2 + k_\perp^2}{[m_N^2 - M_{N\pi}^2(y,k_\perp^2)]^2} \tag{3.27}$$

$$f_{\Delta\pi/N}(y)=\frac{f^2}{96\pi^2 m_\Delta^2}\frac{1}{y^4(1-y)}\int_0^\infty dk_\perp^2\,|G_{\Delta\pi}(y,k_\perp^2)|^2 \times\frac{\left[(m_\Delta+ym_N)^2+k_\perp^2\right]^2\left[(m_\Delta-ym_N)^2+k_\perp^2\right]}{\left[m_N^2-M_{\Delta\pi}^2(y,k_\perp^2)\right]^2} \tag{3.28a}$$

and finally for the vector mesons:

$$f_{NV/N}(y)=\frac{3}{16\pi^2}\int_0^\infty dk_\perp^2\frac{|G_{NV}^2(y,k_\perp^2)|}{\left[m_N^2-M_{NV}^2(y,k_\perp^2)\right]^2}\Bigg\{ \left[\frac{\left[k_\perp^2+(1-y)^2m_N^2-ym_V^2\right]^2+2m_v^2\left[(1+y^2)k_\perp^2+(1-y)^4m_N^2\right]}{y^2(1-y)^3m_v^2}\right]$$

$$+f_{VNN}^2\frac{1}{y^4(1-y)^3m_v^2} \times\Big[\left[k_\perp^2+(1-y)^2m_N^2-ym_v^2\right]^2\left[(1-y)^4m_N^2+(1+y)^2k_\perp^2\right] +16y^2m_v^2\left[k_\perp^4+3m_N^2(1-y)^2k_\perp^2+2(1-y)^4m_N^4\right]\Big] \tag{3.28b}$$

+gvNNf VNN mN

$$\times\left[\frac{\left[k_\perp^2+(1-y)^2m_N^2-ym_V^2\right]^2-8ym_V^2\left[k_\perp^2+(1-y)^2m_N^2\right]}{y^3(1-y)m_v^2}\right]\Bigg\}$$

As examples of the various splitting functions we show $f_{N\pi}$, $f_{\Delta\pi}$ and f_{Np} in Fig. 3.3 [58]. TOPT and a cut-off deduced from high-energy scattering data have been used with parameters given in Sec. 4.1. The ρ*N*-splitting function peaks at larger y compared to the π*N* because the heavier r-meson carries more momentum. On the other hand the πΔ-splitting function peaks at somewhat lower y compared with the π*N* case-because the Δ is slightly heavier than the nucleon.

The results obtained by means of TOPT in the IMF are exactly the same as those derived with covariant perturbation theory. However, in TOPT it is natural to use form factors which depend on $k_\perp^2$ and therefore implicitly on t and u, whereas in covariant perturbation theory the natural choice are form factors which depend on *t* only. This is incorrect, as mentioned before. After transforming variables $(y,k_\perp^2)\rightarrow(u,t)$ [Eqs. (3.21) and (3.22)] one obtains the

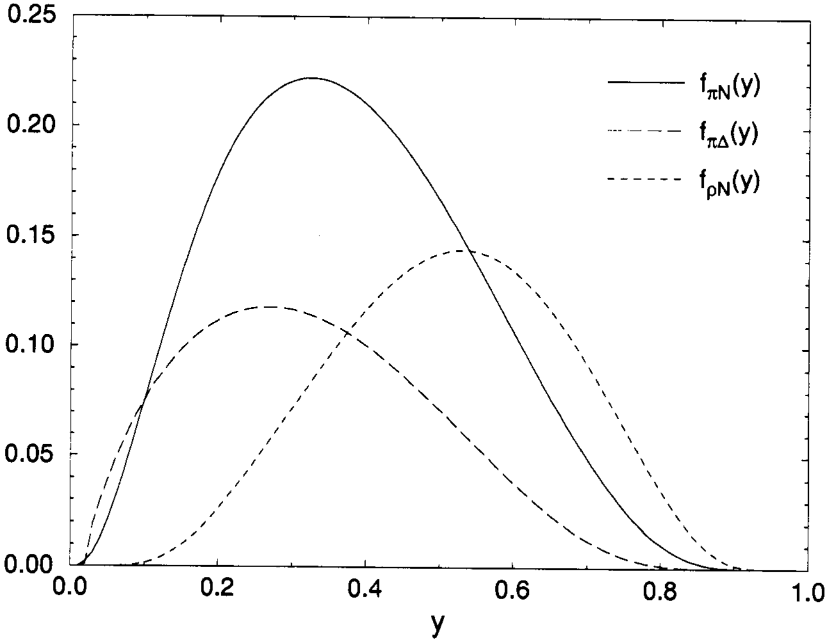

Fig. 3.3. Various splitting functions obtained by means of TOPT in the infinite momentum frame [58].

standard results for $N\pi$ [6, 50, 52, 57] and Dρ [50, 52] contributions. This should be the case, because TOPT is just a different way to calculate diagrams. There is, however, one point which requires a separate discussion in the next section.

3.5. TOPT versus Covariant Perturbation Theory

If the vertex functions used contain a derivative of the meson field, care must be taken or one will find differences between TOPT and covariant perturbation theory. To illustrate this point let us consider the example of the pseudovector $N\pi N$ vertex, given by

$$L_P V = \bar{u}\,\gamma_5\gamma^\mu\,\partial_\mu\pi u \tag{3.29}$$

where for simplicity the coupling constant and isospin structure have been suppressed. The standard covariant techniques lead to the splitting function of the meson

$$f_{MB/N}^{pV}(y) = \frac{1}{16\pi^2}\frac{1}{(1-y)^2 y}\int_0^\infty dk_\perp^2 \left|G\left(1-y,k_\perp^2\right)\right|^2 \times \frac{(m_B+m_N)^2\left[(m_N(1-y)-m_B)^2+k_\perp^2\right]}{\left[m_N^2-M_{BM}^2\left(1-y,k_\perp^2\right)\right]^2} \tag{3.30}$$

The result for the baryon is:

$$\begin{aligned} f_{BM/N}^{pV}(y) = {} & \frac{1}{16\pi^2}\frac{1}{(1-y)^2 y}\int_0^\infty dk_\perp^2 \left|G\left(y,k_\perp^2\right)\right|^2 \\ & \times \left(m_N^2 m_B^2 (1-y)^2 + k_\perp^2 (m_B+m_N)^2 \right. \\ & \left. -2m_N m_B \left(y m_M^2 + k_\perp^2\right) + \frac{1}{(1-y)^2}\left(y m_M + k_\perp^2\right)^2 \right) \\ & \times \frac{1}{\left[m_N^2 - M_{BM}^2\left(y,k_\perp^2\right)\right]^2} \end{aligned} \tag{3.31}$$

Here as mentioned before the two results are not related by Eq. (3.7), which leads to a violation of charge- and momentum conservation. The reason for this puzzle is that by using a derivative coupling, an additional off-shell dependence is introduced into the vertex function, which cannot be suppressed in the IMF-limit. A way out is to use TOPT [41, 55]. Here, however, the problem arises how to choose the meson energy in the vertex. In principle, there are two possible prescriptions:

A) One uses the meson four-momentum k_μ : $\bar{u}_N \gamma_5 \gamma_\mu (-i) k'^\mu u_B$ in the vertex, i.e., the meson energy in the vertex is E_M [Eq. (3.16)]. With this form of the vertex one reproduces the baryon splitting function given by Eq. (3.31). The meson splitting function is related to this result by Eq. (3.7).

B) Instead of k'^μ one uses the difference of the baryon four-momenta $p^\mu - k_\mu$: $\bar{u}_N (p) \gamma_5 \gamma_\mu (-i) (p-k)^\mu u_B (k)$, i.e., the meson energy in the vertex is $E_N - E_B$. With this prescription one gets the meson splitting function given by Eq. (3.30). Again the corresponding result for the baryon splitting function fulfills Eq. (3.7).

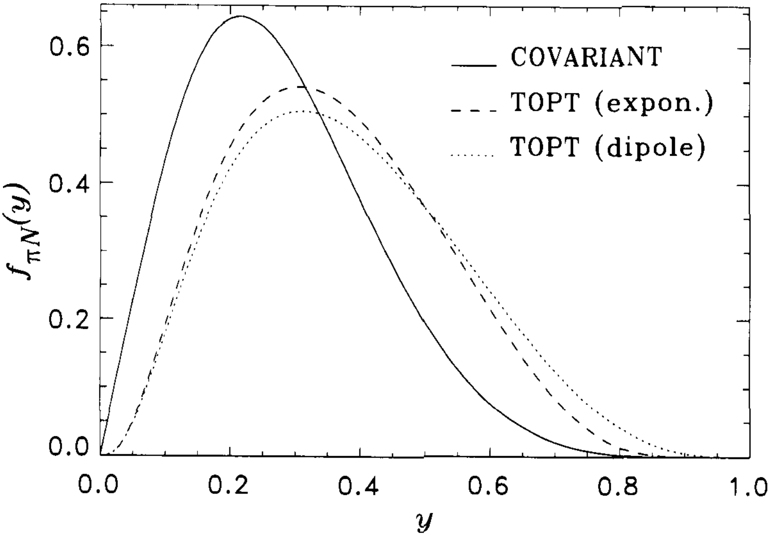

Fig. 3.4. Splitting functions $f_{\pi N}(y)$ evaluated using Covariant and time-ordered perturbation theory. The covariant function is as Fig. 3.5. The cut-offs in the form factors are chosen to give the same value for $\langle n \rangle_{\pi N} = 0.235$ [54].

Thus TOPT, in contrast to a covariant calculation, is consistent with the convolution approach. The remaining point to clarify is which one of the two prescriptions one should use. The natural choice is prescription *B,* because in this prescription the splitting functions for the pseudovector case are identical to those of the pseudoscalar case, if the coupling constants are identified properly. Moreover, in this prescription the structure of the vertex is due to the baryonic current only.

In Fig. 3.4 a comparison is made between the splitting functions $f_{\pi N}(y)$, calculated in covariant and time-ordered perturbation theory, respectively. While the dependence on the functional form of the form factor within TOPT is weak, the results obtained with the two different formalisms deviate appreciably. Even more severe is the violation of the basic symmetry, $f_{\pi N}(y) = f_{N\pi}(1-y)$, in the covariant formalism. Whereas it is automatically fulfilled in TOPT, the two functions, shown in Fig. 3.5, do not have this symmetry at all — the most obvious difference being that $f_{N\pi}(1-y)$ is finite at $y = 1$.

One should bear this result in mind if one calculates semi-exclusive reactions like deep-inelastic electroproduction of neutrons, from which one aims to measure the pion structure function at small x. As 3-momenta are not conserved

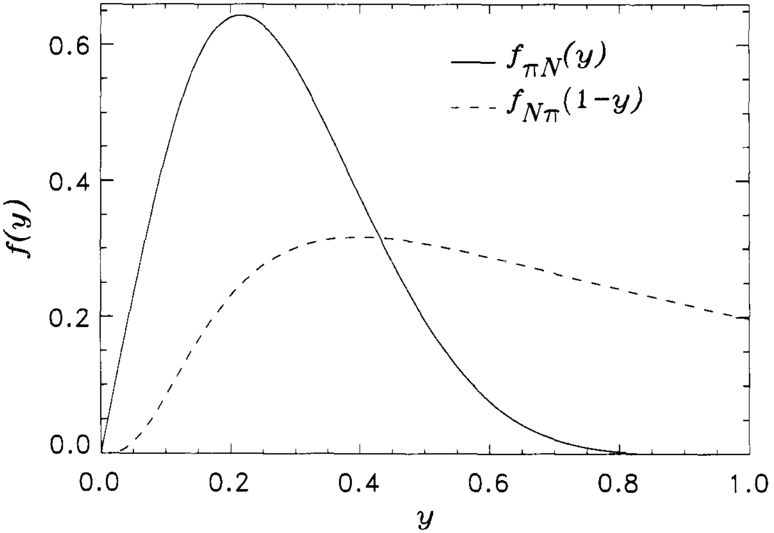

Fig. 3.5. Splitting functions $f_{\pi N}(y)$ and $f_{N\pi}(1-y)$ with dipole form factors and cut-offs chosen to give $\langle n\rangle_{\pi N} = \langle n\rangle_{N\pi} = 0.235$ [54].

in the splitting function, if calculated in the covariant formalism, the neutron- and pion-momentum are not connected with each other, as discussed above.

3.6. Polarized Splitting Functions

The same approach is convenient for the extension to deep-inelastic scattering of polarized particles [27,59]. Let us introduce the probability amplitudes $\phi_{BM}^{\lambda\lambda'}(y, k_\perp^2)$, which describe a nucleon with positive helicity (+ 1/2), being in a Fock state *BM* with baryon helicity A and meson helicity λ'. To calculate $\phi_{BM}^{\lambda\lambda'}(y,k_\perp^2)$, Eq. (3.19) can be used with the spin-averaged vertex.function VIMF replaced by an appropriate helicity dependent one $V_{\mathrm{IMF}}^{\lambda\lambda'}$ (see Appendix B). By analogy with the spin-averaged splitting function [see Eqs. (3.5) and (3.6)] we introduce the polarized splitting fuctions $f_{BM/N}^{\lambda}(y)$ and $f_{MB/N}^{\lambda'}(y)$, which we define as

$$f_{BM/N}^{\lambda}(y) = \sum_{\lambda'} \int_0^\infty dk_\perp^2 \left|\phi_{BM}^{\lambda\lambda'}(y,k_\perp^2)\right|^2 \tag{3.32}$$

$$f_{MB/N}^{\lambda'}(y) = \sum_{\lambda'} \int_0^\infty dk_\perp^2 \left|\phi_{BM}^{\lambda\lambda'}(1-y,k_\perp^2)\right|^2 \tag{3.33}$$

For simplicity, let us specialize our discussion to the $N\pi$ case and use the more suggestive notation $f^{\uparrow}(y) = f^{+1/2}_{N\pi/N}(y)$ and $f^{\downarrow}(y) = f^{-1/2}_{N\pi/N}(y)$. Applying the idea of the convolution model to the polarized quark distributions $q^{\uparrow}(x)$, $q^{\downarrow}(x)$ (the quark distribution of quarks with flavor q and spin parallel or antiparallel to the nucleon spin) leads to the following relations:

$$\delta q_N^{\uparrow}(x) = \int_x^1 f^{\uparrow}(y)\, q_B^{\uparrow}\left(\frac{x}{y}\right)\frac{dy}{y} + \int_x^1 f^{\downarrow}(y)\, q_B^{\downarrow}\left(\frac{x}{y}\right)\frac{dy}{y} \tag{3.34}$$

$$\delta q_N^{\downarrow}(x) = \int_x^1 f^{\uparrow}(y)\, q_B^{\downarrow}\left(\frac{x}{y}\right)\frac{dy}{y} + \int_x^1 f^{\downarrow}(y)\, q_B^{\uparrow}\left(\frac{x}{y}\right)\frac{dy}{y} \tag{3.35}$$

Taking the sum and the difference gives:

$$\delta q_N(x) = \int_x^1 f(y)\, q_B\left(\frac{x}{y}\right)\frac{dy}{y} \tag{3.36}$$

$$\delta \Delta q_N(\mathrm{x}) = \int_x^1 \Delta f(y)\, \Delta q_B\left(\frac{x}{y}\right)\frac{dy}{y} \tag{3.37}$$

with $\Delta q(x) = q^{\uparrow}(x) - q^{\downarrow}(x)$. Here $f(y)$, the splitting function for the unpolarized (spin averaged) case, is given by the sum of $f^{\uparrow}(y)$ and $f^{\downarrow}$ (y);$\Delta f(y)$, the splitting function for the polarized case, by the difference. It is important to note, that the splitting functions $f^{\uparrow}(y)$ and $f^{\downarrow}(y)$ are independent of each other [59], i.e., there are no simple relations, like Clebsch–Gordan coefficients between them.

As an example, we show in Fig. 3.6 the corresponding splitting functions for the $N\pi$ Fock component. As seen from the figure the non-spin-flip (dashed line) and the spin-flip (dotted line) contributions are different. The spin-flip contribution dominates at large momentum fraction of the nucleon [59]. The spin-flip contribution is totally due to the presence of perpendicular momentum in the pion–nucleon wave function. This explains the sensitivity of the spin-flip splitting function to the cut-off parameter of the vertex form factor. It also leads to a similar sensitivity of the polarized splitting function $\Delta f = f^{\uparrow} - f^{\downarrow}$ (dash-dotted line). Here, if integrated over y, the spin-flip and non-spin-flip contributions almost cancel each other. There is no deep reason for this cancellation; it is rather the consequence of the cut-off parameter choice. In the present calculation, the cut-off parameter ($\Lambda = 1.08$ GeV) has been adjusted to the neutron production data (see Sec. 4.10. This cancellation has consequences for the spin content of the nucleon as we will discuss in Sec. 4.7.

Similar formulas can be derived analogously for other Fock states. For particles with higher spin addition assumptions have to be made. For example, in the $\Delta\pi$ case one has to distinguish between the $q^{\uparrow}(x)$ distributions in a Δ

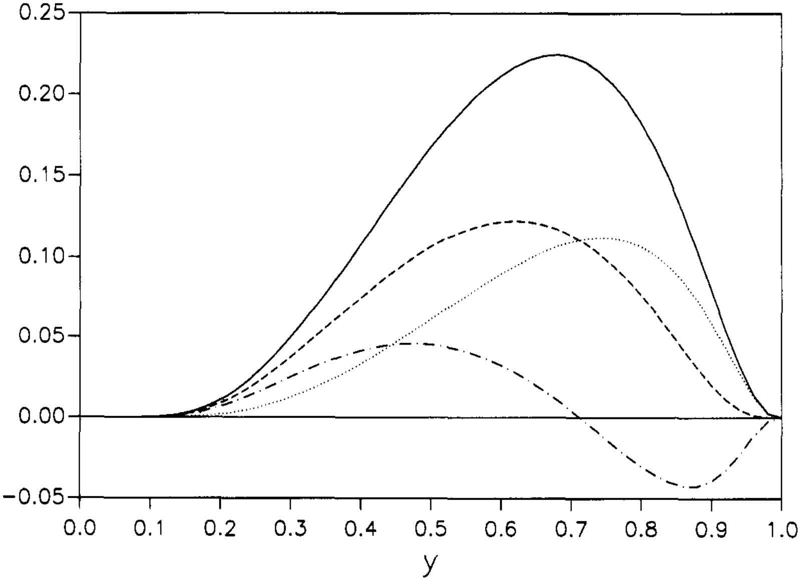

Fig. 3.6. The splitting functions $f_{p\pi^0/p}(y)$ (solid), $\Delta f_{p\pi^0/p}(y)$ (dash dotted), $^{+1/2}_{,\pi^0/p}(y)$ (dashed) and $f_{p\pi^0/p}(y)$ (dotted) with a cut-off parameter of $\Lambda = 1.08$ GeV, [55].

with helicity 1/2 and the similar distribution (we call it $q^{\Uparrow}(x)$) in a Δ with helicity 3/ 2. Assuming the relation $q^{\Uparrow}(x) = 3q^{\uparrow}(x)$ for the bare Δ, which can be easily checked using $SU(6)$ symmetry, it is possible to obtain an equation similar to Eq. (3.27).

In the most general case, assuming that the polarized quark distribution of different helicity states are the same (except helicity factors) one gets:

$$\begin{aligned}\delta\Delta q_N(x) = &\int_x^1 \Delta f_{BM/N}(y)\,\Delta q_B\left(\frac{x}{y}\right)\frac{dy}{y}\\ &+\int_x^1 \Delta f_{MB/N}(y)\,\Delta q_M\left(\frac{x}{y}\right)\frac{dy}{y}\\ &+\int_x^1 \Delta f_{(B'B)M/N}(y)\,\Delta q_{BB'}\left(\frac{x}{y}\right)\frac{dy}{y}\\ &+\int_x^1 \Delta f_{B(MM')}(y)\,\Delta q_{MM'}\left(\frac{x}{y}\right)\frac{dy}{y}\end{aligned} \tag{3.38}$$

with

$$\Delta f_{XY/N}(\mathrm{y}) = \sum_{\lambda} 2\lambda f^{\lambda}_{XY/N}(y) \tag{3.39}$$

where the sum runs over all possible helicities of particle X.

From our experience with the calculation of axial coupling constants (c.f. Sec. 4.7), it is vital to include terms in which (e.g.) the polarized-photon–N interaction leads to the same final states as the polarized-photow–Δ interaction [27, 59, 60, 61]. Indeed, this is precisely the reason that perturbation theory works so well when one carries through the renormalization program in the cloudy bag model [35, 36]. These cross terms for baryons and mesons are, respectively, the third and fourth terms on the rhs of Eq. (3.38).

The formalism outlined here has been applied to the semi-leptonic decay and the "missing" spin of the nucleon.

4. MESON CLOUD AND THE NON-PERTURBATIVE SEA

There exist numerous attempts to link quark models with DIS. The main idea behind such approaches is that the QCD evolution implies a decreasing number of sea-quarks (i.e., virtual $q\bar{q}$-pairs) as the momentum scale, Q^2, decreases. Since most quark models involve three valence quarks (sometimes a small $q\bar{q}$-admixture is also considered), one would expect the model to relate to DIS at some low momentum scale, $Q_2 = Q_0^2$ [62, 63]. There has been considerable success in reproducing the experimental data [61, 64, 65, 66]. However, two important points have to be borne in mind: (i) The evolution equation is first or second order in the running coupling constant and one must therefore worry about applying it below 1 (GeV/c)^2. We note, however, that the agreement between calculations using leading order and next to leading order evolution is very close; (ii) In addition, many of the early calculations did not respect chiral symmetry. That is, no quark model can be consistent with the known symmetries of QCD unless pions are included. Since, as we have seen, pions contain a valence $q\bar{q}$ pair, this pion cloud necessarily constitutes a sea of $q\bar{q}$ pairs in the nucleon.

Thomas [10], and some years later Frankfurt *et al.* [39], used the fact that this pion contribution breaks the $SU(3)$-flavor symmetry of the sea distribution to put a limit on the hardness of the pNN form factor which controls the pion emission — see Eq. (3.27). In Thomas' case the limit is such that a chiral bag radius cannot be too small, say $R = 0.87 \pm 0.10$ fm. In Ref. [39] the $\pi N\Delta$ coupling was also taken into account. In that case the bag radius had to be larger than 1 fm. Frankfurt *et al.*, also concluded that meson-exchange models for the *NN*-interaction are "not well justified on the microscopic level." In both calculations only the *SU*(3) breaking part of the proton sea, i.e., $x\left(\frac{\bar{u}(x)+\bar{d}(x)}{2} - \bar{s}(x)\right)$ was attributed to the $\bar{q}q$-contribution of the pion. Hwang, Speth and Brown [40] took a different point of view: they suggested that at moderate momentum transfer a significant fraction of the proton $\bar{q}q$ sea could be due to the non-perturbative meson contribution. (They also included *K* and *K** mesons.) In that case, the amount of $\bar{u}, \bar{d}$-antiquarks which are due to mesons can be somewhat larger, pushing the allowed cut-off towards 1 GeV. In a recent publication Koepf, Frankfurt and Strikman [119] came to similar conclusions. (Note that they used covariant perturbation theory which suffers from the problems discussed in Chapter 3.) In the past few years, the *πNN* form factor used in meson-exchange potentials has been better understood [67] and meson-exchange potentials with much softer *πNN* form factors have been constructed [68, 69]. Therefore one may conclude that there is no longer any inconsistency disagreement between meson-exchange models and DIS.

The Jülich group [27, 58] has placed considerable importance on using, in Eqs. (3.27)–(3.28b), meson–baryon vertices which are derived from other experimental data — like semi-inclusive neutron production in high-energy proton–proton collisions. They calculated the corresponding meson contributions to the proton and neutron sea-quark distributions using the experimentally known pion structure function. Moreover, it has been shown that this process can also be reversed; if the *πNN* vertex is known, one can obtain from semi-exclusive deep-inelastic scattering processes, the pion structure function down to very small *x,* which will allow one to extract the sea-quark structure function of the pion [70]. In the following, we will discuss this point of view in more detail.

4.1. Meson–Baryon Form Factors derived from Semi-Inclusive *pp-Reactions*

The functional form of the form factors used in deep-inelastic scattering is the same as the form used in meson-exchange *NN* potentials: (a) monopole- and dipole-form as used in the Bonn-potential [33]; (b) Gaussian form as used by the Nijmegen-group [71]. The following analyses by Holtmann *et al.* [27] have been performed with a Gaussian form factor, as given in Eq. (3.25b), where Λ is the inverse of a radius. In some models, like the cloudy bag, the radius is connected with the confining region of the valence quarks [35]. In other models this connection with the confining region is not so obvious.

In order to fix the cut-off parameters, Λ, of the form factors, the authors of Ref. [27] used high-energy particle production data. They included in their

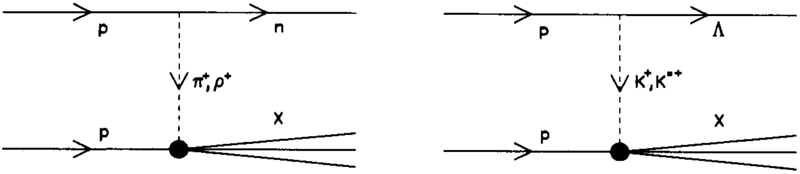

Fig. 4.1. One-Boson-Exchange diagrams for *n* and Λ production.

model the pseudoscalar and vector meson octet. A similar analysis, including the pseudoscalar mesons only, was first performed by Zoller [41]. The neutron and Lambda production data in the reactions $pp \to nX$ and pp $\to \Lambda X$ seems to be best tailored for extracting the cut-off parameters for the $N\pi$ and $N\rho$ as well as for the ΛK and ΛK^* Fock space components. If one restricts the analysis to data with relatively low exchanged four-momenta it is reasonable to assume that the neutron and the Lambda are produced by a simple one-boson-exchange mechanism (OBE) as shown in Fig. 4.1. In complete analogy to modern meson-exchange potentials one also assumes non-Reggeized mesons. Therefore, the region $y \to 0$ and $(1 - y) \to 0$ should not be considered. Fortunately, neither of these regions is important for evaluating the splitting functions. In the OBE approximation the invariant cross section for $pp \to BX$ production has the form:

$$\begin{aligned} E\frac{d^3\sigma(pp \to BX)}{d^3p} &= \frac{y}{\pi}\frac{d^2\sigma}{dy\, dk_\perp^2} \\ &= |\phi_{BM}(y,k_\perp)|^2 \cdot \sigma_{\mathrm{tot}}^{Mp}(s(1-y)) \end{aligned} \tag{4.1}$$

The probability amplitudes, ϕ_{BM}, are defined in Eq. (3.19), where y is the longitudinal momentum fraction of the baryon with respect to the momentum of the incoming proton and $k_\perp$ the corresponding transverse momentum. Moreover $\sigma_{\mathrm{tot}}^{Mp}$ is the total meson–proton scattering cross section. For πp and Kp the total cross sections, $\sigma_{\mathrm{tot}}^{\pi p}$ and $\sigma_{\mathrm{tot}}^{Kp}$, are known experimentally; the corresponding vector meson cross sections are assumed to be equal to the pseudo-scalar ones. It is important to bear in mind that the hadronic and photonuclear reactions are kinematically identical.

The results of such an analysis are shown in Fig. 4.2 (for details see Refs. [27, 58]. As a criterion for the fit, it was assumed that the theoretical result must not exceed the experimental data. This is well fulfilled in the case of the neutron and not so well in the case of the Λ, where the data are not so good. For low $k_\perp^2$ π — and K — exchange, respectively, are the dominant contributions, whereas the vector mesons do not play a role. For

TABLE 4.1
Largest Meson Admixtures in the Nucleon [in %]

Bare	$N-\pi$	$N-\rho$	$D-\pi$	$D-\rho$
58	18	13	6	2

higher $k_\perp^2$ ρ — and K^* — exchange become the dominant mechanism. It turns out that one can choose the same cut-off parameter, Δ_{Mp} = 1.08 GeV, for pseudo-scalar and vector mesons. If one considers this parameter as universal for the meson–baryon-octet, then heavier mesons are strongly suppressed and do not play a role. A corresponding analysis has also been performed for Δ^{++} production. Here the cut-off parameter has to be chosen somewhat small, $\Lambda_{MD} = 0.98 \pm 0.05$ GeV However, this value is much less reliable than the previous one because the data are not very convincing. For example, the double differential cross sections vary by up to a factor of 2, depending on the assumed background. The y-integrated spectra are more precise, with errors of about 30%. The authors of Ref. [27] also found that their results do not depend sensitively on the analytic form of the form factors (exponential, monopole or dipole) as long as they fulfill the basic symmetry given in Eq. (3.7). If one uses conventional form factors which only depend on t, a similar analysis to that shown in Fig. 4.2 fails already for $k_\perp^2 \geq 0.3\,(\mathrm{GeV}/c)^2$.

Table 4.1 gives the probabilities [in %] of finding the various Fock states in the nucleon. Note that the total probability of finding pion- and rho-configurations is nearly 40%. This is in agreement with the results of the Adelaide group [54]. In fact it is amazing how close these probabilities are to those found in the cloudy bag model more than a decade ago [35]. On the other hand, configurations with strange baryons and mesons are very small in the present model. Here, the strange sea of the nucleon is mainly due to the strange sea in the mesons, as we will discuss later. Thus the contribution of the strange sea to the spin of the nucleon is negligibly small in this model.

4.2. Sea-Quark Distributions of the Nucleon

In order to calculate the quark distribution function within the Fock state expansion, see Section 3.1, one needs as input the quark distribution functions of the mesons and the bare baryons. For the quark distribution in the pion, a recent parameterization by Sutton *et al.* [74] has been used. By applying $SU(3)$ symmetry, the distributions of the other mesons were (approximately) determined. Unfortunately, the sea quark distribution of the pion is practically unknown, and one must therefore make assumptions about its magnitude which

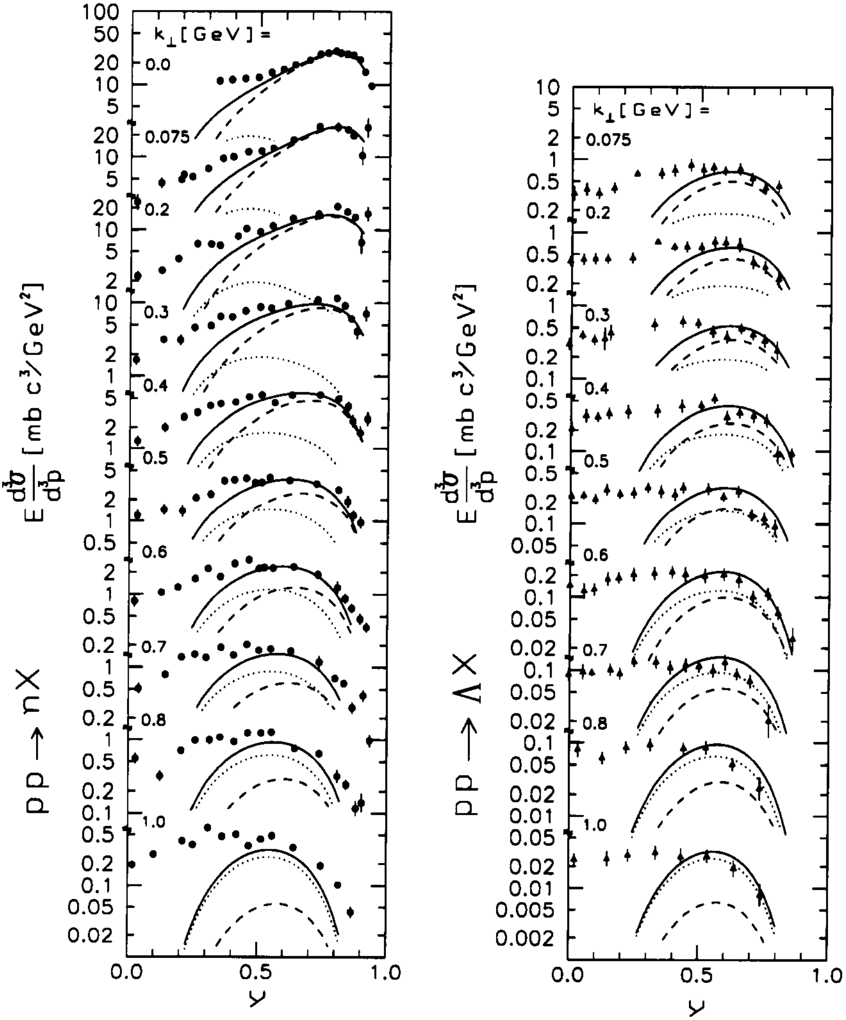

Fig. 4.2. Differential cross sections for $pp \to nX$ **and** $pp \to \Lambda X$ **[72, 73].** Shown are the OBE contributions: pseudoscalar meson (dashed), vector mesons (dotted) and their sum (solid) [27].

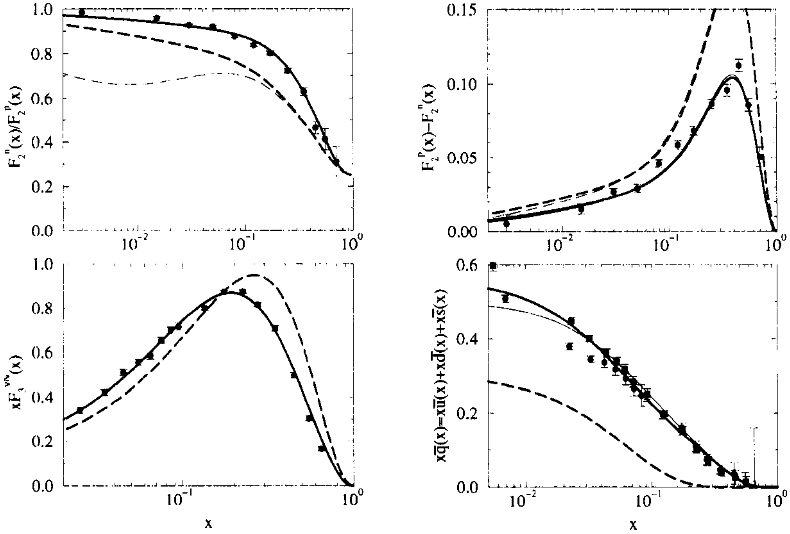

Fig. 4.3. Fit to the experimental data to determine the quark distributions of the 'bare' nucleon, at Q^2 = 4 GeV2 [77, 78]. The thick and thin dashed curves are the 'bare' distributions of fit I and fit II, respectively. The thick and thin full line represent the results of the corresponding meson-cloud model calculation [58]. The scale ofthe $\bar{q}$ (x) experimental data [79] is Q^2 = 3 GeV^2 (circles) and Q^2 = 5 GeV^2 (squares).

simultaneously influence the assumptions about the sea ofthe bare nucleon. In order to determine the valence distribution ofthe bare nucleon self-consistently it was parameterized in such a way that the theoretical valence distributions calculated from Eq. (3.12) agreed with the phenomenological parameterizations. Two different scenarios have been considered: (i) (Fit I) no sea in the bare nucleon, instead 40% ofthe momentum ofthe meson is carried by sea-quarks. (ii) (Fit 11) 20% ofthe meson momentum is carried by the sea, but then one needs a small sea in the bare nucleon. An experimental method to test this has been proposed by Londergan et al. [75]. This sea is assumed to be symmetric in $\bar{u}$ and $\bar{d}$, whereas the strange sea is suppressed by 50%. Both fits agree within the errors with the data. The results ofRef. [58] are shown in Figs. 4.3 and 4.4. In the latter, the changes, especially in the u-valence distribution, due to the coupling to the mesons are clearly seen. One also recognizes the asymmetry in the $\bar{u}$ and $\bar{d}$ distributions which is exclusively due to the Fock space expansion. The model has also been compared with the CCFR-data [76]. As shown in Table 4.2 the agreement between theory and experiment is satisfying.

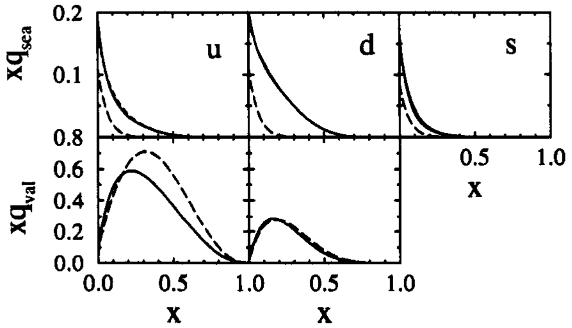

Fig. 4.4. Quark distribution functions of the bare (dashed) and the physical nucleon [SS]. Differences between fit I and fit II (thin and thick line) can hardly be seen.

Recently Steffens *et al.* [66] used quark model wave functions to calculate the bare valence quark distribution function. As shown in Fig. 4.5 the agreement with the phenomenological distribution is also quite good.

4.3. Gottfried Sum Rule and the $\bar{u}-\bar{d}$ Asymmetry

The Gottfried sum rule is perhaps the most famous consequence of $SU(2)$ flavor symmetry of the sea. Because it measures the x-integrated difference between the proton and neutron structure functions, it is sensitive only to the non-singlet $SU(2)$ content of the nucleon. Let us first define the quantity

$$S_G(x,1) = \int_x^1 \frac{dx'}{x'} \left(F_2^{\mu p}(x') - F_2^{\mu n}(x')\right) \tag{4.2}$$

Relating the proton and neutron structure functions to the quark distributions in the proton (i.e., using charge symmetry), we have

$$\begin{aligned} S_G(x,1) &= \frac{1}{3}\int_x^1 dx' \left(u(x') + \bar{u}(x') - d(x') - \bar{d}(x')\right) \qquad (4.3) \\ &= \frac{1}{3}\int_x^1 dx' \left(u_v(x') - d_v(x')\right) - \frac{2}{3}\int_x^1 dx' \left(\bar{d}(x') - \bar{u}(x')\right) \end{aligned}$$

where the valence quark distributions are defined by $q_v \equiv q - \bar{q}$. Since the number of valence quarks in a hadron does not change, we obtain the Gottfried sum rule

$$S_G \equiv S_G(0,1) = \frac{1}{3} \qquad [QPW] \tag{4.5}$$

TABLE 4.2
Comparison of Measured Ratios of Quark Momenta (CCFR-data (76]) with Theoretical Results Obtained with MCM [58]

	EXP	Fit	Fit II
$K = \frac{2\langle xs\rangle}{\langle x\bar{u}\rangle + \langle x\bar{d}\rangle}$	$0.44^{+0.09+0.07}_{-0.07-0.02}$	0.46	0.54
$\eta_n - \frac{2\langle xs\rangle}{\langle xu\rangle + \langle xd\rangle}$	$0.057^{+0.010+0.007}_{-0.008-0.002}$	0.081	0.069
$R_Q = \frac{\langle x\bar{u}\rangle + \langle x\bar{d}\rangle + \langle x\bar{s}\rangle}{\langle xu\rangle + \langle xd\rangle + \langle xs\rangle}$	0.1.53± 0.034	0.176	0.182

provided we make the additional assumption $\int_0^1 dx\bar{d} = \int_0^1 dx\bar{u}$, as would be expected in the simple quark-parton model (QPM).

The early experimental data for $S_G(x, 1)$ [81] did, in fact, suggest a value lower than 1/3, but with errors large enough to be consistent with it. However, armed with the theoretical expectation of $SU(2)$ flavor symmetry, most authors believed that S_G would tend to 1 /3 as the accuracy of the data improved. To the surprise of many, the recent, accurate determination of S_G by the NMC appears to support the idea that $\bar{u} \neq \bar{d}$ [113. Neglecting nuclear effects, the NMC found

$$S_G(x_{\min}, 1) = 0.229 \pm 0.0157 \tag{4.6}$$

where $x_{\min} = 0.004$. The present value which includes an extrapolation to $x = 0$, is $S_G = 0.235 \pm 0.026$ [77], but this may be lowered a further 4–10% by shadowing [41, 53]. The most natural explanation for the smaller than expected value Of S_G is that $\bar{d}(x) \neq \bar{u}(x)$. The value quoted above would imply that $\int_0^1 dx\,(\bar{d}(x) - \bar{u}(x)) = 0.152 \pm 0.06$.

The meson-cloud model offers a simple, and at first sight convincing, explanation. Indeed, as we noted earlier the model had already been used to predict $\bar{d} > \bar{u}$ [10]. As discussed above, one can relate the proton and neutron structure function difference to the quark distribution function of the proton only. As we have seen, the physical proton has a relatively large π^+-neutron component in the Fock space, but a much smaller $\pi^- - \Delta^{++}$ component (the effect of which is further reduced by the $\Delta^0 - \pi^+$ contribution). Therefore the Sullivan process immediately gives a surplus of $\bar{d}$-antiquarks. The realistic meson cloud model explains the observed effect nearly quantitatively. This explanation indicates that the derivation of the GSR is due to deep-inelastic scattering from the (isovector) meson cloud of the nucleon.

This, however, is difficult to understand if we go back to the original formula Eq. (4.2). Here the cloud of π^+ and π^- mesons enters symmetrically, so one expects that their effect should drop out. As we will see in the following, a calculation in terms of the meson cloud does give the correct result as far as

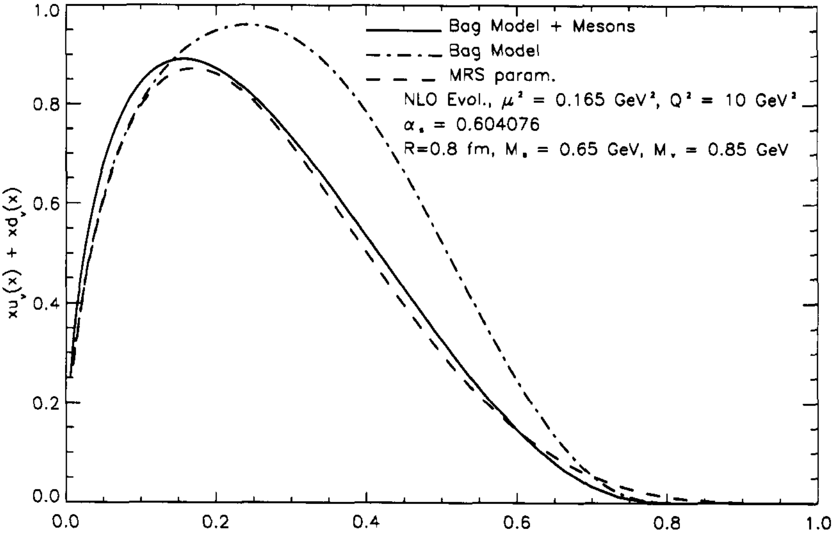

Fig. 4.5. Total valence distribution [66] in the bag-model and in the bag dressed with mesons compared with the *MRS* parametrization [80] of the data. The quark distributions are evolved in next-to-leading order QCD.

the (integrated) Gottfried sum rule is concerned. If, however, one is interested in the x-distribution (i.e., the functional dependence of the rhs of Eq. (4.2)) one has to start with Eq. (4.2). The underlying physics is slightly more subtle than that discussed above. To explain it, we first consider a simplified model involving only bare nucleons and pions:

$$|N\rangle_{\text{phy}} = Z^{1/2}\,|N\rangle_{\text{bare}} + \sum_i \alpha_i \left|\pi^{(i)}\right\rangle |N_i\rangle_{\text{bare}} \tag{4.7}$$

Within this model we obtain the following contributions for $F_2^{\mu p}$ and $F_2^{\mu n}$ from the processes shown in Fig. 3.1

$$F_2^{\mu p}(x) = Z\widetilde{F}_2^p(x) + P_{p\pi 0/p}\widetilde{F}_2^p + P_{p\pi 0/p}F_2^{\pi^0} + P_{n\pi+/p}\widetilde{F}_2^n + P_{n\pi+/p}F_2^{\pi^+} \tag{4.8}$$

$$F_2^{\mu n}(x) = Z\widetilde{F}_2^n(x) + P_{n\pi 0/n}\widetilde{F}_2^n + P_{n\pi 0/n}F_2^{\pi^0} + P_{p\pi-/n}\widetilde{F}_2^p + P_{p\pi-/n}F_2^{\pi^+} \tag{4.9}$$

Z is the probability to find a 'bare' nucleon, $\widetilde{F}_2^p$ and $\widetilde{F}_2^n$ are the structure functions of the 'bare' proton and neutron, respectively, and $\widetilde{F}_2^\pi$ is the pion structure function. We also used the following shorthand notations:

$$P_{N\pi/N}\tilde{F}_2^N \equiv \int_0^{1-x} dy\, f_{N\pi}(y)\, F_2^N\left(\frac{x}{1-y}\right) \tag{4.10}$$

$$P_{N\pi/N}F_2^\pi \equiv \int_x^1 dy\, f_{\pi N}(y)\, F_2^\pi\left(\frac{x}{y}\right) \tag{4.11}$$

Using charge-symmetry we obtain for the difference of the proton and neutron structure function

$$F_2^{\mu p}(x) - F_2^{\mu n}(x) = \left(Z + P_{p\pi o/p} - P_{n\pi+/p}\right)\left(\tilde{F}_2^p(x) - \tilde{F}_2^n(x)\right) \tag{4.12a}$$

$$\begin{aligned} &= \left(Z + P_{p\pi 0/p} + P_{n\pi+/p} - 2P_{n\pi+/p}\right) \\ &\quad \times \left(\tilde{F}_2^p(x) - \tilde{F}_2^n(x)\right) \end{aligned} \tag{4.12b}$$

From Eq. (4.12a) one immediately realizes, that, indeed, the pion structure function does not appear. If one divides Eq. (4.12b) by x and integrates over x one obtains:

$$\begin{aligned} \int \frac{dx}{x}\left(F_2^{\mu p}(x) - F_2^{\mu n}(x)\right) &= \frac{1}{3} - 2\int_0^1 \frac{dx}{x}\int_0^{1-x} dy P_{n\pi+/p}(y)\,\frac{x}{1-y} \\ &\quad \times \left(\tilde{u}_v\left(\frac{x}{1-y}\right) - \tilde{d}_v\left(\frac{x}{1-y}\right)\right) \end{aligned} \tag{4.13}$$

where $\tilde{u}_v$ and $\tilde{d}_v$ are the valence distributions of the 'bare' proton. Here we have used the fact that in our simplified model the probabilities of finding a bare proton, a neutron with a π^0 and a neutron with a π^+ add up to unity, which gives the well known factor 1/3 of the GSR. Deviations from this expected value are proportional to the neutro–π^+ admixture, and the proton–π– admixture in the neutron, respectively. Moreover, one also realizes that the difference in the x-distribution is proportional to the valence quark distribution in the (bare) proton. As mentioned already, as long as one is interested in the integrated value of the GSR both formulations given here are equivalent [51].

If one is interested in the x-distribution, Eq. (4.13) has to be used. Generalizations of Eq. (4.13) to include Δ, vector mesons and strange hadrons are straightforward. The result is that only the admixture of isovector-mesons gives rise to a deviation from the GSR. An additional small contribution comes from strange baryons and mesons [27, 40, 54]. Calculations within meson models of different stages of sophistication have been performed by many authors. Their results essentially agree with the experimental finding. The x-distribution $F_2^p(x) - F_2^n(x)$ was calculated first by Melnitchouk *et al.* [52, 54], who also considered the effect of Pauli-blocking. Their results are shown in Fig. 4.6, where

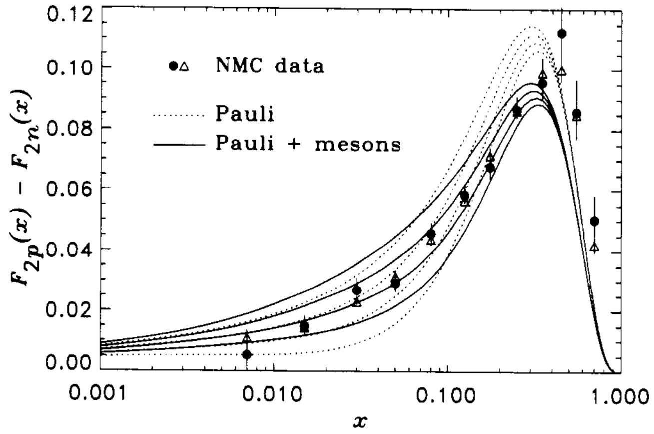

Fig. 4.6. Effect of the Pauli exclusion principle on the proton–neutron structure function difference, as a function of X [54]. The dotted (without meson corrections) and solid (with meson corrections) curves are for $P = 0$ (largest curves) 0.05, 0. 1 and 0.15 (smallest curves).

TOPT in the IMF was used with a dipole form factor (with $\Lambda = 700$ MeV). P denotes the fraction of the valence quark normalization associated with a four-quark bag state spectator to the hard collision [82]. The most noticeable consequence of the meson cloud is a decrease in the peak value at $x \sim 0.3$, which indicates a change in the usual regime of valence distributions. The same effect can be seen in Fig. 4.3, where the results of Ref. [58] are shown. There only the effects of the meson cloud were considered. The various contributions which give rise to the violation of the Gottfried sum rule and to the asymmetry of the sea quark distribution are given in Fig. 4.7 and Table 4.3. In both cases one notices corrections coming from the Δ-configurations.

4.4. Drell–Yan Processes and $\bar{u} - \bar{d}$ Asymmetry

The Drell–Yan (DY) process [83] involves the electromagnetic annihilation of a quark (antiquark) from the incident hadron A with an antiquark (quark) in the target hadron B. The resultant virtual photon materializes as a dilepton pair (l^+l^-) with muons being the pair most readily detected in experiments. This process is schematically shown in Fig. 4.8. The cross-section for the DY process can be written as

$$\frac{d\sigma^{AB}}{dx_1 dx_2} = \frac{4\pi\alpha^2}{9sx_1x_2} K(x_1,x_2) \sum_f e_f^2 \left[q_A^f(x_1)\bar{q}_B^f(x_2) + \bar{q}_A^f(x_1) q_B^f(x_2) \right] \tag{4.14}$$

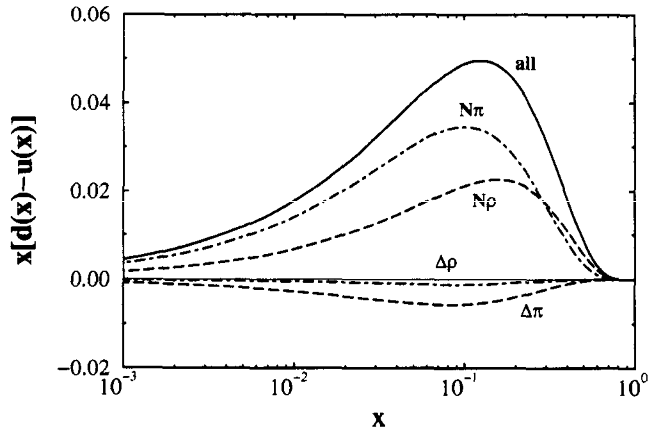

Fig. 4.7. Different contributions to the asymmetry of the sea quark distributions in the model of Ref. (27,581.

where s is the square of the center-of-mass energy and x_1 and x_2 are the longitudinal momentum fractions carried by the quarks of flavor f. The functions $q_A^f(x_1)$ $\left(\bar{q}_A^f(x_1)\right)$ and $q_B^f(x_2)$ $\left(\bar{q}_B^f(x_2)\right)$ are the (anti-)quark distributions of the beam and target, respectively. The factor $K(x_1, x_2)$ accounts for the higher-order QCD corrections that enter the process. Its value over the kinematic range where experiments are carried out is typically 1.5. The values of x_1 and x_2 are extracted from experiment via

$$M^2 = sx_1x_2 \approx 2P_{l^+}P_{l^-}(1 - \cos\theta_{l^+l^-}) \tag{4.15}$$

where M is the mass of the dilepton pair, P_{l^+} and P_{l^-} are the laboratory momenta of the leptons, and $\theta_{l^+l^-}$ is the angle between their momentum vectors. The total longitudinal momentum of the lepton pair $(P_{l^+} + P_{l^-})_L$ fixes $x_1 - x_2$ via

$$x_1 - x_2 \equiv X_F = \frac{2(P_{l^+} + P_{l^-})_L}{s} - 1 \tag{4.16}$$

In order to avoid spurious contributions to the DY yield from vector meson decays, all measurements are made for $M > 4$ GeV, and the region $9 \leq M \leq 11$ GeV is excluded to avoid the Υ resonances.

The absolute value of the Drell–Yan cross section is biased by the uncertainty in extrapolating from time-like to space-like values of Q2 when relating the Drell–Yan process with deep-inelastic scattering which involves the factor

TABLE 4.3
Gottfried Sum-Rule with Different Meson Contributions (S_G^{exp} = 0.235 ± 0.026)
In each line the contribution of the given Fock-states are added [27]

	Z	$\langle \bar{u}-\bar{d} \rangle$	S_G
Bare nucleon	I	0	0.333
$+\pi N$	0.755	–0.141	0.239
$+\pi D$	0.697	–0.106	0.263
All	0.580	–0.142	0.238

K [see Eq. (4.14)]. In order to avoid the uncertainty it is desirable to consider ratios [84,85] rather than absolute cross sections.

Drell–Yan processes have been proposed to measure the $\bar{u}-\bar{d}$ asymmetry directly. In Ref. [86] the various experimental possibilities have been investigated to test their sensitivity. In Fig. 4.9 we show the differential cross section, $M^3 d^2\sigma/dx_F dM$ for dilepton production in $p + d$ collision. The full line is the result of the meson cloud model discussed in Section 4.2, with an asymmetric sea. In order to test the sensitivity to the $\bar{d}-\bar{u}$ asymmetry, a symmetrized sea distribution and a phenomenological distribution with symmetric $\bar{u}, \bar{d}$ sea have been also used in the calculation. Although there is some sensitivity to the $\bar{d}-\bar{u}$ asymmetry, it can be easily compensated by a slightly different normalization factor.

The present experimental data for the Drell–Yan processes in elementary nucleon–nucleon collisions suffer from rather low statistics. Therefore, at present, one is forced to compare a theoretical calculation with the proton–nucleus experimental data. In first approximation the cross section for the production of the dilepton pairs in proton-nucleus scattering can be expressed in terms of the elementary pp and pn processes as

$$\sigma_{pA}^{DY} = Z\sigma_{pp}^{DY} + N\sigma_{pn}^{DY}$$

It has been shown [84,85] that the ratio of the cross section for the scattering of protons from the nucleus with $N - Z \neq 0$ to that from an isoscalar target such as deuterium is sensitive to the $\bar{d}_p(x) - \bar{u}_p(x)$ difference. These ratios have been measured by the E772 Collaboration at FNAL [84] for carbon, calcium, iron and tungsten targets. Neglecting nuclear effects, elementary algebra leads to the following result for the ratio:

$$R_{DY} = \frac{2\sigma^{DY}(p+A)}{A\sigma^{DY}(p+d)} = \frac{2Z}{A} + \frac{N-Z}{A}\,\frac{2\sigma^{pn}(x_1,x_2)}{\sigma^{pp}(x_1,x_2) + \sigma^{pn}(x_1,x_2)}' \tag{4.18}$$

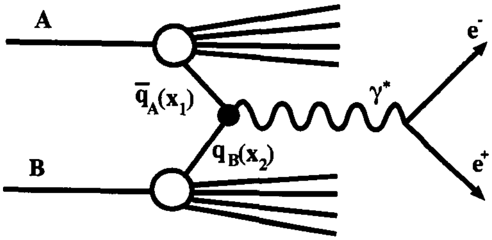

Fig. 4.8. Drell–Yan process: An antiquark (quark) from a beam proton (A) annihilates with a quark (antiquark) from the target proton (B) and creates a lepton pair.

where Z, N, A are numbers of protons, neutrons and the atomic number, respectively. In the large x_2 (target) limit the ratio takes a very simple form [87]:

$$R_{Dy}(x) = 1 + \frac{N-Z}{A}\frac{\Delta(x)}{\bar{u}(x)+\bar{d}(x)'} \quad \text{with} \quad \Delta(x) = \bar{d}(x) - \bar{u}(x) \tag{4.19a}$$

showing that the Drell–Yan processes with non-isoscalar targets are relevant for the issue of the asymmetry. Here $\Delta(x)$ is defined as

$$\bar{u}(x) = \bar{q}(x) - \frac{1}{2}\Delta(x) \quad \text{and} \quad \bar{d}(x) = \bar{q}(x) + \frac{1}{2}\Delta(x) \tag{4.19b}$$

The experimental ratios are consistent with symmetric quark distributions [84, 87] (see Fig. 4.10). Moreover, using asymmetric quark distribution functions (solid and dashed lines) has a rather small effect on the ratio. This renders those data useless for establishing the asymmetry. The ratio obtained with the recent MSR (A) quark distributions [30] almost coincides with the result of the meson cloud model [88]. As seen from the figure these ratios do not provide a sensitive enough test.

The idea of the $\bar{u} - \bar{d}$ asymmetry is not new. It was considered a decade ago by Ito *et al.* [89] as a possible explanation for the slope of the rapidity distribution of dilepton production in the proton–*Pt* collision at Fermilab. An alternative interpretation stimulated by the discovery of the EMC effect invoked the enhancement of the nuclear sea in *Pt* with respect to a collection of free nucleons [8]. Ito *et al.*, suggested to analyze the logarithmic derivative of the rapidity distribution.

$$S(\sqrt{\tau}) = \frac{d}{dv}\ln\frac{d^2\sigma}{dMdy}\Big|_{y=0} \quad \text{with} \quad \tau = x_1x_2 \tag{4.20}$$

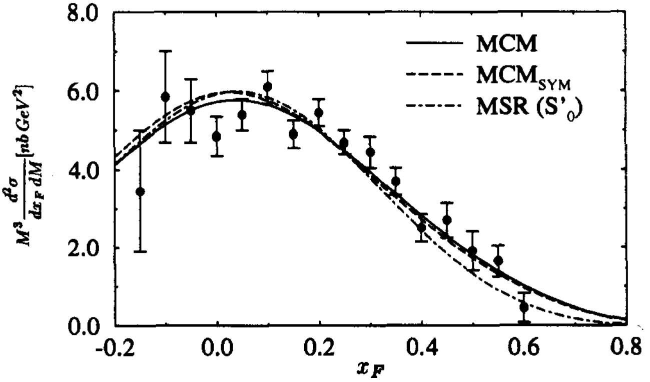

Fig. 4.9. Cross section for the production of the dilepton pairs in proton–deuteron collisions. Shown is the lit of the K-factor for various quark distributions to the experimental data [86].

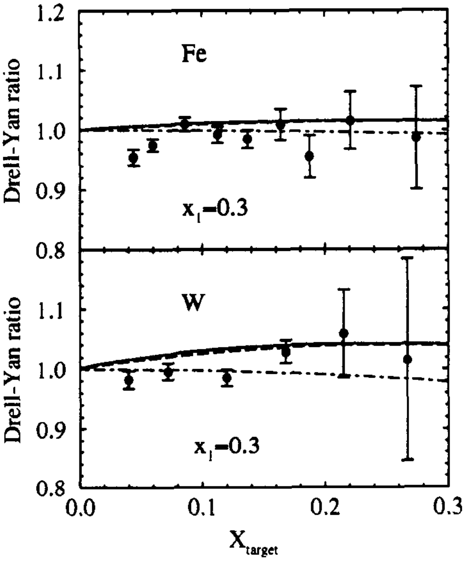

Fig. 4.10. Drell–Yan ratio for iron/deuterium and tungsten/deuterium. The solid line is the result of *MCM*, the dashed line the asymmetric *MSR*(A) and the dash-dotted line the symmetric MSR (S'_0) parametrization [86]. Data are taken from Ref. [84].

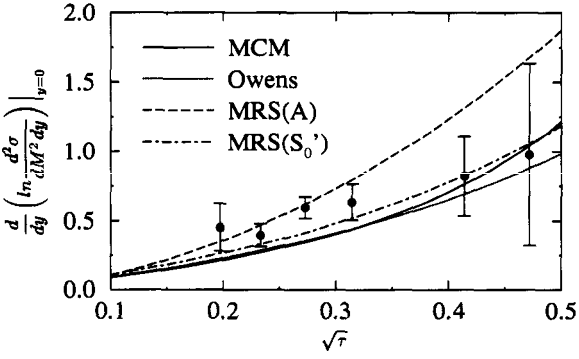

Fig. 4.11. The slope of the rapidity distribution. The full and dashed result is calculated with asymmetric sea quark distributions, the dotted and dash-dotted with symmetric ones [86].

where y = In $(x_1\,/x_2)\,/2$ is the rapidity. This quantity also possesses the desired property of being independent of the K-factor. In terms of the quark distributions the slope can be expressed as product of valence and sea distributions. Therefore the rapidity slope is a quantity which is sensitive not only to the $\bar{u}-\bar{d}$ asymmetry but also to valence quark distributions. In Fig. 4.11 we display the slope of the rapidity distribution calculated with different quark distributions. The solid line is the result ofthe meson model [86]. The dotted line is the result obtained with the Owens parameterization [90] of the quark distributions, the dashed line was obtained with the recent *MRS* (*A*) parameterization [30] with $\bar{u}-\bar{d}$ asymmetry and the dash-dotted line was obtained with *MRS* (S_0') [80] (symmetric) distribution. Figure 4.10 clearly demonstrates that the asymmetry is not the only ingredient and a reasonable description of the experimental data can be obtained with both flavor symmetric and asymmetric distributions.

A quantity which can be extracted almost directly from experiment is

$$A_{DY}(x_1,x_2)=\frac{\sigma_{pp}(x_1,x_2)-\sigma_{pn}(x_1,x_2)}{\sigma_{pp}(x_1,x_2)+\sigma_{pn}(x_1,x_2)} \tag{4.21}$$

which we will call Drell–Yan asymmetry. In Eq. (4.21) σ_{pp} and σ_{pn} are the cross sections for dilepton production in proton–proton and proton–neutron scattering. The Drell–Yan asymmetry (4.21) can be expressed in terms of the quantity $\bar{q}$ and Δ, introduced in Eq. (4.19b)

$$A_{DY}(x_1,x_2)=\frac{[u(x_2)-d(x_2)]\,[3\bar{q}(x_1)-5/2\Delta(x_1)]-[4u(x_1)-d(x_1)]\,\Delta(x_2)}{[u(x_2)+d(x_2)]\,[5\bar{q}(x_1)-3/2\Delta(x_1)]+[4u(x_1)+d(x_1)]\,2\bar{q}(x_2)} \tag{4.22}$$

In the case of a flavor symmetric sea ($\Delta = 0$) it is natural to expect that $A_{DY} > 0$, since $u > d$. However, the sign of A_{DY} can be reversed by increasing the flavor asymmetry of the proton sea ($\Delta \neq 0$).

Two dimensional maps of the Drell–Yan asymmetry as a function of x_1 and x_2 are shown in the form of the contour plots in Fig. 4.12. The different maps were obtained with the Owens parameterization [90] (left-upper comer), symmetric MRS(S_0') [80] (right-upper comer), the new MRS (A) [30] with the $\bar{u}-\bar{d}$ asymmetry built in (left-lower comer) and the prediction of the meson cloud model [86] (right-lower comer). The result obtained with the Owens (symmetric) parameterization and symmetric $MRS\,(S_0')$ parameterization are quite similar. This clearly demonstrates that the asymmetry A_{DY} is the desired quantity — insensitive to the valence quark distributions. It is also worth noting here that A_{DY} is positive in the whole range of (x_1 , x_2). How the $\bar{u}-\bar{d}$ asymmetry influences A_{DY} is shown in two lower panels. It is very promising that A_{DY} obtained with the asymmetric quark distributions (lower panels) differs considerably (please note the change of sign in the lower panels) from the result obtained with the symmetric distribution (upperpanels) and this should make an unambiguous verification of the flavor asymmetry of the sea quarks possible. It is not random in our opinion that the result obtained within the meson cloud model is very similar to that obtained from the parameterization fitted to different experimental data. We stress, in this context, that A_{DY} calculated in the meson cloud model is fairly insensitive to the quark distributions in the bare nucleons (baryons). It is primarily sensitive to the $\bar{u}-\bar{d}$ asymmetry which is fully determined by the quark distributions in the pion (and other isovector mesons), taken here from the pion–nucleus Drell–Yan process. In this analysis it has been assumed that the quark distributions in other mesons are related to those for the pion via $SU(3)_f$ symmetry.

Following the suggestion of Ellis and Stirling, the NA51 Collaboration at CERN has recently measured the A_{DY} asymmetry along the $x_1 = x_2$ diagonal [28]. Due to low statistics, only A_{DY} at low $x = x_1 = s_2$ was obtained. In Fig. 4.13 we show their experimental result (one experimental point) together with the results obtained with different quark distributions. The meaning ofthe lines here is the same as in Fig. 4.10. The result denoted as MCM, obtained with the meson cloud model [58,88] essentially without free parameters, nicely agrees with the experimental data point. In order to better understand the result, and the relation to the $\bar{u}-\bar{d}$ asymmetry, let us express the cross sections in Eq. (4.2 1) in terms ofthe quark distributions. Assuming proton–neutron isospin symmetry and taking $x_1 = x_2 = x$, as for the NA51 experiment, one gets in terms

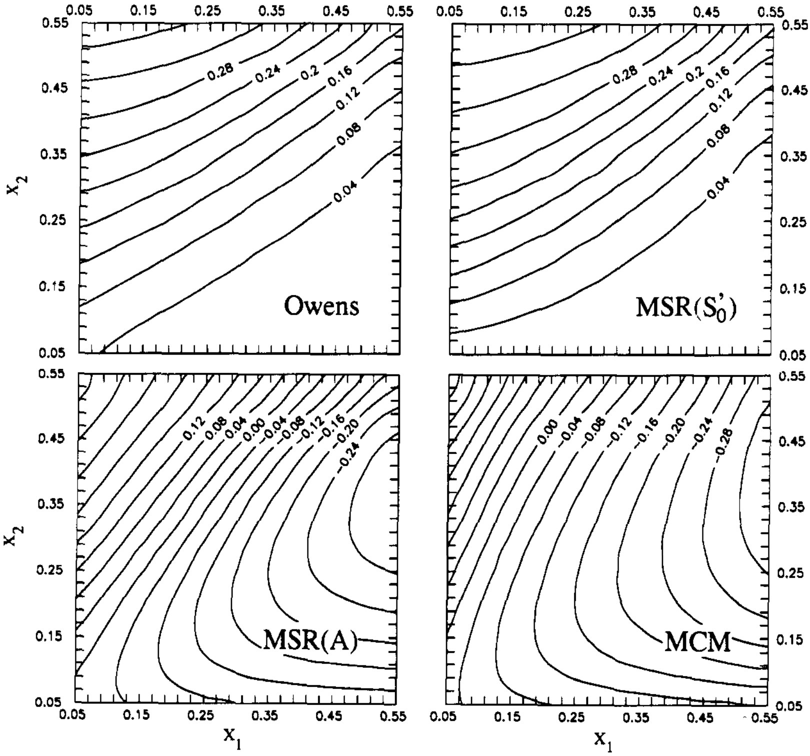

Fig. 4.12. A two-dimensional map ofthe Drell–Yan asymmetry as a function ofx1 and x2 [86]. Shown are results obtained with the Owens parametrization [90] (left-upper comer), symmetric MSR (S_0') (right-upper comer), new MRS(A) with the $\bar{u}-\bar{d}$-asymmetry built in (left-lower corner) and prediction of the meson cloud model [27, 58] (right-lower comer). Note the change of the sign in the lower panels.

of the quark distributions in the proton

$$A_{DY} = \frac{5\left(u-d\right)\left(\bar{u}-\bar{d}\right)+3\left(u\bar{u}-d\bar{d}\right)}{5\left(u+d\right)\left(\bar{u}+\bar{d}\right)+3\left(u\bar{u}-d\bar{d}\right)+4\left(s\bar{s}+4c\bar{c}\right)} \tag{4.23}$$

Let us consider first the case $\bar{u}=\bar{d}$. For a crude estimate one may neglect sea-sea terms (important at small x only) and assume $u_{\text{val}}(x) = 2d_{\text{val}}(x)$, which leads to $A_{DY} = 1/11 > 0$. The same crude estimate in the case of an asymmetric sea in conjunction with the decomposition Eq. (4.19b) yields

$$A_{DY} = \frac{-19\Delta+6\bar{q}}{-9\Delta+66\bar{q}} \tag{4.24}$$

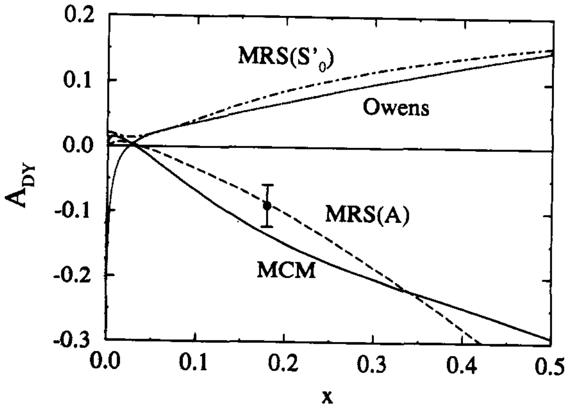

Fig. 4.13. Drell–Yan asymmetry along the $x_1 = x_2$ diagonal [86]. The meaning of the lines here is the same as in Fig. 4.11. The data point is taken from the NA51 Collaboration at CERN [28].

This demonstrates a strong sensitivity to both the $\bar{d} - \bar{u}$ asymmetry and to the absolute normalization of the sea. The lack of dependence on the valence quark distributions in the approximate expression Eq. (4.24) suggests a weak dependence in the exact formula, Eq. (4.23). The negative value obtained by the NA51 experiment, $A_{DY} = -0.09 \pm 0.02 \pm 0.025$, automatically implies $\bar{d} > \bar{u}$ — at least for the measured $x = 0.18$ (provided that the proton–neutron isospin symmetry violation is small(!)) [91]. The data point ofthe NA51 group is so far the most direct evidence for the flavor asymmetry of the sea quarks, which is explicitly show in Fig. 4.14. There A_{DY} has been translated into the ratio $\bar{u}(x)/\bar{d}(x)$ The x dependence of the asymmetry is awaiting further experiments. It is expected that the new experiment planned at Fermilab [92] will be very useful in this respect and will provide the x dependence of the $\bar{u} - \bar{d}$ asymmetry up to $x = 0.4$. It should therefore shed new light on the microscopic structure of the nucleon. The meson-cloud model gives definite predictions for the asymmetry awaiting future experimental verification.

4.5. Polarized Semi-Inclusive Deep-Inelastic Scattering

Despite the various phenomenological successes of the meson cloud model discussed so far, it is important to look for further experimental evidence pointing unambiguously to the existence of a pion and kaon cloud in high energy reactions. Melnitchouk and Thomas [93] have focussed on the semi-inclusive production of polarized Δ^{++} baryons from a polarized proton, $e\vec{p} \to e' \vec{\Delta}^{++} X$ and of a polarized Λ from a polarized proton $e\vec{p} \to e' \vec{\Lambda} X$. They suggested

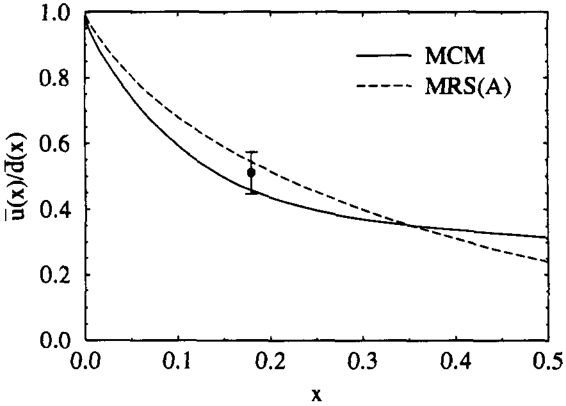

Fig. 4.14. The $\bar{u}(x)/\bar{d}(x)$ ratio as obtained from the meson cloud model [88] and the *MSK*(*A*) parametrization (dashed line) compared with the experimental result of the NA51 Collaboration [28).

experiments at CEBAF and HERMES which could distinguish between the meson-exchange mechanism and parton fragmentation. In Fig. 4.15 the polarization asymmetry $(\sigma^+ - \sigma^-)$ /stot is shown for CEBAF and HERMES kinematics. The two curves represent extreme cases, in which Δ 's are produced entirely via pion emission or diquark fragmentation. In reality, the ratio of polarization cross sections will be some average of the curves in Fig. 4.15. The amount of deviation from the parton model curve will indicate the extent to which the pion-exchange process contributes.

In a similar way, leptoproduction of polarized Λ hyperons from polarized protons can be used to test the relevance of a kaon cloud in the nucleon. The advantage of detecting Λ 's in the final state, as compared with Δ baryons, lies in the fact that the Λ is self-analyzing. It has also been suggested [93] that measurement of the polarization of the Λ in the target fragmentation region could discriminate between models of the spin content of the nucleon in which a large fraction of the spin is carried either by (negative polarized) strange quarks or (positively polarized) gluons. The latter would imply a positive correlation of the target proton and Λ spins, while the spin projection of the Λ along the target polarization axis should be negative in the former model. (Similar effects would also be seen in the reaction $\bar{p}p \rightarrow \bar{\Lambda}\Lambda$ [94, 95]. The present data on semi-inclusive, non-polarized, Λ's, however, indicate that the Λ and Σ hyperon admixtures in the proton wave function might be small (see the discussions in Sections 4.1 and 4.2). The polarization asymmetry for A-production is shown in Fig. 4.16. In first approximation the probability of forming a $\Lambda^{\uparrow}$ and $\Lambda^{\downarrow}$ is

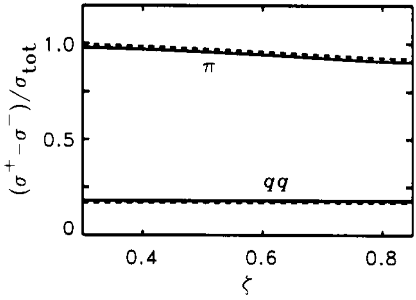

Fig. 4.15. Polarization asymmetry for the π-exchange (upper curves) and parton fragmentation (lower curve) models. The solid and dashed lines are for CEBAF and HERMES kinematics, respectively.

equal in the parton fragmentation process and the asymmetry is zero. Therefore the observation of a large polarization asymmetry in the large ζ region of target fragmentation will be evidence for a kaon-exchange fragmentation mechanism.

4.6. Exclusive Electroproduction of Pions

It has been suggested that the spin averaged splitting functions discussed above may be directly measurable in exclusive electroproduction of pions above the resonance region. This claim is based on the observation [96] that, for the photon virtuality Q^2 greatly exceeding the meson and baryon virtualities k^2, the differential cross section for the reaction $ep \to eMB$ is dominated by the nucleon–pion pole diagram which factorizes

$$\frac{d\sigma}{dxdQ^2} \sim f_{\pi N}(x)\; F^2_{\pi N}(Q^2) \tag{4.25}$$

Here, $F_{\pi(N)}$ (Q^2) is the on-mass-shell electromagnetic form factor of the struck pion (nucleon).

In [96] the splitting functions are interpreted as the densities of (non-perturbative) partons (mesons and baryons) of the physical nucleon and it is suggested that one could study them like parton densities in inclusive DIS. Indeed, from Eq. (4.25) it follows that in exclusive one-pion electroproduction the photon of high virtuality, Q^2, probes the density of mesons and/or baryons in the proton at the value of the light-cone Sudakov variable equal to the Bjorken variable x. Factorization implies a possibility of separate analysis of the light-cone meson—baryon density functions and the electromagnetic form factors of mesons and baryons.

More accurately, the decomposition of the differential cross section of the exclusive reaction $ep \to e\pi^+n$ in terms of the longitudinal and transverse cross

Fig. 1.16. **Polarization asymmetry for the *K*-exchange (solid) model of Λ production, compared with a leading fragmentation approximation estimate for the parton fragmentation process (dashed).**

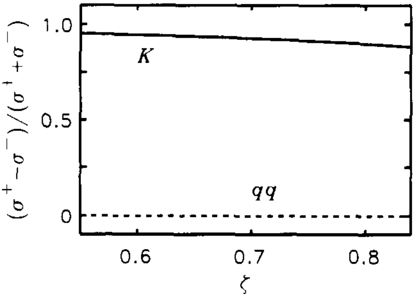

sections reads [96]

$$\frac{d\sigma(ep \to e\pi^+ n)}{dx dQ^2 dk_\perp^2} = 2K_L\left(x, Q^2\right) f_{\pi N}\left(1-x, k_\perp^2\right) F_\pi^2\left(Q^2\right)$$

$$+2K_T\left(x, Q^2\right) f_{\rho N}^T\left(1-x, k_\perp^2\right) \frac{1}{8} Q^2 F_{\rho\pi}^2\left(Q^2\right)$$

where K_L and K_T in (4.26) are the kinematical factors.

In Eq. (4.26) Fw(Q2) is the on-shell charge form factor on the pion. It is worth recalling that in the light-cone parton model the condition $Q_2 \gg k_2$ guarantees the on-shellness of partons [96]. The second (transverse) term in (4.26) arises from the $\rho^+ - \pi^+$ radiative transition which is under the control of the form factor Frp (Q^2). This is a magnetic dipole (M1) transition — hence the enhancement factor, Q^2, in the corresponding term in the electroproduction cross section (4.26).

The density of the transversely polarized ρ-mesons in the proton,$f^T_{\rho N}$, can easily be obtained [96]. It is worth noticing that the ρ-pole dominated transverse cross section is expected to be an increasing function of $k_\perp^2$ at small $k_\perp$. This effect is due to the strong $k_\perp$ -dependence of the tensor term

$$\frac{f}{4m_N} \bar{\Psi} \sigma_{\mu\nu} \Psi \left(\partial^\mu \rho^\nu - \partial^\nu \rho^\mu\right)$$

in the ρ*NN* interaction, which generates terms proportional to $k_\perp^2$ and $k_\perp^4$ in $f^T_{\rho N}$. Observation of this phenomenon is crucial for understanding the mechanism of exclusive electroproduction.

The possibility to detect neutral mesons makes the reaction $ep \to e\pi^0\pi$ particularly interesting as it is free of the pion-pole term and at high Q^2 the baryon pole term is suppressed by extra powers of $1/Q2$. Then the differential cross section reads

$$\frac{d\sigma\left(ep\to e\pi^0 p\right)}{dxdQ^2dk_\perp^2}=K_T\left(x,Q^2\right)f_{\omega N}^T\left(1-x,k_\perp^2\right)\frac{1}{8}Q^2F_{\omega\pi}^2\left(Q^2\right) \tag{4.27}$$

There are two main reasons for the ω-pole dominance. First of all the $\omega\pi\gamma$ coupling constant, absorbed in the radiative transition form factor, $F_{\omega\pi}^2\left(Q^2\right)$, is numerically large. The extra enhancement is due to the factor, Q^2, typical of the magnetic dipole interaction [96].

This observation makes the idea of the precision measurement of the Q^2-dependence of the cross section of the reaction $p\ (e,e'\pi^0)p$ especially appealing, since it provides us with opportunity of direct measurement of the vector meson cloud of the nucleon. Furthermore, as has been emphasized in [96], the early onset of the parton model regime enables one to study the helicity non-conserving form factors $F_{\rho\pi}\left(Q^2\right)$, $F_{\omega\pi}\left(Q^2\right)$ in the substantially non-perturbative region and, what is more important, to retrace the onset of the *pQCD* regime at a very high Q^2 as well.

In a recent detailed analysis [97], it has been also suggested that measurements of fast pions in the final state, in coincidence with the final electron, could be sensitive to a pionic component of the nucleon. Extending the exclusive analysis of Güttner *et al.* [116] in the IMF, Pirner and Povh [97] work within a constituent quark picture in which the probability to find a pion in the nucleon is expressed in terms of the pion distribution function inside a constituent quark.

The differential pion-production cross section for the "leading pion" (integrated over transverse momenta) is written as

$$\begin{aligned}\frac{d\sigma}{dxdydz}\propto &A\ (x,y,z)+B\,(x,y,z)\,F_\pi\left(Q^2\right)\\ &+C\,(x,y,z')\,F_\pi^2\left(Q^2\right)\end{aligned} \tag{4.28}$$

where $z = E_\pi/\nu$ is the fraction of the photon's energy carried by the pion, and where the A and B terms describe soft and hard fragmentation, respectively. The function C reflects coherent scattering from the pion cloud of the constituent quark. Each term in Eq. (4.28) gives a characteristic Q^2-dependence, namely $\log Q^2$, $1/Q^2$ and $1/Q^4$, respectively. To isolate the coherent scattering from the pion one therefore has to restrict oneself to the region of not too high Q^2, where the form factor suppression has not yet eliminated the pion signal.

A useful observation in this analysis is that each of the three processes has a quite distinct z-dependence. The hard-fragmentation process gives a differential cross section which is constant in z, and is important in the intermediate z region ($0.6 \leq z \leq 0.8$). The soft fragmentation mechanism is dominant at small $z, z \leq 0.6$, but dies out rather rapidly at larger z. This fact may enable one to detect the pion-exchange process, which dominates the region $0.8 \leq z \leq 1$, where it predicts a contribution that is several times larger than the constant-z, hard fragmentation mechanism [117]. The conclusion that the pion-exchange process is dominant is consistent with our previous results.

The authors argue, however, that what they suggest is the measurement of the meson cloud ofthe constituent quark and not the meson cloud ofthe nucleon. In their view the meson cloud of the nucleon has already been determined from the pion-electroproduction data on the proton where only a 3% admixture of $n\pi^+$ in the bare proton was found [116]. This should be compared with the corresponding value in Table 4.1, where the $\pi^+ n$ admixture is 12% (and 6% is $\pi^0 p$). This crucial difference in the concept of the meson cloud will be decided very soon experimentally by the ZEUS collaboration at HERA, which is installing a forward neutron calorimeter.

4.7. Meson-Cloud Effects on the Spin-dependent Properties of the Nucleon

The spin structure functions [Eq. (2.10)] of the proton and neutron are related by the Bjorken sum rule, which is a rigorous prediction of QCD

$$\int_0^1 dx\, [g_1^p(x) - g_1^n(x)] = \frac{1}{6} g_A/g_\nu \tag{4.29}$$

It was first derived using current algebra [98] where one can show that the integrated value of $g_1^N(x)$ is given (in the Bjorken limit) by the matrix-element

$$\Gamma_N = \int_0^1 dx g_1^N(x) = \frac{1}{2} \langle N\uparrow |\bar{\Psi}(0)\, Q_{em}^2 \gamma_3 \gamma_5 \Psi(0)| N\uparrow\rangle \tag{4.30}$$

Using the decomposition for the charge squared

$$\frac{1}{2} Q_{em}^2 = \frac{1}{12}\left[\lambda_3 + \frac{1}{\sqrt{3}}\lambda_8 + 2\sqrt{\frac{2}{3}}\lambda_0\right] \tag{4.31}$$

where the λ's are the usual Gell-Mann matrices, one obtains what for the proton is called the Ellis–Jaffe Sum Rule [99].

$$\Gamma_p = \frac{1}{6}[I_0 + I_8 + I_3] \tag{4.32}$$

In terms of the standard $SU(3)$ amplitudes, F and D, for the baryon semi-leptonic decays, the two flavor octet amplitudes are given as

$$I_3 = \frac{1}{2}\langle P\uparrow|\bar{\Psi}\gamma_3\gamma_5\lambda_3\Psi|P\uparrow\rangle = \frac{1}{2}\,(F+D) \tag{4.33}$$

and

$$I_8 = \frac{1}{2\sqrt{3}}\langle P\uparrow|\bar{\Psi}\gamma_3\gamma_5\lambda_8|P\uparrow\rangle = \frac{1}{2}(F-D) \tag{4.34}$$

The flavor singlet amplitude is given as

$$I_0 = \sqrt{\frac{2}{3}}\langle P\uparrow|\bar{\Psi}\gamma_3\gamma_5\lambda_0\Psi|P\uparrow\rangle \tag{4.35}$$

and can be deduced from the experimentally known Γ_p from Eq. (4.32) if one takes F and D from the analysis of the semi-leptonic decays of the baryon octet.

Usually one expresses the Ellis–Jaffe sum rule in terms of the polarized quark distributions.

$$\Delta q = \int_0^1 dx\left[q^{\uparrow}(x) - q^{\downarrow}(x) + \bar{q}^{\uparrow}(x) - \bar{q}^{\downarrow}(x)\right] \tag{4.36}$$

$$\Gamma_p = \int_0^1 g_1^p(x)\,dx = \frac{1}{2}\left(\frac{4}{9}\Delta u + \frac{1}{9}\Delta d + \frac{1}{9}\Delta s\right) \tag{4.37}$$

Correspondingly one expresses the semi-leptonic decay of the baryon octet in the Cabbibo model, where one assumes that the axial currents responsible for the semi-leptonic decays belong to an $SU(3)$ octet. The diagonal matrix elements of these axial currents in this specific model give the well-known connection to the Ellis–Jaffe sum rule. Note, that in Eq. (4.37) the polarization of quarks and anti-quarks enter, where the Cabbibo model considers only the three valence quarks.

$$2g_A^3 = \Delta u - \Delta d = F + D \tag{4.38}$$

$$2\sqrt{3}g_A^8 = \Delta u + \Delta d - 2DS = 3F - D \tag{4.39}$$

$$\mathrm{g0A} = \mathrm{Du} + \mathrm{Dd} + \mathrm{Ds} \tag{4.40}$$

If one assumes that there is no polarized strangeness contribution, i.e., $\Delta s = 0$ as Ellis and Jaffe assumed, g_A^0 is given by Eq. (4.40), and one obtains the result of Ref. [99].

$$\int g_1^p(x)\,dx = \frac{g_A}{12}\left(1 + \frac{5}{3}\frac{3(F/D)-1}{(F/D)+1}\right) \tag{4.41}$$

$$\int g_1^n(x)\,dx = \frac{g_A}{12}\left(-1 + \frac{5}{3}\frac{3(F/D)-1}{(F/D)+1}\right) \tag{4.42}$$

The recent interest in these sum rules originates from the measurements of the spin structure functions of the proton and neutron by the EMC-[100], SMC-[101] and SLAC-[102] collaborations. The first measured value of the proton structure function by EMC caused great excitement because it deviated appreciably from the original Ellis–Jaffe prediction and indicated that only a small fraction of the proton spin is carried by quarks. The latest analysis of the newer data by Ellis and Karliner [103] gives (at $Q^2 = 10\ \mathrm{GeV}^2$).

$$g_A^{(0)} = 0.31 \pm 0.07$$

This is commonly interpreted as meaning that only 1/3 of the spin of the proton comes from the spin of the quarks. While it is not our primary concern here, we stress that such an interpretation is quite incorrect. Because of the axial anomaly in the flavor singlet channel, $g_A^{(0)}$ bears no formal relationship to the spin of the proton [104].

In view of the importance of the meson cloud for the Gottfried sum rule violation, one might expect that it could also play an important role for the nucleon spin. Indeed, an early estimate within the one pion exchange model seemed to indicate that meson cloud effects may play a role in resolving the 'spin crisis' [60]. Because of the close connection of the Ellis–Jaffe sum rule with semi-leptonic decays of the octet baryons we will first review the consequences of the meson cloud for these properties. Modifications of the axial-vector coupling constants due to the meson cloud can be quite important, since the corresponding axial-currents are not protected against renormalization due to the meson cloud [34, 36, 105].

4.7.1. Semi-Leptonic Decays

According to our present understanding, the weak semi-leptonic decays of the octet baryons can be classified into two groups: either a *d*-quark is transformed into a *u*-quark, or an *s*-quark is transformed into a *u*-quark. The matrix elements of the current operators 'responsible' for the semi-leptonic decays of the baryons belonging to the octet can be parameterized in terms of q^2-dependent form factors.

$$\langle B_1 | V_\mu + A_\mu | B_2 \rangle = C \bar{u}_{B_1}$$

$$\times \begin{bmatrix} f_1\left(q^2\right)\gamma_\mu & +i\frac{f_2\left(q^2\right)}{m_1+m_2}\sigma_{\mu\nu}q^\nu & +\frac{f_3\left(q^2\right)}{m_1+m_2}q_\mu \\ +g_1\left(q^2\right)\gamma_\mu\gamma^5 & +i\frac{g_2\left(q^2\right)}{m_1+m_2}\sigma_{\mu\nu}q^\nu\gamma^5 & +\frac{g_3\left(q^2\right)}{m_1+m_2}q_\mu\gamma^5 \end{bmatrix} u_{B_2} \qquad (4.43)$$

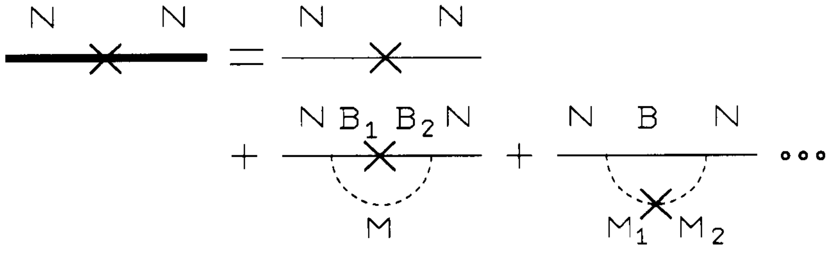

Fig. 4.17. Corrections to an axial current in the meson cloud model.

The factor C here is the Cabibbo factor ($\sin \theta_c$) or ($\cos \theta_c$). At low momentum transfer only two terms, f_1 (vector) and g_1 (axial vector), are important. It is customary to extract from experiments the ratio $g_A/g_V = g_1(0)/f_1(0)$.

Mesonic corrections lead to the renormalization of the axial-vector coupling constants. The vector coupling constants are protected against renormalization by vector current conservation. Mesonic corrections to the axial-vector coupling constants have been taken into account by calculating the loop corrections to the tree level approximation according to

$$\langle N|A^{\circ}_{\mu}|N\rangle_{\text{dressed}} = Z\left(\begin{array}{ll}\langle N|A^{\circ}_{\mu}|N\rangle_{\text{bare}} & +\sum\limits_{B_1B_2M}\Delta f_{(B_1B_2)M/N}\langle B_1|A^{a}_{\mu}|B_2\rangle \\ & +\sum\limits_{M_1M_2B}\Delta f_{(M_1M_2)B/N}\langle M_1|A^{a}_{\mu}|M_2\rangle\end{array}\right) \tag{4.44}$$

The polarized splitting functions Δf were defined in Section 3.6 and A^a_μ are the axial current operators. The corresponding diagrams are shown in Fig. 4.17.

The formalism outlined in Section 3 has been recently applied by two groups to the semi-leptonic decay of the octet baryons. Zoller [59] considered corrections due to the admixture of the pseudoscalar octet and the baryon decuplet, whereas Holtmann *et al.* [27] included, in addition, the vector meson nonet.

To perform numerical calculations within this model requires the knowledge of the axial coupling constants for the bare octet and decuplet baryons, vector mesons and the transitions octet ↔ decuplet. The transitions within the baryonic octet are traditionally parameterized by the so-called anti-symmetric F and symmetric D coupling constants. The axial coupling constant for the transition within the decuplet (H) can be fixed by the relation $2\langle \Delta^{++}|A^3_\mu|\Delta^{++}\rangle = H.\, 2m_\Delta s_\mu$. In analogy one defines the coupling constant for the interference diagram octet ↔decuplet (I) as $2\langle p|A^3_\mu|\Delta^0\rangle = 2\langle \Delta^0|A^3_\mu|p\rangle = I.2\sqrt{m_N m_\Delta} S_\mu$. The matrix elements of the axial-vector current between pseudoscalar mesons vanish. They are, however, finite for vector mesons. Here the structure is analogous to that of the baryonic octet. The corresponding constants are denoted as *FV* and *DV*. Due to parity-conservation the axial coupling constant *FV* vanishes. The vector meson ↔ pseudoscalar meson interference terms have an octet structure analogous to the other cases, with coupling constants called *FI* and *DI*.

In the *SU*(6) model, i.e., in the model in which all particles are described by their *SU*(6) wave functions [12], the axial coupling constants can easily be calculated

$$F = \frac{2}{3}, D = 1, H = 1, I = 4\,\frac{\sqrt{2}}{3}.\ FV = 0, DV = 1, FI = 1, DI = 0 \qquad (4.45)$$

In Table 4.4 various theoretical results obtained with different model-assumption for all possible semi-leptonic decays are compared with the available data [106]. In the column named 'MC, *SU*(6)' the g_A's are shown calculated within the model of Holtmann *et al.*, using the unrenormalized *SU* (6) axial-vector coupling constants [Eq. (4.45)]. In the column labelled 'MC, *SU*(3)' the corresponding results are given with *F* and *D* fitted to the measured values of the axial-vector coupling constants (the remaining parameters *H, I, DV* and *FI* were taken at their *SU*(6) values). For comparison the tree-level (no mesonic corrections) *SU* (6) model and *SU* (3) model (*F* and *D* fitted to the experimental data) are also included. The latter is the 'Cabbibo'-model.

The χ^2 values presented in the last row for each model give an idea of the fit quality. It is well known that the naive *SU*(6) model gives a very poor description of the experimental semi-leptonic decay data. On the other hand, when fitting the *F* and *D* parameters an extremely good description of the existing (5!) data can be achieved. It is commonly believed that any correction to the *SU*(3) model may only destroy this nice agreement. In fact, the inclusion of mesonic corrections with *SU* (6) axial coupling constant improves the description of the data dramatically (X^2/N = 4369 → X^2/N = 8.5). An additional variation of the *F* and *D* parameters can improve the results slightly. As pointed out by Zoller [59], the agreement with the data of the MCM-model plus *SU*(6) coupling parameters is comparable with the Cabbib model. Whereas the latter has two parameters to fit the 5 experimental data, the SU(6)-MCM is completely parameter free, because everything is fixed by previous investigations. On the other hand, it is also clear that the axial coupling parameters derived from the non-relativistic constituent quark model have to be modified due to the fact that in relativistic quark models an appreciable amount of the proton spin arises from the orbital motion of the 3 quarks [107, 108].

TABLE 4.4
A List of All Possible Semileptonic Decays of Baryons within the Nucleon Octet

The axial couplings g_A has been calculated at the tree-level in the $SU(6)$ model ($F = 2/3$ and $D = 1$) and in the $SU(3)$ model F and D ($F = 0.44, D = 0.82$) fitted. Moreover, the results of the same models are shown with inclusion of the meson cloud. For the $SU(3)$ case we find $F = 0.53$ and $D = 1.15$

Decay	$SU(6)$	$SU(3)$	MC, $SU(6)$	MC, $SU(3)$	g_A exP
$\eta \rightarrow \rho$	1.67	1.257	1.241	1.257	1.2573 ± 0.0028
$\Sigma+ \rightarrow \Lambda$	0.82	0.67	0.66	0.74	
$\Sigma^- \rightarrow \Sigma^0$	0.94	0.62	0.77	0.64	
$\Sigma^- \rightarrow \Lambda$	0.82	0.67	0.65	0.75	0.60 ± 0.03
$\Sigma^+ \rightarrow \Sigma^0$	–0.94	–0.62	–0.77	–0.64	
$\Xi^0 \rightarrow \Xi 0$	0.33	0.38	0.27	0.49	
$\Lambda \rightarrow \rho$		–0.87	–0.96	–0.89	-0.857 ± 0.018
$\Sigma^0 \rightarrow \rho$	0.24	0.27	0.19	0.31	
$\Sigma^- \rightarrow \eta$	0.33	0.38	0.27	0.49	0.34 ± 0.05
$\Xi^0 \rightarrow \Sigma^+$	1.67	1.26	1.37	1.39	
$\Xi^- \rightarrow \Lambda$	0.41	0.20	0.35	0.16	$0.3 1 \pm 0.06$
$\Xi^- \rightarrow \Sigma^0$	1.18	0.89	0.97	0.98	
x^2/N	4369	2.0	8.5	6.5	

4.7.2. The Ellis–Jaffe Sum Rule

In order to calculate the sum rule within the MCM one has to calculate the three matrix elements I_0, I_3, I_8 given in Eqs. (4.33)–(4.35). The I_3 and I_8 are directly connected with the semi-leptonic decay of the octet baryons. If one assumes that the polarization of the strange sea can be neglected (as done by Ellis and Jaffe [99]) then $g_A^0 = 2\sqrt{3}g_A^8$ and therefore I_0 is also connected with the leptonic decay. The same two versions of the MCM discussed in the previous section have also been applied to the 'spin-problem' of the nucleon. Zoller [59] considered the baryon and pseudoscalar meson octet and the baryon decouplet. He used $SU(6)$ axial coupling parameters. The polarization of the strange quarks is very small ($\Delta s = 0.005$), and the fraction of the spin (helicity) carried by the quarks is about 80%. In his model the three major Fock space components are:

$$|\mathrm{N}\rangle_{\mathrm{phys}} = 0.568\,|N)_{\mathrm{bare}} + 0.238\,|\pi N\rangle + 0.125\,|\pi\Delta\rangle \qquad (4.46)$$

If one used this decomposition in a static model the matrix element of the spin operator $\hat{S}_z$ between proton states with $S_z = 1/2$ reads:

$$\left\langle \hat{S}_z \right\rangle_p \approx 0.568? * 1/2 + 0.238 * \left(\frac{-1}{6} \right) + 0.125 * \frac{5}{6} = {}_{6}0.35$$

This value should be compared with 1/2. The depolarization effect is due to the spin-flip of the πN component, whereas the $\pi\Delta$ term tends to retain the proton polarization. In the actual, relativistic case, the spin-flip and non-spin-flip terms nearly cancel each other (see Section 3.6) and this results in a vanishing contribution of the πN component to $\left\langle \hat{S}_z \right\rangle_p$. For that reason the corresponding value in the full model is even larger $\left(\left\langle \hat{S}_z \right\rangle_p = 0.4 \right)$.This result depends on the cut-off parameters chosen for the meson–baryon vertices. For harder form factors [59] more of the proton spin is carried by the meson cloud but on the other hand the axial couplings of hyperons become unacceptably small. The results of Holtmann *et al.* [88] are summarized in Table 4.5, which includes the Ellis–Jaffe sum rule for the proton S^p_{EJ} and the neutron, S^n_{EJ}, the Bjorken sum rule S , the polarization of the strange sea Δs and q_0 (which corresponds 2 * $\left\langle \hat{S}_z \right\rangle$). In the *"SU* (6)" model the axial coupling constants are given by Eq. (4.45); in the *"SU* (3)" model the amplitudes *F* and *D* also are fitted to the semi-leptonic decay data. The wave function includes (a) tree level, (b) tree level plus octet baryons and pseudoscalar mesons (oct, ps), (c) as in (b) but also including the decuplet baryons (oct, dec, ps) and (d) denoted by "full" includes, in addition, the vector meson octet.

On the tree level in *SU*(6) all the spin of the proton is due to the spin of the quarks. If one considers the mesonic admixture, 15% of the proton spin arises from the orbital momentum of mesons and bare baryons. In the *SU*(3) case, qo is already reduced to 0.5 on the tree level because of the effective *F* and *D* amplitudes. Mesonic corrections do not further reduce that value (note: the *F* and *D* parameters are refitted). It is important to realize that in the MCM with *SU* (6) parameters one implicitly assumes that the spin of the "bare" nucleon, delta and admixed mesons is 100% quark spin. This, however, is not true in relativistic model where nearly 50% of the nucleon is due to orbital momenta of the quarks (small components of the Dirac wave function). Calculations which include this effect have not yet been done.

The results of the MCM using effective *F* and *D* amplitudes resemble very much earlier calculations within the cloudy bag model [60]. Also here the depolarization due to the πN-admixture is essentially compensated by the $\pi\Delta$ admixture, so that the originally MIT-bag value of $S^p_{EJ} = 0.18$ is only slightly reduced.

TABLE 4.5
The Ellis–Jaffe Sum Rule for Proton and Neutron, the Bjorken Sum Rule and the Axial Flavor Singlet Coupling Constant Obtained with Inclusion of Different Fock States: Octet Baryons with Pseudoscalar Mesons (oct, ps), Octet and Decuplet Baryons with Pseudoscalar Mesons (oct, decu, ps) and with Vector Mesons in Addition (all)

The axial coupling constants for the SU(3) case are: $F = 0.53, D = 1.15$ for (oct, ps) and $F = 0.48, D = 0.91$ for (oct, decu, ps) and $F = 0.53, D = 1.15$ (all).

	S^p_{EJ}	S^n_{EJ}	S_B	Δq_0	Δs_0
$SU(6)$ tree	0.278	0	0.278	1	0
oct, ps	0.212	0.004	0.208	0.779	0.004
oct, decu, ps	0.233	–0.010	0.243	0.804	0.002
all	0.220	0.011	0.209	0.846	0.017
$SU(3)$ tree	0.173	–0.037	0.210	0.489	0
oct,ps	0.154	–0.056	0.210	0.356	0.003
oct, decu, ps	0.169	–0.041	0.210	0.461	0.001
all	0.179	–0.031	0.210	0.541	0.018

The comparison of the two models also sheds some light on the model-dependence of the Ellis–Jaffe sum rule which relies completely on the Cabbibo-model of semi-leptonic decays. Whereas these decays can be equally well described in the parameter free MCM-$SU(6)$ model and the 2 parameter $SU(3)$ (Cabbibo) model, the sum rule and the spin content Δq_0 are very different. In particular one knows that the $U_A(1)$-anomaly [63, 104, 109, 110] may play an important role.

5. MESONS IN THE PROTON AS TARGETS FOR DEEP-INELASTIC SCATTERING

The experimental determination of the quark structure function of the pion is of crucial importance for our understanding of hadron physics. From chiral symmetry one expects that the pion, as a Goldstone mode, might have a quite different structure compared with other mesons and baryons. Actually, quark-models predict that the pion should be a highly collective object and that this might show up in the structure function — as is the case for collective states in nuclear physics.

Up to now the only feasible method to extract the pion structure function has been the πN Drell–Yan production. The disadvantages of this method are that the attainable luminosity is low and that only the valence part of the pion structure function at rather large $x\,(\geq 0.2)$ can be studied — see however [111]. An extension of our knowledge of the pion structure function is possible by using the virtual pions of the meson cloud around the proton as targets in deep-inelastic scattering [70]. As we have discussed before, these pions arise naturally as a consequence of the pion–nucleon coupling and the interaction of high-energy projectiles like nucleons, pions or leptons with the virtual pion of the πN Fock state of the proton. It is a typical stripping reaction, in which the momentum distribution of the spectator nucleon reflects the momentum distribution in the πN (meson–baryon) Fock state.

In Fig. 5. la, we show again the pp-reaction which has been used in Section 4.1 to determine the π^+ and ρ^+ Fock states in the proton. It is important to realize that this reaction is in the same kinematic region as the deep-inelastic electron scattering, shown in Figs. 5.1b and 5.1c. Therefore once the fluxes (splitting functions) $f_{n\pi^+/p}\,(z, p_\perp^2)$ and $f_{\Delta^{++}\pi^-/p}\,(z, p_\perp^2)$ are known, one can reverse the "Sullivan processes" and determine the pion and rho structure functions from the semi-inclusive production of neutrons. As in the pp-reaction we expect that the semi-inclusive reactions

$$\begin{array}{ll} \text{(a)} & \text{ep} \rightarrow e'nX \\ \text{(b)} & \text{ep} \rightarrow e'\Delta X \end{array} \tag{5.1}$$

in the properly chosen kinematical domain, will also be dominated by the pion exchange [33] mechanism of Fig. 5.1. Ifthis is the case, then the straightforward generalization of Eq. (4.1) to semi-inclusive deep-inelastic electron scattering is

$$\frac{d\sigma(ep \rightarrow e'nX)}{dx dQ^2 dz dp_\perp^2} = \frac{2}{3} f_{n\pi^+/p}\left(z, p_\perp^2\right) \times K(x, Q^2) F_2^{e\pi}(x_\pi, Q^2) \tag{5.2}$$

where $F_2^{e\pi}\,(x_\pi, Q^2)$ is the structure function of the pion; $x_\pi = x/\,(1-z)$ is the Bjorken variable in the electron–pion deep-inelastic scattering, with the obvious kinematical restriction $0 < x < 1 - z$, and $K\,(x, Q^2)$ is the standard kinematical factor

$$K(x,Q^2) = \frac{4\pi\alpha^2}{Q^4}\frac{1}{x}\left[1 - y + \frac{1}{2}y^2\right], y = \frac{Q2}{xs}$$

assuming for the sake of simplicity $2xF_1^{e\pi}\,(x) = F_2^{e\pi}\,(x)$. Knowing all kinematical variables, and trusting the theoretical prediction for $f_{n\pi^+/p}\,(z, p_\perp^2)$, one can

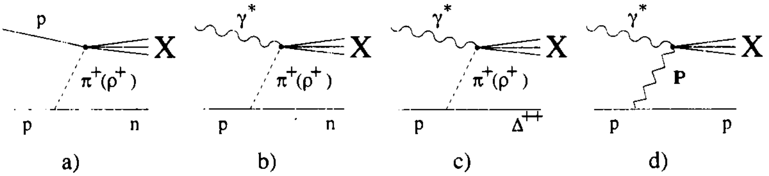

Fig. 5.1. The pion (rho) exchange contributions to the inclusive neutron production (a) in *pp*-scattering, and (b) neutron, and (c) Δ^{++} production in deep-inelastic scattering. Diagram (d) shows the diffractive production of N^*'s by pomeron exchange.

invert Eq. (5.2) and determine the pion structure function from the experimentally measured semi-inclusive cross section. In the HERA experiments, one can go down to the region of very small x_π ($\geq 10^{-4}$). This will be an enormous expansion of the kinematical region studied compared with the πN Drell–Yan experiments, which cannot go much below $x_\pi \sim 0.1$ [74]. Furthermore, such a determination of the pion structure function at HERA would allow one to study the scaling violations in the pion structure function in a broad range of (x_π, Q^2), which is hardly possible in the Drell–Yan experiments.

From the purely experimental point of view, the semi-inclusive reaction $ep \rightarrow e'nX$ is being studied already by the ZEUS collaboration, which has installed a test forward neutron calorimeter (FNC) to complement its leading proton spectrometer [112]. This FNC was tested with neutrons from inclusive proton beam-gas interactions, and an excellent agreement between the measured spectra and the pion-exchange predictions was found.

The principal task is to find the kinematical domain in which the semi-inclusive reaction $ep \rightarrow e'nX$ is dominated by the pion-exchange contribution. The semi-inclusive production of neutrons with $z \sim 0.8$ turns out to be the optimal kinematical domain, and it also corresponds to the domain in which the semi-inclusive cross section is largest. The fluxes for the charge-exchange reactions, $p \rightarrow n$ and $p \rightarrow \Delta^{++}$, as well as the reaction $p \rightarrow p$, are shown in Fig. 5.2. The expected counting rates can be judged by the total number of virtual pions in the nucleon as given in Table 4.1, n_π $(\pi N) \approx 0.18$, n_π $(\pi\Delta) \approx 0.06$, which shows that deep-inelastic scattering on pions, accompanied by $p \rightarrow n, \Delta$ fragmentation, will have a statistical weighting only one order of magnitude lower than that for *ep* scattering.

The background to the pure pion exchange comes from interaction with Fock states which contain heavier mesons $M = K, \rho, \omega$..... Evidently, in such states the heavy mesons M will carry a larger fraction of the momentum of the MN state, and the heavy meson exchange will contribute to the spectrum of neutrons at smaller z in comparison with the pion exchange (we do not discuss

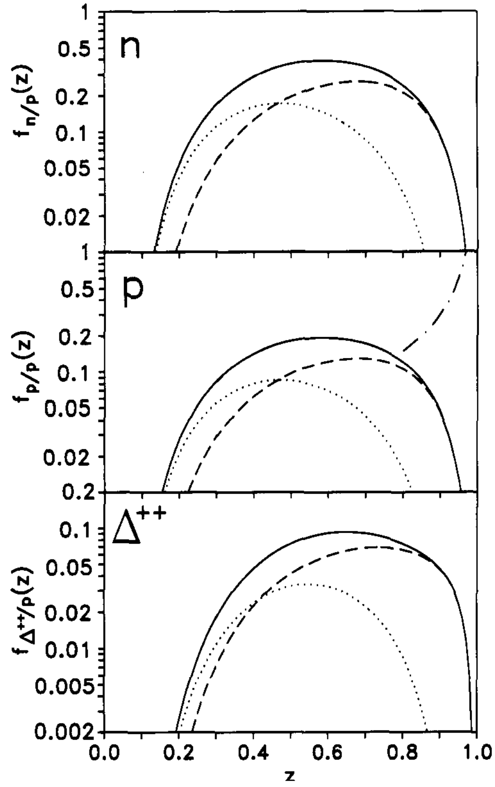

Fig. 5.2. Longitudinal momentum distribution of(a) neutrons, (b) protons, and (c) Δ^{++}. The contributions of the π and ρ exchange mechanisms are shown by the dashed and dotted line. respectively. The contribution from the pomeron exchange mechanism to the $p \rightarrow p$ fragmentation is shown by the dash-dotted line [70].

here the region of $1 - z \ll 1$, where the Reggeization of mesons becomes important). In Fig. 5.2 the effect of the r-meson is shown as a dotted curve. Evidently, choosing the region $z \sim 0.7$–0.8, one can eliminate much of the ρ-exchange background. A still better separation of the π and ρ exchange can be achieved if one compares the $p_\perp$ distributions for the two mechanisms. As shown in Fig. 5.3 the best way of discriminating between the π and ρ contribution is to select only events with $p_\perp^2 \leq 0.1$ (GeV/c)^2. Then the relative contribution of the pion exchange is significantly enhanced.

In the suggested mechanism for semi-inclusive neutron production, the differential cross section (5.2) is a product of the universal flux factor, which only depends on z, and the structure function $F_2^\pi(x_\pi, Q^2)$ which is a function of $x_\pi = x/(1 - z)$. This factorization property allows an important cross check of the model: binning the semi-inclusive cross section data as a function of z should not depend on x_π. Furthermore this z-dependence should be identical

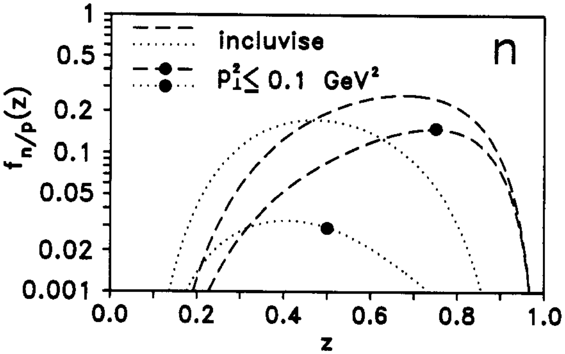

Fig. 5.3. Longitudinal momentum distribution of neutrons (see Fig. 5.28) with the extra condition $p_\perp^2 < 0.1$ (GeV/c)^2 (lower curves) compared to the unconstrained one (upper curves, see Fig. 5.2a). The π exchange contributions are shown by dashed lines; the ρ exchange contributions by the dotted lines.

to the z-dependence of the inclusive spectra of neutrons from the hadronic ρN interactions. Remarkably, the FNC of the ZEUS collaboration enables the latter cross check to be performed in situ, directly comparing the spectra of neutrons from inclusive beam-gas interactions and from deep-inelastic ep scattering. Such a comparison of the two spectra will allow one to verify that the background contribution to $z \sim 0.7$–0.8, from deep-inelastic scattering off the baryonic core, is as small as in hadronic reactions. Reversing the argument, one can determine the x_π dependence of the pion structure function by changing x at fixed values of z and verifying that the xp dependence comes out the same at all values of z.

The above discussion is fully applicable to the semi-inclusive production of Δ^{++}. The longitudinal momentum distribution of Δ^{++} is shown in Fig. 5.2c. As in the $p \to n$ case, the contributions from the π and ρ exchange mechanism are fairly well separated, with the π-exchange contribution dominating at large z. Measuring the Δ^{++} production at HERA will require good experimental resolution of both the proton and π^+ resulting from the Δ^{++} decay, which requires multitrack identification of the leading proton spectrometer. The ZEUS collaboration has such a device operating at HERA [113]. The measurements of Δ^{++} production are important for the direct evaluation of the contribution of the two-step process $p \to \Delta \to n\pi$ to the spectrum of neutrons. The Δ decay background to the spectrum of neutrons is small — isospin symmetry considerations imply that the relative contamination of the neutron spectra $n_\pi(\pi\Delta) / (3n_\pi(\pi N)) \approx 0.1$.

It is important to realize that in order to relate x_π, the Bjorken variable in the electron–pion deep-inelastic scattering and z, the longitudinal momentum fraction carried by the neutron, the basic symmetry for the splitting function [Eq. (3.7)] has to be fulfilled. As discussed in Section 3 this puts stringent restrictions on the form factors in the vertex function which are not fulfilled by the conventional form-factors which depend only on the momentum variable t [118].

6. CONCLUSION

On very general grounds the meson cloud must play an important role in the structure of the nucleon. In particular π-nucleon, π-delta and ρ-nucleon Fock space components constitute nearly 40% of the nucleon wave function. We have explored the phenomenological consequences of the cloud in a variety of experiments and we have shown that it gives large effects in the non-perturbative regime of QCD. The investigations range from semi-inclusive nucleon–nucleon scattering to polarized and unpolarized DIS, semi-inclusive DIS, exclusive electroproduction of mesons, Drell–Yan experiments and semi-leptonic decays of baryons.

The model so far has several outstanding successes:

I. The initial prediction of the asymmetry of the quark sea $\bar{d} > \bar{u}$ has been confirmed some years later by NMC.

II. After determining the πN and πN form factors from semi-inclusive pp data, recent calculations quantitatively reproduce (parameter free) the measured $\bar{d} - \bar{u}$ asymmetry. Also, the calculated shape of $\bar{u}(x) / \bar{d}(x)$ seems to be well described.

III. Deep-inelastic scattering off the meson cloud explains a significant part of the experimental sea-quark structure functions of the nucleon for $Q^2 \leq 5$ GeV^2 and $x > 10^{-2}$.

IV. The meson cloud model reproduces the 5 experimentally known data of the semi-leptonic decay of the baryon octet equally well as the two parameter fit of the Cabbibo model.

V. Valence quark structure functions deduced from a model which combines the bag and meson cloud model agree surprisingly well with the phenomenological ones.

Moreover the model makes some definite predictions which may be tested in the near future:

(i) The polarization of the strange quark sea in the nucleon is very small. Therefore strange quarks carry a negligibly small fraction of the spin of the nucleon.

(ii) The fraction of the spin of the nucleon which arises from the orbital momentum between mesons and baryons is only 15%.

(iii) Using the meson cloud model, a method has been suggested to measure the pion structure function down to $x \approx 10^{-4}$, by exploiting the non-perturbative πN and $\pi\Delta$ Fock components of the nucleon which dominate the fragmentation of protons into fast neutrons and Δ's.

From all that has been reviewed here it should be obvious that the meson cloud model represents an important link between classical nuclear physics and high-energy particle physics. In the first case mesons and baryons are the relevant degrees of freedom whereas the latter is dominated by quarks and gluons. The model which we have presented here extends the meson–baryon dynamics into the non-perturbative regime of QCD and represents therefore an important tool to help to explore it.

ACKNOWLEDGMENTS

It is a pleasure to thank the many colleagues who have contributed to our understanding of the issues presented here. We would like to thank particularly W.-P. Hwang, H. Holtmann, N. Isgur, J. T. Londergan, W. Melnitchouk, N. N. Nikolaev, A. W. Schreiber, A. I. Signal, S. Steffens, A. Szczurek, and V. Zoller. One of us (J. S.) wishes to thank Tony Thomas and Nathan Isgur for their hospitality during his visits at the University of Adelaide and Jefferson Laboratory where this work has been done. This work was supported in part by the Australian Research Council, the US Department of Energy under contract DE-AC05-84ER40 1 50 and the Humboldt senior research award program.

A. LAGRANGIANS

Here we present the interaction Lagrangians we employ in our calculations. They are usually used in meson exchange models [33]. Φ, denotes a spin-1/2 field (N), Ψ a spin-3/2 field (Δ) of Rarita–Schwinger form; with π pseudoscalar fields are denoted, with q vector fields (ρ, ω):

$$L_1 = g \cdot i\bar{\Phi}\gamma_5 \pi \Phi \tag{7.1}$$

$$L_2 = f \cdot \bar{\Phi}\partial_\mu \Phi \Psi^\mu + h.c \tag{7.2}$$

$$L_3 = g \cdot \bar{\Phi}\gamma_\mu \theta^\mu \Phi + f \cdot \bar{\Phi}\sigma_{\mu\nu}\Phi(\partial^\mu \theta^\nu - \partial^\nu \theta^\mu) \tag{7.3}$$

$$L_4 = f \cdot i\bar{\Phi}\gamma_5 \gamma_\mu \Psi_\nu (\partial^\mu \theta^\nu - \partial^\nu \theta^\mu) + h.c \tag{7.4}$$

The anti-symmetric tensor sμv, here is defined as $\sigma_{\mu\nu} = \frac{i}{2}[\gamma_\mu, \gamma_\nu]$.

B. VERTEX FUNCTIONS

Here we list results [58] for helicity dependent vertex functions $V^{\lambda\lambda'}_{\text{IMF}}(y, k_\perp^2)$. y here denotes the longitudinal momentum fraction of the baryon in the nucleon; $\vec{k}_\perp = (k_\perp \cos\varphi, k_\perp \sin\varphi)$ the transverse momentum of the baryon with respect to the nucleon momentum. The contributions are listed according to particle helicities (1/2 → λ, λ′), with λ and λ′ being the baryon and meson helicities respectively.

a) Transitions for L_1 ($N\pi$, $N\eta$, ΣK, ΛK)

$$\frac{1}{2} \to +\frac{1}{2},\ 0 \quad \frac{g}{2}\frac{ym_N - m_B}{\sqrt{ym_N m_B}}$$

$$\frac{1}{2} \to -\frac{1}{2},\ 0 \quad \frac{ge^{-i\varphi}}{2}\frac{k_\perp}{\sqrt{ym_n m_B}}$$

b) Transitions for L_2 ($\Delta\pi$, $\Sigma^* K$)

$$\frac{1}{2} \to +\frac{3}{2},\ 0 \quad -\frac{fe^{+i\varphi}}{2\sqrt{2}}\frac{k_\perp(ym_N + m_B)}{y\sqrt{ym_N m_B}}$$

$$\frac{1}{2} \to +\frac{1}{2},0 \quad \frac{f}{2\sqrt{6}}\frac{(ym_N + m_B)^2(ym_N - m_B) + k_\perp^2(ym_N + 2m_B)}{ym_B\sqrt{ym_N m_B}}$$

$$\frac{1}{2} \to -\frac{1}{2},\ 0 \quad \frac{fe^{-i\varphi}}{2\sqrt{6}}\frac{k_\perp[(ym_N + m_B)^2 - 3m_B(ym_N + m_B) + k_\perp^2]}{ym_B\sqrt{ym_N m_B}}$$

$$\frac{1}{2} \to -\frac{3}{2},\ 0 \quad -\frac{fe^{-2i\varphi}}{2\sqrt{2}}\frac{k_\perp^2}{y\sqrt{ym_N m_B}}$$

c) Transitions for L_3 ($N\rho$, $N\omega$, ΣK^*, $\Lambda K'$)

$$\frac{1}{2} \to +\frac{1}{2},\ +1 \quad \frac{ge^{+i\varphi}}{\sqrt{2}}\frac{k_\perp}{(1-y)\sqrt{ym_N m_B}} - f\sqrt{2}e^{+i\varphi}\frac{k_\perp m_N}{\sqrt{ym_N m_B}}$$

$$\frac{1}{2} \to +\frac{1}{2}, \quad 0 \quad \frac{g}{2}\frac{k_\perp^2 + m_N m_B (1-y)^2 - y m_M^2}{2(1-y)\, m_M \sqrt{y m_N m_B}}$$

$$-\frac{f}{2}\frac{(y m_N - m_B)\left(y^2 m_N^2 - y\left(m_N^2 + m_B^2 + m_M^2\right) + m_B^2 + k_\perp^2\right)}{y m_M \sqrt{y m_N m_B}}$$

$$\frac{1}{2} \to +\frac{1}{2}, \quad -1 \quad \frac{g e^{-i\varphi}}{\sqrt{2}}\frac{y k_\perp}{(1-y)\sqrt{y m_N m_B}} + f\sqrt{2} e^{-i\varphi}\frac{k_\perp m_B}{\sqrt{y m_N m_B}}$$

$$\frac{1}{2} \to -\frac{1}{2}, \quad +1 \quad -\frac{g}{\sqrt{2}}\frac{y m_N - m_B}{\sqrt{y m_N m_B}}$$

$$-f\sqrt{2}\frac{k_\perp^2 - (m_N + m_B)(1-y)(y m_N - m_B)}{(1-y)\sqrt{y m_N m_B}}$$

$$\frac{1}{2} \to -\frac{1}{2}, \quad 0 \quad -\frac{g e^{-i\varphi}}{2}\frac{k_\perp (m_N - m_B)}{m_M \sqrt{y m_N m_B}}$$

$$-\frac{f e^{-i\varphi}}{2}\frac{k_\perp (1+y)\left(y^2 m_N^2 - y\left(m_N^2 + m_B^2 + m_M^2\right) + m_B^2 + k_\perp^2\right)}{y(1-y)\, m_M \sqrt{y m_N m_B}}$$

$$\frac{1}{2} \to -\frac{1}{2}, \quad -1 \quad f\sqrt{2} e^{-2i\varphi}\frac{k_\perp^2}{(1-y)\sqrt{y m_N m_B}}$$

d) Transitions for L₄ (Aρ,Σ∗*K**)

$$\frac{1}{2} \to +\frac{3}{2}, \quad +1 \quad -\frac{f e^{+2i\varphi}}{2}\frac{k_\perp^2}{y(1-y)\sqrt{y m_N} m_B}$$

$$\frac{1}{2} \to +\frac{3}{2}, \quad 0 \quad \frac{f e^{+i\varphi}}{\sqrt{2}}\frac{k_\perp m_M}{(1-y)\sqrt{y m_N} m_B}$$

$$\frac{1}{2} \to +\frac{3}{2}, \quad -1 \quad \frac{f}{2}\frac{m_N m_B (1-y)^2 - y m_M^2}{(1-y)\sqrt{y m_N} m_B}$$

$$\frac{1}{2} \to +\frac{1}{2}, \quad +1 \quad \frac{f e^{+i\varphi}}{2\sqrt{3}}\frac{k_\perp \left[k_\perp^2 - 2(1-y) m_B^2\right]}{y(1-y)\, m_B \sqrt{y m_N} m_B}$$

$$\frac{1}{2} \to +\frac{1}{2}, \quad 0 \quad -\frac{f}{\sqrt{6}}\frac{m_M \left[k_\perp^2 + m_B (1-y)(y m_N - m_B)\right]}{(1-y)\, m_B \sqrt{y m_N} m_B}$$

$$\frac{1}{2} \to +\frac{1}{2}, \quad -1 \quad \frac{f e^{-i\varphi}}{2\sqrt{3}}\frac{k_\perp \left[y m_M^2 - 2 m_N m_B (1-y)\right]}{(1-y)\, m_B \sqrt{y m_N} m_B}$$

$$\frac{1}{2} \to -\frac{1}{2}, \quad +1 \quad \frac{f}{2\sqrt{3}}\frac{2(1-y)\, m_B k_\perp^2 + m_N m_M^2 y^3 - (1-y)^2 m_B^3}{y(1-y)\, m_B \sqrt{y m_N} m_B}$$

$$\frac{1}{2} \to -\frac{1}{2}, \quad 0 \quad \frac{f e^{-i\varphi}}{\sqrt{6}}\frac{k_\perp m_M (y m_N - (1-y) m_B)}{(1-y)\, m_B \sqrt{y m_N} m_B}$$

$$\frac{1}{2}\rightarrow-\frac{1}{2},\quad -1\quad \frac{fe^{-2i\varphi}}{2\sqrt{3}}\,\frac{k_{\perp}^{2}m_{N}}{(1-y)\,m_{B}\sqrt{ym_{N}m_{B}}}$$

$$\frac{1}{2}\rightarrow-\frac{3}{2},\quad +1\quad \frac{fe^{-i\varphi}}{2}\,\frac{k_{\perp}m_{B}\,(1-y)}{y\sqrt{ym_{N}m_{B}}}$$

$$\frac{1}{2}\rightarrow-\frac{3}{2},\quad 0\quad 0$$

$$\frac{1}{2}\rightarrow-\frac{3}{2},\quad -1\quad 0$$

REFERENCES

1. A. W. Thomas, in Progress in Nuclear and Particle Physics **11**, **325** (1984); 20 (1988) 21.
2. J. Aubert *et al.*, Phys. Lett. B123 (1983) 275.
3. D. F. Geesaman, K. Saito, and A. W. Thomas, Ann. Rev. Nucl. Part. Sci. **45** (1995) 337.
4. M. Arneodo, Phys. Rep. **240** (1994) 301.
5. S. D. Drell, D. J. Levy, and T. M. Yan, Phys. Rev. **D1** (1970) 1035.
6. J. D. Sullivan, Phys. Rev. **D5** (1972) 1732.
7. C. H. Llewellyn Smith, Phys. Lett. **128** (1983) 107.
8. M. Ericson and A. W. Thomas, Phys. Lett. **B148** (1984) 181.
9. E. L. Berger, F. Coester, and R. B. Wiringa, Phys. Rev. **D29,** 398 (1984); E. L. Berger and F. Coester, Ann. Rev. Nucl. Part. Sci. **37** (1987) 364.
10. A. W. Thomas, Phys. Lett. **B126** (1983) 97.
11. P. Amandruz *et al.,* Phys. Rev. Lett. **66,** 2712 (1991); Phys. Lett. **B292** (1992) 159.
12. F. E. Close, *An Introduction to Quarks and Partons,* Academic Press, NY (1979).
13. E. Leader and E. Predazzi, *An Introduction to Gauge Theories and the New Physics,* Cambridge (1982).
14. T. Muta, *Foundations of Quantum Chromodynamics,* World Scientific, Singapore (1987).
15. C. T. Sachrajda, in Gauge Theories in High Energy Physics, North Holland, Amsterdam (1983).
16. F. Yndurain, Quantum Chromodynamics, Springer, Berlin (1983).
17. J. L. Alonso and R. Tarrach (eds.) Quantum Chromodynamics, Springer, Berlin (1980).
18. G. Altarelli, Phys. Rep. **81** (1982) 1.
19. N. S. Craigie *et al.,* Phys. Rep. **99** (1983) 69.
20. E. Sather, Phys. Lett. **B274** (1992).
21. E. N. Rodionov, A. W. Thomas, and J. T. Londergan, Mod. Phys. Lett. **A9** (1994) 1799.
22. S. Dasu *et al.,* Phys. Rev. Lett. **61** (1988) 1061.
23. J. Phys. (322, No. 6 (1996) Ed. R. Devenish and J. Sterling.
24. B. Badelek *et al.*, J. Phys. **G22** (1996) 815.
25. A. I. Signal and A. W. Thomas, Phys. Lett. **B191**(1987) 205.
26. X. Ji and J. Tang, Phys. Lett. **B362** (1995) 182.
27. H. Holtmann, A. Szczurek, and J. Speth, Nucl. Phys. **A596** (1996) 631.
28. A. Baldit *et al.,* Phys. Lett. **B332** (1994) 244.
29. A. 0. Bazarko *et al.,* Z. Phis. **C65** (1995) 189.
30. A. D. Martin, W. J. Sterling, and R. G. Roberts, Phys. Rev. **D50** (1994) 6734.

31. W. Melnitchouk and A. W. Thomas, Acta Physica Polonica **B27,** 1407 (1996); Phys. Lett. **B377** (1996)11.
32. S. J. Brodsky *et al.*, Nucl. Phys. **B441** (1995) 197.
33. R. Machleidt, K. Holinde, and Ch. Elster, Phys. Rep. **149** (1987) 1.
34. G. E. Brown and M. Rho, Phys. Lett. **B83** (1979) 177.
35. A. W. Thomas, Adv. Nucl. Phys. **13** (1984) 1.
36. S. Theberge, G. A. Miller, and A. W. Thomas, Can. J. Phys. **60** (1982) 59.
37. R. F. Alvarez-Estrada and A. W. Thomas, J. Phys. **G9** (1983) 161.
38. S. Kumano and J. T. Londergan, Phys. Rev. **D44** (1991) 717.
39. L. L. Frankfurt, L. Mankiewicz, and M. I. Strikman, Z. Phys. **A334** (1989) 343.
40. W.-Y. P. Hwang, J. Speth, and G. E. Brown, Z. Phys. **A339** (1991) 383.
41. V. R. Zoller, Z. Phys. **C53** (1992) 443.
42. S. Deister, M. F. Gari, W. Krümpelmann, and M. Mahlke, Few Body Systems **10** (1991) 1.
43. A. W. Thomas and K. Holinde, Phys. Rev. **C43** (1990) RI 195.
44. G. Janssen, K. Holinde, and J. Speth, Phys. Rev. Lett. **73** (1994) 1332.
45. R. P. Feynman, Photon Hadron Interactions, Benjamin, Reading (1972).
46. S. Weinberg, Phys. Rev. **150** (1966) 1313.
47. W. Melnitchouk, A. W. Schreiber, and A. W. Thomas, Phys. Rev. **D49** (1994) 1183.
48. J. D. Bjorken, Phys. Rev. **179** (1969) 1547.
49. E. M. Henley and G. A. Miller, Phys. Lett. **B251** (1990) 453.
50. S. Kumano, Phys. Rev. **D43** (1991) 59.
51. A. Szczurek and J. Speth, Nucl. Phys. **A555** (1993) 249.
52. W. Melnitchouk, A. W. Thomas, and A. I. Signal, Z. Phys. **A340** (1991) 85.
53. W. Melnitchouk and A. W. Thomas, Phys. Rev. **D47** (1993) 3783.
54. A. W. Thomas and W. Melnitchouk in: Proceedings of the JSPS-INS Spring, School (Shimoda, Japan); World Scientific, Singapore (1993).
55. H. Holtmann, A. Szczurek, and J. Speth, Jülich preprint KFA-IKP (TH) 33 (1993).
56. A. W. Schreiber, P. J. Mulders, and H. Meyer, Phys. Rev. **C46** (1992) 458.
57. V. Dmitrasinovic and R. Tegen, Phys. Rev. **C46** (1992) 1108.
58. H. Holtmann, Dissertation, University of Bonn, Dez. (1995).
59. V. R. Zoller, Z. Phys. **C60,** 141 (1993); Mod. Phys. Lett. **A8** (1993) 1113.
60. A. W. Schreiber and A. W. Thomas, Phys. Lett. **B215** (1988) 141.
61. A. W. Schreiber, A. W. Thomas, and J. T. Londergan, Phys. Rev. **D42** (1990) 2226.
62. A. Le Yaounanc et al., Phys. Rev. **D11** (1975) 2636.
63. G. Parisi and G. Petronzio, Phys. Lett. **B62** (1976) 331.
64. A. W. Schreiber, A. I. Signal, and A. W. Thomas, Phys. Rev. **D44** (1991) 2653.
65. F. M. Steffens and A. W. Thomas, Prog. Theor. Phys. Suppl. **120** (1995) 145.
66. F. M. Steffens, H. Holtmann, and A. W. Thomas, Phys. Lett. **B358** (1995) 139.
67. G. Janssen, J. W. Durso, K. Holinde, B. C. Pearce, and J. Speth, Phys. Rev. Lett. **71** (1993) 1978.
68. J. Haidenbauer, K. Holinde, and A. W. Thomas, Phys. Rev. **C49** (1994) 233I.
69. G. Janssen, Dissertation Mai (1995) University of Bonn.
70. H. Holtmann, G. Levman, N. N. Nikolaev, A. Szczurek, and J. Speth, Phys. Lett. **B338** (1994) 363.
71. M. M. Nagels, T. A. Rijken, and J. J. de Swart, Phys. Rev. D17 (1978) 768.
72. W. Flauger and F. Monning, Nucl. Phys. **109** (1976) 347.
73. V. Blobel etal., Nucl. Phys. **B135** (1978) 379.
74. P. J. Sutton, A. D. Martin, R. G. Roberts, and W. J. Stirling, Phys. Rev. **D45** (1992) 2349.
75. J. T. Londergan, G. T. Garvey, G. Q. Liu, E. N. Rodionov, and A. W. Thomas, Phys. Lett. **B340**(1994) 115.
76. C. Foudas et al., Phys. Rev. Lett. **64** (1990) 1207.

77. M. Arneodo *et al.,* Phys. Rev. **D50** (1994) RI.
78. W. C. Leung *et al.,* Phys. Lett. **B317** (1993) 655.
79. S. R. Mishra *et al.,* Phys. Rev. Lett. **68** (1992) 3499.
80. A. D. Martin, W. J. Sterling, and R. G. Roberts, Phys. Lett. **B306** (1993) 145.
81. A. Bodek *et al.,* Phys. Rev. Lett. **30** (1973) 1087.
82. A. I. Signal and A. W. Thomas, Phys. Rev. **D40** (1989) 2832.
83. S. D. Drell and T. M. Yan, Ann. Phys. **66** (1971) 578.
84. D. M. Alde *et al.,* Phys. Rev. Lett. **64** (1990) 2479.
85. A. Szczurek, J. Speth, and G. T. Garvey, Nucl. Phys. **A570** (1994) 765.
86. A. Szczurek, M. Ericson, H. Holtmann, and J. Speth, Nucl. Phys. **A596** (1996) 397.
87. P. L. McGaughey *et al.,* Phys. Rev. Lett. **69** (1992) 1726.
88. H. Holtmann, N. N. Nikolaev, J. Speth, and A. Szczurek, Z. Phys. A353 (1996) 41 1.
89. A. S. Ito *et al.,* Phys. Rev. **D23** (1981) 604.
90. J. F. Owens, Phys Lett. **B266** (1991) 126.
91, F. M. Steffens and A. W. Thomas, Phys. Lett. **B389** (1996) 217.
92. G. T. Garvey *et al.,* FNAL proposal, **P866** (1992).
93. W. Melnitchouk and A. W. Thomas, Z. Phys. **A353** (1995) 311.
94. J. Haidenbauer, K. Holinde, V. Mull, and J. Speth, Phys. Lett. **B291** (1992) 223.
95. M Albert, J. Ellis, and D. Kharzeev, Phys. Lett. **B356** (1995) 113.
96. J. Speth and V. Zoller, Phys. Lett. **B351** (1995) 533.
97. H. J. Pirner and B. Povh, in Proceedings of the Italian Physical Society, Vol. 44, Ed. J. Arvieux and E. De Santis (1992).
98. J. D. Bjorken, Phys. Rev. **148** (1966) 1467.
99. J. Ellis and R. J. Jaffe, Phys. Rev. **D9** (1974) 1444.
100. J. Ashman *et al.,* Nucl. Phys. **B328** (1989).
101. D. Adam *et al.,* Phys. Lett. **B329** (1994) 399.
102. P. L. Anthony *et al.*, Phys. Rev. Lett. **71** (1993) 959.
103. J. Ellis and M. Karliner, Phys. Lett. **B341** (1995) 397.
104. S. D. Bass and A. W. Thomas, Prog. Part. Nucl. Phys. **33** (1994) 449.
105. K. Kubodera, Y. Kohymma, K. Oikawa, and C. W. Kim, Nucl. Phys. **A439** (1985) 695.
106. Particle Data Group, Phys. Rev. **D45** (1992) 1.
107. N. N. Bogoliubov, Ann. Inst. Henri Poincaré 8 (1963) 163.
108. C. Hayne and N. Isgur, Phys. Rev. **D25** (1982) 1944.
109. H. Fritzsch, Phys. Lett. **B229** (1989) 291.
110. G. M. Shore and G. Veneziano, Phys. Lett. **B224** (1990) 75.
111. J. T. Londergan, G. Q. Liu, E. N. Rodionov, and A. W. Thomas, Phys. Lett. **B361** (1995) 110.
112. S. Bhadra *et al.,* DESY-preprint 94-084 (l994), Nucl. Inst. and Methods, **A354** (1995) 479.
113. ZEUS-Collaboration, The ZEUS-detector, status report (1993).
114. H. Abramowicz *et al.(CDHS* Collaboration), Z. Phis. **C15,** 19 (1982); **C17** (1983) 1283.
115. D. W. Duke and J. T. Owens, Phys. Rev. **D30** (1984) 49.
116. F. Güttner, G. Chandray, H. J. Pimer, and B. Povh, Nucl. Phys. **A429** (1984) 389.
117. B. Kopeliovich, B. Povh, and I. K. Potashnikova, Z. Phys. **C73** (1996) 125.
118. W. Köpf, L. L. Frankfurt, and M. Strikman, Phys. Rev. **D53** (1996) 2586.

Chapter 3

MUON CATALYZED FUSION: INTERPLAY BETWEEN NUCLEAR AND ATOMIC PHYSICS

K. Nagamine
High Energy Accelerator Research Organization (KEK)
Tsukuba-shi, Ibaraki-ken, Japan
and
The Institute of Physical and Chemical Research (RIKEN)
Wako, Saitama, Japan

and

M. Kamimura
Department of Physics
Kyushu University
Hakozaki, Fukuoka, Japan

---

1. INTRODUCTION

Nuclear fusion is a phenomena of well-known nuclear reactions occurring mostly among light nuclei when they come close to each other within the range

---

Advances in Nuclear Physics, Vol. 24, edited by J. W. Negele and E. W. Vogt. Plenum Press, New York, ©1998.

TABLE 1.1
Typical Fusion Reactions

$p + d$	→	^{3}He + γ	(5.5 MeV)
$p + t$	→	^{4}He+ γ	(19.8 MeV)
$d + d$	→	^{3}He + n	(3.3 MeV)
		$t + p$	(4 MeV)
		^{4}He+ γ	(24 MeV)
$d + t$	→	^{4}He + n	(17.6 MeV)
$t + t$	→	^{4}He+2n	(10 MeV)
d+^{3}He	→	^{4}He+p	(18.35 MeV)

of the nuclear interaction distance (a few fm, fm = 10^{-13} cm). Because of a reduction of the sum of the rest masses from the initial state to the final state, one can expect the production of energy from such fusion reactions. The most stable nuclei are in the iron region and, in stellar collapse, nucleosynthesis from fusion occurs for all elements up to iron. For fusion energy in our sun and, indeed, for laboratory fusion energy, only the very lightest elements participate. In Table 1.1, the typical fusion reactions among very light nuclei are summarized.

Most fusion reactions have been studied at high energy (above 100 keV) using accelerators. There, the reaction partners come together closely enough to overcome the Coulomb repulsion. As described in this article, the muon catalyzed fusion (frequently the abbreviation μCF is used hereafter) phenomenon is a nuclear reaction at zero energy in which the negative muon effectively "hides" the positive charge of one of the hydrogen isotopes thus enabling the close approach necessary for fusion. There, our knowledge of the nuclear physics of the fusion reaction at high energy must be extrapolated.

Among two types of muons, namely, μ^+ and μ^-, only the μ^- is involved in muon catalyzed fusion research. The most fascinating features regarding muon catalyzed fusion concern: (1) varieties of phenomena related to the interplay of nuclear phenomena and atomic phenomena which, in turn, are related to the interplay of nuclear and electromagnetic interaction, respectively, and (2) possible future applications to energy resources. This is particularly true regarding the μCF in a deuterium and tritium (D–T) mixture with a high density ø comparable to the liquid hydrogen density, $ø_0$ (0.425×10^{23} nuclei/cc). In the following, the present understanding and future prospects of μCF are summarized with a particular emphasis on the D–T μCF and some limited descriptions on the μCF in DD as well as the other systems listed in Table 1.1.

The basic phenomena of the μCF involve the following two processes: (1) the formation of a small molecule, called a muonic molecule, consisting of two nuclei and a μ^- and an inter-molecular fusion reaction, and (2) a series of chain reactions of the fusion reactions mediated by a single μ^-. Regarding the case of

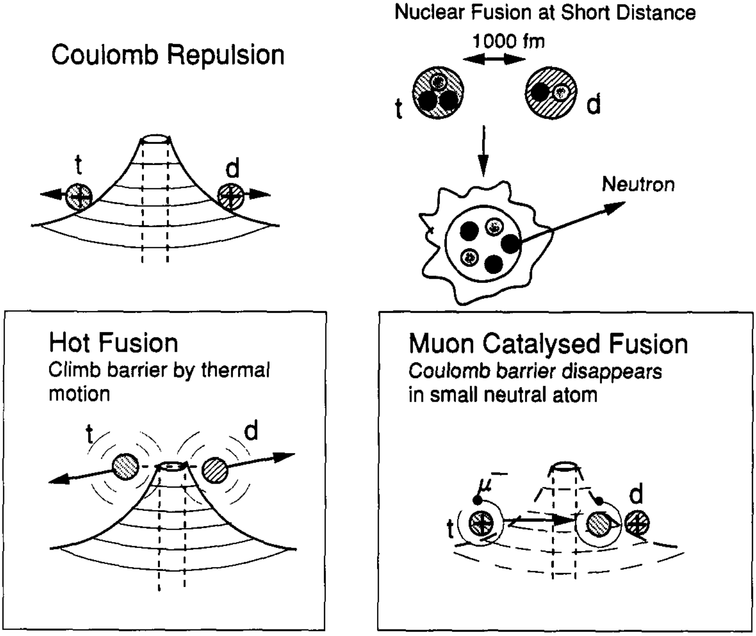

Fig. 1.1. Conceptual view of the role of a negative muon used to remove the repulsive potential between *d* and *t* to catalyze nuclear fusion with reference to thermal nuclear fusion.

the D–T μCF, these two processes are schematically summarized in Figs. 1.1 and 1.2. Sometimes, historically in particular, the chain reaction is presented in the form of a cyclic reaction by connecting the ending part of one unit of the chain reaction to the beginning part, as shown in Fig. 1.3. The basic processes for D–T μCF, the details of which are described in later sections, can be summarized as follows.

After high-energy μ^- injection and stopping in a D–T mixture either a (dμ) or ($t\mu$) atom is formed, depending upon the concentration of D and T (C_d and C_t, $C_d + C_t = 1$). Because of the difference in the binding energy of atomic states (either excited or ground) between ($d\mu$) and ($t\mu$), the μ^- in the atomic state of ($d\mu$) takes a transfer reaction to ($t\mu$) during a collision with the surrounding t in either DT or T_2 like $(d\mu) + t \rightarrow (t\mu) + d$ at the rate of λ_{dt}. Thus formed ($t\mu$) either after thermalization or before, reacts with D_2, DT or T_2 to form a muon molecule, where the formation of a specific state of the ($dt\mu$) molecule through the resonant formation mechanism is important for the fusion rate of $\lambda_{dt\mu}$. Once

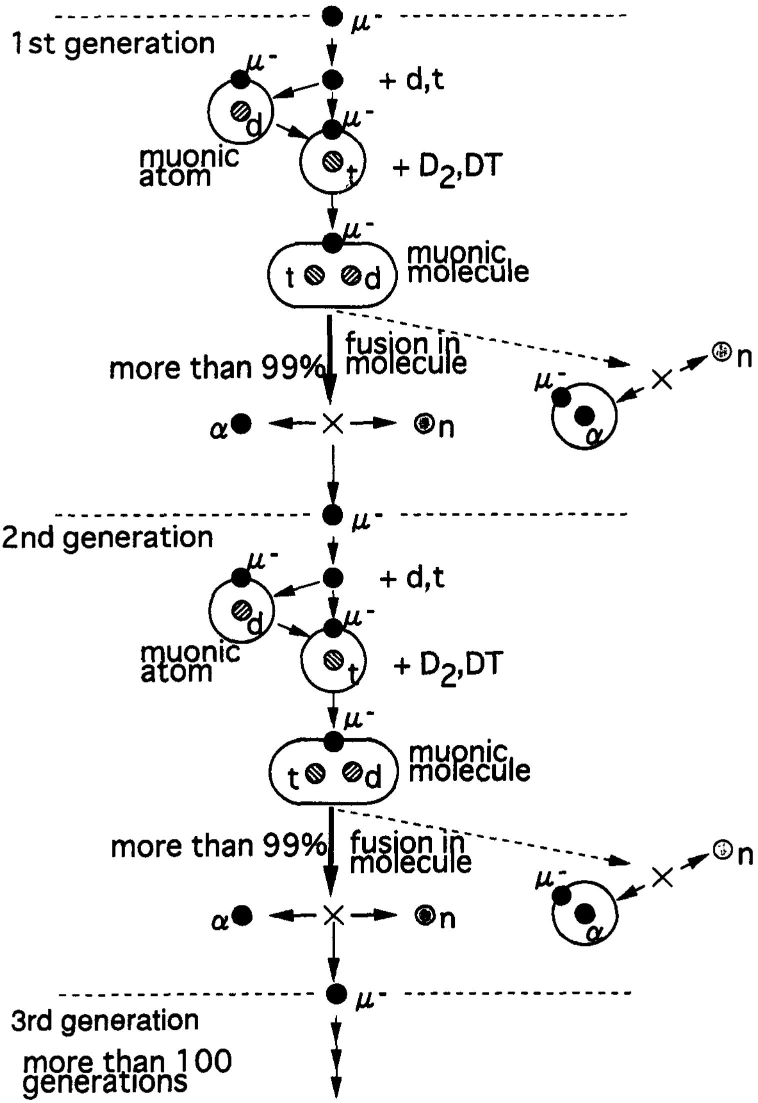

Fig. 1.2. Chain reaction of the muon catalyzed fusion phenomena in a D–T mixture.

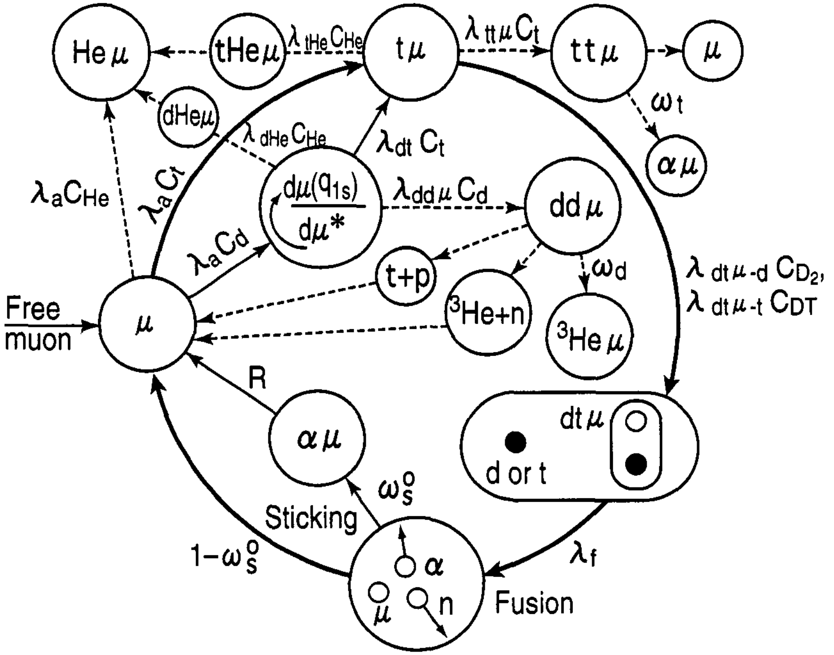

Fig. 1.3. Cyclic reaction representation of the chain reaction of the muon catalyzed fusion phenomenon in a D–T mixture, including possible loss processes other than (α*μ*) sticking.

the (*dtμ*) molecule is formed in the specific state, a rapid cascade transition process of the μ– inside the *dtμ* molecule takes place followed by the fusion reaction in a low-lying molecular state ofthe (*dtμ*), where a distance between *d* and *t* is close enough for the fusion reaction to take place. Then, a 14 MeV neutron and 3.6 MeV a are emitted. After the fusion reaction in the (*dtμ*) molecule, most of the μ^- is liberated to participate in the second *μ*CF cycle. Some small fraction of the μ^- has a possibility to be captured by the recoiling positively charged α. The probability of forming an $(\alpha\mu)^+$ ion is called the sticking probability ω_s. Once the $(\alpha\mu)^+$ is formed, since the μ^- has an initial kinetic energy of 90 keV compared to the 10 keV binding energy of the ground state of (α*μ*), the μ^- can be stripped from the stuck (α*μ*) ion. This process is called regeneration. Thus, μ^- in the form of either a non-stuck μ^- or a regenerated one from the stuck (α*μ*) can participate in the second *μ*CF cycle. Thus the chain continues. From the very first ideas about *μ*CF the question of interest has been: how many cycles can occur during the muon's short lifetime (2.2 μs)?

Some details concerning the D−T*μ*CF cycle are shown in Fig. 1.3. In the (*dμ*) to *t* transfer, there is a possibility that the μ^- is transferred from excited

$(d\mu)$ states. Also, the existence of He impurity is inevitable due to t-decay and μCF, itself; the μ^- loss due to capture to ^{3}He must be taken into account, In addition to Fig. 1.3, since *t, d* and μ^- have spin, there should be a hyperfine (spin-dependent) effect in the formation process of a muon molecule.

In fact, various types of physical processes are involved in these main processes. The fusion reaction in a small muon molecule is the most significant part where nuclear interaction dominates. Also, a nuclear interaction does affect muon sticking and related processes. The remaining processes are due mainly to electromagnetic-interactions. There, in order to understand electromagnetic-interaction related μCF phenomena, the basic roles of the μ^- can be understood by considering the μ^- to be a heavy electron with a mass ratio m_μ/m_e of 207.

Therefore, in order to understand the physics of the μCF, the following classification of the processes is relevant: (1) nuclear-process, fusion reaction in a muon molecule; (2) intermediate-process, muon sticking, regeneration and electromagnetic transitions; (3) atomic and molecular processes, muonic atom formation/intra-atomic cascade and slowing-down, muon transfer among hydrogen isotopes, formation of a muon molecule/intra-molecular transition and a He impurity effect in the μCF of hydrogen isotopes, etc; (4) the application of μCF phenomena. With some emphasis on nuclear physics aspects of μCF, the present review follows this classification.

The concept of the μCF has been introduced independently by Frank [1] and Sakharov [2]. An experimental observation of p–D μCF was made by Alvarez *et al.*, at Berkeley in 1956 [3]. The major historical trend of the μCF studies is summarized in Table 1.2. Several review articles are available regarding the μCF phenomena [4, 5, 6, 7, 8]. Since 1986, almost every year, an international conference has been held. The proceedings report on updated progresses of the μCF research; Tokyo 1986 [9], Leningrad 1987 [10], Florida 1988 [11], Vienna 1990 [12], Uppsala 1993 [13] and Dubna 1995 [14]. Since there exist rather complete review articles [4,5,6,7,8] concerning both experimental and theoretical studies up to the early 90's we would like to focus our main descriptions on *Experimental Studies and Theoretical Studies* after 1990, and summarize the activities before 1990 as *Historical Background.*

Here, we summarize what has happened after 1990 up to today in the field of muon catalyzed fusion. Experimentally, new insights have been provided by the development of new experimental facilities and methodologies: progress in X-ray detection in D$-$TμCF has been made by using instantaneously intense pulsed muons, which are now available at KEK-MSL and RIKEN-RAL; high energy (0.1 eV), $(d\mu)$, $(t\mu)$ reaction studies have been realized by the development of $(d\mu)$, $(t\mu)$ beam method; etc. Also, over time it has come to be recognized that low-energy atomic/molecular processes are affected by the molecular as well as condensed-matter status of the reaction partners. Theoretically, the

TABLE 1.2

Major Historical Trends of Muon Catalyzed Fusion Studies

1947	Hypothesis of the μCF cycle (Frank)
1948	Estimate of the fusion rate λ_f^{dd}, λ_f^{dt} (Sakharov)
1956	Observation of $pd\mu$ fusion (Alvarez)
1957	Calculation of the $dt\mu$ cycle and sticking (Jackson)
1966	Observation of the T-dependence of $\lambda_{dd\mu}$ (Dzhelepov)
1967	Theory of the resonant formation of $dd\mu$ (Vesman)
1977	Prediction of large $\lambda_{dt\mu}$ (Gerstein and Ponomarev)
1979	Observation of the upper limit on $l_{dt\mu}$
1979	Observation of the hyperfine effect in $\lambda_{dd\mu}$ (PSI)
1982	Measurement of $\lambda_{dt\mu,\ \mu dt}$ (LAMPF)
1987	Observation of X-rays from $(\mu\alpha)^+$ in DT μCF (PSI,KEK)
1987	Observation of X-rays from dHeμ (KEK)
1993	Observation of a large $\lambda_{dd\mu}$ in solid D_2 (TRIUMF)
1994	Observation of X-rays from muon transfer (PSI,KEK)
1995	Observation of $\lambda_{dt\mu}$ with eV ($t\mu$) (TRIUMF)
1997	Systematic studies of X-rays, neutrons from DT-μ CF (RIKEN-RAL)

need for precise calculations of the energy levels of the muon molecule (better than ppm accuracy) have promoted progress in theoretical studies of few-body systems, including theories beyond an adiabatic approximation. Further details can be found in the following.

2. NUCLEAR FUSION REACTION INSIDE MUON MOLECULE

Historical Background

As depicted in Fig. 1.1, a nuclear fusion reaction takes place when the two nuclei such as d and t come close to each other within the range of the nuclear interaction (r_n; $\cong$ a few fm). However, because of the Coulomb repulsion between positively charged nuclei, starting from zero relative energy, the realization of nuclear fusion is not easy at all. In the concept of thermal nuclear fusion, additional kinetic energy is given by thermal energy (kT) by satisfying the following condition; $kT \geq e^2/r_n$. By assuming $r_n \cong 10^{-12}$ cm, since the right-hand side of the inequality formula becomes 7×10^4 eV, the required temperature is 7×10^8 K.

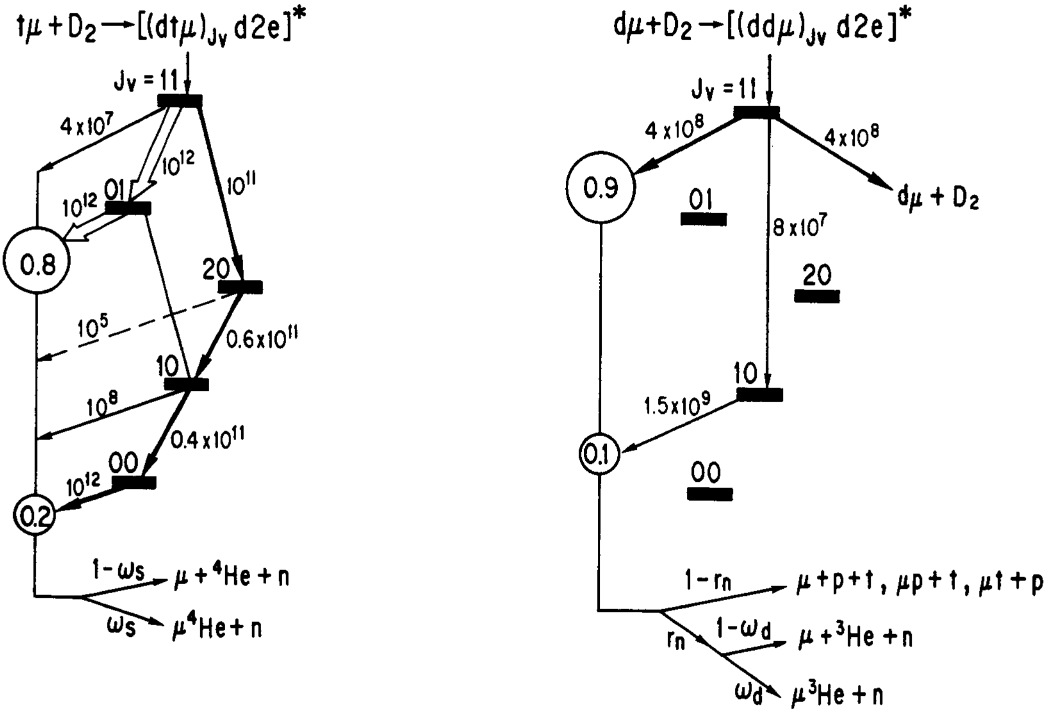

Fig. 2.1. Scheme of cascade processes in *dtμ* and *ddμ* molecules after the resonant molecular formation at (1,1) state, calculated by Bogdanova *et al.* [15].

On the contrary, in the concept of the μCF, the fusion reaction becomes realized by utilizing a neutral small atom formed by the μ^- and hydrogen isotopes and by forming a small molecule (actually molecular ion) among the *d, t* and μ^-. Now, let us consider how small this muon molecule is. The μ^- in the ground state of muonic hydrogen is known to take an orbit with a radius of 270 fm and a binding energy of 2.8 keV. By using an analogy to a conversion from H(1*s*) to H_2^+ (g.s.), where the radius becomes 2-times larger and the binding energy becomes 1/10-times smaller, one can consider the $(H_2\mu^-)^+$ (similarly $(D_2\mu^-)$+, etc) the molecular ion takes a radius of 2×270 fm and a binding energy of $2.8 \times (1/10)$ keV. Thus, since the range of the nuclear interaction (a few fm) becomes not far from the size of the molecule, with the help of zero-point motion of the molecular ion, the fusion reaction proceeds at a high rate.

Historically, the rate of nuclear fusion inside the small muon molecule (λ_f) was calculated [16, 17] by the so-called factorization relations by considering.

$$\lambda_f = a_f |\Psi(R=0)|^2$$

where af is a reaction constant related to the fusion cross section at zero relative energy, which can be obtained by an interpolation from the nuclear reaction data at higher energies and $|\Psi(R)|^2$ is the probability density to find the two nuclei at a distance of *R*. The constant af can be obtained by the interpolation ($v \to 0$) with a description of low-energy cross section of the fusion reaction,

$$\sigma = a_f C_0^2 v$$

where C_0 is the Gamow factor of *s*-wave scattering and v is the relative velocity at infinity. $\lambda_f \sim 10^{12} s^{-1}$ was given in Refs. [16] and [17].

Experimental Studies

Since a nuclear-fusion reaction realized in a muon molecule exhibits the reaction at zero relative energy, the reaction phenomena represent a new aspect of the nuclear interaction. This situation seems to have relevance to the *n–n,* π–π interactions at zero energy. On the other hand, since, in most of the cases, λ_f is too-high to be measured directly, an analysis as well as an interpretation of most of the μCF experiments, in particular for *dtμ* as well as *ddμ*, have been conducted while assuming an "unmeasurable" λ_f, and to measure the other rates in the μCF processes. Several possibilities exist to directly measure the value of λ_f for e.g.,*pdμ*, *ptμ*, etc., as summarized in Table 2.1 a.

TABLE 2.1a
Fusion Rates of Muon at the Ground State of a Typical Muon Molecule (s^{-1}) other than ($dt\mu$) and ($dd\mu$)

Molecule [Jv]	Reaction channel	Ratio(%)	Theory	Experiment
$pd\mu$ [00]		8×10^5	[a]	
	μ^3He+ γ	86	$9.7(1) \times 10^5$ $\left(\lambda_{t,\gamma}^{1/2}\right)$	$3.50(20) \times 10^5$ [c]
			$1.07(6) \times 10^5$ [b] $\left(\lambda_{t,\gamma}^{3/2}\right)$	
	^{3}He+μ	14	$0.62(2) \times 10^5$ $\left(\lambda_{t,\mu}^{1/2}\right)$	0.56(6) × 105
$pt\mu$[00]	μ4He +γ(e^+e^-)	95	1.3 × 106 [a]	6.5(7) x 104 [e]
	^{4}He+ μ	5	1.3 × 105	
$tt\mu$[11]	μ^4He+2n	14	1.2×10^7 [a]	
[10]	^{4}He+2n+μ	86	1.3×10^7	1.5×10^7 [f]
d^3 Heμ				
[J=0]		10^2	[g]	
[J= 0]		$3(1) \times 10^8$	[h]	
[J= 1]		$6(3) \times 10^5$	[h]	

[a] Reference [18]
[b] Reference [19]
[c] Reference [20]
[d] Reference [21]
[c] Reference [22]
[f] Reference [23]
[g] Reference [24]
[h] Reference [25]

In the case of pdμ fusion for liquid H–D mixtures, which has a long history after the observation by Alvarez *et al.* [3], an experiment at PSI [20] measured γ rays (5.5 MeV) after $pd\mu \rightarrow \mu^3$He + γ fusion with reference to neutrons from ddμ fusion. The pdμ is formed in a (Jv = 10) state followed by a fast de-excitation process and the fusion occurs at (00) state [18]. Historically, this fusion reaction is considered to exhibit a significant spin-dependent process in ($d\mu$). Namely, any fusion from the initial spin-quartet (spin 3/2) state ofpd to the ^{3}He ground state was considered to be prohibited by the Pauli principle as long as the spin-singlet and symmetric s-wave configuration alone is assumed for ^{3}He. However, the obtained data in terms of the spin state of *pd*, $\lambda_{f,\gamma}^{1/2} = 0.35\ (2)\ \mu s^{-1}$ and $\lambda_{f,\gamma}^{3/2} = 0.11\ (1)\ \mu s^{-1}$, showed a non-vanishing quartet contribution. The data were excellently explained by a calculation of Friar *et al.* [19], $\lambda_{f,\gamma}^{1/2} = 0.37\ (1)\ \mu s^{-1}$ and $\lambda_{f,\gamma}^{3/2} = 0.107\ (6)\ \mu s^{-1}$; they took

TABLE 2.1b
Theoretical Fusion Rates (s^{-1}) at the State (Jv) of $dt\mu$ and $dd\mu$ Muon Molecules

Authors	State			
	(00)	(01)	(10)	(11)
dtμ :				
Bogdanova et al.[a]	1.0×10^{12}	0.80×10^{12}	1.1×10^{8}	4.2×10^{7}
Struensee et al.[b]	1.30×10^{12}	1.13×10^{12}		
Kamimurac	(1.22–1.28) $\times 10^{12}$	(1.03–1.08) $\times 10^{12}$	(1.32–4.38) $\times 10^{8}$	(0.51–1.71) $\times 10^{8}$
Szalewicz et al.[d]	1.25×10^{12}	1.05×10^{12}		
ddμ :				
Bogdanova[a]			4.3×10^{8} $(0.9)^{e}$	1.5×10^{9} $(0.1)^{e}$

[a] Reference [18]
[b] Reference [26]
[c] Reference [27]
[d] Reference [29]
[c] Probabilities

precise Faddeev-type ^{3}He wave functions based on realistic N–N potentials and the MI operator, including meson exchange effects. The data itself should be considered to be related to the radiative capture rate of the μ^- at zero energy.

As for $pt\mu$ fusion, an experiment at PSI [22] measured γ ray (19.8 MeV) after the $pt\mu \rightarrow {}^4\text{He}\mu + \gamma$ reaction, compared to $pt\mu \rightarrow {}^4\text{He} + \mu$. The fusion occurs in a ($Jv = 00$) state where three hypefine-split sublevels exit [18]. Since γ emission is only possible for the spin-1 state of $(t\mu)$, this process is known to probe the spin-flip process. There, $\lambda_f = 0.065\ (7)\ \mu s^{-1}$ has been obtained.

Regarding $tt\mu$ fusion, there has been none of the refined experiment for the pure T_2 target other than the old PSI experiment [23], where, from the time-evolution of the fusion neutron, the value of λ_f was obtained. The major fusion process is considered to take place in the (10) state by the p-wave cross section [18].

Other than the systems of hydrogen isotopes, the μCF rates in several systems including nuclei beyond hydrogen isotopes, like ^{3}He, ^{6}Li, ^{7}Li, have been considered, mostly theoretically. These results are summarized in Table 2. la. Among them, the greatest concern was paid to the fusion rate in ($d^3\text{He}\mu$), since this fusion reaction might be promising for a possible application to energy sources, other than D–T μCF, due to the spatial concentration of the produced energy output (both p and α are charged particles) and the availability of ^{3}He resource in the moon surface soil [30]. On the other hand, since the expected radius of the $(d^3\mathrm{He}\mu)^{++}$ molecular ion is two-times larger than $(dt\mu)^+$, a substantially reduced fusion rate had been expected. However, as described later, an advanced theoretical calculation based upon a non-adiabatic procedure has produced a rather promising rate. Some experimental trials have been undertaken at KEK and at TRIUMF, where the emission of high-energy protons from the thin layer of a liquid $D_2{}^3\mathrm{He}$ target is expected to occur; $^3\mathrm{He}$ introduction was made by pressurizing $^3\mathrm{He}$ onto the surface of liquid $^3\mathrm{He}$. The result has not yet been conclusive.

Theoretical Studies

There have been several shortcomings in factorization treatments of the fusion rate. First of all, we need knowledge concerning the fusion rate at the excited state of the muonic molecule specified by the rotational quantum number (J) and vibrational one (v), since, as described later, the formation of a muonic molecule takes place in the excited state of the muon molecule. Secondly, distortion of the molecular wave function due to the nuclear interaction should be taken into account. Moreover, a correction is needed in the formula of λ_f due to the dominance of a near-threshold resonance in the reaction cross section.

Advanced calculations of the fusion rates in the muonic molecule dtμ were made by Bogdanova *et al.* [18], and Kamimura [27] within the complex nuclear potential (optical potential) method and by Struensee etal. [26], and Szalewicz *et al.* [29], within the R-matrix method. Two of these calculations [18,261 employed the framework of adiabatic representation, while the others [27,29] used the non-adiabatic one. All of these calculations took into full account the observed energy dependence of the reaction cross section of $d+t \rightarrow \alpha + n + 17.6$ Me V at low energies, including the $j^\pi = 3/2^+$ resonance at $E_{om} = 60$ ke V (Fig. 2.2). In the work of Bogdanova *et al.* [18] and Kamimura [27] theinteraction part of the total three-body Hamiltonian comprises the Coulomb potentials between d, t and μ and the nuclear complex potential between d and t. The latter one is constructed so as to reproduce the observed energy dependence of the fusion cross sections, while the imaginary part of the complex potential accounts for the α-n channel; the absorption cross section directly means the fusion cross section, since there is no reaction channel other than the fusion one in the concerned low-energy region. Twice the imaginary part of the complex eigen-energy, $E_R - iE_I$ stands for the width of the energy level, $\Gamma = 2E_I$, and $\hbar / \Gamma$ corresponds to its life-time. The inverse of the lifetime directly gives the fusion rate λ_f of the $dt\mu$ molecular state. Four types of calculations [18, 26, 27, 29] gave similar results concerning the fusion rates of the $J = 0$ states of $(dt\mu)$ as shown in Table 2. 1b.

In order to understand the overall fusion rate in a muon molecule, the details concerning the intra-molecular cascade transitions should be known. As

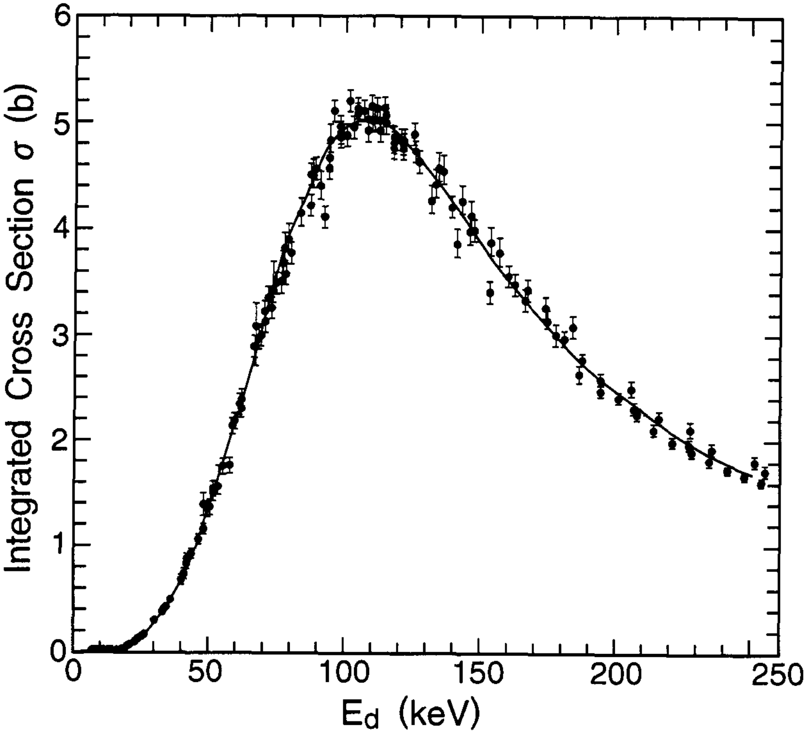

Fig. 2.2. Cross section s/n (E) for the reacton $d + t \to {}^4He + n$, experimental data [28] with a theoretical curve obtained by using the potential used in the fusion-rate calculation for D–T μCF by Bogdanova *et al.* (18], and by Kamimura (27].

described later, the formation of a muonic molecule is done mostly via resonance reactions to form an excited rotational vibrational (Jv) state with $J = v = 1$, which is very weakly bound with respect to the $(t\mu)_{1s} + d$ threshold. The de-excitation of the muonic molecule levels proceeds via Auger transitions, like

$$[(dt\mu)_{Jv} d2e]^* \to [(dt\mu)_{J'v'} d2e]^* + e$$

These Auger de-excitation processes of the muonic molecule have been theoretically estimated by Bogdanova *et al.* [15]. The essential parts of the results are summarized in Fig. 2.1. The μ^- cascades down to the lower levels where the fusion reaction takes place. In Fig. 2.1, the fusion reaction rates and the cascade transition rates for the D–T μCF are summarized; 80% of the fusion takes place at the (Jv) = (01) state and 20% at the (00) state, both of which are formed after cascading down from the (11) state. As also shown in Fig. 2.1, in the case of $dd\mu$, which is formed at the (Jv) = (11) state, the fusion reaction takes place at the (11) and (10) states at a rate of $5 \times 10^8\ s^{-1}$. The theoretical rates are summarized in Table 2. 1b. Combining all of these arguments on the rates of fusion and de-excitation, we can conclude that in a time of 10^{-11} s (rate of 10^{11} s^{-1}) the fusion reaction is completed in the muon molecule after the formation of the (11) state or after the formation of the $dt\mu$ molecule during a collision between ($t\mu$) and D_2.

The fusion reaction rate in $(d^3\mathrm{He}\mu)_{J=0.1}$ was calculated precisely by Kamimura [25] in the same manner as for the ($dt\mu$) molecule. Namely, similar nuclear complex potentials were employed so as to explain the low-energy cross sections of the $d + {}^3\mathrm{He} \rightarrow {}^4\mathrm{He} + p$ reaction dominated by the $3/2^+$ resonance, and the fusion rates were estimated using the imaginary part of the eigenenergies of the complex Hamiltonian. The calculated results are listed in Table 2. 1a. These rates will be referred to in a later section in relation to the muonic molecule of ($d\mathrm{He}\mu$). As described later, since the ($d^3\mathrm{He}\mu$) molecule is formed at $J = 1$, as evidenced by a radiative photon measurement, while a transition to $J = 0$ is not very slow due to rotational transitions, 1 → 0, in ($d\mathrm{He}\mu$) through an external Auger process [31], an overall high fusion rate in $d^3\mathrm{He}\mu$ is expected.

3. MUON STICKING AFTER NUCLEAR FUSION

Historical Background

So far, various experimental methods have been applied in order to investigate the muon catalyzed fusion (μCF) phenomena summarized in Fig. 1.3 for D–T μCF. Let us explain how to obtain the reaction rates such as $\lambda_{dt\mu}$ and λ_{dt}, as well as the loss probability, such as ω_s, experimentally. The measurement of 14 MeV fusion neutrons can be used to obtain the fusion neutron yield, the cycling rate of the μCF, etc., where the decay e^- measurement is mostly used for normalization purposes. Measurements of the characteristic X-ray in the μCF can also provide very valuable insights concerning each process of the μCF. A time-dependent measurement of these fusion neutrons and characteristic X-rays from muonic atoms/molecules can reveal the time evolution of μCF phenomena. Combinations of these experimental methods may provide the most satisfactory information about each process of the μCF cycle. Most of the experiments on DT-μCF conducted at Los Alamos [32,33] and PSI [34,35] around 1990 have focused on neutron measurements; both systematic neutron and X-ray combined measurements were carried out for the first time rather recently at RIKEN-RAL.

Regarding the rate of cycling (λ_c) with a loss probability (*W*) including muon-to-alpha sticking phenomena, several experimental methods have been applied. Here, we summarize relations between the experimental observables and physical parameters in the μCF cycle.

1. (neutron method) Measurements ofthe absolute yield Y_n and disappearance rate λ_n give us the loss rate W_n seen by neutrons [32, 33, 34], thus providing some limiting factor on ω_s.

$$Y_n(t) = \phi\lambda_c e_n^{-\lambda t}$$

$$Y_n \equiv \int_0^\infty Y_n(t)\,dt = \frac{\phi\lambda_c}{\lambda_n}$$

where

ø =DT density (nuclei/cc) divided by the liquid hydrogen density
(0.425 × 10^{23}nuclei/cc)

$\lambda_n = \lambda_0 + \lambda_c W_n$

$W_n = \omega_s +$ other losses

2. (X-ray method) X-ray measurements from $(\mu\alpha)^+$ ions gives directly knowledge about sticking phenomena [36, 37, 38]. The combination of $Y_x(t)$ and $Y_x(t)$ gives a direct measure of ω_s.

$$Y_x(t) = \phi\lambda_c \kappa\omega_s^0 e_n^{-\lambda t}$$

$$Y_x \equiv \int_0^\infty Y_x(t)\,dt = \frac{\phi\lambda_c k\omega_s^0}{\lambda_n}$$

$$\frac{Yx}{Yn} = \kappa\omega_s^0$$

where the *k,* given by the theory of atomic processes of $(\mu\alpha)^+$ ion, is the X-ray yield per sticking and ω_s^0 is the initial sticking right after the fusion reaction in the muon molecule. Actually, wosis the sum ofthe initial sticking to each orbit of the $(\mu\alpha)^+$ ion,

$$\omega_s^0 = \sum_{nl} \omega_s^0(nl)$$

The ω_s which appears in the total loss probability W_n is obtained after correcting for the regeneration factor *R*,

$$\omega_s = \omega_s^0(1-R)$$

Again, since the regeneration process depends upon the initial state of the $(\mu\alpha)^-$ ion, the ws should be written as

$$\omega_s = \sum_{nl} [1 - R(nl)]\, \omega_s^0(nl)$$

3. (ionmethod) Detectionofthe $(\mu\alpha)^+$ ion gives us further direct knowledge about sticking phenomena. The detection ofthe in-flight $(\mu\alpha)^+$ by a solid state detector [39, 40] gives us a measure ofthe initial sticking ω_s^0. On the other hand, the measurements ofa total amount ofionization loss in a DT mixture gives us the final sticking ω_s [41, 42].

The experiments so far conducted as well as the values so far obtained are summarized in Fig. 3.1a, where values of the effective sticking of ws are presented as a function of ø.

Theoretical studies on the α-sticking have been initiated by Jackson [16], who used a sudden approximation. The probability of a $(\mu\alpha)^+$ atom formation in an *nl* state is given by

$$\omega_s^0(nl) = \sum_m |F(nlm)|^2$$

where

$$F(nlm) = \int \phi_{nlm}^*(\mathfrak{r})\, e^{-i\mathfrak{q}\cdot\mathfrak{r}}\, \Psi_{in}(\mathfrak{r})\, d\mathfrak{r}$$

and $ø_{nlm}(\mathfrak{r})$ is the wave function of $(\mu\alpha)_{\mathrm{nlm}}$,-$q = m_\mu v$ (v: velocity of $(\mu\alpha)$); $\Psi_{in}(\mathfrak{r})$ is the normalized muon wave function at the instant of fusion, which can be expressed through the muon-molecule wave function, $\Psi_{jv}(\mathfrak{r}, \mathfrak{R})$ by $\Psi_{in}(\mathfrak{r}) = N\Psi_{jv}(\mathfrak{r}, \mathfrak{R} = 0)$, where $\mathfrak{R}$ the inter-nuclear distance and $\mathfrak{r}$ is the muon coordinate with respect to the c.m. ofthe two nuclei, with N being the normalization constant.

Experimental Studies

Here, we wish to present some recent achievements of the X-ray measurements on μ–α sticking phenomena. The most important α-sticking probability ws to be determined is that for the D–T μCF with high density and high C_t, where more than 100 fusion neutrons per single μ^- have been observed. There, the ws strictly places an upper limit on the energy-production capability from the D–T μCF. The conventional neutron method for observing the loss probability should be considered as an indirect method for the determination of ω_s.

The X-ray method, which is practically the only one which can be applied to a direct ω_s measurement for a high-density and high-C_t D–T mixture requires a relation between the observed X-ray intensity and the sticking probability ω_s. Theoretical studies on this subject were first carried out by Cohen [43] and Markushin [44], and later by various other authors [45, 46 ,47, 48]. These are summarized in Table 3.2. For instance, Cohen has predicted a K_α (2p → 1*s*) X-ray intensity per fusion $Y(K_\alpha)$ being 0.24% for a D–T mixture with a density of 1.2ø$_0$, where the calculation was started with an initial sticking probability of 0.848%. There, starting from the predicted atomic states formed right after the initial sticking ω_s^0, the X-ray emission during the slowing-down of $(\alpha\mu)$ was calculated by considering all possible processes, such as μ^- stripping (reactivation), excitation and de-excitation in $(\alpha\mu)$ atoms etc. At the same time, these theories have predicted the regeneration probability (R) for free μ^- production during the slowing-down of $(\alpha\mu)$ atoms.

Since 1986, X-ray measurements have been applied to the direct measurements of the μ–α sticking probability in D–T μCF at PSI [36], at UTMSL/KEK [37, 38] and recently at RIKEN/RAL. There, the experiment at PSI was performed with continuous muons for a low-C_t (~ 10^{-4}) D–T mixture, and that at KEK-MSL and RIKEN/RAL with pulsed muons for high-C_t (from 0.1 to 0.7). As for X-ray detection in $dt\mu$–μCF, the radiation background of the bremsstrahlung associated with t beta-decay is serious; the background, the energy of which extends up to 17 keV, does mask all ω_s-related X-rays ($E(K_\alpha)$: 8.2 keV, $E(K_\beta)$: 9.6 keV, etc.). The use of pulsed muons, now available at KEK [49] or at RIKEN/RAL [50], is really helpful; by operating the detection system only in a short time interval around a muon pulse, a significant improvement in the *S/N* ratio can be expected [37, 38].

Following the first successful observation of K_α X-ray from $(\mu\alpha)^+$ in high-f and high-C_t (C_t = 0.3) D–T mixtures at UTMSL/KEK [38], systematic data on ω_s and λ_c have been obtained in high-density (liquid and solid ø = 1.2 ~ 1.5) and high-C_t (C_t = 0.1 ~ 0.7) D–T mixtures at RIKEN-RAL. Several important improvements exist for the experimental method: (1) a high intensity and low-background pulsed μ^- beam is used; (2) in order to obtain data for a ^{3}He-free pure D–T mixture, in-situ ^{3}He removal as well as a chemical-analysis apparatus have been introduced; (3) by using combined data on both the absolute yields and the time slope (decay time) constants for X-rays and neutrons (Y_X, λ_x, Y_n,λ_n), one can obtain the cycling rate λ_c loss rate W_n and X-ray per sticking $\kappa\omega_s^0$ independently, and restriction on κ is obtained by comparing $W$and $\kappa\omega_s^0$. The actual steps for analyzing the data are as follows: a) from the time slope constant of the neutron yield Yn, the value of $\lambda_c W_n$ (= ($\lambda_n - \lambda_0$) / ø) is obtained, while, from the absolute neutron yield Y_n, the value of λ_c (= $Y_n \lambda_n$ / ø) is obtained, so that both λ_c and W_n are obtained from the fusion neutron data; b) after confirming the time

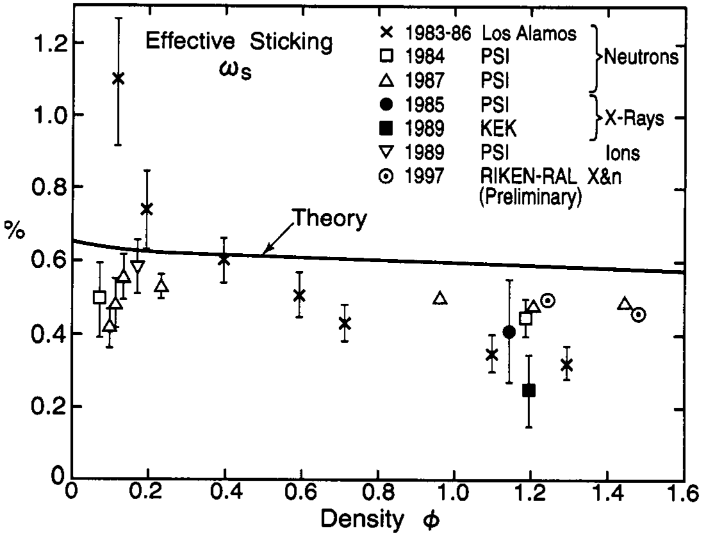

Fig. 3.1a. The existing data concerning the sticking probability ω_s vs density φ in the muon catalyzed fusion ofa D–T mixture, where the data was obtained from Los Alamos [33], PSI [34,35,36] and KEK [38]. Also, preliminary data from RIKEN-RAL of the average of the data for G = 0.3,0.4 and 0.5 is shown.

slope constant of the X-ray yield Y_x (t) being consistent with that of the fusion neutron λ_n, the value of $\kappa\omega_0$ is obtained by taking the ratio Y_x/Y_n, so that the effective sticking seen by X-ray ω_s (X) is obtained by using the theoretical values of κ and R listed in Table 3.2 ($Y_x / Y_n \times (1 - R) / \kappa$); c) the overall consistency of these analysis can be checked by the condition $W_n \geq \omega_s$.

The experimental values are summarized in Fig. 3. 1b. The results concerning ω_s can be summarized as follows, while the results concerning $\lambda_{dt\mu}$ are summarized in a later section: 1) the ws obtained by using the step mentioned above is consistent with the condition ws $\geq$ Wn only when we take the values of $\kappa(R)$ predicted by the theories [47,48] and thus obtained ws (X) becomes almost consistent with ω_s (n) obtained from W_n after correcting the contributions of loss processed due to $dd\mu$, $tt\mu$ formation; 2) the observed X-ray intensity ratio I (K_β) / I (K_β) from the stuck $(\mu\alpha)^+$ ion is close to the lowest value of the theoretical values also predicted by the same theories [47,48]; 3) the observed ω_s, obtained thus, is smaller than the theoretical one, namely, ω_s (exp) $\cong$ 0.5% vs ws (theory) $\cong$ 0.6%, as shown in Fig 3. la; 4) there is a maximum in the fusion neutron yield at $C_t \sim 0.5$, which is not consistent with the existing data at Los

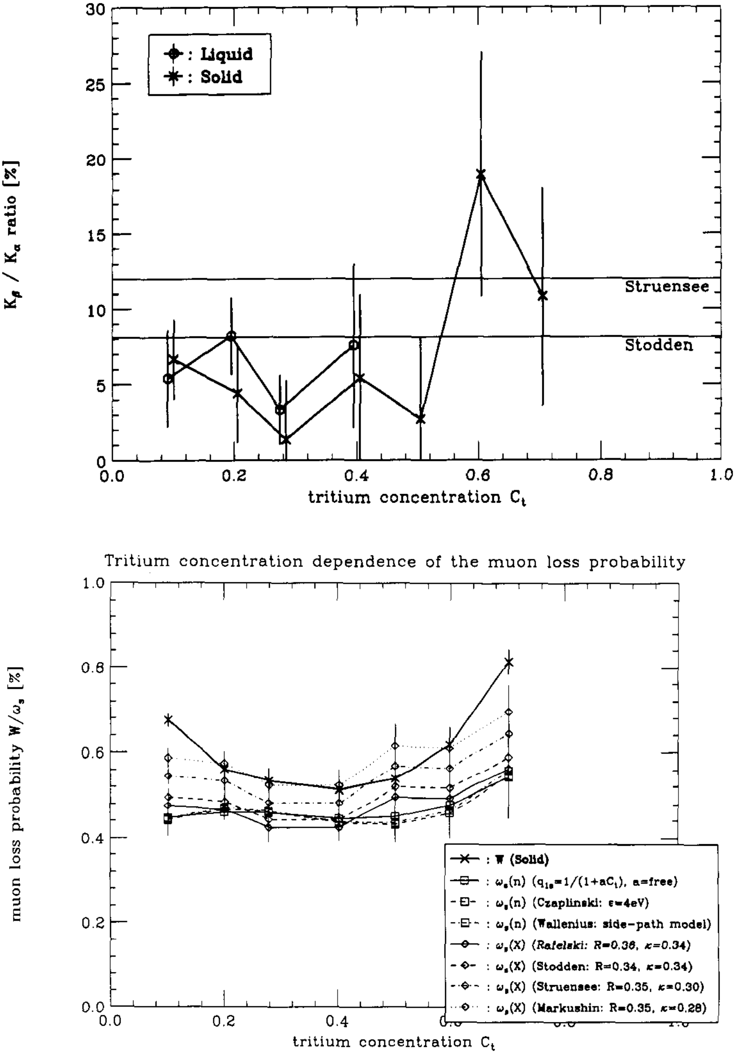

Fig. 3.1 b. Preliminary data on ws obtained by simultaneous X-ray and neutron measurements in a solid D–T mixture with reference to the total loss probability W_n seen by neutrons, where correction was made for X-ray with R and K indicated and for neutron with parameters using q_{ls} indicated (upper). The obtained K_β / K_α ratio in a liquid and solid D–T mixture (lower).

TABLE 3.1
Theoretical Initial Muon Sticking Probabilities w0s (%) at the (*J*,*v*) State of a *dtμ* Molecule with and without a Nuclear Interaction

Author		State	
		(00)	(01)
(Without nuclear interaction)			
Hu	[a]	0.897	0.8649
Ceperley Alder	[b]	0.895	
Bogdanova et al.	[c]	0.846	0.848
Haywood et al.	[d]	0.886	0.888 (2)
Kamimura I	[e]	0.8859	0.8896
(with nuclear interaction)			
Bogdanova et al.	[e]	0.93	
Kamimura	[f]	0.925 (4)	0.927(4)
Jezioski et al.	[g]	0.917	0.915
Cohen et al.	[h]	0.912	0.913

[a] Reference [53]
[b] Reference [51]
[c] Reference [52]
[d] Reference [54]
[c] Reference [55]
[f] Reference [27]
[g] Reference [56]
[h] Reference [57]

Alamos (C_t ~ 0.3) nor at PSI (C_t ~ 0.3); 5) ω_s seems to have a weak Ct dependence. Improved experiments are now in progress.

Theoretical Studies

At an earliest stage of the theoretical studies, the initial muon wave function $\Psi_{in}(r)$ was taken as the simplest form of the μ^- in μ^5He) atom (Born–Oppenheimer approximation), which results in $\omega_s^0 = 1.2\%$. In papers after 1985, the non-adiabatic motion of the muon in the *dtμ* molecule was taken into account. New methods to solve non-adiabatically the Coulomb three-body problem includes a Green-function Monte-Carlo method [51], the adiabatic representation method [52], variational methods with a Hylleraas basis [53, 54] and the Jacobian-coordinate coupled-channel method [27]; ω_s^0 calculated from these three-body wave functions are listed in the upper half of Table 3.1. The non-adiabatic nature of the *dtμ* wave function reduces the initial sticking by some 25%.

The effect of the nuclear *d–t* interaction on the sticking was then studied using the nuclear optical potential model [27, 55] and with *R*-matrix theory [56, 57]. In the former method, the nuclear *d–t* potential (cf. Section 2) is directly added to the Coulombic Hamiltonian in order to examine the change in the muon wave function at the nuclear coalescence. In the latter method, the effect of the nuclear interaction is indirectly included by imposing an appropriate nuclear boundary condition on the $dt\mu$ wave function at the channel radius. Both methods gave similar results, as shown in the lower half of Table 3.1 ; the nuclear-interaction effect increases the initial sticking by 3%.

In order to investigate the nuclear-interaction effect beyond the sudden approximation, Kamimura [58] formulated a four-body ($t + p + n + \mu$) model of the fusion (t+ (Pn) $\rightarrow$ (tp) +n) and investigated the initial sticking problem starting with the fundamental reaction theory. The sudden approximation is equivalent to the so-called zero-range plane-wave Born approximation (PWBA) in reaction theory. In order to greatly improve the part of PWBA, he formulated the zero-range coupled-channel Born approximation (CCBA), which includes, as effects of the strong n–α interaction, the distortion of the plane wave and coupling among the $n\text{–}(\alpha\mu)_{nl}$ channels (*nl* includes the continuum states). By this formulation it was found that the final-state-interaction effects do change the absolute value of the transition matrix to each ($\alpha\mu)_{nl}$ state, but, as long as the excitation energies of the $(\alpha\mu)_{nl}$ states are safely negligible compared with the fusion energy 17.6 MeV, the change in the transition matrix is independent of the $(\alpha\text{–}\mu)$ states, including the continuum; this means that the initial sticking ω_s^0 does not change since it is the ratio of the transition strength to the bound state of $(\alpha\mu)$ to that to all states, including the continuum. Furthermore, from the structure of the transition matrix, the release of the zero-range approximation of the transition interaction does not seem to significantly change that ratio for calculating w0s. This prediction [58] was realized afterwards in some efforts [18,59] to improve the sudden approximation. Another remaining and meaningful improvement of the initial-sticking calculation will be to replace the initial $dt\mu$ wave function by $dt\mu + \alpha n\mu$, for which the Hamiltonian with a nuclear dt–$\alpha\mu$ coupling interaction is diagonalized within the L^2-integrable basis functions [27].

By adopting the value of the initial sticking probability in Table 3.1, several authors [43, 44, 48] have calculated the effective sticking ω_s, while taking into account all of the processes involved in the regeneration of the muon from the $(\alpha\mu)$ atom, such as Coulomb excitation and deexcitation, Auger transitions, Stark mixing, muon transfer, ionization and radiative deexcitation. From the values of R at ($\text{ø} = 1.24\text{ø}_0$) in Table 3.2, one can obtain $\omega_s = 0.6$. The density dependence of the theoretical values of ws in $dt\mu$-μCF summarized in Fig. 3.la appear to be consistently higher than the experimental values; in terms of the effective sticking, theoretical calculations predict $\omega_s \cong 0.6\%$, while experiments

TABLE 3.2
Theoretical Predictions on the X-Ray Intensity and Regeneration Factor, for $\alpha\mu$ in D–T μCF

Reference	$Y(K_\alpha)^a$ $\left(\frac{\text{photon}}{\text{fusion}}\right)$ (%)	$\kappa(K\alpha)$ $\left(\frac{\text{photon}}{\text{sticking}}\right)$	R^b	$\frac{(1-R)}{\kappa}$	$\frac{Y(K_\beta)^c}{Y(K_\alpha)}$
Cohen[d]	0.25	0.28	0.35(5)	2.3	0.12
Markwhin[e]	0.25	0.28	0.35	2.3	0.12
Takahashi[f]	0.24	0.27	0.30	2.6	0.18
Struensee and Coheng	0.27	0.30	0.35	2.2	0.12
Rafelski[h]	0.30	0.34	0.36	1.9	0.07
Stodden[i]	0.30	0.34	0.34(3)	1.9	0.081

[a] For ω_s^0 = 0.886% and $ø = 1.2ø_0$

[b] For $ø = 1.2ø_0$

[c] For $ø = 1.2ø_0$

[d] Reference [43]

[c] Reference [44]

[f] Reference [45]

[g] Reference [46]

[h] Reference [47]

[i] Reference [48]

report $\omega_s \cong 0.4\%$. After several trials, the gap has not been filled so far. This is one of the most important problems to be solved in the μCF studies. Clearly, a lower value of ω_s increases the number of fusion cycles catalyzed by the muon.

4. ATOMIC AND MOLECULAR PROCESSES BEFORE AND AFTER FUSION

4.1. Hydrogen Muonic Atom Slowing-Down

Historical Background

All of the processes in μCF start with the μ_- injection into a D–T or D_2 mixture at high energies (MeV or higher). Then, the μ^- begins a slowing-downprocess by ionization of the surrounding molecules/atoms and is eventually captured by the *d* or *t* to form a muonic *d* or *t* atom with a population proportional to the concentration.

It was pointed out both theoretically and experimentally that when a hydrogen-isotope target stays at liquid-hydrogen density $ø_0$, the time required for muonic atom formation is less than 10^{-12} s [4, 5]. The atomic state of the muonic atom involves a radial quantum number, n, of about 14 ($\approx (m_\mu/m_e)^{1/2}$), Then, the intra-atomic cascade transition takes place via an Auger process at the earlier stage (among higher atomic orbits) and a radiative process at the later stage, where a Stark-mixing process takes on a significant role at high target density. The cascade process to the ground state of the muonic atom at $ø = ø_0$ is considered to take less than 10^{-11} s [4]. The thus-formed neutral atoms undergo a further slowing-down process through a series of elastic collisions with the surrounding atoms/molecules and eventually achieve thermalization.

The above-mentioned picture of muonic atom formation → intra-atomic cascade → thermalization should be subject to a drastic change when the muonic hydrogen is formed in a high-density hydrogen-isotope mixture, e.g., a $(d\mu)$ or $(t\mu)$ atom in D–T mixture. More rapid processes might be competing with either the cascade or thermalization processes. As described later, significant examples exist, such as muon transfer from an excited atomic state, muon-molecule formation at epithermal energy, etc. In any case, it has been recognized that we need more advanced knowledge concerning the most fundamental process of elastic scattering of a neutral hydrogen atom with the surrounding atoms and molecules.

Experimental Studies

Elastic scattering and competing processes of neutral $d\mu$ and $t\mu$ can be quantitatively described in the form of the energy dependence of the cross sections. Originally, the elastic scattering of e.g., $t\mu$ has been considered to collide with the nucleus of d, t

$$(t\mu) + d \rightarrow (t\mu) + d$$

However, as has been pointed out experimentally [60], a realistic calculation is required under the condition that the nucleus of the collision partner is situated inside the D_2, DT, T_2 molecules. There, energetic $(d\mu)$ produced by the Ramsauer–Townsend effect in solid $H_2(D_2)$ was subject to slowing-down by an added D_2 layer with various thickness, where $d\mu$ stopping was monitored by the occurrence of DD μCF; a comparison was made with a Monte-Carlo calculation based upon various types of elastic-scattering cross sections.

A significant experimental progress for studies of the slowing-down, neutral muonic hydrogen atom e.g., the experiment mentioned above, has been brought about by a beam development of energetic $d\mu$, $t\mu$ atoms [61]. There, the basic idea is again due to knowledge concerning elastic scattering between muonic hydrogen atoms with hydrogen isotopes. As theoretically predicted [62], there is a significant Ramsauer–Townsend minimum, at energies in the eV region, in the cross section between $d\mu$ or $t\mu$ in H_2; after slowing-down of $d\mu$ or $t\mu$ in H_2, the medium becomes transparent. Therefore, when μ^- is injected into H_2

with some optimized concentration of D_2 or T_2, $d\mu$ or $t\mu$ undergo emission into vacuum from a sold $H_2(D_2)$ or H_2 (T_2) surface [61].

Also, in the actual situation of μCF experiments, a condensed phase, such as the liquid and solid phase, is used. In experiments with the solid phase of D_2, the thermalization takes a different form compared to that in the gas phase; the thermalization of $(d\mu)$ is not completed because of the existence of an "energy gap" in solid D_2 [63]. So far, several pieces of significant evidence exist for a condensed-matter effect on the incomplete thermalization: (1) the $\pi^- p$ atom at its formation in liquid hydrogen was found to have a kinetic energy from 1 eV to more than 100 eV [4]; (2) as explained later, recent data concerning muon transfer from excited $(p\mu)$ to d can only be explained by the existence of an energetic $(p\mu)$; (3) also, again, as explained later, an energetic $(d\mu)$ might explain a large $\lambda_{dd\mu}$ in solid D_2.

Theoretical Studies

Theoretical studies on the elastic scattering of muonic hydrogen atoms from hydrogen isotopes has been extended to include an environment effect. In Fig. 4.1, typical theoretical calculations are summarized for the elastic scattering of $d\mu$ from a d nucleus, from a D atom and from a D_2 molecule [64, 65]. Also, theoretical calculation have been extended to include a condensed-matter effect, where H_2, D_2, T_2 are formed in liquid or solid [66]. There, it is shown that in solids the phonon spectrum does change the elastic scattering cross section.

4.2. Muon Transfer among Hydrogen Isotopes

Historical Background

When the μ^- is injected into a D–T mixture with D_2, T_2 and DT, the atomic states of $(d\mu)$ and $(t\mu)$ are produced roughly proportional to the concentration, C_d or C_t $(C_d + C_t = 1)$. In a D–T mixture with a density ø of around ø$_0$, after injection with MeV energy, it takes 10^{-10} s for the μ^- to reach the ground state of either $(d\mu)$ or $(t\mu)$, Then, the μ^- remains during most of its lifetime in the ground state, where the nuclear capture rate to either d or t is negligibly small (400 s^{-1} for $d\mu$), Since the ground-state energy of $(t\mu)$ is deeper than that of $(d\mu)$ by 48 eV, the μ^- at the ground state of $(d\mu)$ can easily be transferred through the reaction $(d\mu) + t \to (t\mu) + d$ via a collision with t in either T_2 or DT. Theoretical studies on the ground-state transfer reaction among hydrogen isotopes have been carried out by several groups [67, 68, 69, 70, 71, 72, 73], and results of the transfer rate at thermal energies ($\sim 2.7 \times 10^8$ s^{-1}) have explained the observed values.

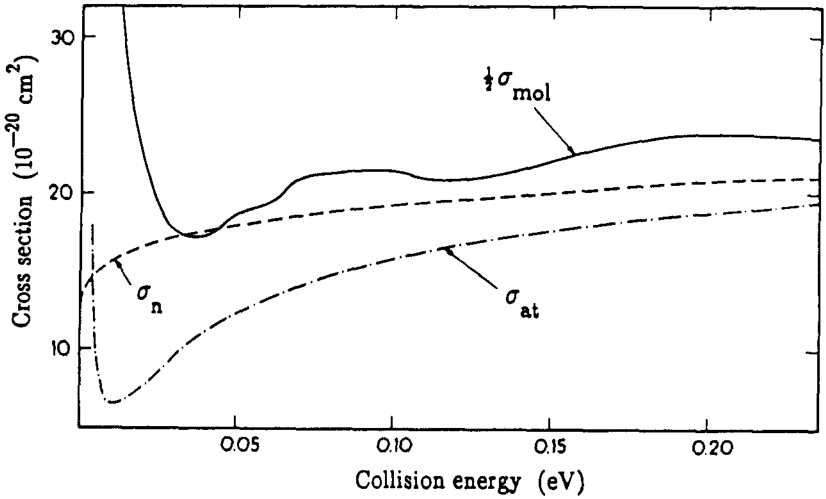

Fig. 4.1. Low-energy elastic scattering cross section for a dμ(↑↓) atom from d nucleus (σ_n), D atom (σ_{at}) and D2 molecule (σ_{mol}) at 300 K, calculated by Adamczak and Melezhik [64].

Since the cascade transition rate of the μ^- in $(d\mu)$ or $(t\mu)$ is comparable to the radiative transition rate, there is a possibility for the μ– to take a transfer reaction to $(t\mu)$ from its excited state of $(d\mu)$, By denoting q_{1s} to be a probability for the μ^- to reach to the ground state, the problem of the μ^- transfer at the excited state is sometimes called the q1s problem; $q_{1s} = 1$ corresponds to the μ^- transfer after the μ^- reaches the ground state. Moreover, it has been pointed out that the $(d\mu) \rightarrow (t\mu)$ transfer reaction might occur at the epithermal energy of $(d\mu)$.

Some qualitative arguments can be summarized concerning the q_{1s} values at various C_t, ø and $\epsilon(d\mu)$, as shown in Fig. 4.2a. Some indirect knowledge exists about the values of q_{1s} in D–T μCF based on C_t dependence measurements of fusion neutrons in a D–T mixture [74].

Experimental Studies

Experimentally, it is possible to directly measure the value of q_{1s} by using a difference in the energy of e.g., the K_α X-ray either between $(d\mu)$ and $(t\mu)$ for a $(d\mu)$ to t transfer reaction or between $(p\mu)$ and $(d\mu)$ for a $p\mu)$ to d transfer. Depending upon which X-ray is detected, we can simply conclude whether the transfer reaction does occur from excited states or from the ground state (see Fig. 4.2b).

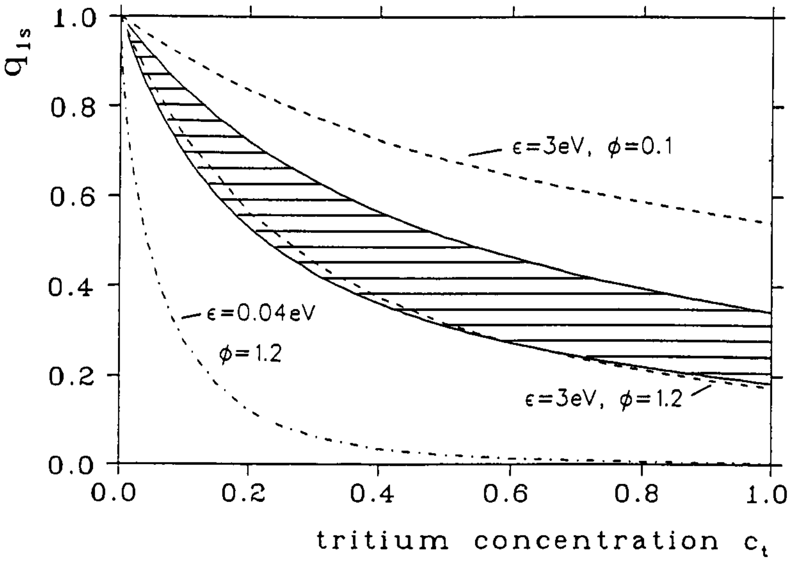

Fig. 4.2a. Theoretical prediction of the q_{1s} values [75] in the $(d\mu) + t \to (t\mu) + p$ transfer reaction and the experimental ones [76], extracted from neutron data in D–T μCF as a function of C_T at various $(d\mu)$ energies E and densities 4.

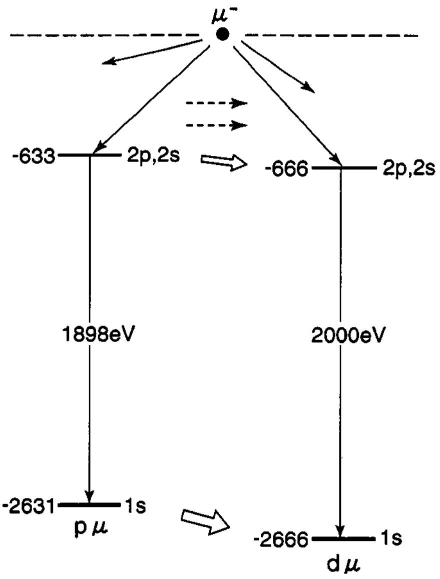

Fig. 4.2b. Scheme of $K\alpha$ X-rays studied concerning q_{1s} problems in the muon-transfer reaction of $\mu p + d \to \mu p + p$.

Such experiments became feasible only by adopting a high-resolution X-ray spectrometer. So far, two experiments have been carried out for the $(p\mu)$ to d transfer; (1) by using CCD charge-coupled devices at PSI [77] and (2) by using 7-channel segmented Si(Li) detectors at UTMSL/KEK and at RIKEN/RAL [78]. The results are depicted in Fig. 4.3a. There, we can easily notice that the experimentally obtained q_{1s} takes substantially weaker C_d dependence compared to the theoretical predictions. Possible explanations are as follows: (1) at the time of transfer reaction, $(p\mu)$ takes a high energy close to 5 eV [75]; (2) some unknown process exists in the cascade transitions of $(p\mu)$ or $(d\mu)$.

Theoretical Studies

Theoretical studies have been extended to cover the q_{1s} problem, energy dependence of the initial state, etc. Namely, fully quantum-mechanical calculations of muonic atom-nucleus collisions including muon transfer from the ground state have been extended up to ~ 50 eV cm energy by several groups with adiabatic representation methods [70, 71] and with non-adiabatic methods [72,73]. However, a fully quantum-mechanical approach to muon transfer from excited states is still in progress [80], though this is one of the most important theoretical problems to be solved in the μCF studies in relation to the q_{1s} problem. The difficulty in this approach is due to the long-range interaction ($\propto R-^2$) between the excited-state channels and the increased number of coupled channels. So far, a semi-classical calculation of the excited-state transfer has been performed [67].

An example of a possible unknown process may be the possible existence of the side-path proposed by Froelich and Wallenius [79], as depicted in Fig. 4.3b. The excited $(t\mu)_{2s}$ states formed via a transfer reaction from the excited $(d\mu)_{2s}$ states does collide with D_2 to resonantly form a $(dt\mu)$.* molecule with $n = 2$, which mostly decays into the $(d\mu)_{1s} + t$ channel [81]; apparently, $(d\mu)_{1s}$ is formed. This process can be considered as muon transfer from $(t\mu)_{2s}$ to $(d\mu)_{1s}$ via three-body resonances of $(dt\mu)$, This enlarges the $(d\mu)_{1s}$ population and improves the agreement with the experimental q_{1s}.

4.3. Formation of the Muon Molecule

Historical Background

The lifetime of μ^- in vacuum and in a muonic hydrogen atom is 2.20 μs, corresponding to a decay rate of $\lambda_0 = 0.455 \times 1\ 06\ s^{-1}$. Due to the heavy mass, the atomic ground state of μ^- around d or t is small (260 fm) and tightly bound (–2.7 ke V). A small neutral atom $(t\mu)$ may come close to d in D_2 or DT to form

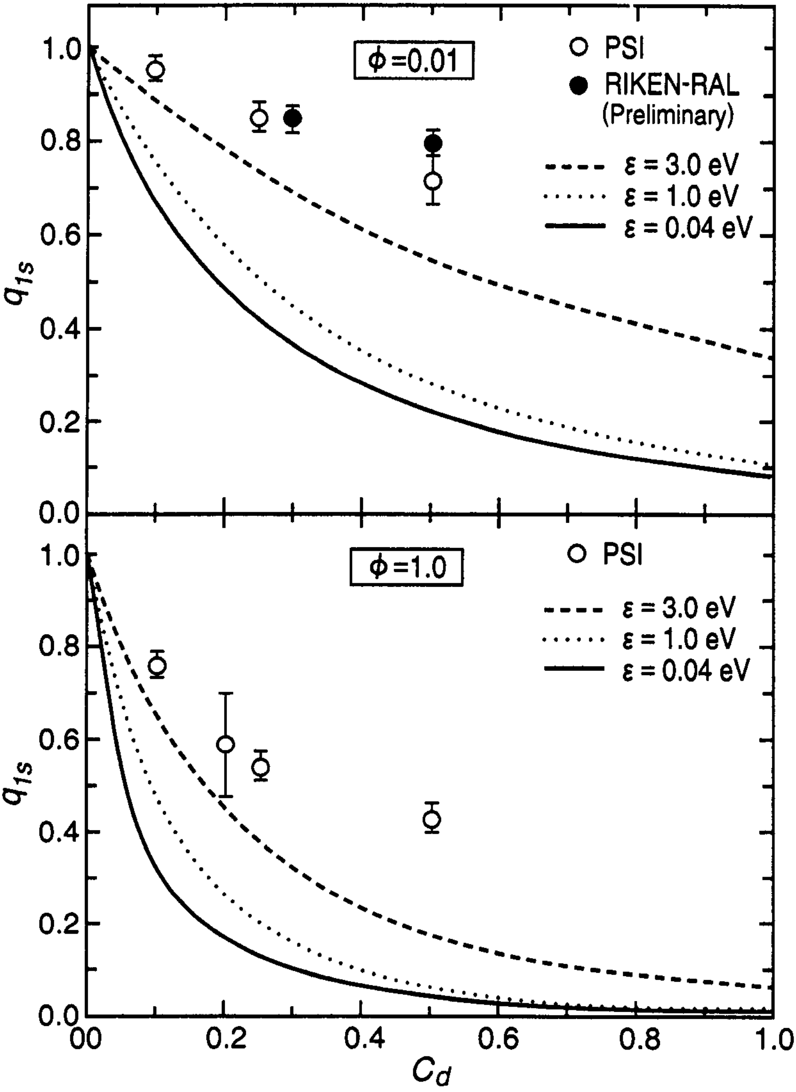

Fig. 4.3a. Experimental results of qls in $\mu p + d$ observed by X-ray measurements [77,78] and theoretical predictions [75].

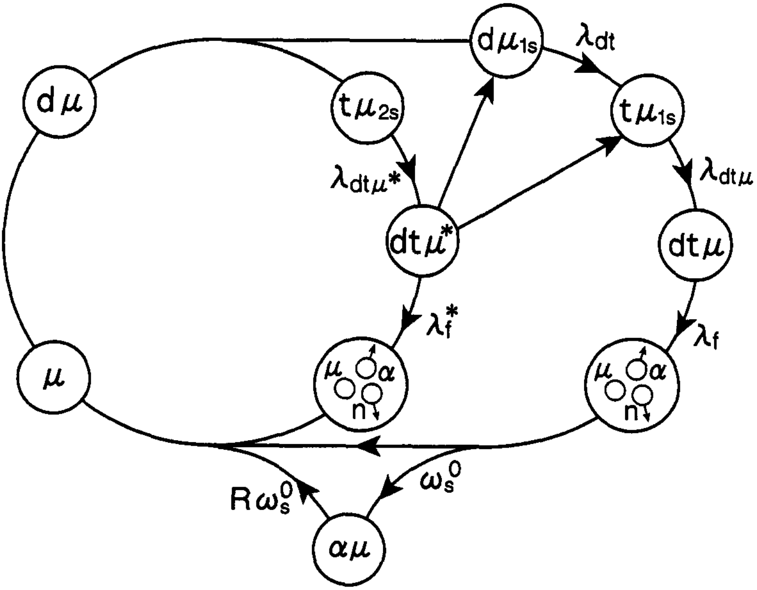

Fig. 4.3b. Schematic diagram of $dt\mu$–μCF cycle including side-path through the resonant formation of an excited molecule $(dt\mu)^*$ by Froelich *et al.* [79].

a small molecule of $(dt\mu)^+$, whose ground state is small in size (520 fm) and tightly bound (−300 eV). Usually, the rate of formation of a tightly bound molecular state is relatively slow. The most promising way is the so-called Auger capture, for example,

$$(d\mu) + D_2 \rightarrow [(dd\mu)\, de] + e^-$$
$$(t\mu) + D_2 \rightarrow [(dt\mu)\, de] + e^-$$

The theoretically predicted rate [82] for the final state of a muonic molecule becomes fairly slow, such as 10^6 s^{-1} (comparable to λ_0).

However, Ponomarev and collaborators [83] have theoretically predicted that an extremely shallow bound state with both a rotational and vibration angular momentum of one $(Jv) = (11)$ exists at an energy of $\epsilon_{11} = -0.6$ eV, measured from the threshold energy of $(t\mu)_{1s} + d$. Because of the existence of this shallow bound state, substantially enhanced formation rates are expected by the following reaction process called resonant molecular formations, as can be seen in Fig. 4.4:

$$(t\mu) + D_2 \rightarrow [(dt\mu)_{11}\, d2e]^* \qquad (\lambda_{dt\mu\text{–}d})$$
$$(t\mu) + DT \rightarrow [(dt\mu)\, 11\ t2e]^* \qquad (\lambda_{dt\mu\text{–}t})$$

Experimentally, the formation rate of muon molecule can be obtained through the relations between the observed cycling rate λ_c and the rate of the processes, e.g., λ_{df} and $\lambda_{dt\mu}$, shown in the diagram of Fig. 1.3. Let us consider high- density and high-C_t D–T μCF and assume that the atomic capture rate ($\lambda_{d\mu}$ and $\lambda_{t\mu}$) and fusion rate (λ_f) are sufficiently high compared to the muon decay rate ($\lambda_{d\mu}$, $\lambda_{t\mu}$, $\lambda_f \gg \lambda_0$). Then, the cycle time (λ_c^{-1}) is due to the waiting time of $d\mu$ for muon transfer to t and that to form the molecule.

$$\frac{1}{\lambda_c} \equiv \frac{q_{ls}C_d}{\lambda_{dt}C_1} + \frac{1}{\lambda_{dt\mu}C_d}$$

Here, the factor $q_{1s}\ C_d$ is the probability that the muon reaches the ground state of $d\mu$, reflecting the fact that the transfer rate in the excited states of $(d\mu)$ are very rapid, as is the excited-state cascade.

In the above formula for λ_c the maximum λ_c can be obtained for

$$C_t = (1+\gamma)^{-1}\ , \qquad \gamma = (\lambda_{dt}/q_{ls}\lambda_{dt\mu})^{1/2}$$

In a D–T mixture, there are three molecules D_2, DT and T_2 with the concentration ratios C_{D2}, D_{DT} and C_{T2} , respectively determined by the rate of chemical equilibrium. Thus, the rate $\lambda_{dt\mu}$ can be decomposed into the sum of two terms,

$$\lambda_{dt\mu} = \lambda_{dt\mu\text{–}d}C_{\mathrm{D}_2} + \lambda_{dt\mu\text{–}t}C_{\mathrm{DT}}$$

The idea of resonant molecular formation was experimentally confirmed, at least qualitatively, by the Dubna group in 1979 [84], and in more detail by the experiments at Los Alamos [33] and at PSI [34], where both “three-body effects” and a strange temperature dependence have been discovered. At the same time, a very rapid formation rate (order of 6 × 108 s^{-1}) was experimentally established for ø = $ø_0$ for a temperature range of up to 500 K [32]. These experimental data are summarized in Fig. 4.5a. Theoretical predictions based upon the resonant molecular formation have not been able to explain the observed temperature dependence of the molecular-formation rate; according to theoretical predictions, there should be a steeper decrease in $\lambda_{dt\mu}$ towards the lowest temperature.

Experimentally, the existence of nonlinear many-body collisions in

ldtμ–d has been consistently confirmed [33, 34]. There, the resonant process between $(t\mu)$ and D_2 proceeds under the influence of the other D_2,

$$(t\mu) + D_2 + D_2 \rightarrow [(dt\mu)\ d2e]^* + D_2$$

Experimental data have shown that such an effect does exist only for $(t\mu)$ + D_2 and not for (tμ) + DT. At the same time, the effect is effective only for $C_t \geq$ 0.3. Assuming $\lambda_{dt\mu} = \left[\lambda^{(1)}_{dt\mu\text{–}d} + \lambda^{(2)}_{dt\mu\text{–}d}\phi\right] C_d + \lambda^{(1)}_{dt\mu\text{–}t}C_t$, from the Los Alamos

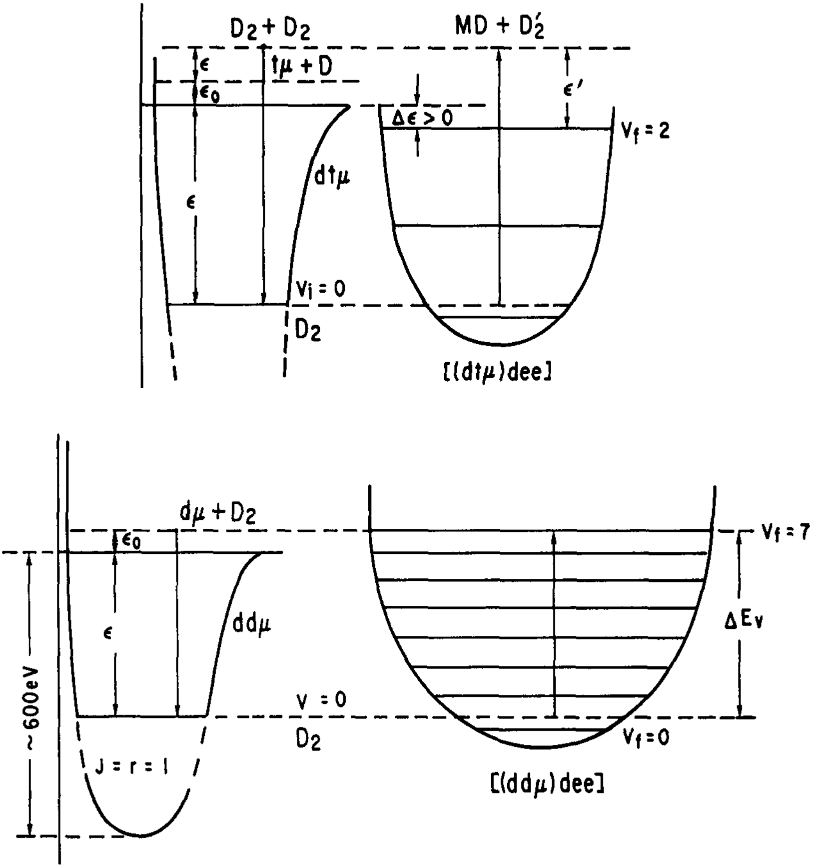

Fig. 4.4. Energy-level diagram for resonant molecular formation; *dt*μ vs *ddμ*.

experiment [33], the following values are obtained; $\lambda^{(1)}_{dt\mu-d} = 206\,(29)$, $\lambda^{(2)}_{dt\mu-d} =$ 450 (50) and $\lambda^{(1)}_{dt\mu-d} = 23$ (6) in the unit of 10_6 s_{-1} at the temperatures below 130 K.

The larger rate of $\lambda_{dt\mu-d}$ compared to $l_{dt\mu-t}$ predicts that an enhanced λ_c would be obtained for a non-equilibrated D–T mixture where D_2 and T_2 exist without forming DT (before the chemical reaction $D_2 + T_2 \rightarrow \frac{1}{2} D_2 + DT + \frac{1}{2} T_2$ is completed). This experiment has been conducted both at LAMPF and at PSI [74].

The importance of an ortho/para state of D_2 in $\lambda_{dt\mu}$ has been considered ei-

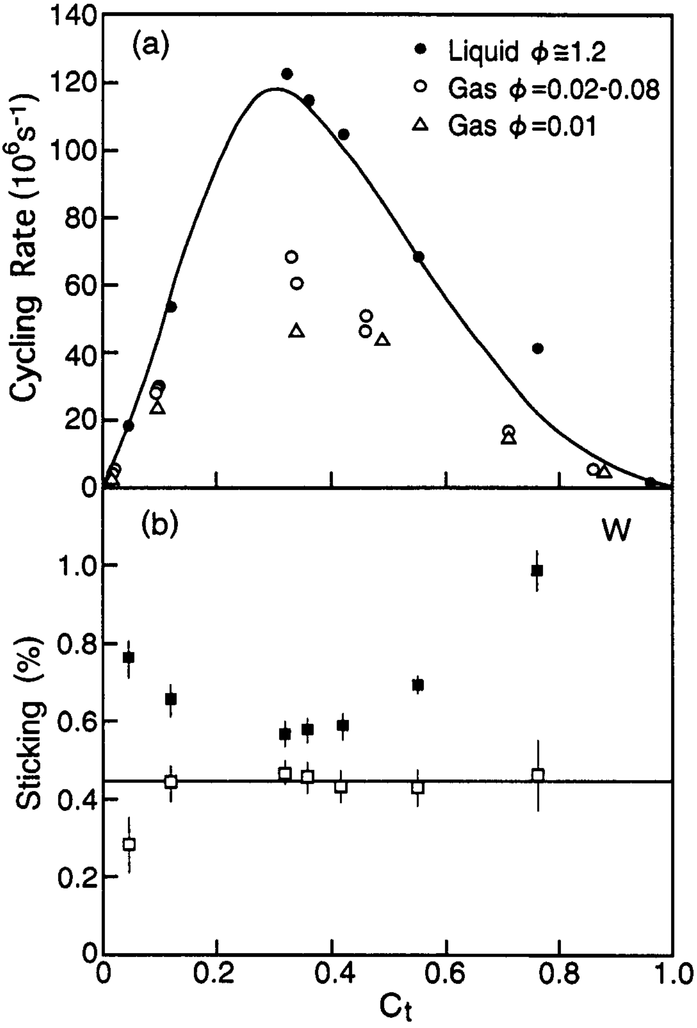

Fig. 4.5a. Experimental data concerning the cycling rate in DT-μCF as a function of C_T at various ø[34] and as a function of ø at various C_T [33].

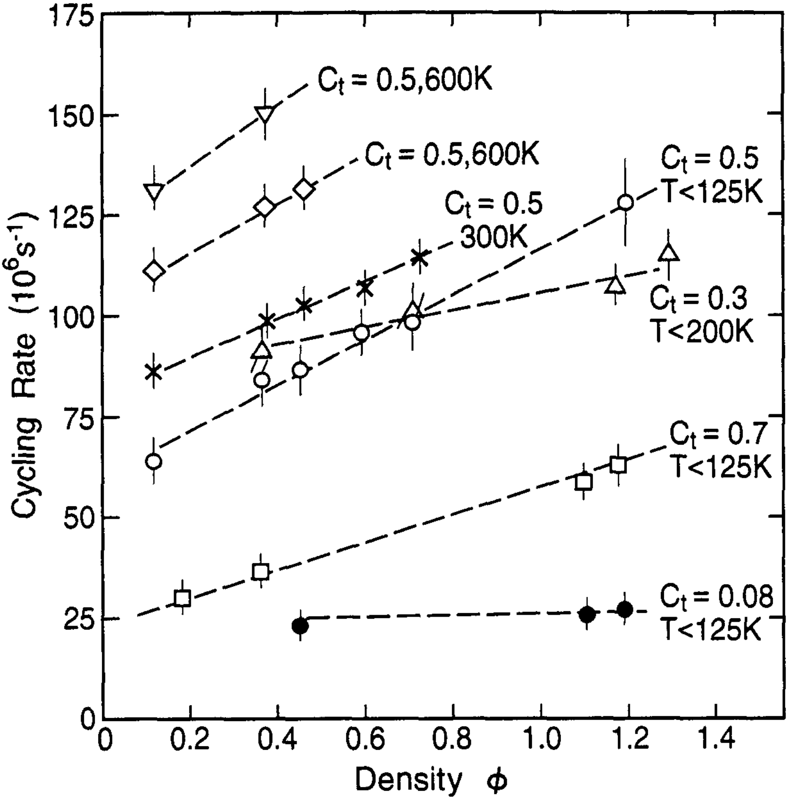

Fig. 4.5a. *(continued)*

ther in a gas or solid D–T mixture [85, 87]. Such an experiment has not yet been carried out yet.

Compared to the formation of $(dt\mu)$ the formation of $(dd\mu)$ can be more quantitatively explained by theoretical predictions. Actually, the idea of resonant molecular formation was suggested by Vesman [88] with a reference to an enhanced $(dd\mu)$ formation rate; sometime the resonant formation is called the Vesman mechanism. Experimentally, two components have been observed in the fusion neutron time spectrum, which can be interpreted as the dependence of the $(d\mu)$ spin-state on the molecular formation rate and with a hyperfine conversion rate in $d\mu$ ($F = 3/2 \rightarrow F = 1/2$) $\lambda_{d\mu}^{hf}$. Thus, the observed data at each temperature can be subdivided into two components. As can be seen in Fig. 4.6, the agreement seems to be perfect within a temperature range down to 30 K.

Thus, an overall agreement between theory and experiment has been achieved for DD μCF, and has not been obtained entirely for D–T μCF. This general ten-

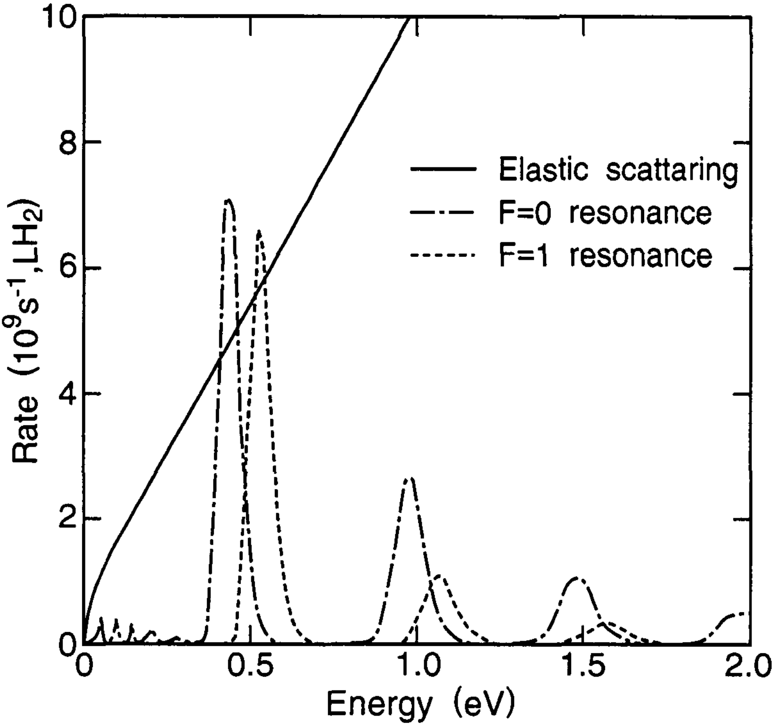

Fig. 4.5b. Predicted resonance structure of $t\mu + D_2$ at various energies of ($t\mu$) and 4 K and liquid-hydrogen density of D_2 compared with the rate of energy loss due to elastic scattering for two hyperfine states of $t\mu$ cited in Ref. [92].

dency can be qualitatively explained by considering the energy balance between the resonating muon molecular state and the electronic molecular state. As depicted in Fig. 4.4, an energy deficiency exists for DD μCF, while an energy excess exists for D–T μCF.

Experimental Studies

Recently, there has been remarkable progress in our understanding of the formation mechanism of a $dt\mu$ muon molecule. In order to observe the resonant molecular formation of energetic hot ($t\mu$) with D_2, two types of experiments were conducted. The epithermal mechanism of $dt\mu$ fusion was discovered at PSI [90] in triple H/D/T mixtures of hydrogen isotopes. The mechanism, discussed below, provides a wide range of opportunities to understand the reaction

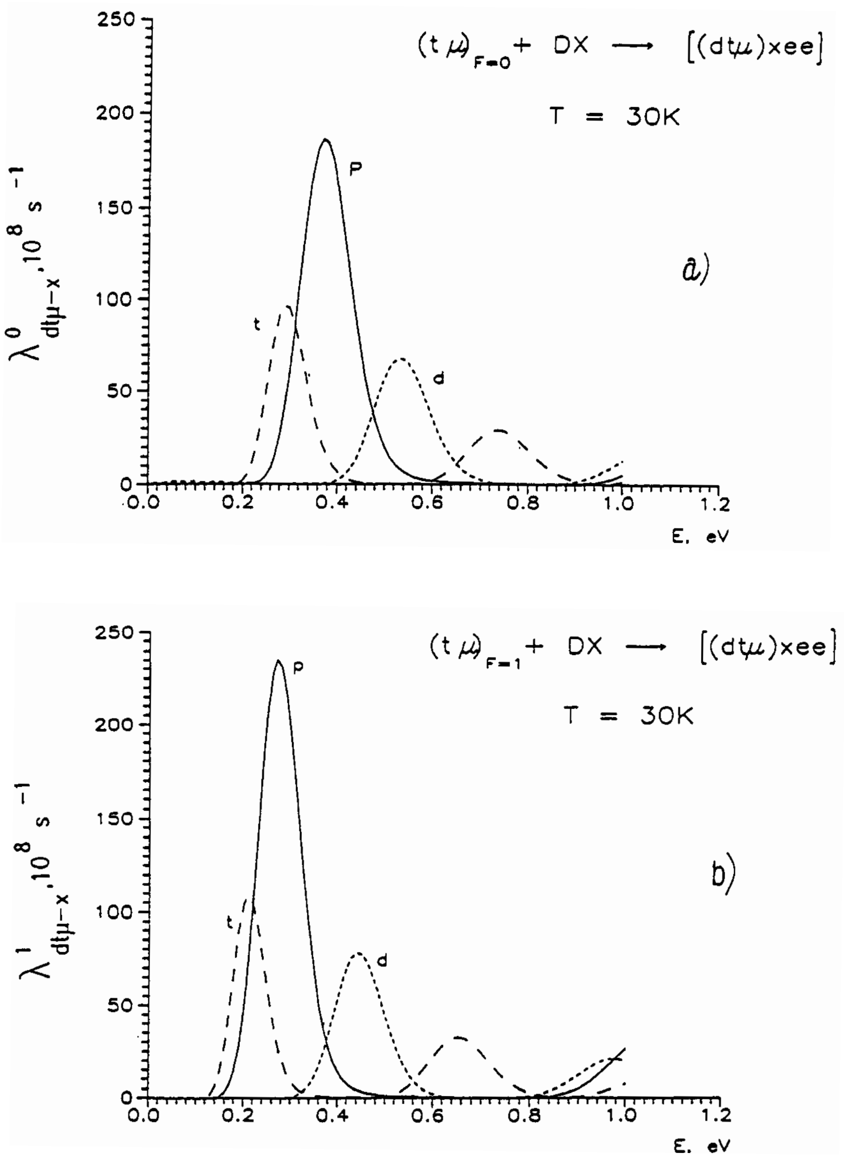

Fig. 4.5c. Dependence of the resonance reaction rates $\lambda_{dt\mu-x}$ (E), $x = (p,d,t)$, on the energy E of the $t\mu$ atom at $T = 30$ K; (a) $F = 0$, (b) $F = 1$, from Faifman and Ponomarev [86].

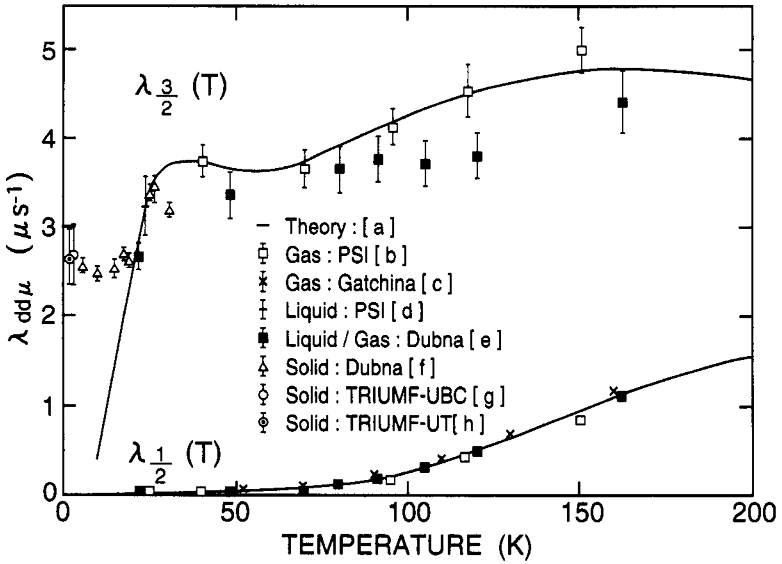

Fig. 4.6. Molecular-formation rates $\lambda_{dd\mu}^{(3/2)}$ and $\lambda_{dd\mu}^{(1/2)}$ measured in gas, liquid and solid, and theoretical predictions for gas and liquid. The data of TRIUMF-UBC and TRIUMF-UT are from Ref. [89] and Ref. [60] respectively. The rest are referred to in Ref. [89].

mechanism of various branches of the fusion cycle, especially, fast atomic and molecular processes with hot $t\mu$ atoms at high density. After the discovery of the epithermal mechanism in a triple mixture, several calculations were made of physical processes which actually takes place [86, 91].

In a triple mixture, fast (tu) and ($d\mu$) atoms with an initial kinetic energy 45 eV and 43 eV are generated via isotope-exchange reactions;

$$(p\mu) + t \rightarrow (t\mu) + p + 182.8 \text{ eV}$$
$$(p\mu) + d \rightarrow (d\mu) + p + 134.7 \text{ eV}$$

with high rates of $\lambda_{pt} = 0.7 \times 10^{10}$ s^{-1} and $\lambda_{pd} = 1.7 \times 10^{10}$ s^{-1} respectively at ø =1 [86].

The emerging fast ($d\mu$) atoms transfer to fast ($t\mu$) with E = 20 eV via a charge-exchange reaction

$$(d\mu) + t \rightarrow (t\mu) + d + 48.0 \text{ eV}$$

also with a high rate of $\lambda_{dt} \cong 10^{10}$ s^{-1}. Therefore, at amoderate concentration C_t, the ($t\mu$) atoms are mainly formed with an initial kinetic energy of20 eV due to the processes $(p\mu) \rightarrow (t\mu)$ and $(p\mu) \rightarrow (d\mu) \rightarrow (t\mu)$. Owing to the Ramsauer–Townsend effect, since the eV-$(t\mu)$ atom has a large mean-free-path, it has a significant chance to collide with a host molecule to from a muonic molecule $(dt\mu)$ via the Vesman mechanism before thermalization.

Valuable experimental information has been obtained by employing a H/D/T mixture with small C_d and C_t [76]. There, all $(t\mu)$ atoms are formed through transfer processes of $p\mu \rightarrow t$ or $d\mu \rightarrow t$, producing hot $(t\mu)$ atoms. The characteristic epithermal peak in the fusion neutron time spectrum was seen in an experiment at PSI which was qualitatively explained by the following formation process; $t\mu$+ HD $\rightarrow$ $[(dt\mu)\,\text{pee}]^*$. The details concerning a resonating state in HD will be mentioned later.

Another way to observe $dt\mu$ formation with energetic hot $(t\mu)$ is an experiment with an eV $(t\mu)$ beam; an eV $(t\mu)$ "beam" is obtained from the solid layer of H_2 + 0.1% T_2, where a recoiling eV $(t\mu)$ after $(p\mu) + t \rightarrow (t\mu) + p$ reaction can be emitted from the surface ofthe solid layer with the help ofa reduced cross section between $(t\mu)$ and H_2 due to the Ramsauer–Townsend mechanism. The eV $(t\mu)$ was injected into a separated D_2 layer, and the energy dependence in $\lambda_{dt\mu}$ was measured by time-of-flight technique at TRIUMF [92]. As theoretically predicted [63] (see Fig. 4.5b), the existence of a resonance at 0.5 eV has been confirmed; there, the need of a reduction in an energetic $t\mu + D_2$ resonance structure by a factor oftwo was also noticed.

Recent experiments involving X-rayheutron measurements on D–T μCF in high-density and high-C_t D–T mixture at RIKEN-RAL have also produced, in addition to muon sticking phenomena, important new insights concerning the formation mechanism of $dt\mu$. The results can be summarized as follows:

1, The density dependence, which had been observed from the gas phase to the liquid phase (ϕ = 1.2) [33, 34], seems to exist from liquid to solid (ϕ = 1.5) from $C_t = 0.28$ to $C_t = 0.70$, suggesting that the three-body collision effect in $\lambda_{dt\mu}$ does coexist under the condensed-matter effect.

2. The 3He accumulation effect, really significant in solid but not significant in liquid, has been precisely measured in order to be used for an interpretation of $\lambda_{d\mu}$.

As for the well-understood DD μCF, as summarized in Fig. 4.6, it was found that there is a marked deviation between the experiment and theory below 20 K, corresponding to the solid phase [60, 89,93, 94]. The deviation should be explained by the following two mechanisms (either one of two or both of them): a) due to a non-thermalization effect [64] during the slowing-down of $(d\mu)$, the existence of an energy gap in solid D_2 does suppress complete slowing-down, thus producing a non-thermalized epithermal $(d\mu)$ (energy of about 20 K); b) the reaction mechanism of the molecular formation may be dramatically changed due to a change in the final-state energy spectrum [87, 95].

Theoretical Studies

An accurate calculation of the energy of the $(Jv) = 11$ state of $(dt\mu)$, €_{11}, was one of the main subjects of a theoretical study of muon catalyzed fusion throughout the 1980's. As a pure Coulomb-interacting three-body problem, the energy was given as $\text{€}_{11} = -0.64$ eV by Vinitsky *et al.* [96], and −0.656 eV by Gocheva *et al.* [97], with an adiabatic representation. Using a variational method with an elliptic basis, Vinitsky *et al.* [98], and Korobov *et al.* [99], gave $\text{€}_{11} = -0.6589$ eV and −0.65968 eV, respectively. Finally, $\text{€}_{11} = -0.66001$ eV was obtained by Szalewicz *et al.* [100], with a Hylleraas basis, −0.660104 eV by Kamimura [101] with a Gaussian basis in Jacobian coordinates and −0.6601 72 eV by Alexander and Monkhorst [102] with Slater geminals. It should be noticed that, at this level of accuracy, the energy €_{11} may be affected by ~ 0.1 meV by an uncertainty in the masses of d, t and μ [101].

Among the various computational methods employed in the above studies, the most general, flexible and rapid one may be the Jacobian-coordinate coupled-rearrangement-channel method [101], which has been commonly used in calculations of the energy levels, fusion rate, sticking probability, muon transfer reaction and dissociation of excited molecules. A formulation in Jacobian coordinates is very advantageous for a correct description of the very loosely bound states, the dissociation process and the scattering states; use of basis functions spanned over the three rearrangement channels suffers little from the linear dependence between the large-scale basis functions, working entirely in 64-bit precision arithmetic on supercomputers. This method has also been applied [103] very accurately to the three-nucleon bound states (^{3}H, ^{3}He) with a faster convergence of the solution than in the Faddeev-method calculations [103].

There are several corrections to €_{11} which are larger than 1 meV. These include nuclear finite-size effects, nuclear polarization effects, relativistic and QED (vacuum polarization) effects, hyperfine effects and energy shifts caused by the host molecule. The total corrections to €_{11} amount to ~ +60 MeV, for a review of these corrections, see another publication [4].

Theoretical studies are needed for understanding the surprising aspects in the $dt\mu$ formation rates; (a) strange temperature dependence and (b) three-body collision effects. A theoretical calculation which had been used to calculate the transition matrix elements in the dipole approximation has been extended to include the quadrupole terms [104]. However, except for a slight reduction in the absolute rate, an explanation for the temperature dependence does not take a significant improvement.

A theoretical understanding of the origin of the three-body collision effects has been obtained only qualitatively. As suggested in the argument related to Fig. 4.4, in a $(t\mu)y + D_2$ collision, a partner is needed to absorb any excess energy for the resonance condition. Petrov [105] has shown how to incorporate the three-body effect in the form of the resonance-width, while Menshikov *et al.* [106], have developed a theoretical treatment which includes the effect of the potential from the surrounding molecules. On the other hand, Leon [107] has developed a theory based upon a microscopic multi-step process.

The possible existence of resonance states above the $d\mu + t$ threshold has been discussed in several theoretical papers [108, 109].These states are the so-called Feshbach type resonance; three-body electric correlation effects produces the resonance states. The fusion rates and sticking probabilities have also been calculated [8]. The existence of a state at around 1815 eV (with reference to the lowest $(t\mu)_{1s}$ has been discussed based on a complex coordinate-rotation method [110]. There have been no experimental studies to see the effect of these resonance states. The formation rate of these states and the rate of slowing-down due to elastic scattering should be calculated before we see such an effect.

In $(dt\mu)$ formation, the lowest accessible vibrational transitions lie below the threshold (as shown in Fig. 4.4, the kinetic energy of the collision partners would have to be negative to reach them) the strongest resonant contributions to molecular formation since are due to higher vibrational transitions, which correspond to the kinetic energy of the collision partners of several hundred MeV. In a triple mixture of H/D/T, three types of resonant reactions are possible:

$$t\mu + D_2 \rightarrow [(dt\mu)dee]$$
$$t\mu + DT \rightarrow [(dt\mu)tee]$$
$$t\mu + HD \rightarrow [(dt\mu)pee]$$

The rates of the first two reactions and the third one were calculated by Faifman and Ponomarev [86] for a $(t\mu)_{F=0.1}$ energy of $E \leq 1$ eV (Fig. 4.5c). The fast muonic atoms $(t\mu)$ realize the above three reactions with the high rate of $10^{10}s^{-1}$ at energies of the $(t\mu)$ atoms, $E = 0.2$–0.5 eV before thermalization. Physical processes which take place in the triple mixture H/D/T were extensively studied by a Monte-Carlo simulation by Markushin *et al.* [91].

4.4. He Impurity Effect

Historical Background

The effect of the existence of He impurities in D–T μCF is inevitable problem for the following two reasons: a) due to t beta-decay, when there is no ^{3}He removal system, ^{3}He accumulates steadily (100 ppm per day); b) the product of ^{4}He after D–T μCF also accumulates, which may cause serious problems.

On the other hand, the μ^- transfer phenomena from *p, d, t* to ^{3}He, ^{4}He is of special interest for the following reasons: (a) this transfer reaction is known not only to be the most fundamental process other than transfer among hydrogen isotopes, but also to be anomalously fast compared to the conventional direct exchange process; (b) this transfer reaction gives us an opportunity to learn about the structure of a muon molecule by X-ray spectroscopy.

Historically, the formation of the (d^4Heμ) state was proposed by Popov *et al.*, in order to explain the anomalously high μ^- transfer rate from hydrogen isotopes to the He impurity [111,112]. According to this model, the following process is expected to take place (see Fig. 4.7); instead of a direct exchange reaction of $(d\mu) + {}^4\mathrm{He} \rightarrow [(d^4\mathrm{He}\mu)\ e^-]^+ + e^-$, the molecular ion is formed through $(d\mu) + {}^4\mathrm{He} \rightarrow [(d^4\mathrm{He}\mu)\, e^-]^+ + e^-$, where the molecule ($d^4$Heμ) is preferentially formed in the $J = 1$ state of the ($2p\sigma$) state. In this case, the characteristic photon spectrum can be predicted: aunique peak energy (6.8 keV versus 8.2 keV of K_α line in Heμ) with a broad and asymmetric shape (Fig. 4.7).

At UT-MSLKEK, such an experiment was carried out for a liquid D_2 target with He impurity (430 ppm), which was dissolved by pressurizing the liquid D_2 surface with 2 atmospheres of He gas [113]. The observed results are shown in Fig. 4.7 for the time-integrated energy spectrum at a delayed time after μ-injection (from 0.28 to 7.5μs). There, a characteristic asymmetric and broad photon peak was observed with a central energy of 6.85 (4) keV and a width of 0.74 (4) ke V, agreeing quite well with the theoretical reductions [111, 112].

Based upon the predicted energy spectrum and the observed one, one can conclude that a radiative transition photon was observed. The present result nicely confirms the model of the muon-transfer mechanism through the formation of a muon molecule. At the same time, this result can be considered to be the first experiment to actually “see” a muon molecule.

Experimental Studies

After the first X-ray observation of a (d^4He μ) molecule, a ($d\mu$)-to-He transfer experiment has been extended to see the isotope effect, namely to study the difference with 3He. The expected nature of (d^4He μ) molecule in terms of the energies of the molecular levels predicts that no big difference exists between the radiative photon intensities that could be seen in these two transfer reactions.

The X-ray spectra first observed at UTMSL/KEK [114], as seen in Fig. 5.1, has shown a surprising difference at around 6.8 keV, a significant peak can be seen in $d^4\mathrm{He}\mu$, while only a weak one can be seen in $d^3\mathrm{He}\mu$ In combination with the difference in the muon-molecule formation rate and concentration, the expected difference in 6.8 keV-photon intensity becomes 0.138. Later, similar results and a more precise energy spectrum were obtained at PSI using a CCD detector [115].

Theoretical Studies

There are four types of decay modes of the muonic molecules $(d^{3,4}\mathrm{He}\mu)_{J=1}$ which have attracted strong theoretical interest:

1. Radiative decay: $(d\,^{3,4}\mathrm{He}\mu)_{J=1} \rightarrow (^{3,4}\mathrm{He}\mu)_{1s} + d + \hbar\nu(\sim 6.8\,\mathrm{keV})$,
2. Fusion decay: $(d^3\mathrm{He}\mu)_{J=1} \rightarrow {}^4\mathrm{He} + p + \mu$,
3. Particle decay: $(d^{3,4}\mathrm{He}\mu)_{J=1} \rightarrow (^{3,4}\mathrm{He}\mu)_{1s} + d$,
4. Auger decay: $\left[(d^{3,4}\mathrm{He}\mu)^{e-}_{J=1}\right] \rightarrow (^{3,4}\mathrm{He}\mu)_{1s} + d + e^-$.

Calculations of the radiative decay of $(d^4\mathrm{He}\mu)$ by Aristov *et al.* [111], and by Hara and Ishida [121] have explained the observed photon spectrum, which provided the first direct evidence for the existence of muonic molecules. The radiative decay rate λ_r given by [116] is $1.55 \times 10^{11}\ \mathrm{s}^{-1}$ for $(d^3\mathrm{He}\mu)J{=}1$ and $1.69 \times 10^{11}\ \mathrm{s}^{-1}$ for $(d^4\mathrm{He}\mu)_{J=1}$.

The fusion reaction rate λ_f of $(d^3\mathrm{He}\mu)_{J=1}$ is given in Table 2.1 a. We can see that the fusion process is negligible compared with the radiative decay from the states with $J = 0$ and $J = 1$. It is then needless to say that no fusion occurs in the $(d^4\mathrm{He}\mu)$ molecule, Therefore, it is clear that the fusion branch is not an origin of the observed strong reduction of the radiative decay in $(d^3\mathrm{He}\mu)$ compared with that in $(d^4\mathrm{He}\mu)$.

It was first predicted by Kamimura [116] that strongly reduced radiative decay branching ratio should be observed in the case of $(d^3\mathrm{He}\mu)$; while for $(d^3\mathrm{He}\mu)$ particle decay is much stronger than the radiative decay, this is not the case for $(d^4\mathrm{He}\mu)$. The enhancement of particle decay in $d^3\mathrm{He}\mu$ compared with that in $d^4\mathrm{He}\mu$ essentially comes from the fact that the kinetic energy (zero-point oscillation) in the former is larger than that in the latter, simply due to the smaller

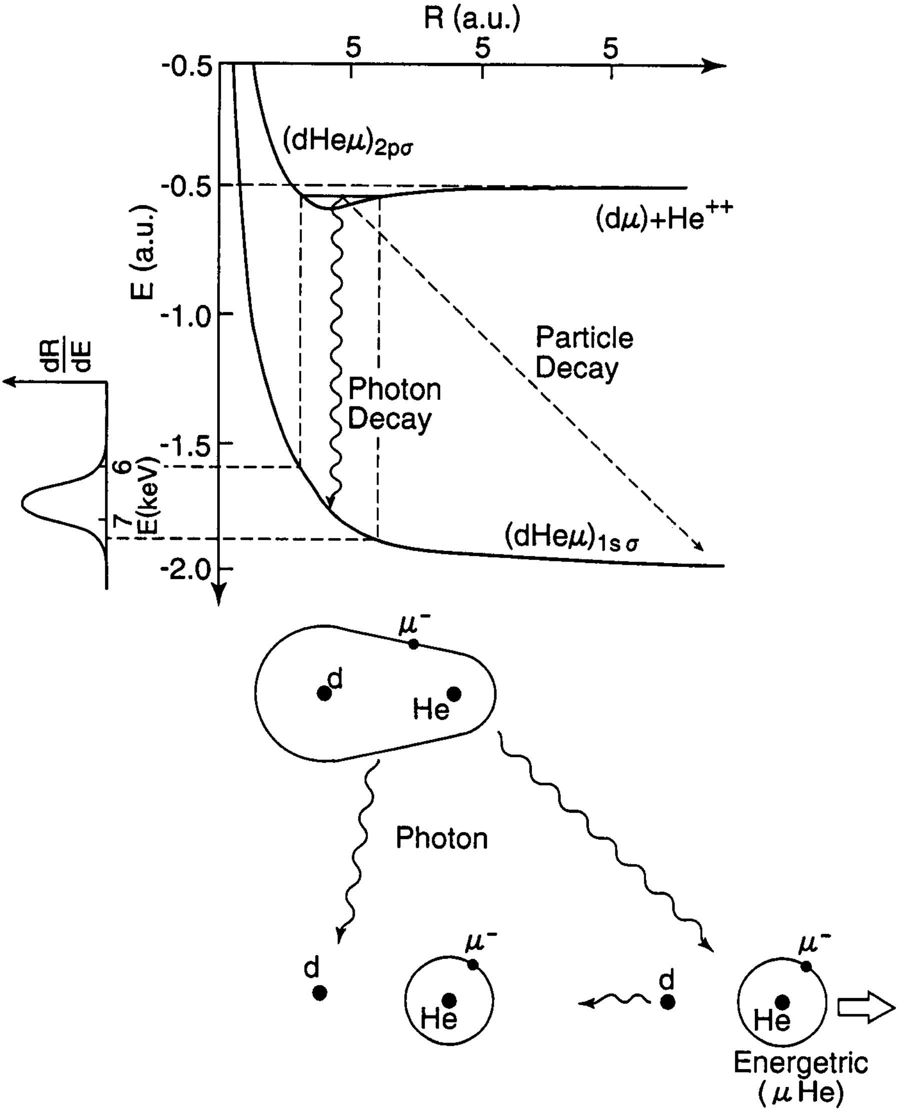

Fig. 4.7. Schematic energy diagram explaining μ^- transfer from *d* to He through the formation of a (*d*He*μ*) molecule with a predicted photon energy spectrum of the radiative transition and the observed photon spectrum from liquid D_2 with 193 ppm ^{4}He and that with 250 ppm ^{3}He [114].

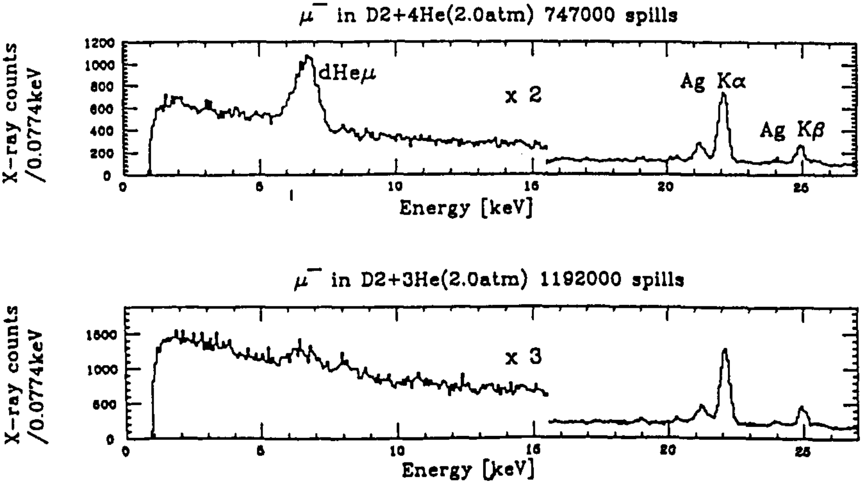

Fig. 4.1. *(continued).*

TABLE 4.1

Properties of a Hydrogen–Helium–Muon Molecule; Binding Energies, E_B (eV) Radiative-Decay Rates $\lambda\gamma(10^{11}\ s^{-1})$ and Particle-Decay Rates λ_p $(10^{11}\ s^{-1})$

System	Ref.	$J=0$			$J=1$		
		EB	$\lambda\gamma$	λp	*EB*	$\lambda\gamma$	$\lambda\pi$
$p^3He\mu$	[a]	69.0	2.11	47.3	38.1	1.74	31.6
$p^4He\mu$	[a]	75.4	2.24	35.4	45.4	1.89	24.8
$d^3He\mu$	[a]	70.6	1.80	3.58	48.2	1.58	2.77
	[b]	70.946	1.75e	4.70	48.419	1.55^e	5.06
	[c]				48.421		5.29
	[d]	69.96		8.0	46.75		7.0
$d^4He\mu$	[a]	78.7	1.94	1.85	57.6	1.74	1.38
	[b]	77.430		1.60	58.221	1.69^e	1.67
	[c]				58.225		1.80
	[d]	77.96		2.3	56.10		2.4
$t^3He\mu$	[a]	72.3	1.70	0.79	53.4	1.53	0.66

[a] A. V. Kravtsov *et al.* [1 17]

[b] Y. Kino and M. Kamimura [1 18]

[c] V. I. Korobov [2 19]

[d] S. S. Gerstein and V. V. Gusev [I20]

[c] S. Hara and T. lshihara [I21]

mass of ^{3}He. Along with this consideration, further prediction was made of an even stronger reduction of radiative decay in (p^4Heμ) than in (d^3Heμ).

In order to calculate more accurately the width of such highly excited (~ 8 keV) Feshbach-type resonances, Kino and Kamimura [118] developed a direct numerical method to solve the resonant states under the explicit scattering boundary condition for the d–(Heμ)$_{1s}$ channel. The resulting energy and width of the $J = 0$ and 1 resonance are listed in Table 4.1 together along with the results by other authors. We can thus see that the branching ratio of the radiative decay is given by

$$\frac{\lambda_r}{\lambda_r + \lambda_p} = \left\{ \begin{array}{lll} 0.234 & \text{for} & (d\,^3\text{He}\mu)_{J=1} \\ 0.503 & \text{for} & (d\,^4\text{He}\mu)_{J=1} \end{array} \right\}$$

This predicts that the ratio of the strength of the radiative decay from (d^3Heμ) to that from (d^4Heμ) is 0.234/0.503 = 0.465 as long as the formation probabilities of the two muonic molecular states are normalized to be the same. This ratio explains well the observed value of the ratio, 0.38 ± 0.06 [114].

Auger decay of the hydrogen–helium muonic molecules was investigated by Kravtsov *et al.* [117]. They concluded that the Auger rate is independent of the isotopic content of the molecule and amounts to ~ 25% of radiative one. Although deexcitation from $J = 1$ to $J = 0$ via an inner-Auger effect is energetically not allowed for (dHeμ) molecules, the possibility of deexcitation via an outer-Auger effect has been pointed out by Czaplinski *et al.* [31]. More extensive theoretical and experimental studies of the decay mechanism are expected in order to thoroughly understand these interesting muonic molecules.

5. ENERGY PRODUCTION OF MUON CATALYZED FUSION

Initially the ideas about μCF were motivated by the dream of achieving fusion energy from, perhaps, thousands of fusion catalysis by each muon. These hopes were dampened by the early experiments in which only a hundred or so catalyses were found, largely because of ^{4}He-sticking. However, other possible applications followed. At this moment, the following three subjects are under serious discussions towards realization; a) an energy source; b) a 14 MeV neutron source and c) an ultra-slow μ^- source. Let us re-evaluate here the first subject, namely, the potential of μCF for energy production.

In order to consider the energy-production efficiency, it is required to know how much energy is needed to produce a single muon (a muon cost). There have been several discussions on the optimization of the π^- production and $\pi^- \rightarrow$

TABLE 5.1
Examples of Pion and Muon Cost Estimations

Author	Reaction	π^-/E (GeV)	μ^-/E (GeV)	Conditions
Petrov and Shabelski[a]	t(1 Gev)–t	0.25	0.20	50% elastically scattered t is unused
	t(1 GeV)–C, Be	0.22	0.17	
	d(1 GeV)–C	0.17	0.125	
Jändel[b]	d–D–T (ø < 0.1)		0.5	infinite D–T target
Kuzminov, Petrov and Shabelski[c]	d(0.8 Gev)–[D–T (ø = 0.50)]	0.19		multiple NN collision and 10 T field considered
Letysheva *et al.*[d]	d(2 GeV)–C, Be	0.22		internuclear cascade code

[a] Reference [122, 123]
[b] Reference [124]
[c] Reference [125]
[d] Reference [I26]

μ^- conversion. For π^- production, the fundamental processes in the nucleon-nucleon inelastic process are $nn \rightarrow pn\pi^-$ and $np \rightarrow pp\pi^-$. Therefore, the use of accelerated nuclei other than protons is inevitable. A deuteron beam as well as a triton beam have been considered for a cost (energy) estimation for economical μ^- production.

Following the argument made by Petrov *et al.* [122, 123], a realistic solution seems to be as follows. By using a 1 GeV/nucleon t (d) beam bombarded onto Li or Be nuclei, we can obtain 0.22 (0.17) π^- from a single t(d). By using a large- scale superconducting solenoid with a reflecting mirror, one can expect 75% efficiency for μ^- conversion from a single π^- Thus, a 1 GeV energy of t (d) produce 0.17μ^- so that one μ^- can be produced by an energy of 6 (8) GeV. Further, by selecting the values mentioned for π^- production in a t–t collision [122] the eventual cheapest cost would be about $\pi^-/4$ GeV and $\mu^-/5$ GeV.

Several ideas have been proposed for reducing the muon cost. Studies have been done for optimizing the type of incident accelerated particle, particle energy and choice of the fixed target. By summarizing these studies [124, 125, 126], as shown in Table 5.1, the optimization does not seem to exceed the value mentioned above ($\pi^-/4$ GeV). Another method to reduce the π^- production cost is to use a colliding beam. In this case, the energy of the center-of-mass motion, which is wasted at a fixed target geometry, would be efficiently used. It is claimed that $\pi^-/1.8$ GeV (0.55p-/GeV) can be realized by a d–d collider [127]. However, the realization of a collider with megawatts in each beam is totally uncertain.

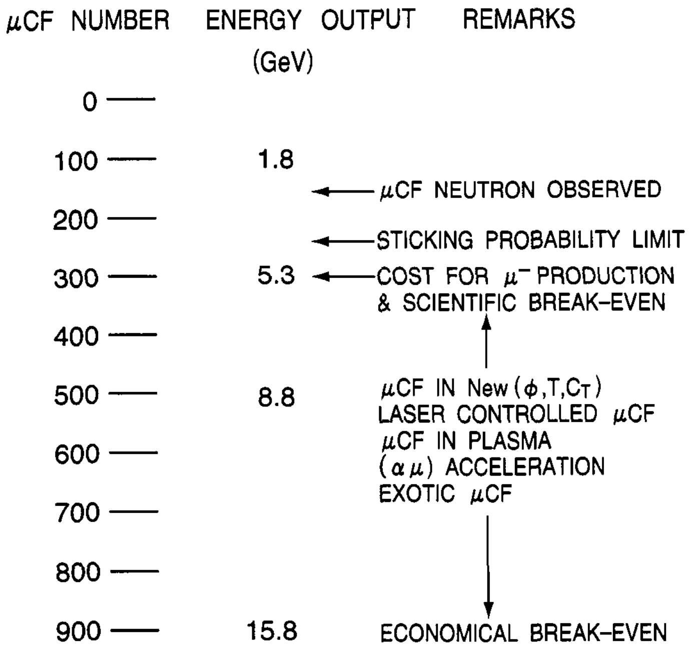

Fig. 5.1. Number of fusions and produced energy from *dtμ*-*μ*CF with required remarks.

As for the development of high-efficiency scheme of $\pi^- \rightarrow \mu^-$ conversion, because of the strong demand for an intense μ^- beam from fundamental physics experiments of a) lepton flavor non-conservation, and b) $\mu^+\mu^-$ colliders, there have been a number of proposals for a realistic form. Some of these examples [122, 128, 129, 130, 131, 132] are summarized in Table 5.2.

On the other hand, the energy-production capability $E^{\mathrm{out}}_{\mu cF}$ of the μCF is determined by $E^{\mathrm{out}}_{\mu cF} = 17.6 \times Y_n$ (MeV) in the case of D−T μCF, which has a stringent limiting factor due to the sticking probability ws like $E^{\mathrm{out}}_{\mu cF} \leq 17.6 \times \omega^{-1}_s$ (MeV). The situation pertaining to $E^{\mathrm{out}}_{\mu cF}$ is summarized in Fig. 5.1.

Several remarks can be given for a possible increase in the energy- production capability from the D–T μCF: a) since the conditions so far used for the D−T target in the μCF experiment, namely, density, temperature and C_t as well as the energy of the $(t\mu)$ atoms $E_{t\mu}$ controlled by the mixture of H_2 into D–T mixture have not been satisfactory, there might exist more favorable conditions toward higher energy production; the μCF experiment at a higher density D–T mixture, like $ø \equiv 2ø_0$, should be the typical example; b) in order to increase $\lambda_{dt\mu}$, more favorable matching condition in terms of resonant molecular formation might exist which will be realized by exciting the molecular levels of D_2 or DT by e.g.,

TABLE 5.2

Proposed High Efficiency $\pi^- \rightarrow \mu^-$ Converter for an Intense μ^- Source at Various High- Intensity Hadron Accelerators

Project	Institute	Accelerator			$P(d)/s$	μ^-/s	μ-/$p(d)$	μ^-/Power (p,d) (MW)
L.F.N.C[a]	INR–Moscow	*p*,	500 MeV,	100 μA	6.3×10^{14}	10^{11}	1.6×10^{-4}	1.6×10^{16}
L.F.N.c.[b]	AGS–BNL	*p*,	24 GeV,	3 μA	2.0×10^{13}	4×10^{11}	0.020	5.6×10^{14}
$\mu^+\mu^-$ Collidec	BNLetc.	*p*,	30 GeV,	0.25 μA	$2.5 \times 10^{13}/15$	$4 \times 10^{12}/15$	0.16	2.2×10^{14}
μCF *n*-Source[d]	PSI	*d*,	1.5 GeV,	12 mA	7.5×10^{16}	10^{15}	0.013	4.2×10^{15}
General Purpose[e]	JHF–KEK	*p*,	3 GeV,	200 μA	1.3×10^{15}	1.3×10^{13}	0.01	2.2×10^{15}
μCF Reactor[f]	Gatchina	*d*,	1.5 GeV,	12 mA	7.5×10^{16}	1.5×10^{16}	0.20	2.2×10^{14}

[a] Reference [I28]
[b] Reference [I29]
[c] Reference [130]
[d] Reference [I31]
[e] Reference [I32]
[f] Referece [I23]

lasers; c) in order to decrease ws, or in order to increase *R*, several ideas have been proposed, and, among them, the use of a D-T plasma where enhanced regeneration is expected due to an elongated $(\alpha\mu)^+$ mean-free path [133] as well as the application of electric field acceleration of $(\mu\alpha)^+$ [134] might be worth trying; d) in an actual 10 ~ 100 MW power plant, if it exists, there might be several μ^- associated atoms or molecules interacting with each other, and thus causing a new non-linear phenomena possibly associated with a higher energy production which should be examined by using a high-brightness muon beam, like slow μ^-.

Contrary to the energy-production solely via the μCF, the concept of muon catalyzed hybrid reactor has been proposed by Petrov [135] and later by Eliezer *et al.* [136]. There, the accelerated 1 GeV/nucleon d beam is bombarded on a Li or Be target with the remaining beam stopping in ^{238}U, where ~ 30% of the beam is spent on π^- production and 70% is spent on ^{238}U fission and ^{238}Pu production as electronuclear breeding. The produced π^- is used for the μCF in D-T mixture, where produced 14 MeV neutron stops in the blanket of ^{238}U and ^{6}Li producing ^{239}Pu and T. The Pu thus produced is used for a thermal nuclear reactor and the fission energy is used to feed the accelerator and the rest of the system. It is concluded that the proposed hybrid system can double the electric-power output of non-hybrid electronuclear breeding. There is an argument against the use of the μCF for fuel production of a thermal nuclear reactor because it brings all the problems of nuclear reactor, like radioactive waste disposal, etc.

In summary, the possibility of energy production by μCF still remains elusive. It is tantalizingly close but still just beyond reach. The physics remains exciting and, perhaps, some new discoveries will bring it closer.

6. FURTHER APPLICATION OF MUON CATALYZED FUSION

6.1. 14 MeV Neutron Source

When thermal nuclear fusion becomes realistic, it is pointed out to be important to develop a material to be used for the first wall next to the inner-most core ofthe fusion reactor. For this purpose, it is important to investigate a highly irradiation test facility for 14 MeV neutrons. One practical idea is to have an intense source of a 200 keV *d* beam and produce 14 MeV neutrons via the $d + t \to \alpha + n$ reaction [137]. In parallel to this idea, the 14 MeV neutrons from the μCF can be considered to be an alternative way for such a materials irradiation facility.

Some realistic schemes have been considered [131, 138]. Let us consider a 1.5 GeV (1 2 μA) deuteron accelerator available. By placing a 30–50 cm graphite target in the confinement field of a 5–10 T superconducting solenoid, intense pion production and efficient μ^- production can be realized. There, the μCF in the D–T target occurs, followed by intense 14 MeV neutrons (on the order of $10^{14}n$ /cm^{2}s) for the material under testing placed at one surface of the DT container. Most importantly, the power consumption by the μCF method is substantially lower compared to that in the 200 keV *d* accelerator method (~ 1 / 10!). An alternative idea has been proposed by Petrov [139]. Some realistic plant design is in progress.

6.2. Slow μ^-

For the case of negative muons (μ^-), it has been found to be very difficult to produce an intense slow μ^- beam due to the following reasons: (1) because of a strong absorption of stopped π^- inside matter, the π^- -to- μ^- decay cannot be realized inside the target material, so that there is no surface μ^-, except for a small probability for liquid H_2 or He; (2) because of muonic atom formation, the stopped μ^- cannot be liberated from the stopping material after thermalization inside the condensed matter, and, thus, no re-emission can be expected for the case of μ^-. The situation is, of course, very different for slow μ^+ production.

For a more realistic estimation, the kinetics in μCF must be taken into account. In order to overcome the second difficulty, a new idea has been proposed for the source of slow μ^-, which will be realized with the help of μCF phenomena [140]. The principle is as follows (see Fig. 6.1): (a) at the disappearance of the core nuclei of 5He at the instant of μCF, a slow μ^- with an energy of around 10 keV is released; (b) this liberation process is known to be repeated up to 150 times during the μ^- lifetime; (c) after successive liberation processes of slow μ^-, we can expect that a significant fraction of the μ^- stopping inside a thin solid D–T layer would be re-emitted from the surface.

When there are no leakage processes from the D–T layer, (solid and C_t being around 0.3 ~ 0.5) the conversion efficiency can be estimated to be the ratio of the range of the 10 keV μ^- (0.3 μm) versus that of the incoming μ^- with an energy of, say, 1 MeV (0.9 mm). The multiplication factor due to the number of μCF cycles is $\cong\sqrt{150}$, thus giving $\sqrt{150}\times 0.3\times10^{-3} / 0.9 = 0.004$. For a more realistic estimation, the kinetics in μCF must be taken into account. For instance, the diffusion length of the neutral ($d\mu$) or ($t\mu$) gives a significant correction to the value mentioned above. Assuming 1 μm for the diffusion length of ($d\mu$) and (tμ) in the D-T layer with a 7 μm layer thickness, the conversion efficiency from stopping 1 MeV a μ^- (below 10 keV) emissions is around 2×10^{-4} instead of 4×10^{-3}.

In order to enhance the conversion efficiency, a two-layer structure was proposed by G. M. Marshall which would form an optimized D–T layer on a 1 mm thick H_2 layer with 0.1% T2 (see Fig. 6. 1), the range of the injected MeV μ^- can be effectively reduced due to the Ramsauer–Townsend effect. Already, in

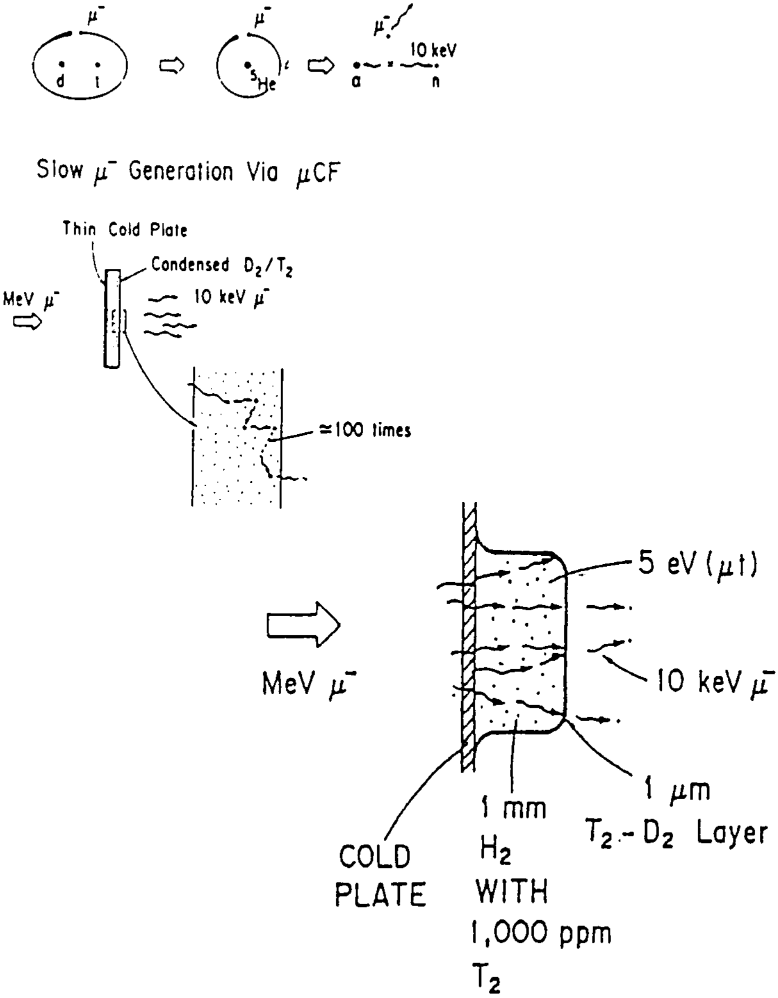

Fig. 6.1. Schematic view of low-energy μ^- production from D–T μCF in a thin solid layer of a D–T mixture and its extended version with a Ramsauer-effect enhancement.

order to confirm the reduced range concept, test experiments have been carried out at UTMSL/KEK and at TRIUMF for DD μCF by using 2 eV ($d\mu$) from the $H_2(D_2)$ mixture. There, a value of 1.5 μm was obtained. Assuming that eV ($t\mu$) stopping in the D_2 layer is similar to eV ($t\mu$) stopping in the D–T layer, one can obtain the conversion efficiency from 1 MeV μ^- to the slow μ^- in a two-layer configuration, like 2×10^{-4} [0.9 (mm)/1.5 (μm)] $\times \epsilon_{t\mu} = 0.12\, \epsilon_{t\mu}$, where $\epsilon_{t\mu}$ is the emission probability of eV ($t\mu$) from stopping μ^-. From our knowledge, is around 0.1, leading to a conversion efficiency of 0.012 [141].

The generation of intense slow μ^- has an important application field, namely, as a μ^- ion source for $\mu^+\mu^-$ colliders; for the TeV lepton colliders, acircular accelerating and colliding machine is possible only for muons which have much lower synchrotron radiation loss than electrons and yet live long enough to form colliding beams. A slow muon source, as already realized for the μ^+ [142] along with the slow μ^- source described here, can be efficiently used for a realistic cooling method of muons [143].

7. CONCLUSIONS AND FUTURE PERSPECTIVES

Sometimes, each step in the historical development of an event is described by the time-sequential progress of (a) introduction, (b) succession, (c) change and (d) conclusion/finale. According to our understanding, at the time of the present review, the μCF studies stay at the time of "change."

During the earlier two steps, the μCF studies have realized marked significant progress like; a) rapid formation rate of muon molecule via resonant formation processes, b) quantitative understandings (at least trial) of μ to a sticking, c) muon transfer among *p, d, t* and the importance of a transfer from excited states, etc. The interaction between theory and experiments has proceeded nicely by exchanging surprising new discoveries.

There are several reasons, as described in earlier chapters, why we call the present stage of the μCF research "change."

Experimentally, the importance of a "condensed-matter effect" has been consistently appreciated regarding the following experimental evidence;

a) anomalous T-independent and large $\lambda_{dd\mu}$ in solid D_2;
b) the existence of an epithermal (dμ) and enhanced stopping-rate of ($d\mu$) in a solid D_2 layer;

Also, new experimental situations such as energetic ($t\mu$) and ($d\mu$), have been employed to investigate exotic reaction phenomena beyond thermal equilibrium reactions with an energy of kT. There, the following new insights have been obtained:

a) by using an eV ($t\mu$) beam, direct evidence has been obtained for the existence of a 0.5 eV resonance in ($\lambda_{dt\mu}$);

b) by using H/D/T triple mixture, an enhanced formation of ($dt\mu$) has been detected due to the effect of a high-energy resonance.

Theoretically, for a satisfactorily scientific understanding of the μCF cycles, it is interesting and important i) to study the deceleration and acceleration of muonic hydrogen atoms during a muonic cascade, ii) to calculate elastic and inelastic scattering and transfer reactions of excited muonic hydrogen atoms in a fully quantum mechanical manner, iii) to calculate the rates of formation and dissociation of muonically excited states of $dt\mu$ molecules, and iv) to revisit the muon–4He initial sticking in any advanced treatment. The calculations ii) and iii) are expected to contribute to a resolution of the q_{1s} problem.

In application fields, "change" has been detected in the following directions;

a) The 14 MeV neutron source, by μCF phenomena is now attracting much attention, so that realistic plant designs are going on in several institutions;

b) Because of strong requests from particle physicists, an intense μ^- source design is now seriously in progress, which may help us to learn a realistic way to achieve a μ^-/π^- conversion rate of 0.75.

Throughout these steps up to today, there are several experimental facts which have been left unexplained by any theoretical study. Significant examples are as follows;

a) T-dependence of $\lambda_{dt\mu}$ in particular, dependence towards $T \rightarrow 0$.

b) Three body collision effect in $\lambda_{dt\mu}$ exhibiting its ø-dependence.

From "change" to "finale," several future perspectives can be suggested.

1, Experimentally, there should be eventual studies over a wider range of conditions for the D–T mixture (ø, T, C_t, C_{He}, ortho/para, etc). Thus, by covering the entire region of the μCF under various condensed-matter environments one can elucidate the "few-body μCF problem" under "many-body background."

2. It is interesting and important to study μCF under exotic conditions: μCF in molecular-state controlled D_2 or DT by e.g., lasers, μCF in D–T plasma, etc., with the help of a strong pulsed μ^- source. Such an experiment is not beyond our reach at all.

3. Also, under the condition of the availability of more than 10^{10}/s intense μ^- (with hopefilly pulsed time-structure), non-linear μCF phenomena might become effective; the existence of e.g., one $[(dt\mu)\,d2e]^+$ might be affected by the second one, etc.

Thus the field of μCF remains vigorous with many challenging issues to be confronted and with the continued promise of fascinating physics.

ACKNOWLEDGMENTS

We acknowledge the contributions of our collaborators in the μCF studies; Drs. T. Matsuzaki, K. Ishida, S. N. Nakamura, N. Kawamura, S. Sakamoto, M. Iwasaki, Y. Watanabe, and Y. Kino and J. Wallenius. Helpful discussions with Professors I. Shimamura, the late T. Ishihara, T. Watanabe, M. Leon, J. S. Cohen, and P. Froelich are also acknowledged. We are grateful to encouragements from Professors T. Yamazaki, T. Nishikawa, A. Arima, H. Narumi, and E. W. Vogt.

REFERENCES

1. F. C. Frank, Nature **160** (1947) 525.
2. A. D. Sakharov, Report FIAN, M. (1948) I.
3. L. W. Alvarez *et al.,* Phys. Rev. **105** (1957) 1127.
4. W. H. Breunlich, P. Kammel, J. Cohen, and M. Leon, Ann. Rev. Nucl. Sci. **39** (1989) 311.
5. J. S. Cohen, Nucl. Instr. **B42** (1989) 419.
6. L. I. Ponomarev, Contemporary Phys. **31** (1990) 219.
7. C. Petitjean, Nucl. Phys. **A543** (1992) 79c-98c.
8. P. Froelich, Advances in Physics **41** (1992) 405.
9. Proceedings of μCF-86 (Tokyo); Muon Catalyzed Fusion **1** (1987).
10. Proceedings of μCF-87 (Gatchira); Muon Catalyzed Fusion **213** (1988).
11. Proceedings of μCF-88 (Sanibel Island); AIP Conference Proceedings **181** (1989).
12. Proceedings of μCF-90 (Vienna); Muon Catalyzed Fusion **5/6** (1990).
13. Proceedings of μCF-92 (Uppsala); Hyperfine Interactions **82** (1 993).
14. Proceedings of μCF-95 (Dubna); Hyperfine Interactions **101/102** (1996).
15. L. N. Bogdanova *et al.,* Sov. Phys. JETP **56** (1982) 931.
16. J. D. Jackson, Phys. Rev. **106** (1957) 330.
17. Ya. B. Zel'dovitch and S. S. Gershtein, Sov. Phys. USPEKHI, **3** (1961) 593.
18. L. N. Bogdanova *et al.,* Sov. J. Nucl. Phys. **34** (1981) 662; L. N. Bogdanova, Muon Catalyzed Fusion **3** (1988) 359.
19. J. L. Friar *et al.,* Phys. Rev. Lett. **66** (1991) 1827.
20. C. Petitjean *et al.,* Muon Catalyzed Fusion **5/6** (1990/91/261.
21. L. Bracci *et al.,* Phys. Lett. **A134** (1989) 435.
22. P. Baumann *et al.,* Muon Catalyzed Fusion **5/6** (1990191) 87.
23. W. H. Breunlich *et al.,* Muon Catalyzed Fusion **1** (1987) 121.
24. A. V. Kravtsov *et al.,* JETP Lett. **40** (1984) 875.

25. M. Kamimura, private communication to K. Nagamine, as reported in p.27 of Proceedings [11].
26. M. C. Struensee *et al.,* Phys. Rev. **A37** (1988) 340.
27. M. Kamimura, AIP Conf. Proc. **181** (1989) 330.
28. N. Jarmie *et al.,* Phys. Rev. **C28** (1984) 2031,
29. K. Szalewicz and B. Jeziorsky, Muon Catalyzed Fusion **5/6** (1990/1991) 241.
30. L. J. Wittenberg *et al.,* Fusion Technology **10** (1986) 167.
31. W. Czaplinski *et al.,* Z. Phys. **D37** (1996) 283.
32. S. E. Jonesetal., Phys. Rev. Lett. **51** (1983) 588, 1757.
33. S. E. Jones *et al.*, Phys. Rev. Lett. **56** (1986) 588.
34. W. H. Breunlich *et al.,* Phys. Rev. Lett. **58** (1987) 329.
35. C. Petitjean *et al.,* Muon Catalyzed Fusion **2** (1988) 37.
36. H. Bossy *et al.,* Phys. Rev. Lett. **59** (1987) 2864.
37. K. Nagamine, T. Matsuzaki, K. Ishida *et al.,* Muon Catalyzed Fusion **1** (1987) 137.
38. K. Nagamine, T. Matsuzaki, K. Ishida *et al.,* Muon Catalyzed Fusion **5** (1990) 239; K. Nagamine, T. Matsuzaki, K. Ishida *et al.,* Hyperfine Interactions **82** (1993) 343.
39. S. E. Jones, AIP Conf. Proc. **181** (1989) 2; M. A. Paciotti *et al.,* ibid 38.
40. J. D. Davies *et al.,* AIP Conf. Proc. **181** (1989) 52.
41. C. Petitjean *et al.,* Muon Catalyzed Fusion **516** (1990/91) 261.
42. T. Case *et al.,* Muon Catalyzed Fusion **516** (1990/91) 327; **K.** Lou *et al.,* ibid 525.
43. J. S. Cohen, Phys. Rev. Lett. **58** (1987) 1407.
44. V. E. Markushin, Muon Catalyzed Fusion **3** (1988) 395.
45. H. Takahashi, Muon Catalyzed Fusion **1** (1987) 623.
46. M. C. Struensee and J. S. Cohen, Phys. Rev. **A38** (1988) 44.
47. H. E. Rafelski *et al.,* Prog. Part. Nucl. Phys. **22** (1989) 279.
48. C. D. Stodden *et al.,* Phys. Rev. **41A** (1990) 1281.
49. K. Nagamine, Hyperfine Interactions **8** (1981) 787; Z. Phys. **C56** (1992) 5215.
50. K. Nagamine, T. Matsuzaki, K. Ishida *et al.*, Hyperfine Interactions **85** (1994) 343; **101/102** (1996) 521.
51. D. Ceperley and B. J. Alder, Phys. Rev. **A31** (1985) 1999.
52. L. N. Bagdanova *et al.,* Nucl Phys. **A454** (1986) 653.
53. C.-Y. Hu, Phys. Rev. **A34** (1986) 2536.
54. S. E. Haywood *et al.,* Phys. Rev. **A37** (1988) 3393.
55. L. N. Bogdanova *et al.,* Sov. J. Nucl. Phys. **50** (1989) 848.
56. B. Jeziorski *et al.*, Phys. Lett. **A43** (1991) 1640.
57. J. Cohen, G. M. Hale, and C. Y. Hu, Hyperfine Interaction **101/102** (1996) 349.
58. M. Kamimura, Muon Catalyzed Fusion **1** (1987) 333.
59. V. S. Melezhik, Hypefine Interactions **101/102** (1996) 365.
60. P. Strasser *et al.,* Phys. Lett. **B368** (1996) 32.
61. G. M. Marshall *et al.,* Proc. Int. Symp. on Muon Catalyzed Fusion, Oxford (1986)(RAI-90-022); B. M. Foster *et al.,* Hyperfine Interactions **65** (1990) 1007.
62. M. Bubak and M. P. Faifinan, Preprint JINR **E4-89-464** (1987).
63. V. E. Markushin, Hyperfine Interactions 101/102 (1996) 155.
64. A. Adamczak and V. S. Melezhik, Muon Catalyzed Fusion **2** (1988) 131.
65. V. E. Markushin *et al.,* Hypefine Interactions **82** (1993) 373.
66. A. Adamczak, Hyperfine Interactions 101/102 (1996) 113.
67. L. Manshikov and L. I. Ponomarev, Sov. Phys. JETL Lett. **39** (1984) 542.
68. V. S. Melezhik, Muon Catalyzed Fusion **2** (1988) 117.
69. K. Koboyashi *et al.,* Muon Catalyzed Fusion **2** (1988) 191.
70. C. Chiccoli, Muon Catalyzed Fusion **7** (1992) 87.
71. V. 1.Korobov, Hyperline Interactions **82** (1993) 31.

72. M. Kamimura, Muon Catalyzed Fusion **3** (1988) 335; Y. Kino and M. Kamimura, Hyperfine Interactions **82** (1993) 45.
73. A. A. Kvitsensky *et al.*. Phys. Rev. **A47** (1993) 994.
74. P. Acherbauer *et al.,* Hyperfine Interactions **82** (1993) 357.
75. W. Czaplinski *et al.,* Phys. Rev. **A50** (1994) 518 and 525.
76. P. Ackerbauer *et al.,* Hyperfine Interactions **101/102** (1996) 67.
77. B. Lauss *et al.,* Hyperfine Interactions **101/102** (1996) 285.
78. S. Sakamoto *et al.,* Hyperline Interactions **101/102** (1996) 297.
79. P. Froelich and J. Wallenius, Phys. Rev. Lett. **75** (1995) 2108.
80. I. Shimamura, A. lgarashi and T. Shirai, a talk at ∝CF-95 (Dubna).
81. Y. Kino and M. Kamimura, Hyperfine Interactions **101/102** (1996) 191,
82. L. I. Ponomarev and M. P. Faifman, Sov. Phys. JETP **44** (1976) 886.
83. S. S. Gershtein and L. J. Ponomarev, Phys. Lett. **72B** (1977) 80.
84. V. M. Bystritsky *et al.,* Sov. Phys. JETP **53** (1981) 877.
85. M. Leon and J. S. Cohen, Phys. Rev. **A31** (1985) 2680.
86. M. P. Faifman and L. I. Ponomarev, Phys. Lett. **B265** (1991) 201.
87. K. Fukushima, Phys. Rev. **A48** (1 993) 4 130.
88. E. A. Vesman, JETP Lett. **5** (1967) 91.
89. P. E. Knowles *et al.,* Hyperfine Interactions **101/102** (1996) 21.
90. T. Case *et al.,* Muon Catalyzed Fusion **5/6** (1990191) 327.
91. V. E. Markushin *et al.,* Muon Catalyzed Fusion **7** (1992) 155; Hyperfine Interactions **82** (1993) 373.
92. G. M. Marshall *et al.,* Hyperfine Interactions **101/102** (1996) 47.
93. G. M. Marshall *et al.,* in Muonic Atoms and Molecules, ed. L. Shaller and C. Petitjean (Birkhausen Verlog, Basel/Boston/Berlin (1993).
94. D. L. Demin *et al.,* Hyperfine Interactions **101/102** (1996) 13.
95. L. 1. Menshikov and V. V. Filchenkov, Hyperfine Interactions **101/102** (1996) 207.
96. S. I. Vinitsky *et al.,* Sov. J. Phys. JETP **52** (1980) 353.
97. A. D. Gocheva *et al.,* Phys. Lett. **B153** (1985) 349.
98. S. I. Vinitsky *et al.,* Sov. Phys. JETP **64** (1986) 417.
99. V. I. Korobov *et al.*, Phys. Lett. B196 (1987) 272.
100. K. Szalewicz *et al.,* Phys. Rev. **A336** (1 987) 5494.
101. M. Kamimura, Phys. Rev. **A38** (1988) 621.
102. S. A. Alexander and H. J. Monkhorst, Phys. Rev. **A38** (1988) 26.
103. H. Kameyama, M. Kamimura, and Y. Fukushima, Phys. Rev. **C40** (1989) 974: M. Kamimura and H. Kameyama, Nucl. Phys. **A508** (1990) 17c.
104. M. P. Faifman, Hyperfine Interactions **101/102** (1996) 179.
105. Y. V. Petrov, Phys. Lett. **163B** (1985) 28.
106. L. I. Menshikov and L. I. Ponomarev, Phys. Lett. **1670** (1986) 141.
107. J. S. Cohen and M. Leon, Phys. Rev. **39A** (1989) 946; M. Leon, Phys. Rev. **39A** (1989) 5554.
108. P. Froelich and K. Szalewicz, Phys. Lett. **A129** (1988) 321.
109. S. Hara and T. Ishihara, Phys. Rev. **A40** (1989) 4232.
110. C-Y. Hu and A. K. Bhatia, Muon Catalyzed Fusion **516** (1990/91) 439.
111. Yu. A. Aristov *et al.,* Sov. J. Nucl. Phys. **22** (I981) 564.
112. A. V. Kravtov *et al.*. Phys. Lett. **A83** (1981) 379.
113. T. Matsuzaki *et al.,* Muon Catalyzed Fusion **2** (1986) 217.
114. K. Ishida *et al.,* Hyperfine Interactions **82** (1993) 185.
115. Gartner *et al.,* Hyperfine Interactions **82** (1993) 195.
116. M. Kamimura, private communication (1991) cited in the report Ref. [114].
117. A. V. Kravtsov *et al.,* Z. Phys. **D29** (1994) 49.

118. Y. Kino and M. Kamimura, Hyperfine Interactions **82** (1993) 111.
119. V. I. Korobov, Hyperfine Interactions **101/102** (1996) 329.
120. S. S. Gershtein and V. V. Gusev, Hyperfine Interactions **82** (1993) 185.
121. S. Hara and T. Ishihara, Phys. Rev. **A39** (1989) 5633.
122. Yu. V. Petrov and Yu. M. Shabelski, Sov. J. Nucl. Phys. **30** (1979) 66.
123. Yu. V. Petrov, Atomken. Kerntech. 46 (1985) 25.
124. M. Jaendel *et al.,* Muon Catalyzed Fusion 3 (1988) 577.
125. V. V. Kuzninov *et al.,* Hyperline Interactions 82 (1993) 423.
126. L. N. Latysheva *et al.,* Hyperfine Interactions **101/102** (1996) 669.
127. G. Chapline and R. Moir, LLNL Report (1986).
128. V. S. Abadjev *et al.,* INR preprint 786192 (1992).
129. W. Molzon *et al.,* UCI Physics: Technical Report #96-30.
130. R. Palmer *et al.,* Nuclear Physics B (Proc. Suppl.) **51A** (1996) 61.
131. C. Petitjean, PSI Report PSI-PR-93-09 (1993).
132. A. Bogacz, K. Ishida, and K. Nagamine, internal report (1996).
133. K. I. Menshikov and L. I. Ponomarev, JETP Lett. **46** (1987) 312.
134. H. Daniel, Muon Catalyzed Fusion **5/6** (1990/91) 335.
135. Yu. V. Petrov, Nature **285** (1980) 466; Yu. V. Petrov, Atomnaya Energia **63** (1987) 333.
136. S. Eliezer, T. Tajima, and M. Rosenbluth, Nucl. Phys. **27** (1987) 527.
137. M. Martone, ENEA-Frascati (1990).
138. S. Monti, ENEA NUC-RIN Bologna (1991).
139. Yu. V. Petrov *et al.,* PNPI Preprint (1992).
140. K. Nagamine, Proc. Japan Academy **65B** (1989) 225.
141. K. Nagamine *et al.,* Muon Catalyzed Fusion **5/6** (1990/91) 376.
142. K. Nagamine, Y. Miyake, K. Shimomura *et al.,* Phys. Rev. Lett. **74** (1995) 4814.
143. K. Nagamine, Nucl. Phys. **51A** (1996) 115.
144. M. Leon, LA-UR-93-3538 (1993).

INDEX